



POLITECNICO
MILANO 1863

SCUOLA DI INGEGNERIA INDUSTRIALE
E DELL'INFORMAZIONE

Design and Operation of a binary ORC power plant for the exploitation of single and two-phase geothermal resources

TESI DI DOTTORATO IN
SCIENZE E TECNOLOGIE ENERGETICHE E NUCLEARI (STEN)
- ENERGY AND NUCLEAR SCIENCE AND TECHNOLOGY

Author: **Tristan Leonard Merbecks**

Student ID: 10834168

Advisor: Paola Bombarda, Martin O. Saar, Paolo Silva

Co-advisors: Dario Alfani, Claudio Pietra, Joseph Bonafin

Academic Year: 2021-24

Cycle: XXXVI

The doctoral research has been carried out in the context of an agreement on joint doctoral supervision between Politecnico di Milano, Italy, and ETH Zurich, Switzerland.

Abstract

Historically, power generation from two-phase and single-phase (liquid) geothermal resources has been confined to direct steam plants and binary plants respectively. Binary plant technology tends to provide a number of operational advantages over direct steam plant technology: ease of maintenance, effective surface handling and re-injection of possible co-produced Non-condensable gases (NCG), which can be harmful or have a Global Warming Potential (GWP). **The present work focuses on the comparison between the two technologies, with particular emphasis on two-phase geothermal fluids.** The design of geothermal power plants is a demanding task; different technologies, plant configurations and working fluids must be considered, and the optimum plant design is strongly dependent on the inlet conditions, composition, thermophysical properties and phase behaviour of the geofluid. Moreover, the impact and cost of handling and re-injecting non-condensable gases must be accounted for.

Geofluid modelling has historically been focused on two research fields: 1) partitioning the geofluid into separate phases, and 2) the estimation of the thermophysical properties of these phases. Recognising potential synergies between these models, *GeoProp* is introduced, a novel geofluid modelling framework, which addresses this niche by coupling existing state-of-the-art fluid partitioning simulators, such as *Reaktoro*, with high-accuracy thermophysical fluid property computation engines, like *CoolProp* and *ThermoFun*.

Simulation of geothermal power plants using commercial software, such as *Aspen Plus v11* faces some drawbacks; 1) accuracy of the thermophysical properties and phase behaviour models, particularly for geofluids with a multi-component chemical composition, and 2) important phenomena, such as wet expansion effects in steam turbines, are difficult to capture. With this in mind, *PowerCycle* has been developed, a novel power plant simulation tool, which allows the use of virtually any thermophysical property model (e.g. *CoolProp* and *GeoProp*), and provides geothermal power generation specific component models for turbines, heat exchangers, pumps/compressors etc.

With these tools the thermodynamic and techno-economic performance of binary Organic Rankine Cycle (ORC) and single flash Direct Steam Cycle (DSC) geothermal power plants

is compared for two-phase geothermal resources in the range of 423 K to 548 K; a parametric study on the effect and handling of NCG integrates the investigation. For thermodynamic optimised power plants, binary ORCs were found to produce equal power with respect to single flash DSC plants at geofluid vapour qualities as high as 85 %. For technoeconomically optimised plants equal specific power plant cost were obtained for vapour qualities as high as 80 %. With regards to the handling of NCG, binary ORCs are better suited than single flash DSCs, for all considered scenarios (venting to the atmosphere, re-injection into the reservoir and partial dissolution). DSCs spend significant power on re-pressurising NCG for disposal, be it for venting to the atmosphere or re-injection into the reservoir. While the latter is virtually uneconomical for single flash DSC geothermal power plants it could be easier to realise with binary ORC power plants, due to the higher NCG pressures at the plant outlet and thus lower re-pressurisation power requirements.

Keywords: geothermal energy, organic Rankine cycle, direct steam cycle, geofluids, non-condensable gases, thermophysical properties

Abstract in lingua italiana

Storicamente, la generazione di energia elettrica da risorse geotermiche con fluido bifase e monofase liquido è stata limitata rispettivamente agli impianti a vapore diretto e agli impianti binari. Gli impianti binari offrono una serie di vantaggi operativi rispetto agli impianti a vapore diretto, tra cui la facilità di manutenzione e il trattamento e reiniezione ottimale degli eventuali Non-condensable gases (NCG) co-prodotti, che possono essere dannosi o avere un Global Warming Potential (GWP). **Il presente lavoro è incentrato sul confronto tra le due tecnologie, con particolare riferimento all'ambito dei fluidi bifase.** La progettazione di queste centrali geotermiche è un compito impegnativo; devono essere prese in considerazione diverse tecnologie, configurazioni dell'impianto e fluidi di lavoro, e la progettazione ottimale dell'impianto dipende fortemente dalle condizioni di ingresso, dalla composizione, dalle proprietà termofisiche e dal comportamento del geofluido. Inoltre, è necessario tenere conto dell'impatto e del costo del trattamento e reiniezione dei gas incondensabili.

La modellazione dei geofluidi si è storicamente concentrata su due ambiti di ricerca: 1) la ripartizione del geofluido in fasi separate e 2) la stima delle proprietà termofisiche di queste fasi. Riconoscendo le potenziali sinergie tra questi modelli, viene introdotto *GeoProp*, un nuovo framework per la modellazione dei geofluidi, che affronta questa occorrenza accoppiando simulatori di ripartizione dei fluidi rappresentativi dello stato dell'arte, come *Reaktoro*, con motori di calcolo delle proprietà termofisiche dei fluidi ad alta precisione, come *CoolProp* e *ThermoFun*.

La simulazione di centrali geotermiche utilizzando software commerciali, come *Aspen Plus v11*, presenta alcuni inconvenienti: 1) l'accuratezza delle proprietà termofisiche e dei modelli di comportamento di fase, in particolare per i geofluidi con composizione chimica multicomponente, e fenomeni importanti, come gli effetti legati all'espansione all'interno della curva limite nelle turbine a vapore, sono difficili da riprodurre. Per questo motivo, è stato sviluppato *PowerCycle*, un nuovo strumento di simulazione per impianti geotermoelettrici, che consente di utilizzare virtualmente qualsiasi modello di proprietà termofisiche (ad esempio *CoolProp* e *GeoProp*), e fornisce modelli dei singoli componenti specifici dell'impianto geotermico (turbine, scambiatori di calore, pompe/compressori ecc).

Con questi strumenti sono state confrontate le prestazioni termodinamiche e tecno-economiche delle centrali geotermiche binarie ORC e a singolo flash DSC per le risorse geotermiche bifase nell'intervallo 423 K to 548 K: uno studio parametrico sull'effetto e la gestione dei NCG completa l'analisi.

Per le centrali elettriche ottimizzate dal punto di vista termodinamico, si è riscontrato che gli ORC binari producono la stessa potenza dei DSC con titolo di vapore del geofluido fino a 85 %. Per gli impianti ottimizzati dal punto di vista tecno-economico, sono stati ottenuti gli stessi costi specifici della centrale per titolo del vapore fino a 80 %. Per quanto riguarda la gestione dei NCG, gli ORC binari sono più adatti dei DSC single flash, per tutti gli scenari considerati (sfiato in atmosfera e reiniezione). I DSC consumano una notevole quantità di energia per ripressurizzare i NCG per lo smaltimento, sia per lo sfiato nell'atmosfera che per la re-iniezione nel giacimento. Quest'ultimo aspetto rende virtualmente impraticabile dal punto di vista economico la reiniezione nel caso di impianti a flash singolo DSC, ma potrebbe essere più facile da realizzare con le centrali binarie ORC, grazie alla minor richiesta di potenza di ripressurizzazione.

Parole chiave: energia geotermica, ciclo Rankine a fluido organico, ciclo a vapore diretto, geofluidi, gas incondensabili, proprietà termofisiche

Acknowledgements

Firstly, I would like to thank my supervisors: Paola Bombarda for her support and guidance throughout the past three years of this journey; Martin O. Saar for hosting me in the GEG group at ETH Zurich during my year long secondment; Claudio Pietra, Joseph Bonafin for welcoming me in the Turboden offices in Brescia for three months; Allan Leal for stimulating chats about chemical equilibria and thermophysical properties; Dario Alfani for his mentorship; and finally, Paolo Silva.

I would also like to thank Turboden S.p.A for hosting me in their offices in Brescia for three months; Mario Gaia, for his continued interest in my work; Maren Brehme without whom Easygo would not have been possible, and Paromita Deb for organising the training weeks and keeping us Easygoers in check.

Many thanks also to Lorenzo Galieti whose codebase *wopycle* served as inspiration for the creation of *PowerCycle*, and his co-laboration in our joint submission to the EGW 2023.

A special thanks goes to my family and friends: first and foremost my wife, Alexandra, for going out on a limb and following me to Zurich, Brescia and Milan, for her endurance, patience and support throughout the past three years, particularly the final thesis write-up and the numerous conference attendances abroad; my parents and siblings for encouraging me to embark on this adventure in Italy and Switzerland, my parents in-law for welcoming me on their farm for many well-needed respites; my fellow Easygoers Andrea, Anna, Hagen, Lorenzo and Nicolas for much needed fun outside of the office, be it swimming in the Limmat, BBQs, fondue nights or Apericena.

Funding

The EASYGO project (www.easygo-itn.eu) has received funding from the European Union's Horizon 2020 Research and Innovation Programme under the Marie Skłodowska-Curie Grant Agreement No 956965.

A.M.M Leal and M.O Saar thank the Werner Siemens Foundation (Werner Siemens-Stiftung) for its support of the Geothermal Energy and Geofluids (geg.ethz.ch) Group at ETH Zurich, Switzerland, as well as the Energi Simulation Foundation (energisimulation.com) for partial funding of this research.

The contributions by D. Alfani were carried out within the NEST - Network 4 Energy Sustainable Transition (D.D. 1243 02/08/2022, PE00000021) and received funding under the National Recovery and Resilience Plan (NRRP), Mission 4 Component 2 Investment 1.3, funded from the European Union - NextGenerationEU. This manuscript reflects only the authors' views and opinions, neither the European Union nor the European Commission can be considered responsible for them.



Disclaimer

The content of this work reflects only the author's view. The Research Executive Agency (REA) is not responsible for any use that may be made of the information it contains.

This manuscript reflects only the authors' views and opinions, neither the European Union nor the European Commission can be considered responsible for them.

Data Availability

All data and code associated with this thesis, is available under an Apache 2.0 license on GitHub (https://github.com/EASYGO-ITN/ESR13_Thesis/tree/main) and Zenodo (<https://zenodo.org/records/13975117>).

Contents

Abstract	i
Abstract in lingua italiana	iii
Acknowledgements	v
Funding	vii
Disclaimer	ix
Data Availability	xi
Contents	xiii
1 Introduction	1
1.1 Origins of Geothermal Heat	2
1.2 Geothermal Systems	3
1.2.1 Hydrothermal Systems	4
1.2.2 Enhanced Geothermal Systems	6
1.2.3 Advanced Geothermal Systems	6
1.2.4 Geothermal Fluid	7
1.3 Geothermal Power Generation	8
1.3.1 Direct Steam Cycle: Dry Steam	8
1.3.2 Direct Steam Cycle: Flash	9
1.3.3 Binary Cycle	10
1.4 Research Objectives	11
1.5 Project Outline	12
2 Thermophysical Property Modelling	13
2.1 Geofluids	13

2.2	Equations of State	14
2.2.1	Ideal Gas Law	14
2.2.2	Real Gas Law	14
2.2.3	Cubic Equations of State	14
2.2.4	Excess Property Formulations	15
2.2.5	Incompressible Binary Mixtures	19
2.2.6	Chemically reactive Systems	19
2.2.7	Empirical Models	26
2.2.8	Calculation Libraries	26
2.3	GeoProp	27
2.3.1	Structure	27
2.3.2	Validation	29
2.3.3	Examples	32
2.3.4	GeoProp v2	32
2.4	Case Studies	34
2.4.1	Cooling Curves of Geothermal Geofluids	34
2.4.2	Model Comparison	36
3	Geothermal Power Generation	39
3.1	Direct Steam Cycles	39
3.1.1	Dry Steam	39
3.1.2	Flash Steam	40
3.1.3	Optimisation	43
3.2	Binary Cycles	47
3.2.1	Classical Rankine Cycle	48
3.2.2	Organic Rankine Cycle	49
3.2.3	Working Fluids	50
3.2.4	Configurations	52
3.2.5	Optimisation	60
3.2.6	Intuitions for cycle and working fluid selection	65
3.3	NCG Handling	74
3.4	Scale Handling	78
3.4.1	Calcite Scale	78
3.4.2	Silica Scale	78
3.5	Turbines	79
3.5.1	Working Principle	79
3.5.2	Impulse vs. Reaction Stages	81

3.5.3	Types of Turbines	82
3.5.4	Wet Expansion	84
3.6	Heat Exchangers	87
3.6.1	Working Principle	87
3.6.2	Shell & Tube Heat Exchangers	91
3.7	Equipment Costs	92
3.7.1	Steam Turbines	92
3.7.2	ORC Turbines	93
3.7.3	Shell & Tube Heat Exchangers	94
3.7.4	Condensers	96
3.7.5	Pumps	96
3.7.6	Compressors	97
3.7.7	Fans	98
3.7.8	Power Plants	99
4	Power Plant Modelling	101
4.1	Architecture	101
4.2	Fluid Properties	102
4.2.1	Architecture	102
4.2.2	Calculation Engines	103
4.2.3	Stream	105
4.3	Base Components	105
4.3.1	Turbine	105
4.3.2	Heat Exchanger	109
4.3.3	Pump & Compressor	112
4.3.4	Multi-Stage Compressor	114
4.3.5	Mixer and Joint	116
4.3.6	Separator	117
4.4	Economic Model	118
4.5	Optimisation	120
4.6	Validation	120
4.6.1	Fluid Properties	121
4.6.2	Turbine	122
4.6.3	Heat Exchanger	124
4.6.4	Direct Steam Cycle	130
4.6.5	Binary ORC	133
5	Power Plant Simulations	137

5.1	Commercial Software	137
5.1.1	Objectives	137
5.1.2	Geothermal Sources	137
5.1.3	Power Plant Configurations	138
5.1.4	Model Description	140
5.1.5	Case 1: Pure Water	141
5.1.6	Role of Salinity and NCG	143
5.1.7	ELECNRTL vs. SP2009	145
5.1.8	Case 2: Salinity and NCG	148
5.1.9	Observations	150
5.2	Thermodynamic Optimisation	151
5.2.1	Plant Configurations	151
5.2.2	Boundary Conditions	154
5.2.3	Optimisation Configuration	154
5.2.4	Performance Analysis: DSC	155
5.2.5	Performance Analysis: Binary ORC	159
5.2.6	Direct Comparison	173
5.2.7	Conclusions	178
5.3	Techno-Economic Optimisation	179
5.3.1	Plant Configurations	179
5.3.2	Boundary Conditions	179
5.3.3	Optimisation Configuration	179
5.3.4	Performance Analysis: DSC	180
5.3.5	Performance Analysis: ORC	182
5.3.6	Direct Comparison	190
5.3.7	Conclusions	192
5.4	Impact of Drilling Costs	194
5.4.1	Boundary Conditions	194
5.4.2	Optimisation Configuration	194
5.4.3	Results	195
5.5	Impact of NCG handling	197
5.5.1	NCG Venting	197
5.5.2	NCG Re-injection	203
5.5.3	Re-injection with partial dissolution	211
5.5.4	Conclusion	215

6.1	Overall Motivation	217
6.2	Thermophysical Property Modelling	217
6.3	Power Plant Modelling	218
6.4	Power Plant Simulations	219
6.4.1	Commercial Software	219
6.4.2	Thermodynamic Optimisation	219
6.4.3	Techno-economic optimisation	220
6.4.4	Impact and handling of NCG	221
6.5	Future Work	222
 Bibliography		 225
 Nomenclature		 237
 List of Figures		 245
 List of Tables		 255
 List of Listings		 259
 List of Publications		 261
 A Chemical Equilibrium		 263
 B Spycher-Pruess Partition Model		 265
B.1	The Equilibrium Constant	267
B.2	The Fugacity Coefficient	268
B.3	The Activity Coefficient	271
B.4	Validation	272
 C Exergy Analysis		 275
C.1	Exergy Analysis	275
C.1.1	Exergy	275
C.1.2	Open System Analysis	277
 D GeoProp Code Examples		 279
D.1	GeoProp	279
D.1.1	Getting Started	279

E	Power Cycle Validation	281
E.1	Fluid Properties	281
E.2	Turbine - Wet expansion	282
E.3	Pump	284
E.4	Compressor	285
E.5	Multi-Stage Compressor	286

1 | Introduction

The global energy sector is facing significant pressures that will require significant structural changes over the coming decades. On the one hand, the global demand for all forms of energy is rising, driven both by population growth and continued improvements in global living standards and quality of life. Simultaneously, energy sources and supply chains are changing, in an effort to transition away from fossil fuels, due concerns over global climate change, towards renewable and non-polluting energy sources.

In their 2023 annual report, the International Energy Agency (IEA [45]), estimates that global population will increase from 8 billion in 2023, to 8.5 billion in 2030 and 9.7 billion by 2050. Meanwhile, global economies are anticipated to grow by on average 2.6% per annum, a significant portion of which in Africa, Asia and the Middle East. Their stated policies scenario, predicts that the total final energy consumption across industry, buildings, transport and other energy uses will increase from 440 EJ (4.4×10^{20} J) today by 1.0 % per annum until 2030 and then 0.5 % per annum until 2050 to 530 EJ (5.3×10^{20} J), an almost 20 % increase compared to 2023. Moreover, these changes are accompanied by increase in demand for electricity (from around 85 EJ (8.5×10^{19} J) in 2023 to almost 150 EJ (1.5×10^{20} J) by 2050) driven by electrification of industry, modes of transport and buildings.

In light of this, technologies tapping into Earth's natural energy reserves, such as wind, solar and geothermal energy have emerged as cost effective and clean alternatives for all final energy uses [45]. Particularly geothermal energy is proving to be an attractive and versatile option for grid-scale renewable and dispatch-capable production of both electricity and heat.

Direct steam cycle (DSC) power plants with flash have historically dominated the geothermal power generation landscape and represent the majority of geothermal electricity generation to date. Binary organic Rankine cycles has disrupted the geothermal industry by allowing low-enthalpy resources to be exploited for power generation, which would otherwise have been uneconomical using DSCs [30].

The following sections aim to provide further background on the origin of the geothermal

heat contained within the Earth's subsurface, the types of geothermal systems, and ways in which the geothermal heat can be utilised.

1.1. Origins of Geothermal Heat

Planet Earth contains approximately 2×10^{31} J of thermal energy [40], enough to meet our current annual energy demand for the next 50 billion years. There are two main sources of the thermal energy stored within the Earth. The first is left-over heat from the formation of the Earth, as a result of the gravitationally induced pressures and friction between the rocks that formed our planet. This *primordial* heat accounts for about 20% of the total thermal energy stored within the earth, the other 60% [37] can be attributed to decay of long-lived isotopes of Uranium (^{238}U and ^{235}U), Thorium (^{232}Th), and Potassium (^{40}K), which releases energy.

Table 1.1: Half-life and heat production by radioactive isotope [37].

Isotope	Half-Life / 10^9 year	Heat Production / $10^3 \text{ J kg}^{-1} \text{ year}^{-1}$
^{238}U	4.5	2.97
^{235}U	0.71	18.01
^{232}Th	13.9	0.83
^{40}K	1.3	0.92

The center of the planet is estimated to have a temperature of the order of 5000°C [70], while we experience more moderate temperatures of the order of 10°C at the planet's surface. This difference in temperatures, results in a net heat flow from the center towards the surface of about $4 \times 10^{13} \text{ W}$, or 1260 EJ ($1.26 \times 10^{21} \text{ J}$) annually, from where it is radiated into space, on land the heat flux is typically around 50 mW m^{-2} .

In the absence thermal anomalies, the *normal* temperature gradient is around 30 to 33°C km^{-1} [30], meaning that temperatures exceeding 100°C or 150°C are not encountered at depths shallower than 3.0 km and 4.5 km respectively, see Figure 1.1. Drilling experiments have achieved depths exceeding 12 km [71], however, commercial boreholes typically do not exceed 5 km due to escalating drilling cost as a result of increasing rock hardness and formation temperature with depth. Most commercial geothermal projects are thus located in areas with much higher geothermal gradients, which allow temperature in excess of 150°C to be targeted at shallower depths.

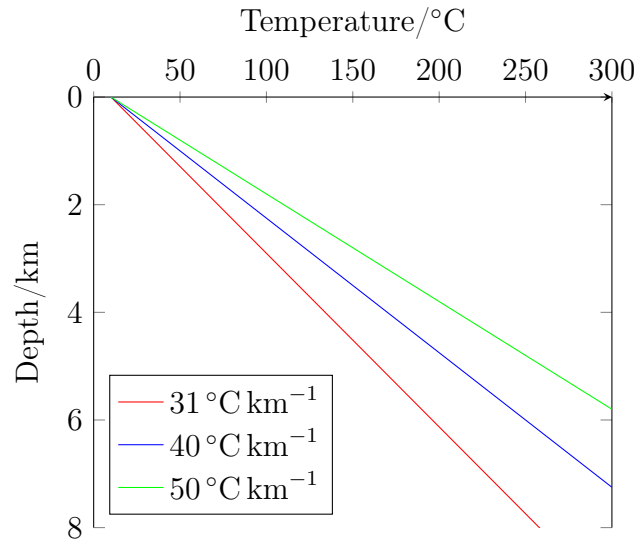


Figure 1.1: The sub-surface temperature for different geothermal gradients

The geothermal gradient is closely linked to the heat flux in the sub-surface, which in turn is strongly dependent on geological and tectonic setting. For example, in compressional settings, where two plates move towards one another, subduction can lead to a partial melting of the subducted plate and the creation of magmatic zones near the surface, raising the heat flux. Subduction, has led to geothermal resources in most land masses bordering the Pacific, Cocos and Nazca tectonic plates. Similarly, in extensional settings, rifting, where two plates move apart from one another with the gap being filled with material from the asthenosphere, and thinning of the plate itself can increase the local heat flux. Rifting has led to geothermal resources in Iceland, the Azores and East Africa, while thinning has given rise to the non-magmatic geothermal Basin and Range region in Nevada, United State, [30].

Ultimately, the geothermal gradient is highly site specific and may not be linear. For example, faults may provide preferential fluid pathways, thus allowing hot fluids to reach shallower depths raising the local temperature.

1.2. Geothermal Systems

The following section aims to provide background on the three main types of geothermal systems and the make-up of geothermal fluids.

1.2.1. Hydrothermal Systems

There are many naturally occurring geothermal systems, more commonly referred to as *hydrothermal systems*, see Figure 1.2.

In hydrothermal systems, surface water (e.g. precipitation) percolates into the sub-surface via faults and fractures under the force of gravity (A to B), which provide low-resistance pathway deep into the Earth. At some depth, these pathways may intersect a formation of even lower resistance, causing the fluid to preferentially flow into this formation. In the presence of a heat source, the fluid begins to heat up and rise, due to its reducing density with temperature (B to C). Other high permeability faults intersecting the formation, then provide a low-resistance pathway back to the surface (C to E). The difference in density between the hot fluid and cold fluid, results in a higher potentiometric surface for the hot fluid allowing the fluid to naturally circulate - this is commonly referred to as a *thermosiphon*. At the surface the fluid then enters the Water Cycle and is eventually returned in the form of precipitation, closing the loop (E to A).

Depending on the temperature of the heat source (F), the fluid may arrive at the surface as a liquid, or, if the fluid pressure drops to the fluids saturation pressure (D), as a vapour, or vapour-liquid two-phase mixture. The presence of such hydrothermal systems can most commonly be deduced from surface features such as fumaroles, hot springs, mud pits, geysers etc. and are still an important instrument in the discovery of geothermal resources today.

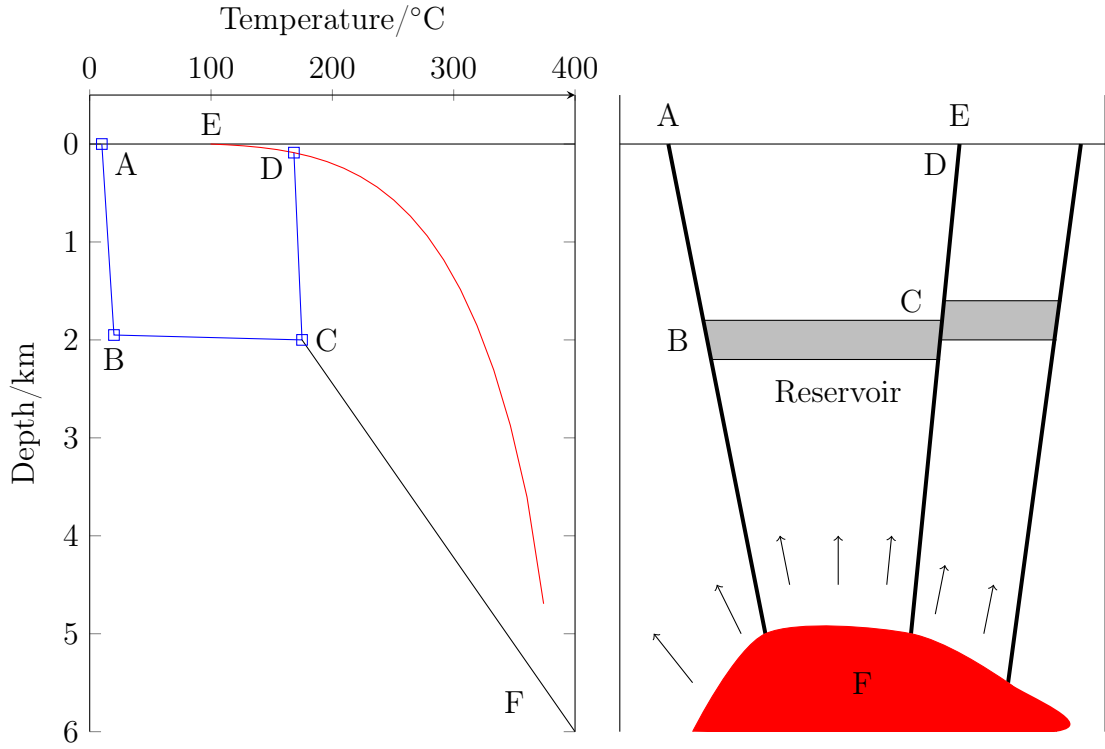


Figure 1.2: Schematic of a hydrothermal system. Left, the fluid path and temperature (blue), the saturation curve (red), and the conduction from the heat source (black). Right, the geological cross-section showing the faults (black), the reservoir (grey), the heat source (red) and the condition from the heat source. Graphic adapted from Kruger et al. [49] and DiPippo [30].

In summary, the key features of a hydrothermal system are the heat source, the reservoir, a supply of water to extract the heat and a recharge mechanism to replenish the produced water.

In a commercial setting, hydrothermal systems are typically exploited by drilling two wellbores into the reservoir; one to produce the hot fluid to surface, and the other to re-inject the cold fluid into the reservoir - this is commonly called a *doublet*. The wellbores essentially replace the faults as the low-resistance pathways for the fluid to/from the reservoir.

Where the formation pressure is insufficient for the fluid to reach the surface, pumps may be used to pressurise the fluid and deliver it to the surface. However, pumps need to be installed below the flash-point to avoid cavitation, which can damage the pump internal components. There are two different types of pumps, Electrical Submersible Pumps (ESPs) where the motor is located within the wellbore and is cooled by the fluid rushing past it, and Line Shaft Pumps (LSPs), where the motor is located at the surface

and drives the impeller via a continuous shaft. To prevent overheating of the motor the use of ESPs is limited to lower temperature applications. On the other hand, the application of LSPs is limited by the length of the shaft and the requirement for a vertical wellbore.

1.2.2. Enhanced Geothermal Systems

Due to the generally increasing temperature with depth, deeper geothermal systems tend to be more sought after, however, may not display sufficient, if any, permeability to allow circulation of fluids through the formation. Enhanced Geothermal System (EGS) seek to address this issue by using stimulation techniques, such as hydraulic fracturing or hydro-shearing to create or re-activate fracture networks within the rock to allow the circulation of fluids, and therefore the extraction of heat. Although the idea was first presented in the 1970s, [81], and has been shown to be technically feasible, to date there are only few commercially active EGS sites, such as Soultz-sous-Forêts[1], or Rittershoffen [1]. Utah FORGE is a prominent research initiative into EGS [4].

The main challenges preventing commercial adoption of EGS are:

- *Induced Seismicity* - the circulation of fluids may reactivate the fracture network, causing low magnitude tremors felt at the surface that may in some cases damage buildings, as was the case at a potential EGS site in Basel in 2006 [28].
- *Flow Rates* - the circulation rates must be sufficiently high for the project to reach an economically viable scale, however this reduces the residence time within the formation and may result in incomplete heating of the fluid.
- *Clogging* - over time scales and other particulates can clogging parts of the fracture network reducing the overall permeability and in turn limit the flow rates and heat removal [61].
- *Early Thermal Breakthrough* - enhanced geothermal systems are typically smaller than hydrothermal systems and thus at equal heat removal, the EGS will be exhausted sooner.

1.2.3. Advanced Geothermal Systems

Unlike Hydrothermal systems or EGS, where the fluid is in direct contact with the formation, in advanced geothermal systems, a self-contained network of wellbores is used to extract the heat from the reservoir, with the fluid being contained within the closed-loop at all times. This configuration has as several advantages over hydrothermal and EGS

systems as it reduces the dependence on the formation properties, which pose a major source of uncertainty for any geothermal project. More over, as the working fluid is fully contained within the wellbore at all times, the risk of induced seismicity or contamination of drinking water aquifers is all but eliminated.

While there are some demonstration and test sites (e.g. Geretsriede, Germany), the long-term commercial viability of these systems has not yet been proven. Particularly, due to the significant drilling required for these systems and the lower rate of heat transfer posing a potential limitation on the scale [19, 62].

1.2.4. Geothermal Fluid

The working fluid in geothermal energy extraction is typically the in-situ reservoir fluid, which is primarily comprised of water, but may also contain dissolved minerals and gases. To avoid confusion with the power plant working fluid, it is often referred to a *geofluid* or *brine*. The geofluid composition is derived from the fluids present when the formation was first deposited, the chemical equilibration with the formation over geological timescales, as well as the migrations of tertiary fluids (e.g. methane) into the formation.

Changes in temperature and pressure (e.g. by producing the geofluid to surface and extracting its heat) or composition (e.g. injection of water), disturb the geofluid's chemical equilibrium, which can lead to the precipitation of dissolved species. In the case of solid species, this mineralisation, also commonly referred to as *scaling*, poses serious operational issues as the scales can deposit in all parts of the production system and pose an additional resistance to flow and heat transfer. Scaling can be controlled through chemical inhibitors or ensuring that temperatures and pressures make mineralisation thermodynamically unfavourable.

Dissolved gases also pose an important operational challenge, as they can be harmful and toxic (e.g. Hydrogen Sulphide, H_2S , or Mercury, Hg), have a global warming potential (e.g. carbon dioxide, CO_2 , or methane, CH_4), or have a strong odour (e.g. Hydrogen Sulphide, H_2S). Collectively these gases are commonly referred to as NCG because they cannot be liquefied at ambient or near-ambient conditions, making their handling costly. Common issues and technological options related to the handling of NCG will be dealt with in more detail in Section 3.3.

1.3. Geothermal Power Generation

Where geothermal resources are hot enough, it is possible to convert the thermal energy into electrical energy. This is achieved using two different power plant technologies; DSC and binary cycle power plants. The below sees to provide an overview of the most prominent types of geothermal power plants.

1.3.1. Direct Steam Cycle: Dry Steam

Dry steam plants operate on the highest enthalpy resources, where the geofluid arrives at the surface as a saturated vapour. While they are the earliest examples of geothermal power plant, the specific geological conditions required for fully vapourised geofluids mean that there are only a small number of these sites globally. The most prominent dry steam power plants are those at Lardarello, Italy, or The Geysers, USA, [30].

The steam is then expanded in a turbine, which drives a generator to generate electricity. The low-pressure steam from the turbine is then cooled condensed to separate the NCG, which is then treated (not pictured) to remove pollutants (e.g. H_2S) before typically being vented to the atmosphere. The liquid is re-injected into the geothermal reservoir to minimise pressure decline in the reservoir and maximise the lifetime of the resource. Figure 1.3 provides a schematic of a dry steam geothermal power plant.

As of 2016, there were a total of 68 dry steam geothermal power plants across the United States, Italy, Indonesia, Japan, Iceland and New Zealand, producing a total of 2.87 GW, representing 24.0 % of total geothermal power production [30].

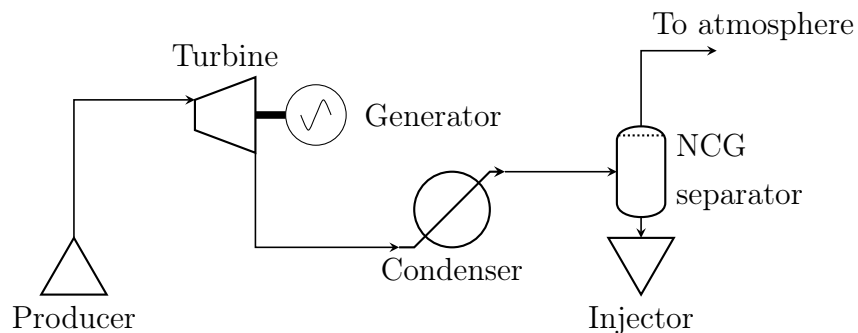


Figure 1.3: Schematic of a dry steam geothermal power plant. Adapted from [30]

1.3.2. Direct Steam Cycle: Flash

Flash plants operate on lower enthalpy resources, where the geofluid arrives at the surface either as a liquid or low vapour quality. As such, the geological requirements for flash power plants are far less niche compared to dry steam plants.

The hot geofluid, single phase liquid or a vapour-liquid mixture, is expanded in a valve to liberate more vapour, which is then separated from the liquid and sent to the turbine. In the turbine the vapour is expanded further, which drives a generator and generates electricity. The low-pressure steam is then condensed and the NCG is removed from the condenser and then treated (not pictured) to remove pollutants (e.g. H_2S) before typically being vented to the atmosphere. The condensate is repressurised and then, together with the left-over brine, re-injected into the reservoir. Figure 1.3 provides a schematic of a flash geothermal power plant.

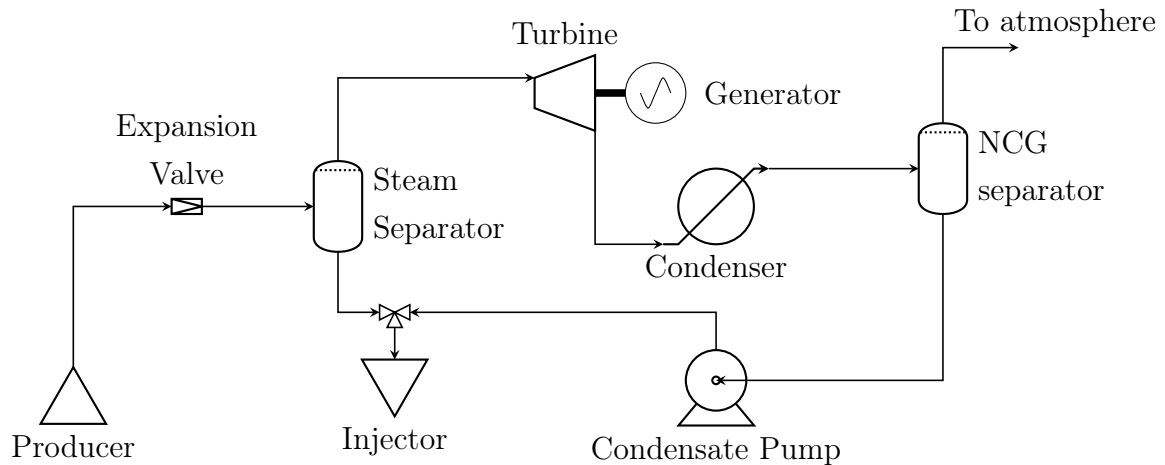


Figure 1.4: Schematic of a direct steam cycle with flash geothermal power plant. Adapted from [30]

The degree of flashing is a compromise between liberating more steam from the geofluid and specific enthalpy change across the turbine. Additional flashing stages can be used to liberate more vapour from the geofluid, see Figure 1.5. While such *dual-flash* plants are quite common, there only exist a handful of *triple-flash* plants [30].

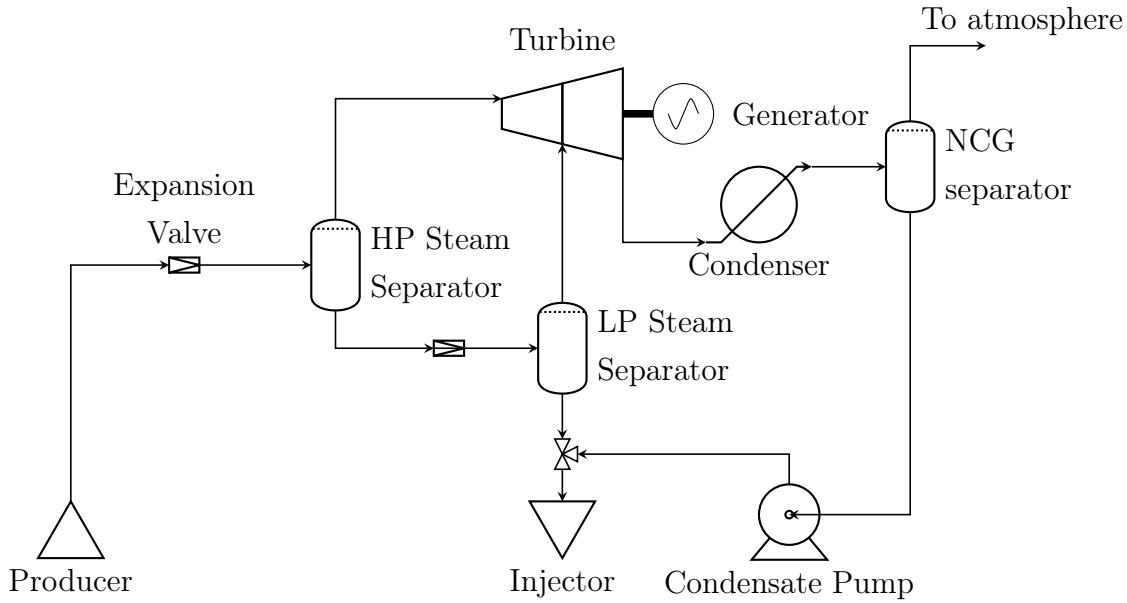


Figure 1.5: Schematic of a direct steam cycle with double flash geothermal power plant. Adapted from [30]

As of 2016, there were a total of 243 flash geothermal power plants across the Philippines, the United States, Mexico, Indonesia, Iceland, Japan and Kenya, producing a total of 7.33 GW, representing 61.4 % of total geothermal power production [30].

1.3.3. Binary Cycle

Binary plants allow the exploitation of low-enthalpy geothermal resources, no or insufficient vapour can be generated for commercial operation of a flash plant - this has opened a great number of otherwise uneconomical resources up for exploitation.

In a binary power plant, see Figure 1.6 the hot geofluid is used to heat and evaporate a secondary fluid, also referred to as the cycle working fluid, or colloquially *working fluid*. The working fluid vapour is then expanded in a turbine, which drives a generator to generate electricity. The low pressure vapour is then condensed, re-pressurised and then returned to the pre-heater inlet, closing the loop. A recuperator may be used to recover heat from the working fluid leaving the turbine, and to use it to partially pre-heating the working fluid.

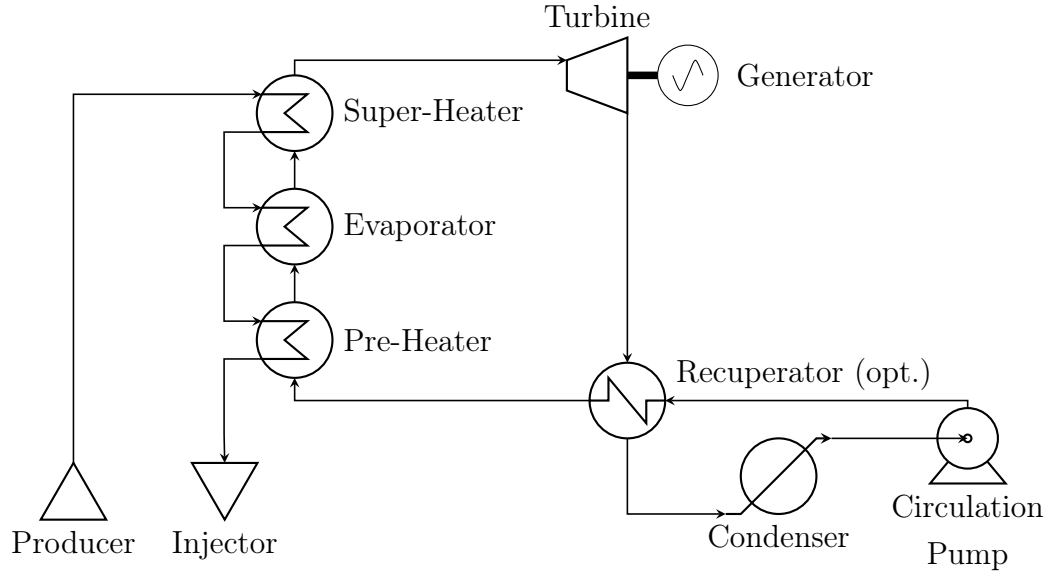


Figure 1.6: Schematic of a binary ORC geothermal power plant. Adapted from [30]

The most popular type of binary geothermal plant use an ORC, where the working fluid is some organic fluid, typically a hydrocarbon or a refrigerant. Another example of a binary cycle, is the Kalina cycle, which uses a mixture of water and ammonia mixture as the working fluid, however there are currently only a small number of active power plants using this cycle configuration (e.g. Húsavík in Iceland [3] or Bruchsal in Germany [2]).

As of 2016, there were a total of 203 binary geothermal power plants across the United States, New Zealand, Turkey, Kenya, Guatemala and the Philippines, producing a total of 1.25 GW, representing 10.4 % of total geothermal power production [30].

1.4. Research Objectives

The global objective of this work is to investigate electrical power generation from two-phase geothermal heat sources using both binary ORC and DSC technology in an effort to establish thermodynamic and techno-economic application envelopes. Here, the effect of impurities, such as NCG, on power generation, as well as the parasitic losses associated with the disposal of NCG is an area of interest, and could represent a novel-niche for binary ORC geothermal power. To assess the thermodynamic and techno-economic performance of these two technologies, a holistic model of the geofluid, power plant and economics is required.

Thus, the three key research objectives are the:

1. Curation or development of a reliable and robust methodology for modelling the

thermophysical properties and phase behaviour of real geofluids (i.e. water and NCG, water and salts, water and salts and NCG).

2. Curation or development of a simulation tool to evaluate the thermodynamic and techno-economic performance of both DSC and binary ORC geothermal power plants.
3. Evaluation and comparison of the thermodynamic and techno-economic performance of DSC and binary ORC geothermal power plants for ideal and real geofluids (i.e. pure water and water with NCG respectively), including different disposal scenarios for co-produced NCG.

1.5. Project Outline

Chapter 2 covers the review of existing thermophysical property modelling approaches and the development of *GeoProp*

Chapter 3 provides technical background on key aspects of geothermal power generation, including the different power plant technologies, turbines, heat exchangers, as well as equipment costs.

Chapter 4 documents the development of *PowerCycle*, detailing the component performance and cost models as well as their validation.

The investigations into the thermodynamic and techno-economic performance of binary ORC and single flash DSC geothermal power plants, as well as the impact of impurities and their handling are covered in chapter 5.

Conclusions are summarised in chapter 6.

Appendix A provides supplementary information on the thermodynamic criteria for chemical equilibrium. Appendix B details the implementation of the Spycher Pruess 2009 (SP2009) partitioning model and changes to the original model. Appendix C details the governing equation for the second law performance analysis. Appendix D provides code examples for the use of *GeoProp*, and finally, appendix E provides additional validations for *PowerCycle* component models.

2 | Thermophysical Property Modelling

The geofluid's phase behaviour and its thermophysical properties are fundamental inputs to the design of any geothermal power plant. These properties are expensive to obtain experimentally. In the absence of holistic or predictive models to handle the broad range of geofluid compositions we must often rely on mathematical models, equations of state and calibrating model parameters based on what little field data is available.

This chapter aims to provide an overview of the current state-of-the-art modelling approaches for predicting the thermophysical properties of fluids in general and more specifically geofluids. We then present a calculation framework that combines these modelling approaches, and illustrate its use in a number of case studies. Finally, we present a unified calculation framework that combines a number of properties estimation frameworks, which can be used for simulating power plants and other physical processes.

2.1. Geofluids

Geofluids typically have three main constituents: water, minerals and gases[30]. The compositions of minerals depends not only on the chemical composition of the reservoir rock, but also the composition the waters migrating through the rock and the left over waters from the original deposition of the reservoir rock. Na, Ca, K, Fe, Cl, SO_4 and HCO_3 are common minerals found in geothermal geofluids. For the gases, CO_2 , CH_4 and H_2S are common constituents. CO_2 is either produced as part of the dissolution of the reservoir rock (e.g. in case of a carbonate reservoir) or, similarly to H_2S , migrates into the formation from deeper within the Earth (e.g. magmatic origin). CH_4 is typically created deeper within the Earth in hydrocarbon source rock and then migrates into the reservoir. Kottsova and Brehme [48] and Project [79] have collated geofluid compositions from a large number of geothermal wells across Europe.

2.2. Equations of State

In thermodynamics, substances can exist in different *states*, where each *state* is uniquely defined by *state variables*, such as the temperature, pressure, and volume/density of the substance. In this context, an Equation of State (EOS) is any mathematical expression that correlates the state variables of a substance, allowing the all thermodynamic properties for any given state to be determined. The following sections aim to provide background on the most common EOSs.

2.2.1. Ideal Gas Law

The simplest EOS is the *Ideal Gas Law*, Equation 2.1, which links the pressure, molar volume and temperature, and describes the behaviour of a gases, assuming non-interacting, spherical particles of zero volume.

$$PV_m = RT \quad (2.1)$$

2.2.2. Real Gas Law

Over time, as experimental techniques and equipment improved, temperature and pressure dependent deviations from the ideal gas law were observed. To capture these deviations the Compressibility Factor (Z) was introduced, leading to the *Real Gas Law*, Equation 2.2. Standing and Katz provided graphical methods for evaluating Z from the reduced temperature and pressure, based on the law of corresponding states.

$$PV_m = ZRT \quad (2.2)$$

2.2.3. Cubic Equations of State

van der Waals was the first to present a cubic EOS based on the the insight that particles did indeed have an irreducible volume and that there are short-ranged attractive interactions between particles. This is now known as the van der Waals (VDW) EOS, Equation 2.3. One significant advance of the VDW EOS is that its domain is not restricted to just gases, but also allows the behaviour of liquids to be approximated - though it is considered non-predictive and typically underestimates liquid densities.

$$P = \frac{RT}{V_m - b} + \frac{a}{V_m^2} \quad (2.3)$$

To improve on the accuracy of liquid phase predictions modifications to the original VDW EOS were suggested. These modifications have primarily focused on the definition of the attraction term, for example Redlich and Kwong modified the attraction term to include a temperature dependence and the irreducible volume, Equation 2.4, Soave further modified the EOS proposed by Redlich and Kwong by including a temperature dependent α term, Equation 2.5 and Peng and Robinson changed the definition of the denominator in the attraction term, Equation 2.6. These EOS are commonly referred to as the Redlich-Kwong (RK) EOS, Soave-Redlich-Kwong (SRK) EOS and Peng-Robinson (PR) EOS, respectively.

$$P = \frac{RT}{V_m - b} + \frac{a}{\sqrt{T}V_m(V_m - b)} \quad (2.4)$$

$$P = \frac{RT}{V_m - b} + \frac{a\alpha(T)}{V_m(V_m - b)} \quad (2.5)$$

$$P = \frac{RT}{V_m - b} + \frac{a\alpha(T)}{V_m^2 + 2V_m b - b^2} \quad (2.6)$$

Cubic EOS above can also be used to model mixtures and have been successfully applied in the petroleum sector for many decades. When applied to mixtures, mixing rules are applied to determine the overall values of a , see Equation 2.7, and b , see Equation 2.8. Here, Binary Interaction Coefficients (BIC), k_{ij} , are used to account for differences in the interactions between different species, and are usually obtain by tuning against experimental data of the mixture's phase behaviour.

$$a = \sum_{i=0}^N \sum_{j=0}^N x_i x_j \sqrt{a_i a_j} (1 - k_{ij}) \quad (2.7)$$

$$b = \sum_{i=0}^N x_i b_i \quad (2.8)$$

2.2.4. Excess Property Formulations

Peneloux et al. [74] first investigated the use of *Excess Property* formulations, for example in terms of the Helmholtz free energy, as single mathematical formulation to obtain all

thermodynamic properties. Here, the *excess* refers to the difference between the actual thermodynamic property or potential at a given state and that of an ideal gas. The equations below shows the Helmholtz free energy EOS (HEOS) for Nitrogen [95], where $\delta = \frac{\rho}{\rho_c}$ and $\tau = \frac{T_c}{T}$ with ρ_c and T_c being the critical density and temperature respectively; and a_1 to a_7 , the N_k s, the i_k s, the j_k s, the l_k s, the ϕ_k s, the β_k s and the γ_k s as fluid specific correlation parameters - a total of 154 parameters in the case of Nitrogen.

$$\frac{a(\delta, \tau)}{RT} = \alpha^0(\delta, \tau) + \alpha^r(\delta, \tau) \quad (2.9)$$

$$\alpha^0(\delta, \tau) = \ln \delta + a_1 \ln \tau + a_2 + a_3 \tau + \frac{a_4}{\tau} + \frac{a_5}{\tau^2} + \frac{a_6}{\tau^3} + a_7 \ln[1 - e^{-a_8 \tau}] \quad (2.10)$$

$$\alpha^r(\delta, \tau) = \sum_{k=1}^6 N_k \delta^{i_k} \tau^{j_k} + \sum_{k=7}^{32} N_k \delta^{i_k} \tau^{j_k} e^{(-\delta^{l_k})} + \sum_{k=33}^{36} N_k \delta^{i_k} \tau^{j_k} e^{-\phi_k(\delta-1)^2 - \beta_k(\tau-\gamma_k)^2} \quad (2.11)$$

As a result of their complexity, these HEOS are typically only created for fluids where large experimental datasets over a wide range of thermodynamic conditions exist [56]. Given the high-accuracy of HEOS, limited only by the experimental uncertainty [56], they are primarily developed as reference EOSs for specific common-use fluids to calculate thermodynamic property charts and look-up tables for scientific and industrial use.

One such reference EOS is the HEOS developed by Wagner and Pruß for the properties and phase behaviour of water, better known as the IAPWS95 [44] formulation or the Wagner-Pruß (WP) EOS. This original model was developed further by Wagner et al. leading to the IAPWS97 [44] formulation, which primarily improves the speed and is more commonly used in industry than scientific use. Similar reference EOS have also been developed for other common geofluid components, such as carbon dioxide [94] (i.e. the Span-Wagner (SW) EOS), nitrogen [95], methane [88] and hydrogen sulphide [55].

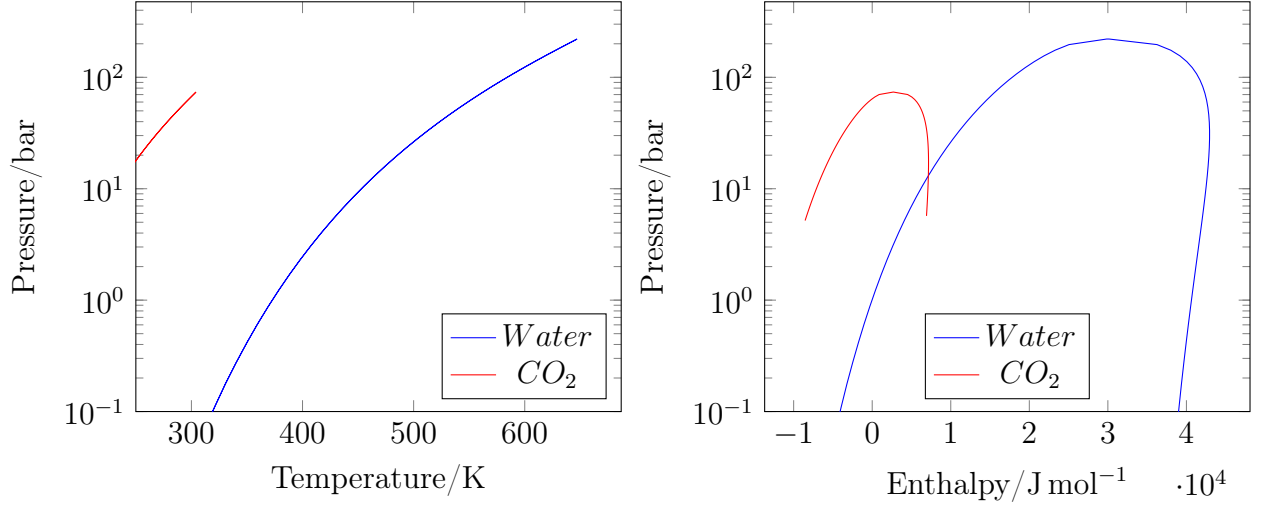


Figure 2.1: The saturation curves for water and carbon dioxide in Pressure-Temperature and Pressure-Molar Enthalpy domains. Calculated using the Water and Carbon Dioxide HEOS implemented in *CoolProp*.

Mixtures

Methodologies for modelling mixtures of reference EOS have been developed [54], but require an additional set of parameters for each component pair to capture their interactions. The equations below outline the general formulation of the mixture model, with N_k , d_k , t_k common to all mixtures and F_{ij} , ξ_{ij} , β_{ij} , ϕ_{ij} and ζ_{ij} specific to each component pair.

$$A = A^{id\,mix} + A^{excess} \quad (2.12)$$

$$A^{id\,mix} = \sum_{i=1}^n x_i \cdot [A_i^0(\rho, T) + A_i^r(\delta, \tau) + RT \ln x_i] \quad (2.13)$$

$$A^{excess} = RT \sum_{i=1}^{n-1} \sum_{j=i+1}^n x_i x_j F_{ij} \sum_{k=1}^{10} N_k \delta^{d_k} \tau^{t_k} \quad (2.14)$$

$$\delta = \frac{\rho}{\rho_{red}} \quad (2.15)$$

$$\tau = \frac{T_{red}}{T} \quad (2.16)$$

$$\rho_{red} = \left[\sum_{i=1}^n \frac{x_i}{\rho_c} + \sum_{i=1}^{n-1} \sum_{j=i+1}^n x_i x_j \xi_{ij} \right]^{-1} \quad (2.17)$$

$$T_{red} = \sum_{i=1}^n x_i T_{c_i} + \sum_{i=1}^{n-1} \sum_{j=i+1}^n n x_i^{\beta_{ij}} x_j^{\phi_{ij}} \zeta_{ij} \quad (2.18)$$

As a result of the complexity of the formulation, the convergence can be challenging and may not be guaranteed for all compositions, temperatures and pressure of interest. The convergence was investigated using binary mixtures of water and carbon dioxide over a range of temperatures (298 K to 573 K corresponding to 25 °C to 300 °C) and pressures (1 bar to 300 bar) using *CoolProp* [20], see Section 2.2.8.

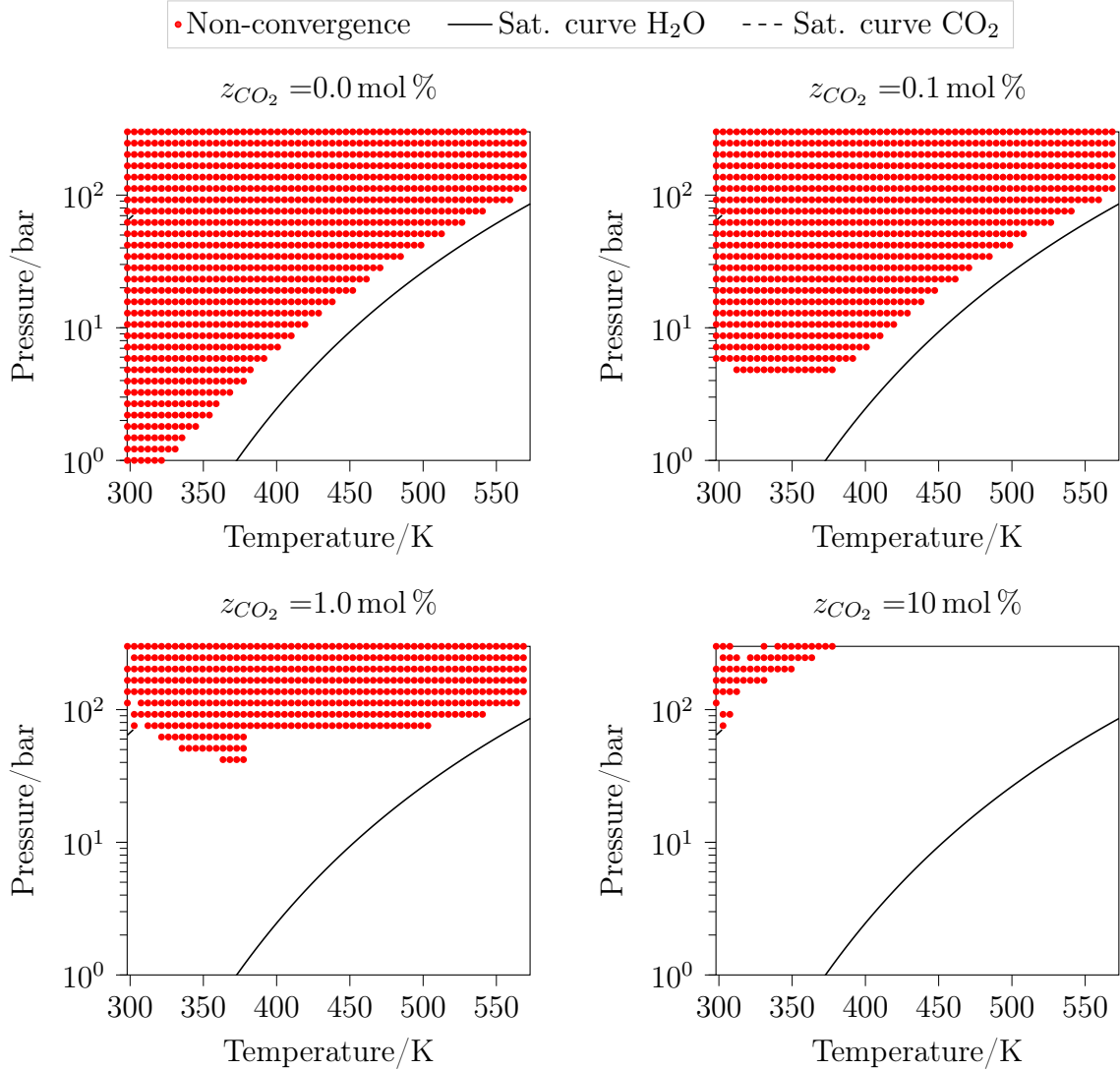


Figure 2.2: Convergence maps of the water-carbon dioxide binary HEOS mixture implemented in *CoolProp* for a range of compositions.

From Figure 2.2, for pure water ($z_{CO_2} = 0.00$ mol %), the HEOS formulation does not converge for a broad range of temperatures and pressures, appearing to shadow the

saturation line of pure water. Convergence generally improves for quasi pure water ($0.00 \text{ mol } \% \leq z_{CO_2} < 0.05 \text{ mol } \%$), however the HEOS formulation does not converge at elevated (approaching reservoir-like) pressures. The areas of non-convergence appear to be correlated where the fluid is expected to be liquid (i.e. low temperatures and high pressures).

2.2.5. Incompressible Binary Mixtures

Furthermore, EOS have also been developed for some industrially relevant mixtures, like seawater [89], lithium bromide solution [80], and calcium chloride solution [78] or potassium carbonate solution [110]. However, the application range of such binary incompressible fluid EOS is limited, Table 1, due to the scope in which these fluids are used /handled in industry (e.g. seawater in desalination plants or lithium bromide in adsorption cooling). Moreover, no interaction models exist to allow mixtures of these binary mixtures (e.g. seawater and lithium bromide) or binary mixtures with other pure components (e.g. seawater and carbon dioxide) to be modelled.

Table 2.1: The applicability range of various incompressible fluid EOS. x_{min} and x_{max} are the lower and upper limit for the amount of the species other than water.

Fluid	$T_{min}, ^\circ C$	$T_{max}, ^\circ C$	$x_{min}, \%$	$x_{max}, \%$
Seawater	0	120	0	12
Lithium Bromide	0	227	0	75
Calcium Chloride	-55	20	15	30
Potassium Carbonate	-100	0		40

2.2.6. Chemically reactive Systems

An alternative approach is to treat the geofluid as a chemically reactive system. In such a system, the constituent species can partition into different phases (e.g. gaseous, aqueous – a water-rich liquid phase, solid, etc.), react with each other to form new species or dissociate into other species, Figure 2.3. Determining the amounts and composition of all phases at equilibrium, at a given temperature and pressure, is equivalent to assessing the geofluid’s phase behaviour and also allows the thermophysical properties of the individual phases and overall fluid to be obtained.

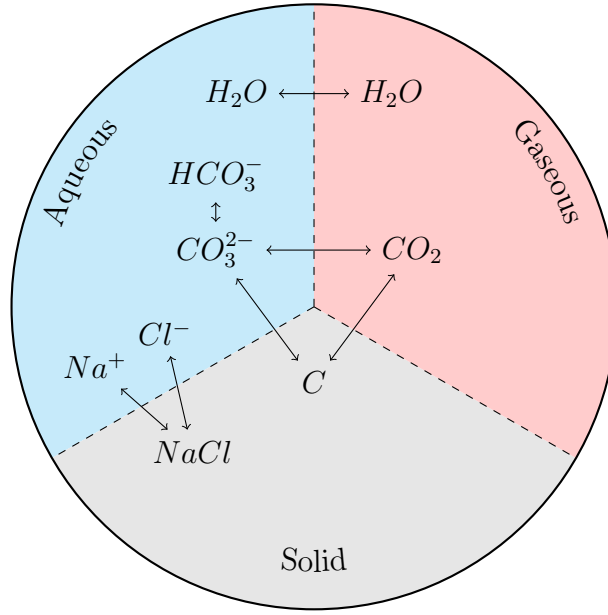


Figure 2.3: Schematic of a possible chemical reactive system describing a geofluid

A unit amount of geofluid of arbitrary overall composition can be approximated as a closed thermodynamic system (i.e. no mass transfer into or out of the system). From the Second Law of Thermodynamics, such systems reach equilibrium when the system entropy reaches a global maximum. For systems at constant temperature and pressure, it can be shown that this is consistent with the Gibbs free energy, 2.19 of the system reaching a global minimum, also see Chemical Equilibrium.

$$G = H - TS \quad (2.19)$$

Thus, determining the equilibrium state (i.e. finding the phase amounts and compositions) represents a minimisation problem (i.e. $\min G(P, T, \mathbf{n})$), subject to the constraint that the total mass of each chemical element (i.e. H, O, Na, Cl, etc.) is conserved across all species and phases considered (i.e. $\sum_{i=0}^N w_{ij} n_i = b_j$, where w_{ij} is the number of atoms of element j that make up species i , n_i is the amount of species i , and b_j is the total amount of element j in the system).

A convenient expression for calculating the Gibbs free energy of the system can be obtained by combining the differential form of the Gibbs free energy (at constant temperature and pressure), Equation 2.20, with the First Law of Thermodynamics (i.e. $dU = \delta Q + \delta W + \sum_{i=1}^N \mu_i dn_i$), assuming fully reversible processes (i.e. $\delta Q = TdS$) and mechanical work (i.e. $\delta W = pdV$), followed by integration over the molar amounts.

This allows the Gibbs free energy of the system to be calculated from the amounts of each species and their respective chemical potential, Equation 2.21. Here, G is Gibbs free energy, P is pressure, T is temperature, U is internal energy, V is volume, S is entropy, μ_i is the chemical potential of species i , n_i is the number of moles of species i and \mathbf{y} is the vector of all species' mole fractions.

$$dG|_{P,T} = dU + PdV - TdS \quad (2.20)$$

$$G(P, T, \mathbf{n}) = \sum_{i=1}^N n_i \mu_i(P, T, \mathbf{y}) \quad (2.21)$$

The partial derivatives of the chemical potential are the partial molar enthalpy, Equation 2.22, the partial molar entropy, Equation 2.23, and the partial molar volume, Equation 2.24, - the thermodynamic properties of interest.

$$h_i(P, T, \mathbf{y}) = \frac{\partial \left(\frac{\mu_i(P, T, \mathbf{y})}{T} \right)}{\partial \left(\frac{1}{T} \right)} \bigg|_{P, \mathbf{y}} \quad (2.22)$$

$$s_i(P, T, \mathbf{y}) = - \frac{\partial (\mu_i(P, T, \mathbf{y}))}{\partial T} \bigg|_{P, \mathbf{y}} \quad (2.23)$$

$$v_i(P, T, \mathbf{y}) = \frac{\partial (\mu_i(P, T, \mathbf{y}))}{\partial P} \bigg|_{T, \mathbf{y}} = \frac{1}{\rho_i(P, T, \mathbf{y})} \quad (2.24)$$

Note. For convenience the above equations can also be re-written as shown in Equation 2.25, where $\Psi_i(P, T, \mathbf{y})$ is a placeholder for a thermodynamic property and the choice of x and $f(x)$ depends on the thermodynamic property of interest, see Table 2.2.

$$\Psi_i(P, T, \mathbf{y}) = \frac{\partial (f(x) * \mu_i(P, T, \mathbf{y}))}{\partial x} \quad (2.25)$$

Table 2.2: The definition of the auxiliary variable and function by partial molar property.

Ψ_i	x	$f(x)$
h	$\frac{1}{T}$	x
s	T	-1
v	P	1

The calculation of the chemical potential is broken down into two components; the standard chemical potential of the species at a reference state, and the species' activity, Equation 2.26. The species' activity is defined as the difference between the actual chemical potential and the standard chemical potential, Equation 2.27.

The reference state is chosen by convention: For liquid or gaseous species, the reference composition, y^o , is that of the pure component, whereas for aqueous species (e.g. Na^+), a 1-molal solution of the solute is chosen, with all other species at infinite dilution. Meanwhile, the reference pressure for liquid and aqueous species is taken as the system pressure (i.e. $P^o = P$), whereas for gases, the reference pressure is taken to be 1 bar (i.e. $P^o = 1$ bar).

$$\mu_i(P, T, \mathbf{y}) = \mu_i(P^o, T^o, \mathbf{y}^o) + RT \ln a_i(P, T, \mathbf{y}) \quad (2.26)$$

$$RT \ln a_i(P, T, \mathbf{y}) \equiv \mu_i(P, T, \mathbf{y}) - \mu_i(P^o, T^o, \mathbf{y}^o) \quad (2.27)$$

With the above in mind, determining the equilibrium composition and thermophysical properties of a geofluid at a given temperature and pressure requires three inputs: 1) The amounts of all elements across all species, 2) the chemical potential of all species at their respective reference state (also called the standard chemical potential) and 3) the activity of all species.

The elemental amounts can be obtained from the geofluid composition, which is specific to each geothermal site as it is dependent on several factors, such as reservoir rock composition, temperature and pressure. Thus, the geofluid composition can only reliably be obtained from geofluid samples.

Standard Chemical Potential

The species' standard chemical potential can be obtained from peer-reviewed open-source databases, such as SUPCRT92 [47] or SUPCRTBL [108]. Frameworks, such as ThermoFun [69] and Reaktoro [51], implement several models for computing standard thermodynamic properties from such databases. Alternatively, high-fidelity EOS for species, such as water and carbon dioxide, can be used. Computationally cheaper EOS, such as SRK or PR, can be used, provided their input parameters (e.g. critical properties, acentric factor, etc.) have been calibrated to the specific component in question.

Activity Models

The species' activity can be calculated from phase and species-specific activity models. The simplest activity models approximate the fluid as an ideal fluid (i.e. Ideal Gas, Ideal Solution or Ideal Solid). However, this approach limits their application to low concentrations (for Ideal Solutions) or low pressures and high temperatures (for Ideal Gases), where the species exhibit ideal behaviour and where interactions among molecules are negligible. For gaseous species, such as CH_4 , N_2 , H_2S , etc., the SRK EOS or the PR EOS may also be used to approximate the real gas behaviour and interactions among other gaseous species.

Various activity models have been proposed for the different types of aqueous species. For example, the Setschenow equation [87] for neutral species, the HKF-Debye-Hückel model [42] for water and ionic species, or the Pitzer model for various aqueous species [77]. Moreover, species-specific activity models have been developed for common mixtures of species. For example, for mixtures of H_2O , CO_2 , CH_4 and some mineral species, models by Duan and Sun, Spycher et al. and Spycher and Pruess, amongst others, can be used. The selection of an activity model is ultimately dependent on the species present, their relative amounts as well as the system temperature and pressure.

Limitations

In principle, chemically reactive systems allow any number of species and reactions to be modelled. However, the main barrier to this approach, being applied universally to geofluid modelling in a geothermal context, is the availability of appropriate activity models for all species - particularly gaseous water (i.e. steam). While the WP EOS represents the highest fidelity model for the properties of water and steam [44], it is computationally expensive and it only works with a single component: water. For this reason, most geochemical modelling codes (e.g., PHREEQC, GEMS, Reaktoro) adopt

cubic equations of state for the vapour phase, such as the PR EOS or the SRK EOS, to permit other gases such as CO_2 , H_2S , O_2 , and others to be considered. However, this can result in deviations from the expected phase behaviour when water steam is in higher proportion compared to other gases or simply the only gaseous species.

For example, for pure water at a pressure of 10 bar the WP EOS predicts a saturation temperature of around 453 K. To model the same fluid using a chemically reactive system we assume a system consisting of only an aqueous and a gaseous water species (i.e. $H_2O^{(aq)}$ and $H_2O^{(g)}$). This system was then simulated in *Reaktoro*, see 2.2.8, as part of a Vapour-Liquid Equilibrium (VLE) calculation, for a pressure of 10 bar and a temperature between 445 K and 465 K. The SUPCRTBL database was used for the standard thermodynamic properties and different EOS (ideal gas and SRK) as activity models for the vapour phase (i.e., $H_2O^{(g)}$). The specific volume of the fluid was evaluated for each state and compared against values calculated via the WP EOS (Figure 2.4). In the case of *Reaktoro*, the saturation temperature was inferred by the temperature at which the transition from liquid-like to vapour-like densities occurs.

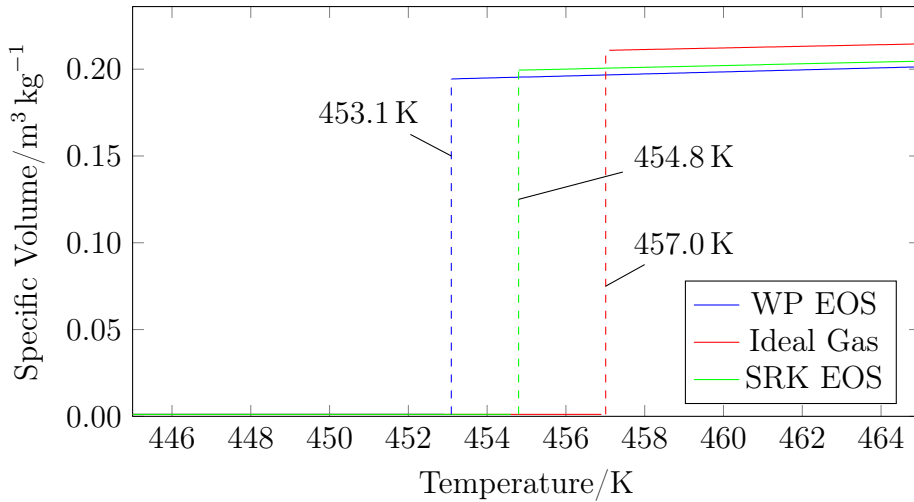


Figure 2.4: The specific volume of pure water at a pressure of 10 bar over temperatures 445 to 465 K calculated with *Reaktoro* using the Ideal Gas and SRK EOS, compared to the WP EOS.

Depending on the equation of state selected in *Reaktoro*, the specific volume differs from the values predicted by the WP EOS by 1.3 % (SRK) and 6.5 % (Ideal Gas) (Figure 2.4). These differences indicate that the partial derivatives of the chemical potential (in this case with respect to pressure) of gaseous water equation, see Equation 2.24, are inconsistent with the WP EOS. Consequently, in direct steam cycle geothermal power plants, the steam turbine would be designed and optimised for different volumetric rates and

velocities, resulting in sub-optimal turbine designs.

Furthermore, the transition from liquid-like to vapour-like specific volume occurs at higher temperatures compared to WP EOS, indicating that the selected EOS (i.e., SRK and Ideal Gas) result in the chemical potential of gaseous water to be overestimated. By definition, at saturation, the chemical potential of the same chemical species in different phases is the same (i.e. $\mu_i^L = \mu_i^G$).

Although the differences in saturation temperature are small in relative terms (less than 0.7% in the case of the SRK activity model), the absolute differences (2 K in the case of the SRK activity model), when compared to key power plant design parameters, such as the minimum approach temperature difference in the heat exchange equipment (typically between 5 K and 10 K), are significant, representing differences of 20 % to 40 %. This can affect the required heat transfer area, which is the primary driver for the cost of heat exchange equipment.

Repeating the above experiment for different system pressures (Figure 2.5), for the SRK activity model, the deviations range between 0.28 % and 0.68 % in relative terms, and 1.16 K to 3.6 K in absolute terms, while for the Ideal Gas activity model the saturation temperature deviation increases from 0.28 % (corresponding to 1.06 K) at 1 bar to 3.32 % (corresponding to 18.4 K) at 64 bar. The latter can be explained by the deviation from ideal gas behaviour at elevated pressures. Thus, for pressures exceeding 2.5 bar (corresponding to a saturation temperature of 400 K for pure water), the SRK activity model provides more accurate saturation temperature estimates than the Ideal Gas activity model.

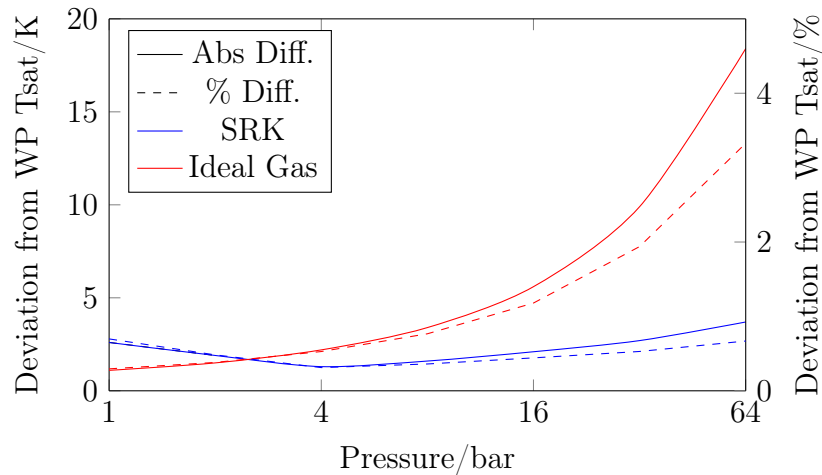


Figure 2.5: The deviation of saturation temperature (from the WP EOS) when computed as part of a VLE calculation in *Reaktoro* assuming either the ideal gas and SRK EOS for the vapour phase and the SUPCRTBL thermodynamic database.

2.2.7. Empirical Models

Empirical models for specific geofluid mixtures, most commonly for mixtures comprised of water, and carbon dioxide as well as impurities, such as CH_4 , N_2 and H_2S , have been developed. An example of this is a model originally presented by Spycher et al. [97] for the mutual solubilities of carbon dioxide and water at low temperatures (12 °C to 100 °C). This model was later extended to higher temperatures (12 °C to 300 °C) by Spycher and Pruess [96]. Corrections for salinity are applied using an approach similar to that of Duan and Sun [31].

While such empirical models can be used to determine equilibrium phases and compositions, they do not provide methods for estimating the thermophysical properties of the fluid. Moreover, these models make simplifying assumptions, particularly regarding the reactivity of the various aqueous species, meaning that advanced phase behaviours, such as scaling/mineralisation, cannot be captured.

2.2.8. Calculation Libraries

There are a number of calculation libraries that implement HEOS for pure fluids and their mixtures, for example *CoolProp* [20], *REFPROP* [57] and *FluidProp* [27]. Out of the former, only *CoolProp* is fully open-source, while the others are commercial libraries and represent an black box.

Reaktoro [51] is a unified open-source framework for modelling chemically reactive systems. *Reaktoro* pairs the aforementioned thermodynamic databases, EOS and activity models with scalable optimisation algorithms [53] and on-demand machine learning acceleration strategies [50, 52]. *Reaktoro* was used in Walsh et al. to produce a computer code to compute both thermodynamic and thermophysical properties, such as viscosity and thermal conductivity. The core *Reaktoro* calculation engine is written in C++ for performance reasons, with Python API provided for more convenient usage in Jupyter Notebooks and/or with the rich ecosystem of Python libraries.

ThermoFun [69] is an open-source framework for calculating the thermodynamic properties of species and reactions from thermodynamic databases such as SUPCRT98 or SUPCRTBL. The core *ThermoFun* calculation engine is written in C++ for performance reasons, but also offers a Python API for more convenient usage. *ThermoFun* is integrated into *Reaktoro*, where it can be used to provide the standard thermodynamic properties of species.

2.3. GeoProp

The aforementioned frameworks/models fall into two categories: partition models for determining the number, amounts and composition of equilibrium phases; and property models for estimating the thermophysical properties of fluids of known composition. GeoProp was developed in recognition of these synergies and allows different partitioning and property frameworks/models to be coupled with another (Figure 2.6), all while maintaining the flexibility of customising the underlying calculation engines, [65].

2.3.1. Structure

The main underlying data structure, a *Fluid*, is a container for the compositional data of the geofluid. The individual species are stored in *Phases*, both in their native phase (i.e. aqueous, gaseous or mineral) and in a total phase, capturing all species. The *Fluid* can be passed from one calculation engine (e.g. partition model or property model) to another, with the required input data and parameters being automatically passed to the underlying models. The user defines the initial species and their total amounts. The phase compositions are populated after performing a partitioning calculation, while the thermophysical properties are updated following the property calculation.

The *Partition* module equilibrates an input *Fluid* and partitions the *Fluid* into the equilibrium phases. This determines the number, amounts and composition of the equilibrium phases at the given temperature and pressure. To date, two partition models are available: a) *Reaktoro* and b) *SP2009* (details of adaptation of the original model by Spycher and Pruess can be found in Spycher-Pruess Partition Model). However, the open architecture of GeoProp allows other partition models to be included. Additionally, the user retains the ability to fully customise the underlying equilibrium and partitioning calculations, such as selecting non-default activity models in *Reaktoro*.

The *Property* module evaluates the properties of a given *Fluid* at the specified pressure and temperature. This module currently uses two calculation engines: a) *CoolProp* and b) *ThermoFun*.

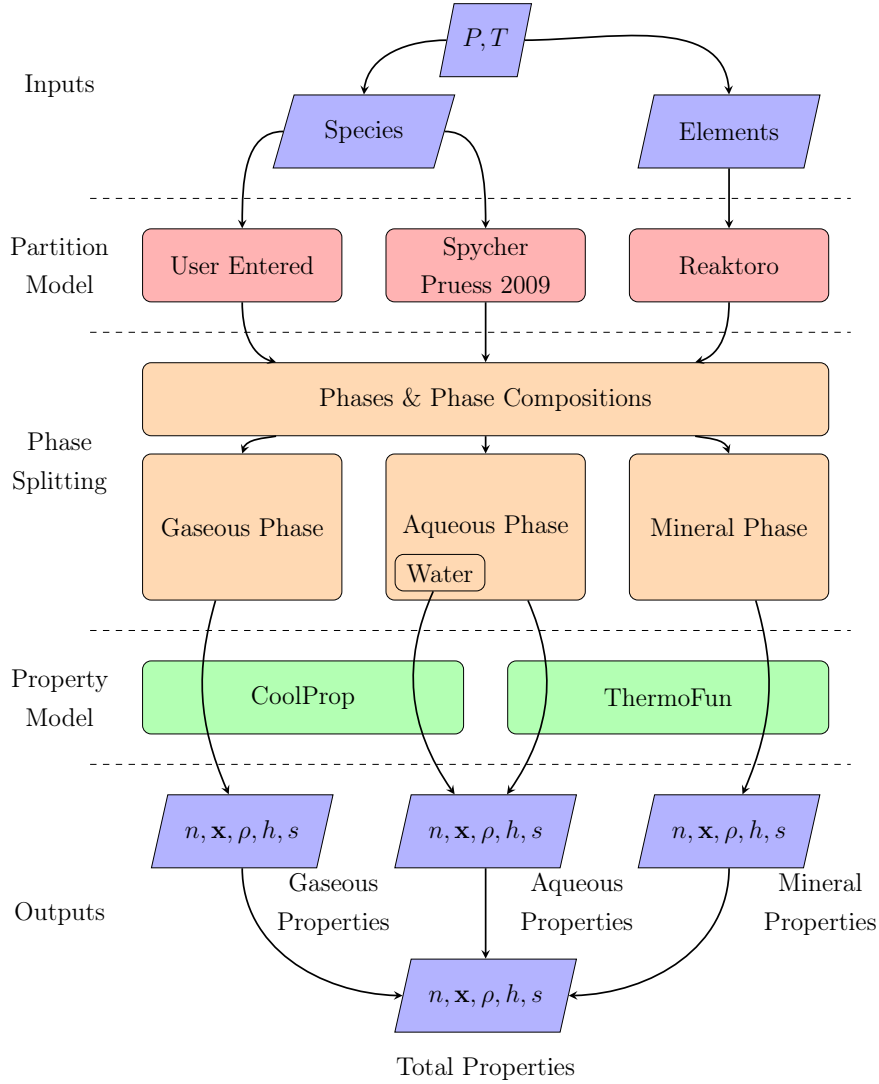


Figure 2.6: Flow diagram of GeoProp for partitioning geofluids and calculating their thermophysical properties

Property Estimation

The properties of gaseous phase species are evaluated in *CoolProp* using a mixture of pure components and the default BIC data, which effectively takes the role of the activity model correcting the partial molar properties from ideal to real conditions. In case of non-convergence, an ideal mixture is assumed (i.e. mixture effects are negligible), allowing the pure component properties to be calculated and then aggregated to the phase properties.

ThermoFun is used to calculate the properties of all aqueous species besides water, which is calculated using *CoolProp*'s implementation of the WP EOS. Aqueous species are assumed to be dilute and hence mixture effects are insignificant (i.e. unit activity for all aqueous species). As such, the species chemical potential, $\mu_i^{(aq)}(P, T, \mathbf{y})$, approaches that

at the reference conditions, $\mu_i^{(aq)}(P, T, \mathbf{y}^o)$, since the activity contribution approaches zero (i.e. $RT \ln a_i(P, T, \mathbf{y}) \rightarrow 0$ as $a_i \approx 1$). In turn this allows the pure component properties, $\Psi_i^{(aq)}(P, T, \mathbf{y}^o)$, to be used, see Equation 2.28, where $\Psi_i^{(aq)}$ is a placeholder for properties such as the specific enthalpy, entropy or density of component i , and x as well as $f(x)$ are the supplementary variable and function to calculate the property, see Equation 2.25 and Table 2.2 in Section 2.2.6. To obtain the aqueous phase properties, the species properties, $\Psi_i^{(aq)}$, are aggregated using Equation 2.29.

$$\Psi_i^{(aq)}(P, T, \mathbf{y}) \approx \frac{1}{M_{r_i}} \frac{\partial \mu_i(P, T, \mathbf{y}^o) * f(x)}{\partial x} \quad (2.28)$$

$$\Psi^{(aq)}(P, T, \mathbf{y}) = \frac{\sum_{i=0}^N m_i^{(aq)} \Psi_i^{(aq)}(P, T, \mathbf{y})}{\sum_{i=0}^N m_i^{(aq)}} \quad (2.29)$$

Mineral phase properties are computed with *ThermoFun*, assuming that each mineral constitutes a separate pure phase. Thus, unit activities are assumed, allowing the pure component properties, $\Psi_i^{(s)}(P, T, \mathbf{y}^o)$, to be used, Equation 2.30, which are then aggregated to the overall mineral phase properties, Equation 2.31.

$$\Psi_i^{(s)}(P, T, \mathbf{y}) \approx \frac{1}{M_{r_i}} \frac{\partial \mu_i(P, T, \mathbf{y}^o) * f(x)}{\partial x} \quad (2.30)$$

$$\Psi^{(s)}(P, T, \mathbf{y}) = \frac{\sum_{i=0}^N m_i^{(s)} \Psi_i^{(s)}(P, T, \mathbf{y})}{\sum_{i=0}^N m_i^{(s)}} \quad (2.31)$$

The properties of all phases are aggregated to the overall fluid properties employing a mass-fraction-based mixing rule, Equation 2.32.

$$\Psi^{(t)}(P, T, \mathbf{y}) = \frac{\sum_{j=0}^K m^j \Psi^j(P, T, \mathbf{z})}{\sum_{j=0}^K m^j} \quad (2.32)$$

2.3.2. Validation

We use geofluid samples, collected from geothermal fields near Makhachkala, Dagestan in Russia, by Abdulagatov et al. as the primary validation dataset. This dataset includes the fluid density, speed of sound and specific enthalpy (inferred from density and speed of sound measurements) for various temperatures. The composition of the fluid samples is summarised in Table 2.3. The salinity of these fluids ranges between about 1.7 g L^{-1} to 15 g L^{-1} . For reference, seawater has a salinity of 35 g kg^{-1} [66].

Table 2.3: The composition of the geothermal fluid samples near Makhachkala [5] in mg L^{-1} . Species exclusively below the detection threshold of 0.1 mg L^{-1} have been omitted.

Species		Sample		
		No. 68	No. 129	No. 27T
<i>Cations</i>	B	1.2	2.4	59.3
	Ba	<0.1	<0.1	1.7
	Ca	49.2	2.8	73.6
	K	10.2	4.7	145
	Li	0.2	0.1	2.2
	Mg	32.9	1.3	28.5
	Na	396	590	7540
	P	<0.1	0.2	<0.1
	S	240	211	39.8
	Se	2.4	0.2	<0.1
	Si	13.8	12.3	29.4
	Sr	1.1	0.1	6.7
Anions	Cl	152	276	7387
	SO ₄	749	616	30.7
Total		1667.7	1830.0	15345.9

We also consider several “synthetic” datasets. For example, seawater is a good analogue for simple geothermal brines as it is primarily comprised of water and NaCl. Although lithium bromide is not typically present in large quantities in geothermal fluids, it is also considered to test the applicability of GeoProp to unconventional brines. The thermophysical properties of these fluids were obtained from the MITSW and LiBr incompressible binary mixture EOS, implemented in *CoolProp*. Moreover, with these EOS, it is possible to explore a wider range of salinities and temperatures.

A final benchmark is performed against the ELECNRTL electrolyte model in *ASPEN Plus v11*, a common process simulation.

The fluids were recreated in GeoProp and *Aspen Plus v11*, and then equilibrated over a range of temperatures, determining their thermophysical properties (Figure 2.7, Figure 2.8 and Figure 2.9). We find that GeoProp reproduces the “measured” densities of all fluids at

all temperatures to within 3 %, narrowly outperforming the ELECNRTL model in *Aspen Plus v11*. For the specific enthalpy, both GeoProp and *Aspen Plus v11* reproduced the measurements to within 1 %.

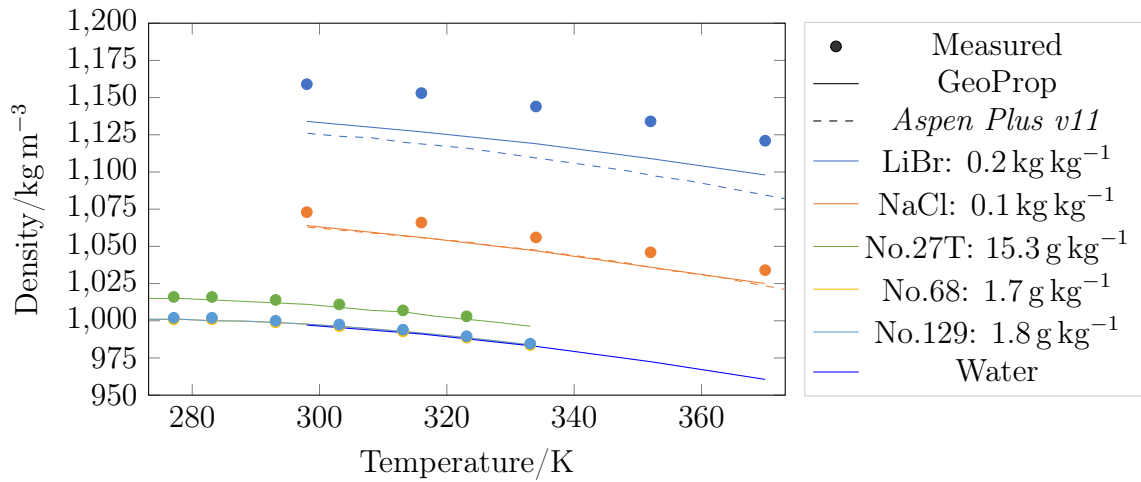


Figure 2.7: The density of various brines as a function of temperature at 1 bar pressure. Solid circles represent “measured” data and lines represent property models

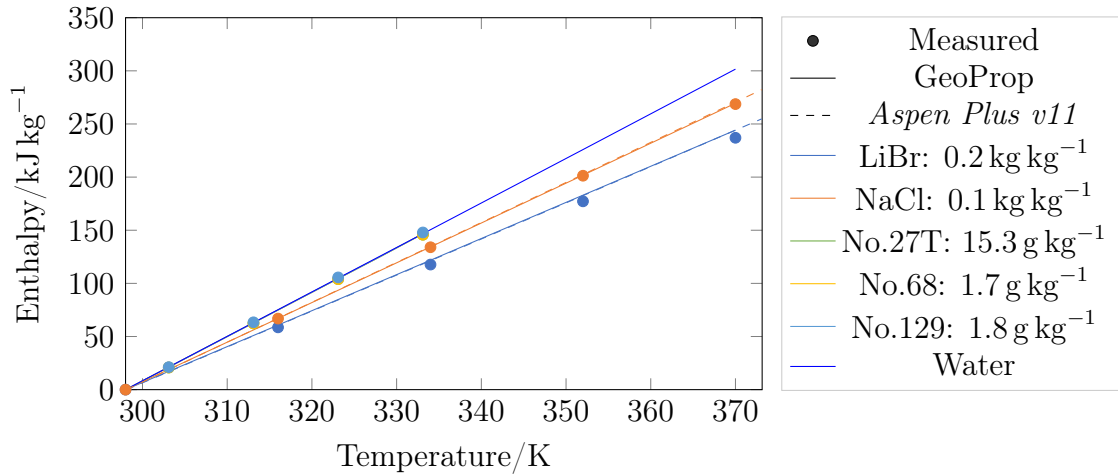


Figure 2.8: The specific enthalpy of various brines as a function of temperature at 1 bar pressure. The reference temperature is 298 K or 25 °C. Solid circles represent “measured” data and lines represent property models.

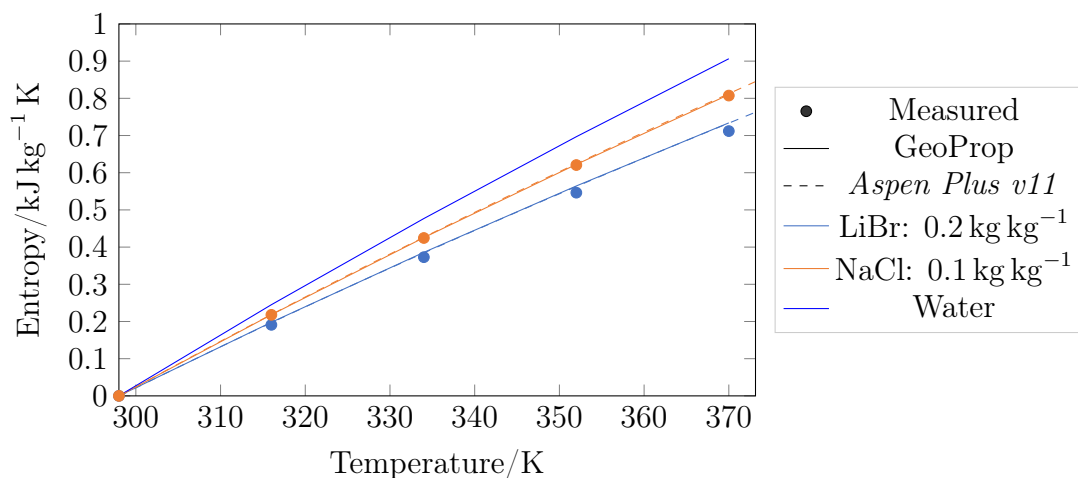


Figure 2.9: The specific entropy of various brines as a function of temperature at 1 bar pressure. The reference temperature is 298 K or 25 °C. Solid circles represent “measured” data and lines represent property models.

2.3.3. Examples

For code examples on using *GeoProp*, please refer to GeoProp Code Examples or the *GeoProp* Github repository <https://github.com/EASYGO-ITN/GeoProp>.

2.3.4. GeoProp v2

Given the open-source architecture of GeoProp, it is in principle possible to extend the functionality of GeoProp v1 to include further partition and property models. However, the first implementation of the properties back-end is somewhat static, making it difficult for users to extend the functionality to other property estimation engines.

Moreover, the initial approach divides the models into two classes without recognising that in fact they are all *models* and the only difference between them are their capabilities. For example, in GeoProp v1, *CoolProp* is treated purely as a property model, when in reality it also has some partitioning-like capabilities. A summary of the *models* currently used and their capabilities can be found in Table 2.4.

With the above in mind, a revised plug-in based architecture is proposed. This streamlines the process of adding *models* to GeoProp by simply requiring an *interface* or *driver* script, without having to adjust the overall GeoProp architecture. Besides the default configuration, this enables the user to define custom thermophysical property models by specifying arbitrary combinations of the *models*. While the general workflow is unchanged, the new architecture can be seen in Figure 2.10.

Table 2.4: Model capabilities.

Model	Partition	Properties		
		Vapour	Aqueous	Mineral
<i>CoolProp</i>	✓	✓	✓	
<i>Reaktoro</i>	✓	✓	✓	✓
<i>SP2009</i>	✓			
<i>ThermoFun</i>			✓	✓
...				

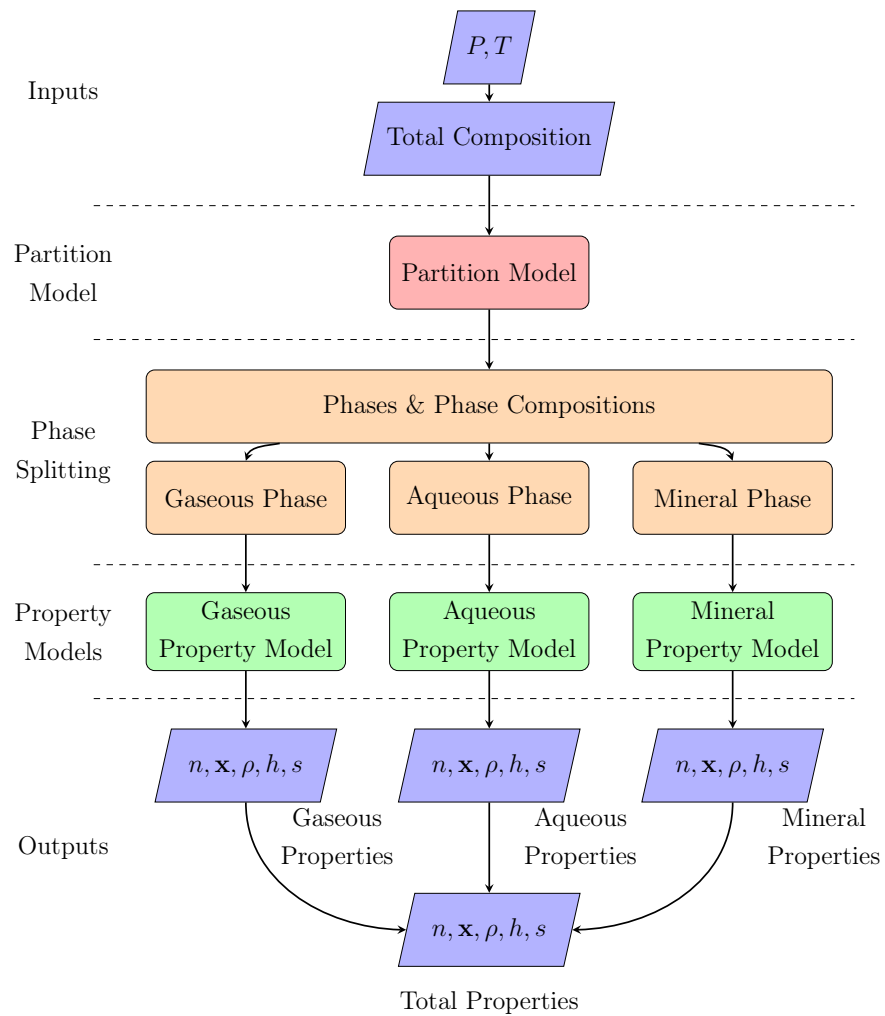


Figure 2.10: Flow diagram of GeoProp v2 for partitioning geofluids and calculating their thermophysical properties

2.4. Case Studies

2.4.1. Cooling Curves of Geothermal Geofluids

A common approach for investigating the comparative performance of different geothermal power plant technologies is to consider the geofluid to be pure water. However, this approach neglects the impact that impurities, such as dissolved salts and non-condensable gases, can have on the phase behaviour and thermophysical properties.

Table 2.5: Used compositions and models of the considered geofluids.

	Units	Geofluid			
		Water	Brine	Water & NCG	Brine & NCG
<i>Component</i>					
H_2O	kg kg^{-1}	1.00	0.95	0.95	0.90
$NaCl$	kg kg^{-1}	-	0.05	-	0.05
CO_2	kg kg^{-1}	-	-	0.05	0.05
Partition Model	-	WP EOS	<i>Reaktoro</i>	SP2009	SP2009
Property Model	-	WP EOS	Default - i.e. <i>CoolProp</i> & <i>ThermoFun</i>		

These differences can be illustrated by considering the Primary Heat Exchanger (PHE) in a simple binary ORC geothermal power plant and calculating the heat released by different geofluids as a function of reinjection temperature. Four geofluids, Table 2.5 are considered and their temperature-heat content (TQ) curves are generated in GeoProp, Figure 2.11.

The inlet conditions are defined in terms of a common temperature of 473 K (200 °C) and a heat content of 1135 kJ kg^{-1} (relative to 298 K and 1.013 25 bar). The heat content corresponds to that of pure water at 473 K and a vapour quality of 0.2 kg kg^{-1} . The same inlet temperature has been considered in order to investigate similar geothermal heat sources, while the heat content has been fixed to have Primary Heat Exchangers units of similar capacity. For the other three fluids, the vapour quality and inlet pressure are calculated in GeoProp assuming an inlet temperature of 473 K and a heat content of 1135 kJ kg^{-1} . The resulting inlet conditions are summarised in Table 2.6.

Table 2.6: Used compositions and models of the considered geofluids.

Conditions	Units	Geofluid			
		Water	Brine	Water & NCG	Brine & NCG
<i>Inlet</i>					
Mass Rate	kg s^{-1}			1.00	
Temperature	K			473	
Heat Content	kJ kg^{-1}			1135	
Pressure	bar	15.55	14.4	16.53	16.26
Vapour Quality	kg kg^{-1}	0.200	0.223	0.265	0.318

Unlike *Water*, *Brine* experiences a small temperature glide in the two-phase region as condensing water reduces the effective salinity of the aqueous phase, thereby reducing the saturation temperature. Moreover, liquid “Brine” has a lower specific heat capacity than liquid *Water*, as indicated by the steeper slope.

Thus, a binary ORC operating on a liquid-dominated *Brine*-like geofluid has a higher cycle working fluid mass rate to geofluid mass rate ratio compared to a *Water*-like geofluid. Consequently, for the same net power, a higher mass rate of the *Brine*-like geofluid is required. In turn, the higher geofluid mass rate also affects the heat exchanger design, in particular the required heat transfer and, hence, the cost.

Above 440 K, the specific heat capacity of *Water & NCG* deviates from *Water* significantly, which can be attributed to the presence of NCG, reducing the boiling point of the geofluid, allowing the water species to remain in the vapour phase at lower temperatures. For example, at the inlet, the vapour quality of *Water & NCG* is 0.265 kg kg^{-1} , compared to just 0.200 kg kg^{-1} for *Water*. Discounting the initial NCG content of 0.050 kg kg^{-1} , this means that an additional 0.015 kg kg^{-1} of water is in the vapour phase. Similarly, when the vapour quality of *Water* reaches zero, *Water & NCG* still has a vapour quality of 0.09 kg kg^{-1} , implying that about 0.04 kg kg^{-1} of water still remains in the vapour phase.

The curvature of the TQ curve for *Water & NCG* (Figure 9) also has practical implications, as it reduces the average temperature difference between the hot geofluid and the cold working fluid, compared to the *Water* case. This increases the heat transfer area required and, in turn, the cost of the heat exchanger.

The *Brine & NCG* case has a slightly higher vapour quality, compared to the *Water & NCG* case. This can be attributed to the presence of Na^+ and Cl^- ions.

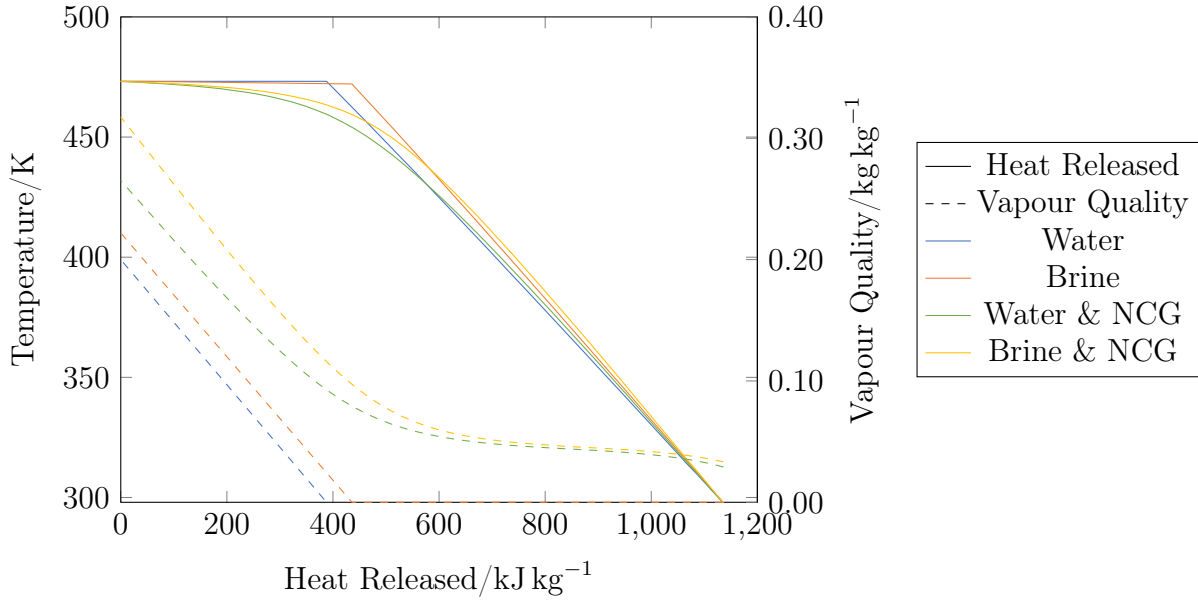


Figure 2.11: The temperature and heat released by different geofluids as well as the corresponding vapour quality. The heat content is relative to 298 K (25 °C) and 1.013 25 bar.

2.4.2. Model Comparison

A particular focus of this work is geothermal power generation from two-phase and NCG-rich geofluids. In this respect, it is important to have the appropriate tools for describing these fluids over the typical range of temperatures and pressures encountered in the geothermal energy system. This case study aims to compare the SP2009 model against the HEOS mixture model implemented in *CoolProp*. The primary objective of this study is to compare the equilibrium compositions of the water-rich and carbon dioxide-rich phases.

A mixture of water and carbon dioxide was modelled using an HEOS mixture in *CoolProp* using the default binary interaction data from Gernert. Similarly to the comparison above, this approach relies on the fluid to be two-phase at the temperature and pressure of interest in order for the mole fraction to be representative. In this respect, the same 1:10 ratio of carbon dioxide to water was used to ensure two-phase behaviour over a wide range of conditions.

```

1 mixture = cp.AbstractState("HEOS", "Water&CarbonDioxide")
2 mixture.set_mole_fractions([10/11, 1/11])

```

Regarding the definition of phases, the same caveats as with the ELECNRTL model apply, the HEOS mixture considers vapour and liquid phases, whereas the SP2009 model

considers a carbon-dioxidereich and a water-rich phase. These definitions are congruent for most conditions, however below the critical temperature of carbon dioxide, it is possible for both water and carbon dioxide to be in their liquid state.

Comparing the equilibrium mole fraction of water in the vapour/carbon dioxide-rich phase, see Figure 2.12, it can be seen that the HEOS mixture and SP2009 models are in close agreement at the lower temperatures and pressures. Unlike the ELECNRTL model, the HEOS mixture model appears to capture the phase transition at temperatures below 31 °C. At higher pressures and temperatures more significant deviations are observed, for example at 250 °C and 600 bar, the ratio of the equilibrium mole fractions of water is around 0.75, representing a difference of 25 %. Perhaps due to the complexity of the formulation, it is worth noting that the calculations did not converge for all conditions considered, see the gaps in the lines in Figure 2.12.

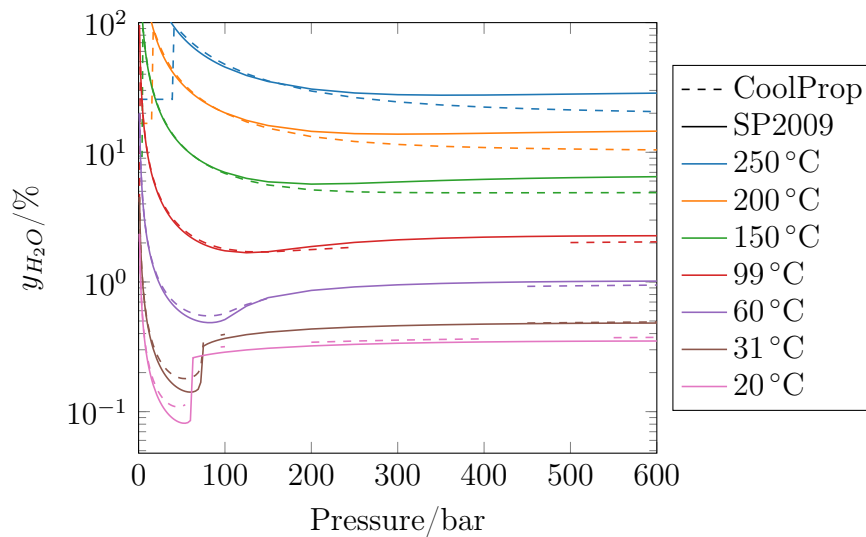


Figure 2.12: The equilibrium mole fractions of water in a carbon dioxide-rich phase, as a function of temperature and pressure, as calculated using the HEOS mixture model in *CoolProp* and the SP2009 model

Comparing the equilibrium mole fraction of carbon dioxide in the liquid/water-rich phase, see Figures 2.13, 2.14, the HEOS mixture model and the SP2009 appear in close agreement for temperatures up to 150 °C.

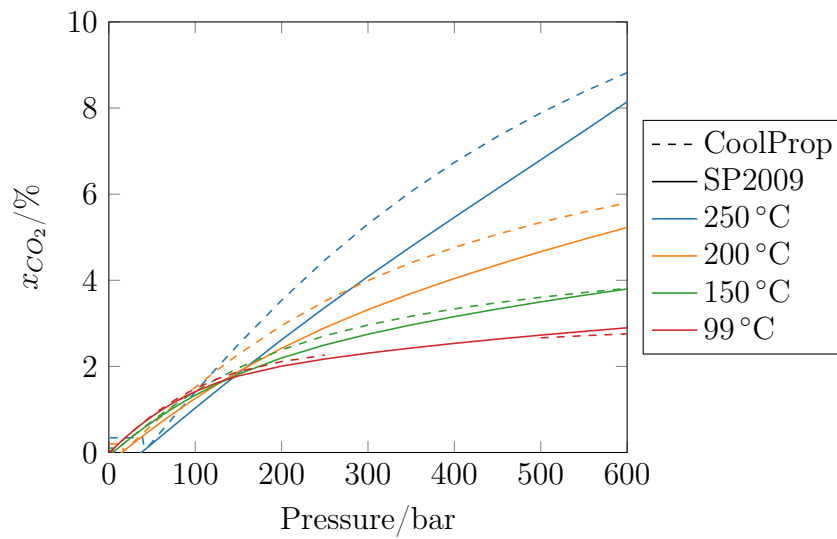


Figure 2.13: The equilibrium mole fractions of carbon dioxide in a water-rich phase, as a function of temperature and pressure, as calculated using the HEOS mixture model in *CoolProp* and the SP2009 model

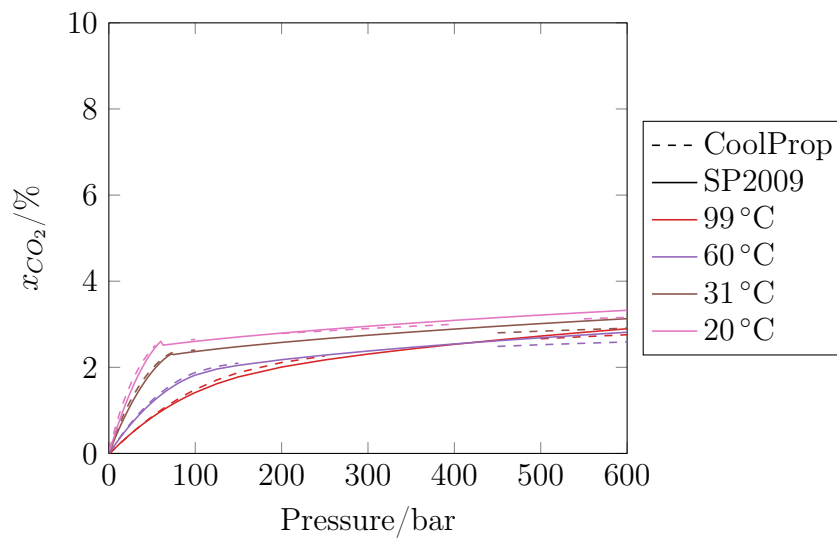


Figure 2.14: The equilibrium mole fractions of carbon dioxide in a water-rich phase, as a function of temperature and pressure, as calculated using the HEOS mixture model in *CoolProp* and the SP2009 model

3 | Geothermal Power Generation

3.1. Direct Steam Cycles

Direct steam cycles are typically used for the exploitation of medium to high enthalpy geothermal resources. Under these conditions, the geofluid arrives at the surface in its vapour state, or vapour can be readily liberated, by reducing the fluid pressure. Electrical power is generated directly from the geofluid, by expanding the high-pressure vapour in a turbine.

The following section aims to provide background on the different types of DSC geothermal power plants in use around the globe, the assessment of their thermodynamic performance and optimisation thereof, as well as the costs of such power plants.

3.1.1. Dry Steam

Dry steam geothermal power plants are used when the geofluid arrives at the surface in its vapour state. This limits their use to but the highest enthalpy resources, such as The Geysers, USA, or near Larderello, Italy, where incidentally the world's first geothermal power generation was demonstrated.

The vapour arriving at the wellhead is treated, removing solids (i.e. carried up from the formation, product of corrosion or scales) and moisture, which could be damaging to the turbine internals, Figure 3.1. The dry high-pressure vapour is then expanded in a turbine, converting the thermal energy to rotational work, which in turn drives a generator to generate electricity. The low-pressure vapour is then condensed before being re-pressurised and re-injected into the formation. In case the geofluid is rich in NCG, they are separated and may undergo treatment, to remove H_2S or mercury, with the remaining NCG being vented to atmosphere.

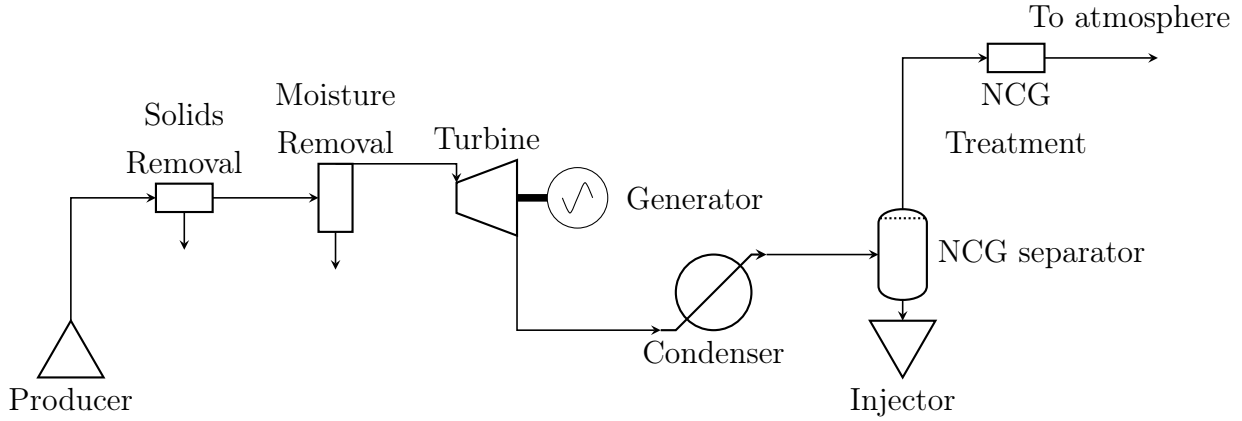


Figure 3.1: Schematic of a dry steam geothermal power plant. Adapted from [30]

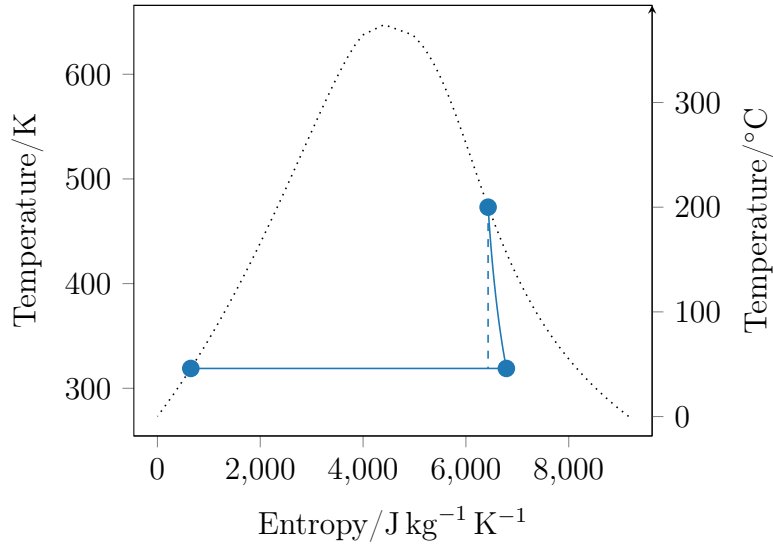


Figure 3.2: T-S diagram of a typical dry steam geothermal power plant.

However in light of the global drive for de-carbonisation, further treatment of the NCG to remove high GWP components, such as carbon dioxide or methane, or complete re-injection into the reservoir may be required in future. The NCG handling options are further explored in Section 3.3

3.1.2. Flash Steam

Flash steam geothermal power plants are used for medium enthalpy sources, where the geofluid arrives at surface in its liquid state or a low vapour quality two-phase state.

The geofluid arriving at surface is flashed (i.e. reducing its temperature) to increase the vapour quality, also see Section 3.1.3, separating the resulting liquid and vapour phases

in a separator, Figure 3.3. The liquid stream, also referred to as *brine*, is reinjected into the reservoir. The high-pressure vapour is then dried, to prevent damage to the turbine internals, before being expanded in the turbine, driving the generator to generate electricity. The low-pressure vapour is condensed before being re-pressurised and re-injected into the reservoir. In case the geofluid is rich in NCG, they are separated and may undergo treatment, to remove H_2S or mercury, with the remaining NCG being vented to atmosphere.

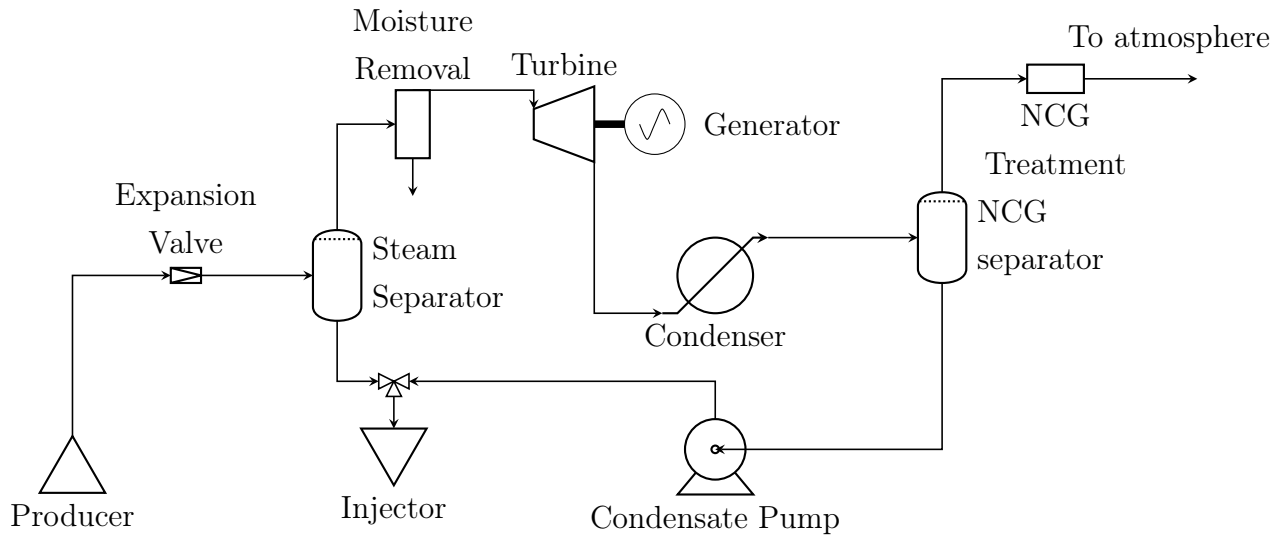


Figure 3.3: Schematic of a flash steam geothermal power plant. Adapted from [30]

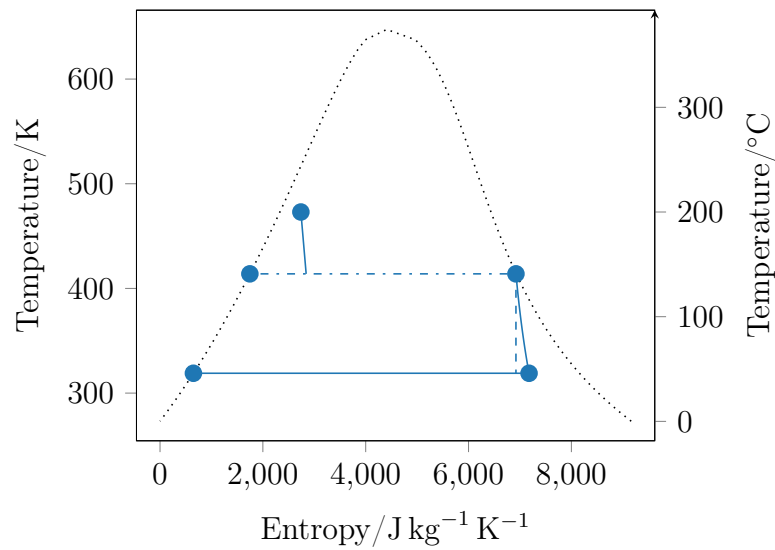


Figure 3.4: T-S diagram of a typical flash steam geothermal power plant.

In a variation of the above configuration, it is possible to *flash* the liquid geofluid multiple

times, Figure 3.5. Here, following the initial flash (to pressure P_1), the liquid brine is flashed again (to pressure P_2 , liberating more vapour. The high pressure steam is expanding in the turbine to the pressure of the second flash (P_2), where the two vapour streams are mingled before being fully expanded. This procedure can be repeated an arbitrary number of times, though do to the increased cost and complexity of the process, in practise at most three flashes are performed in a commercial setting. The flash pressures represent a useful optimisation parameter for improving the thermodynamic performance of the power plant, Section 3.1.3.

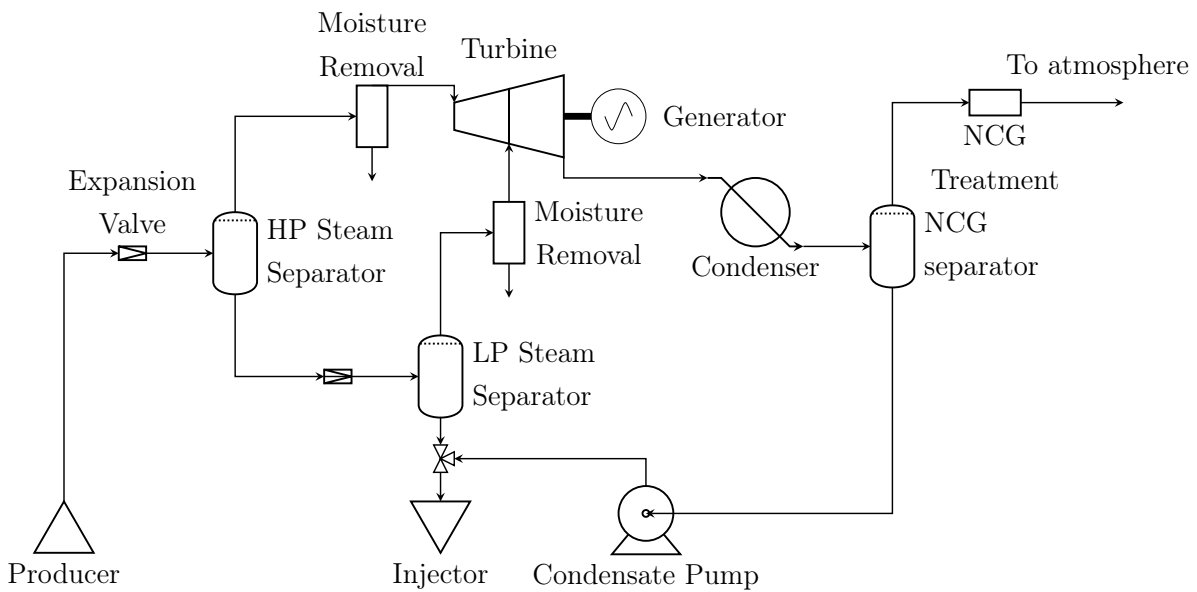


Figure 3.5: Schematic of a dual flash steam geothermal power plant. Adapted from [30]

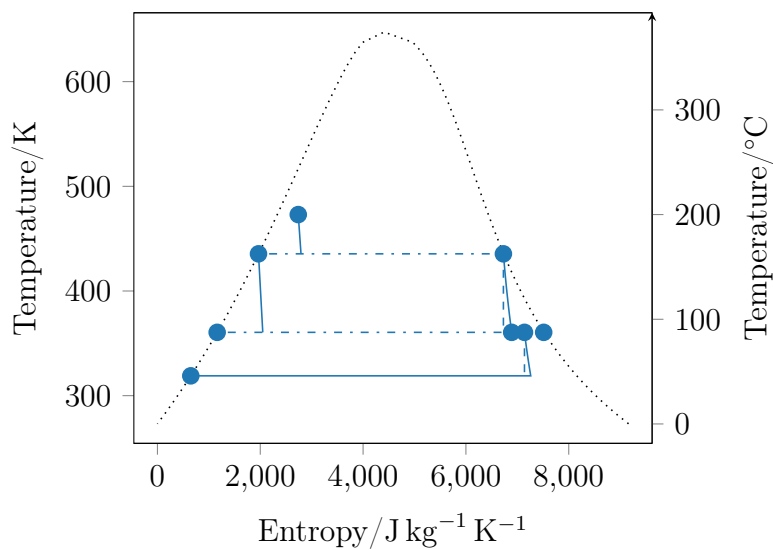


Figure 3.6: T-S diagram of a typical dual flash steam geothermal power plant.

3.1.3. Optimisation

The optimisation of DSC geothermal power plants, primarily concerns choosing the optimum mass rate, and if the geofluid is flashed, the number of flashes and the corresponding flash temperature(s)/pressure(s). This is illustrated in three case studies below:

Mass Rate Optimisation

The following case study was first presented by DiPippo [30].

The mass rate of geofluid produced from the geothermal reservoir is dependent on the Wellhead Pressure (WHP), with a higher WHP corresponding to a lower mass rate. However, the turbine power is also dependent on vapour inlet pressure, with a higher inlet pressure (and thereby pressure difference across the turbine) corresponding to a higher turbine power.

Assuming a dry steam plant with the turbine being located sufficiently close to the wellhead for frictional losses in the piping to be negligible, and a fixed condensation pressure of 1 bar.

The well performance curve (i.e. the relationship between the mass rate and the WHP) can be obtained from well tests, or appropriate modelling software. In this case the well performance curve is approximated by Equation 3.1 [30], the normalised form is shown in Figure 3.7. \dot{m} is the mass flow rate, \dot{m}_{max} is the maximum mass flow rate of the well (i.e. when the wellhead pressure is 0 bar), P is the wellhead pressure and $P_{shut-in}$ is the wellhead pressure for which the well ceases to flow.

$$\dot{m} = \dot{m}_{max} \sqrt{1 - \left(\frac{P}{P_{shut-in}} \right)^2} \quad (3.1)$$

Assuming the specific enthalpy of the geofluid is independent of the WHP (i.e. heat losses along the wellbore are independent of mass rate), the performance of the turbine can be calculated using Equation 3.2, assuming an isentropic efficiency η_{isen} of 85%. Where $h_{out,isen}$ is calculated assuming an isentropic expansion from the WHP P_{WH} to the condensation pressure P_{cond} . The resultant turbine performance curve can be seen in Figure 3.7.

$$\Delta h = h_{in} - \eta_{isen} * (h_{in} - h_{out,isen}) \quad (3.2)$$

Combining the two performance curves, with each reaching zero at opposite extremes of the WHP, the optimum can in this case be found to be around 580 kW kg^{-1} for a WHP of 6.8 bar.

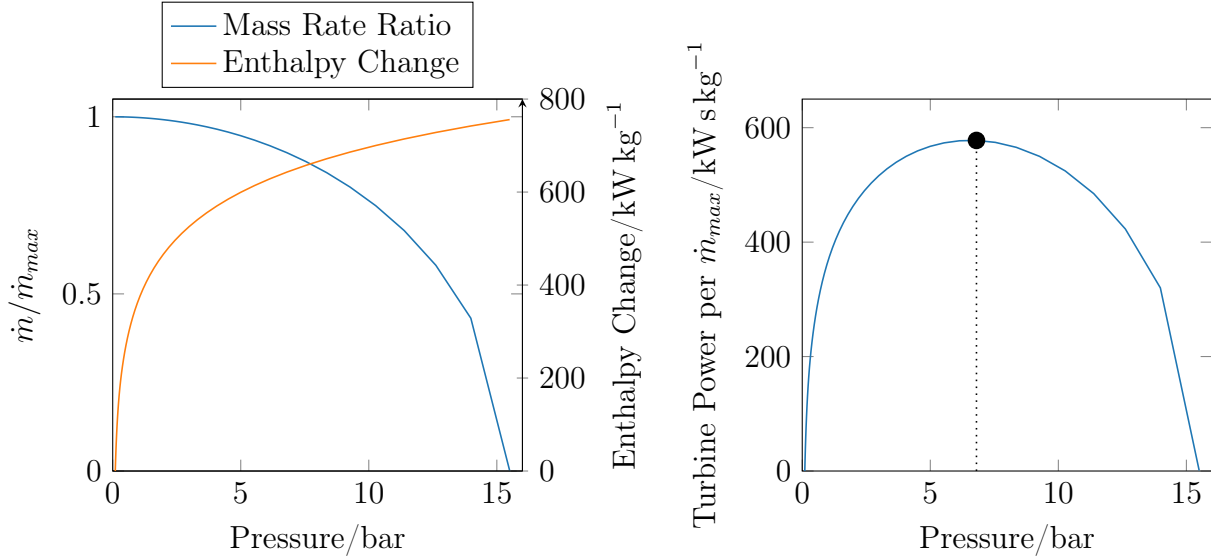


Figure 3.7: Optimisation of the WHP to maximise the turbine power. On the left, the normalised well performance curve (blue) and the corresponding enthalpy change across the turbine (assuming a condenser pressure of 1 bar) for an isentropic efficiency of 85 % assuming a dry expansion. On the right, the turbine power as a function of the WHP, the optimum is achieved at WHP of 6.8 bar corresponding to a turbine power of 580 kW kg^{-1}

Flash Temperature Optimisation

The following case study was first presented by DiPippo [30].

In DSC power plants using geofluid flashing, optimising the flash temperature(s)/pressure(s) is crucial of optimising the overall plant performance. Assuming a fixed inlet rate, there are two trade-offs that need to be balanced: a) flashing the geofluid to lower temperatures/pressures generally increases the vapour mass rate, but b) reduces the pressure difference across the turbine, see Figure 3.8.

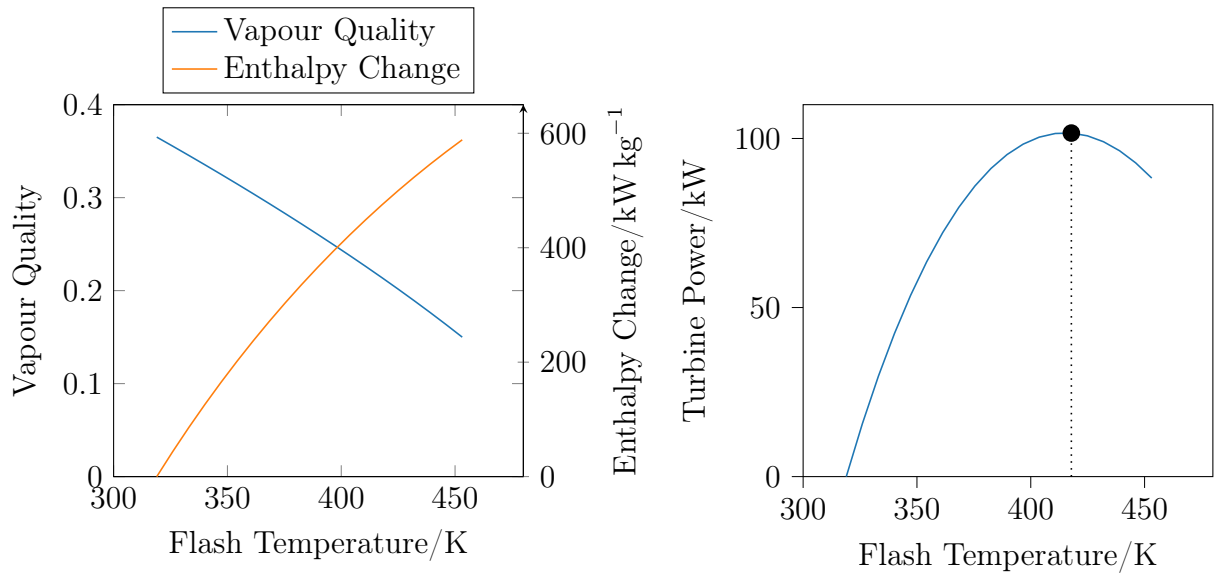


Figure 3.8: Optimisation of the flash temperature to maximise the turbine power for an inlet mass rate of 1 kg s^{-1} , an inlet temperature of 453 K (180°C), vapour quality of 15% and a condenser pressure of 0.1 bar . On the left, the vapour quality post flash (blue) and the corresponding enthalpy change across the turbine assuming an isentropic efficiency of 85% . On the right, the turbine power as a function of the flash temperature, the optimum is achieved at a flash temperature of 415.5 K (142.5°C) corresponding to a turbine power of 103.5 kW

In reality, the mass rate and flash temperature optimisation are best combined to ensure the overall performance of the plant can be optimised in an integrated fashion, see Figure 3.9.

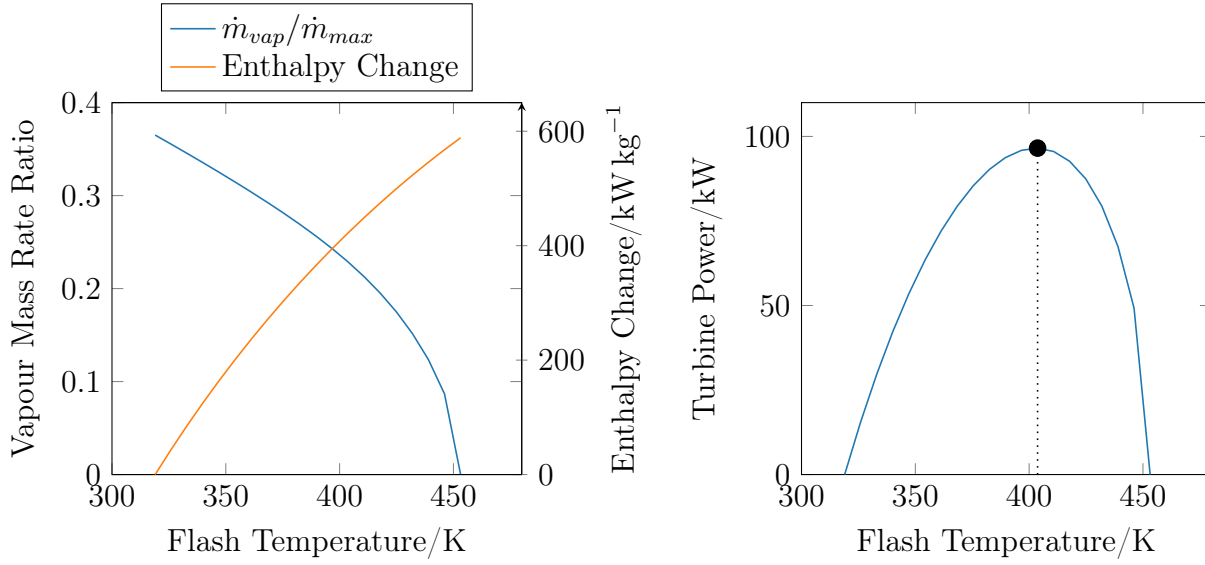


Figure 3.9: Maximisation of the turbine power by considering the inter-relation of the well performance curve and the enthalpy change across the turbine. For a well performance curve following Equation 3.1, an shut-in temperature of 453 K (180 °C) and vapour quality of 15 %, as well as a condenser pressure of 0.1 bar. On the left, the vapour mass rate post flash (relative to the maximum geofluid mass rate) (blue) and the corresponding enthalpy change across the turbine assuming an isentropic efficiency of 85 %. On the right, the turbine power as a function of the flash temperature, the optimum is achieved at a flash temperature of 403.7 K (130.7 °C) corresponding to a WHP of 2.74 bar, a relative mass rate of 0.96 and a turbine power of $96.5 \text{ kW kg}^{-1} \text{ s}$

Number Flashing Stages Optimisation

Increasing the number of flashes increases the overall vapour mass rate, however, as the remaining pressure difference across the turbine reduces with each flash, the newly liberated vapour contributes less and less to the overall turbine power. This can be seen in Figure 3.10, where increasing the number for flash stages from two to three increases the turbine power by about 1 %, but from three to four adds 0.33 % and from four to six only increases power by 0.26 %. In this respect, the optimisation of the number of stages is primarily an economic consideration, due to the increased plant cost and complexity. For this reason, commercial power plants utilise at most a triple flash configuration (e.g. the Nga Awa Purua [30])

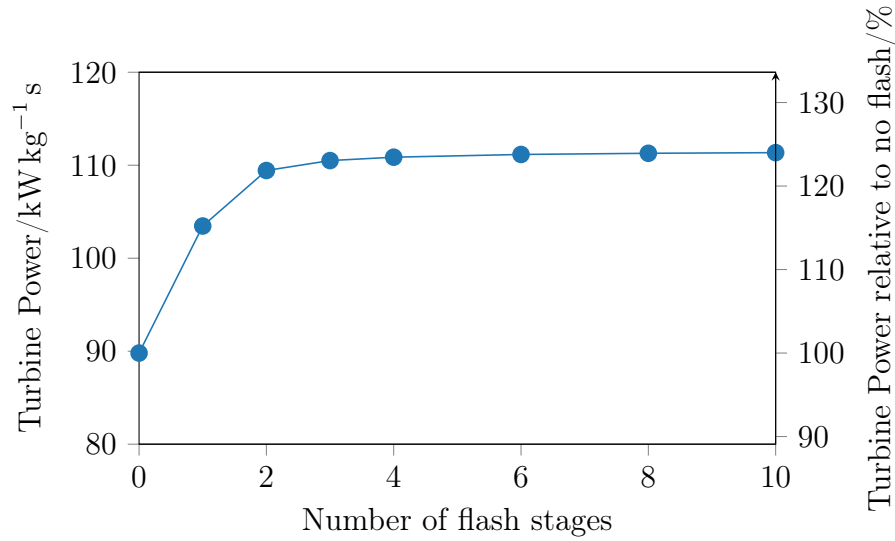


Figure 3.10: The optimum turbine power as a function of the number of flash stages, for an inlet mass rate of 1 kg s^{-1} , an inlet temperature of 453 K (180°C), an inlet vapour quality of 15% and a condensation pressure of 0.1 bar .

3.2. Binary Cycles

Binary cycle geothermal power plants are primarily used to generate electrical power from low enthalpy resources, where the geofluid arrives at the surface in its liquid state and flashing does not liberate sufficient quantities of steam for cost-effective power generation. In a binary cycle geothermal power plant, the thermal energy contained within the geofluid is transferred to a secondary fluid, also referred to as the cycle working fluid, which subsequently undergoes a power cycle to generate electricity Figure 3.11.

The following sections aim to provide background on binary geothermal power plants using Organic Rankine Cycle (ORC).

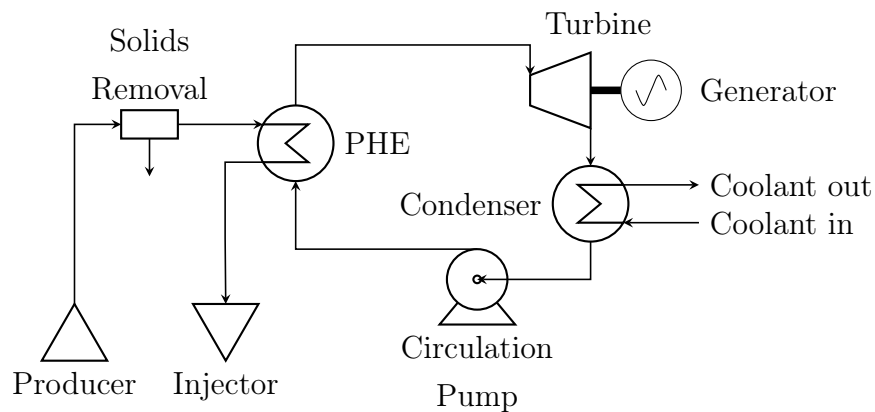


Figure 3.11: Schematic of a binary geothermal power plant.

3.2.1. Classical Rankine Cycle

In the classical Rankine cycle, pressurised water is vaporised using a heat source, and then drives a turbine to generate electricity. The low-pressure vapour is then condensed and re-pressurised closing the loop.

However, due to the high critical temperature of water, it is unsuitable for use as a cycle working fluid in low-temperature application. This can be attributed to three factors, 1) poor alignment with the cooling curve of the heat source, leading to high exergetic losses and thus low efficiency; 2) sub-atmospheric evaporation and condensation pressures, leading to air-ingress into the system, increasing utility costs; and 3) wet expansion in the turbine leading to low turbine efficiencies

Figure 3.12 shows a thermodynamically optimised saturated Rankine cycle using water as the cycle working fluid. Here both the evaporation and condensation pressures are sub-atmospheric, 0.85 bar and 0.08 bar corresponding to saturation temperatures of 368 K (95 °C) and 315 K (42 °C). If the cycle is super-heated, Figure 3.13 to avoid complications related to the wet expansion of steam, then the evaporation pressure has to be reduced to 0.41 bar corresponding to boiling temperature of 350 K (76.7 °C). However this comes at the expense of an additional heat exchange unit to super-heat the vapour.

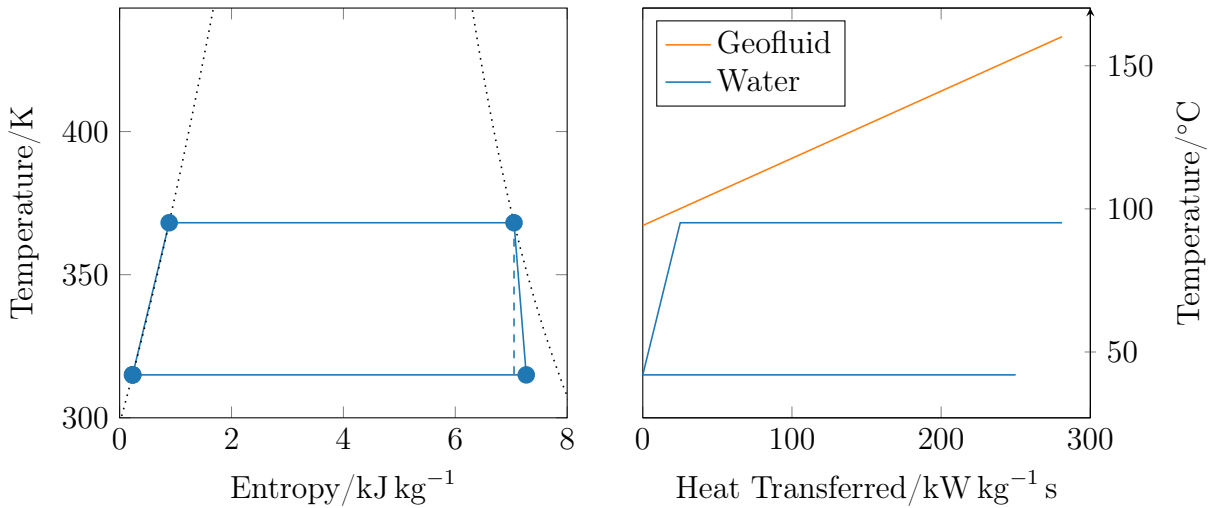


Figure 3.12: Temperature-Entropy and Temperature-Heat transfer diagrams of a saturated Rankine cycle operating on a liquid water-dominated saturated geofluid at 433 K (160 °C). The cycle operating parameters were optimised to maximise the specific net power.

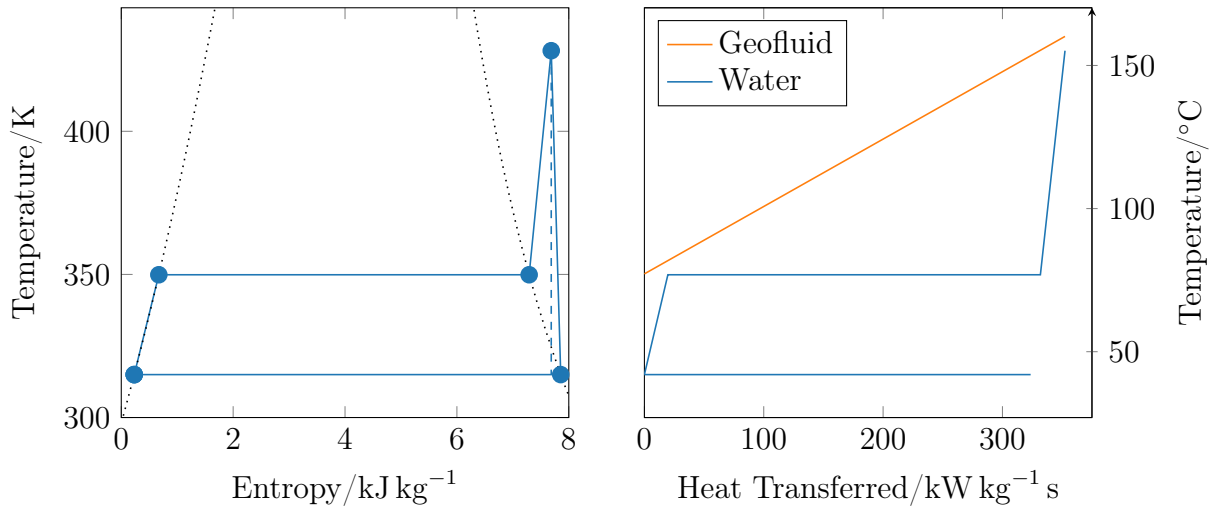


Figure 3.13: Temperature-Entropy and Temperature-Heat transfer diagrams of a superheated Rankine cycle, operating on a water-dominated saturated geofluid at 433 K (160 °C). The cycle operating parameters were optimised to maximise the specific net power.

3.2.2. Organic Rankine Cycle

Organic Rankine Cycle (ORC)s follow a classical Rankine cycle, Figure 3.14, with the exception of the choice of working fluid. Instead of water organic fluids, such as hydrocarbons or refrigerants, are used.

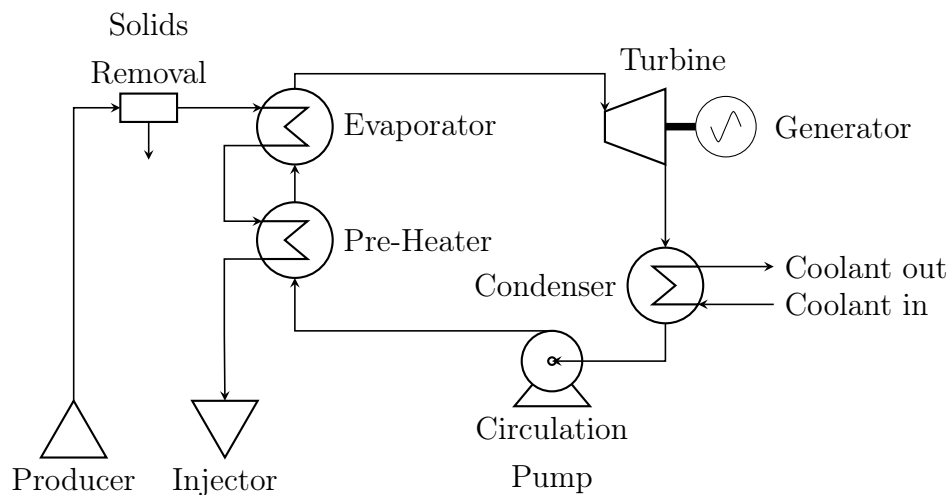


Figure 3.14: Schematic of a binary ORC geothermal power plant. Adapted from [30]

Organic substances have lower critical temperatures than water, allowing the evaporation and condensation to occur above atmospheric pressures, thus preventing the ingress of

air into the system; on the other hand this can lead to loss of working fluid over time. In the ORC shown in Figure 3.15, using n-Butane as the working fluid, evaporation and condensation occur at pressures of 16.8 bar and 4.00 bar respectively.

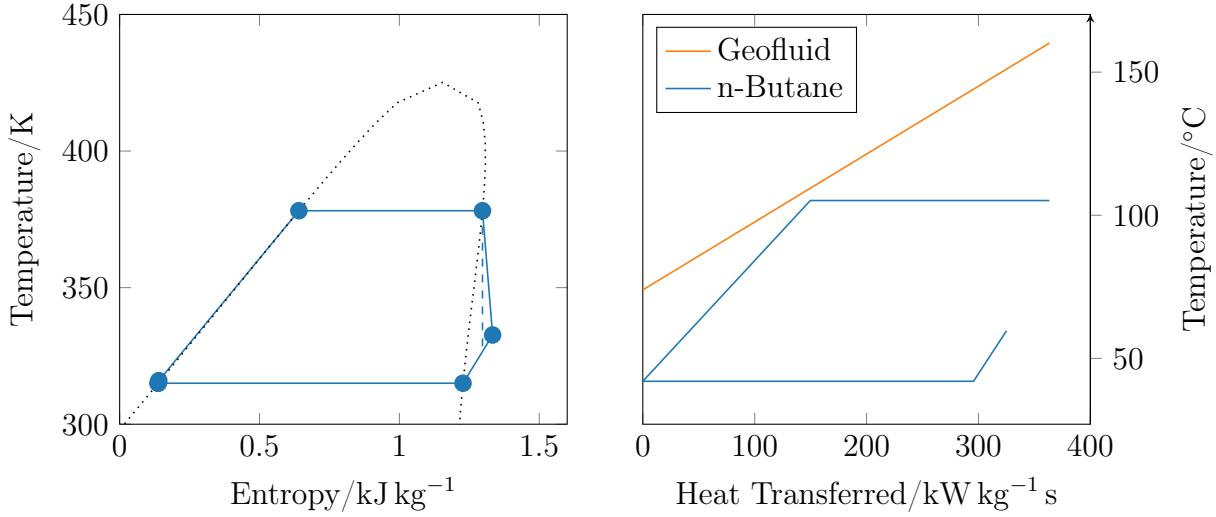


Figure 3.15: Temperature-Entropy and Temperature-Heat transfer diagrams of a binary ORC geothermal power plant using n-Butane as the working fluid for a saturated water-dominated geofluid at a temperature of 433 K (160 °C) at the inlet. The cycle parameters to yield maximum specific net power

Another advantage over Rankine cycles, is that due to the higher cycle pressures the volumetric flow rates are much lower allowing the plant components to be more compact and hence cheaper.

3.2.3. Working Fluids

The cycle working fluid is selected from a vast pool of potential fluids, see Table 3.1 and Figure 3.17, based on a number of metrics, such as its thermophysical properties, cost and availability, safety aspects like chemical stability, flammability and toxicity, as well as environmental considerations such as its Ozone Depletion Potential (ODP) and GWP.

In terms of the thermophysical properties, as will be shown in Section 3.2.6, whether a well aligned critical temperature or a high latent-heat is preferable for achieving high overall plant efficiencies, is primarily dependent on the nature of the heat source. For single-phase heat sources, working fluids with well-aligned (i.e. low critical temperatures) are preferred, whereas for two-phase sources working fluids with high latent heat are favourable. High thermal conductivity of the candidate fluid improves the overall heat

transfer coefficients in all heat transfer equipment, and low specific heat of the fluid in its vapour state can help reduce the duty, and thus cost, of the condenser unit, [43].

Another important aspect relates to the phase behaviour of the candidate fluid, and in particular the shape of the phase envelope in the temperature-entropy domain, which determines, whether expansion of the fluid vapour can be conducted with or without formation of liquid droplets. The formation of liquid droplets can be detrimental to both the turbine efficiency but also damage the turbine internals, see Section 3.5 for further details. Candidate fluids fall into one of three categories, *wet* corresponding to a negatively sloped dew line, *dry*, corresponding to a positively sloped dew line, and *isentropic*, corresponding to a vertical dew line, see Figure 3.16, with dry or isentropic fluids being preferred working fluids [30]. However, experiments have shown that expansion across the phase envelope does not necessarily result in liquid drop-out, if the outlet vapour is in a super-heated state, due to the fluid remaining in a meta-stable vapour state [22, 67].

The possible working fluids can be categorised as hydrocarbons, refrigerants, siloxanes, other organics and inorganic substances, Figure 3.17. As a result of the Montreal Protocol [85] many of the chlorofluorocarbon (CFC), hydrochlorofluorocarbon (HCFC) and hydrofluorocarbon (HFC) based refrigerants have been banned due to their high ODP or face bans in coming years, under the Kigali amendment, due to their high GWP.

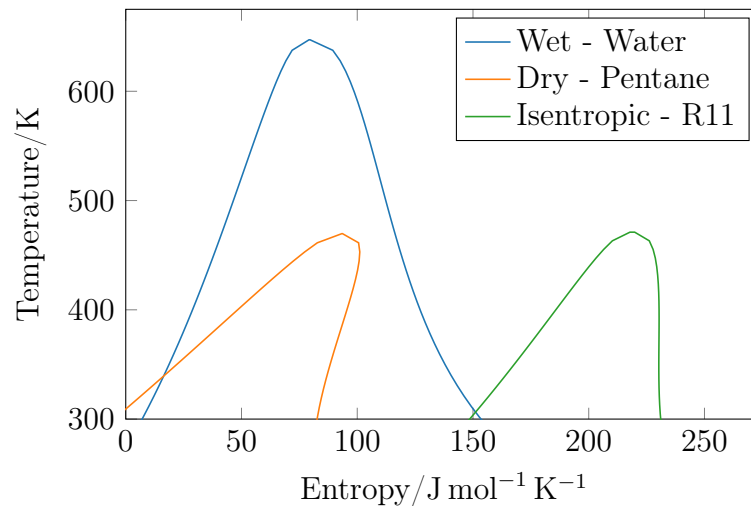


Figure 3.16: Temperature-Entropy phase envelopes of dry, wet, isentropic fluids. [14]

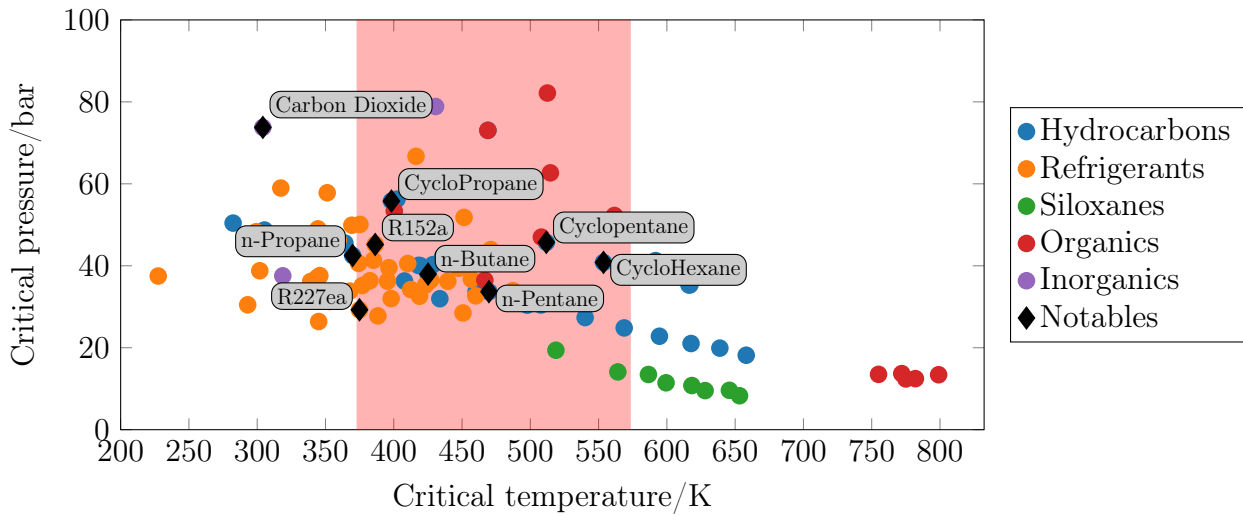


Figure 3.17: Critical temperatures and pressures of various ORC working fluids, [10, 20]

Table 3.1: Environmental and Health properties of candidate working fluids [30]

Fluid	$T_{\text{crit}} / \text{K}$	Toxicity	Flammability	ODP	GWP	Banned?
R-12	385.12	None	None	1.0	4500	Yes
R-114	418.83	None	None	0.7	5850	Yes
Propane	369.89	Low	Very High	0	3	No
i-Butane	407.81	Low	Very High	0	3	No
n-Butane	425.125	Low	Very High	0	3	No
i-Pentane	460.35	Low	Very High	0	3	No
n-Pentane	469.70	Low	Very High	0	3	No
R-32	351.26	Very Low	Low	0	675	No
R-134a	374.21	Very Low	None	0	1300	No
R-245fa	427.01	Low	None	0	1020	No

3.2.4. Configurations

The following section aims to provide background on the different strategies used to increase the efficiency of ORCs

Recuperative Cycle

Where the turbine exhaust has a sufficiently high temperature, it can be used to pre-heat the pressurised working fluid before entering the pre-heater, Figure 3.18. This has two main advantages: 1) reducing the duty and thus size and cost of the condenser; and 2) reducing the duty of the PHE, which can be of operational importance when handling geofluids prone to scaling at lower temperatures, also see Section 3.4.

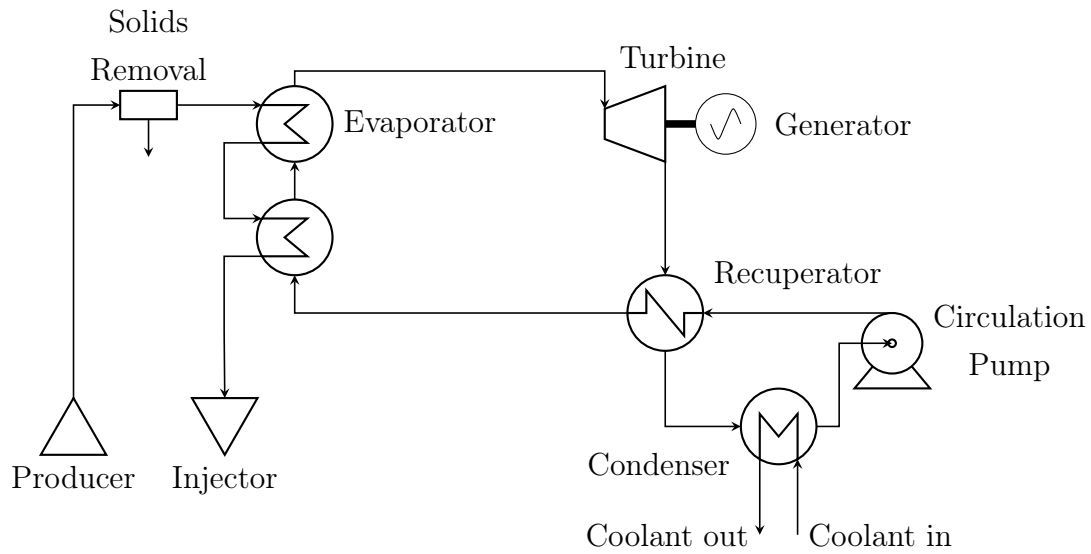


Figure 3.18: Schematic of a binary ORC geothermal power plant with recuperation. Adapted from [30]

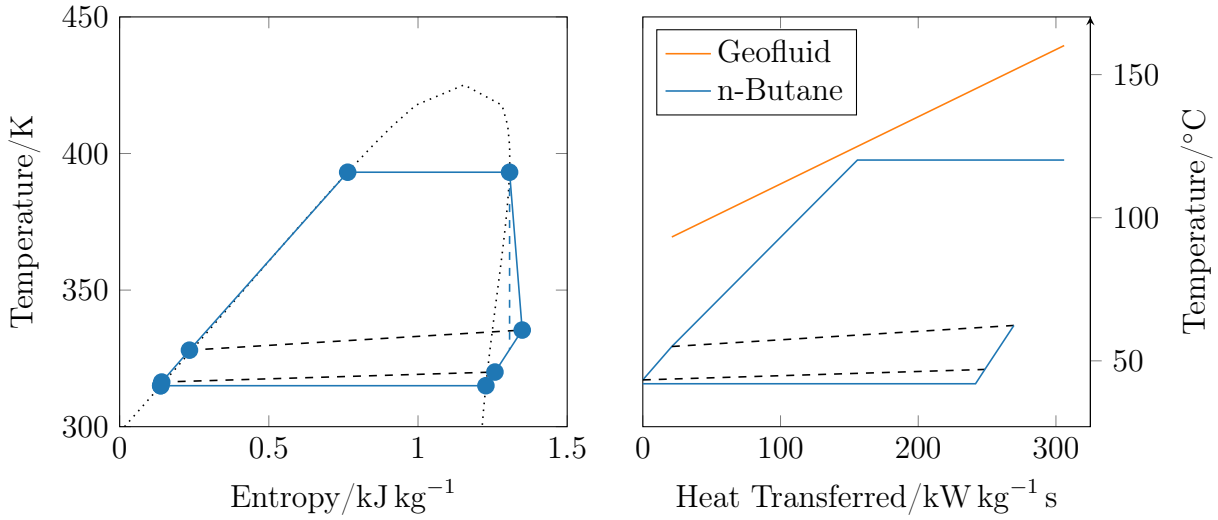


Figure 3.19: Temperature-Entropy and Temperature-Heat transfer diagrams of a recuperative binary ORC geothermal power plant using n-Butane as the working fluids for a saturated water-dominated geofluid at a temperature of 433 K (160°C) at the inlet. The cycle parameters were not optimised.

Double Pressure

In double pressure cycles evaporation occurs at two distinct pressure levels, an intermediate pressure and a high pressure. In this configuration, the low-pressure working fluid is pressurised to the intermediate pressure and then pre-heated to its boiling point, Figure 3.20. The working fluid is then split into two streams, one is vaporised and sent to the turbine while the other is pressurised to a higher pressure, thus raising its boiling point, before being vaporised and then sent to the turbine. The streams can then either be expanded in two separate turbines or using a dual-inlet turbine.

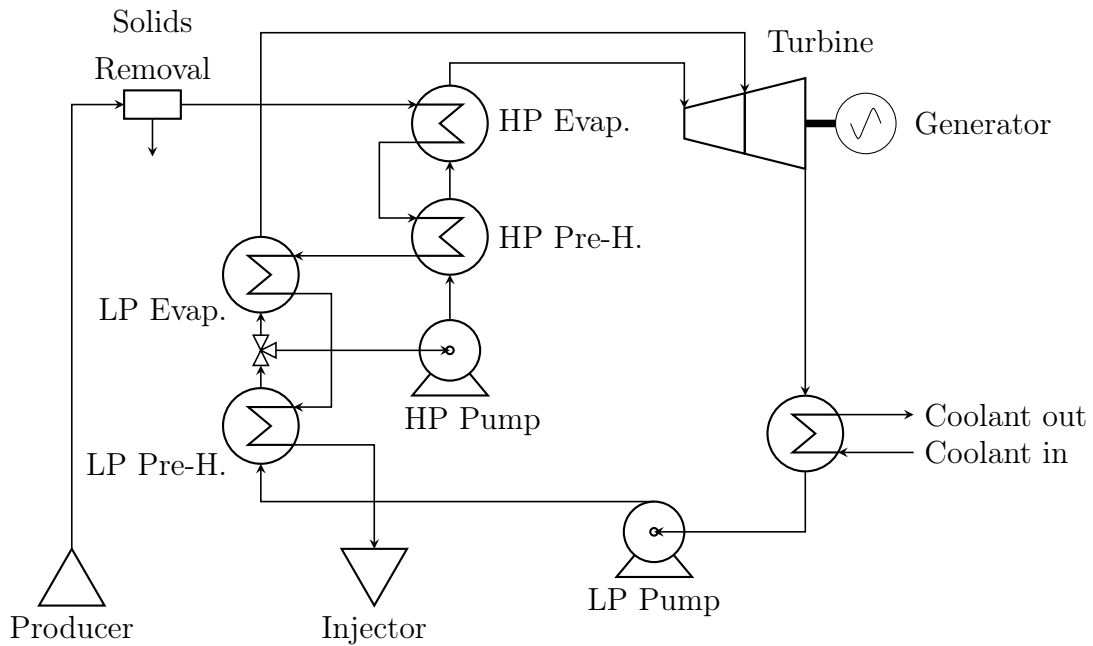


Figure 3.20: Schematic of a double pressure binary ORC geothermal power plant. Adapted from [30]

The use of double- or multi-pressure cycles has the advantage of obtaining a closer match between the heat profiles of the geofluid and the cycle working fluid in the PHE, see Figure 3.21, reducing exergetic losses and raising the cycle efficiency.

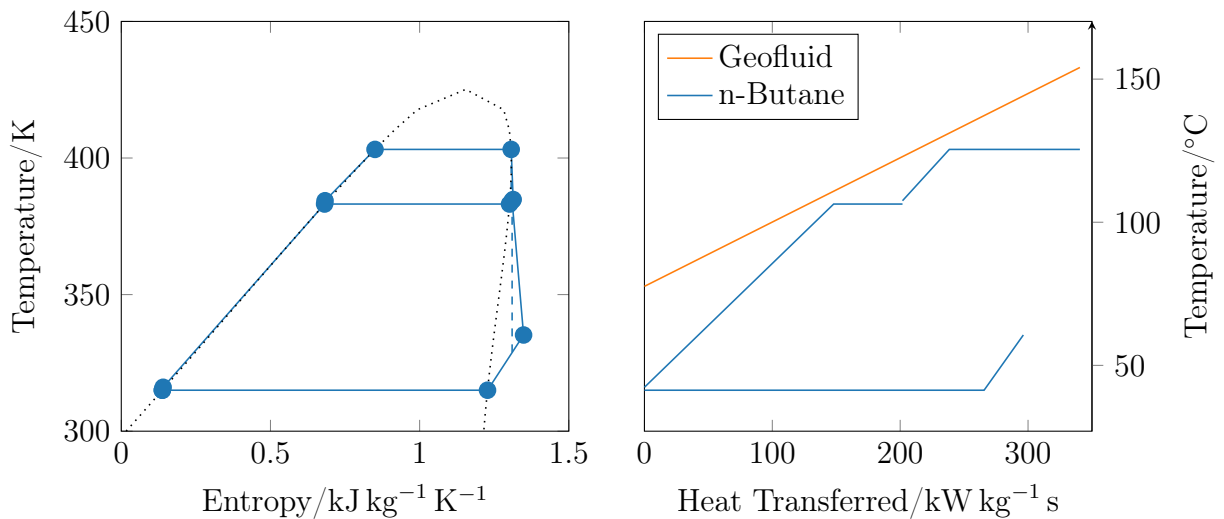


Figure 3.21: Temperature-Entropy and Temperature-Heat transfer diagrams of a double pressure binary ORC geothermal power plant using n-Butane as the working fluids for a saturated water-dominated geofluid at a temperature of 433 K (160 °C) at the inlet. The cycle parameters were not optimised.

Dual Fluid

To obtain a closer match between the heat profiles of the cycle working fluid and the geofluid, and improve the cycle efficiency, two different cycle working fluids can be used. This effectively results in a high temperature ORC and a low temperature ORC, Figure 3.22.

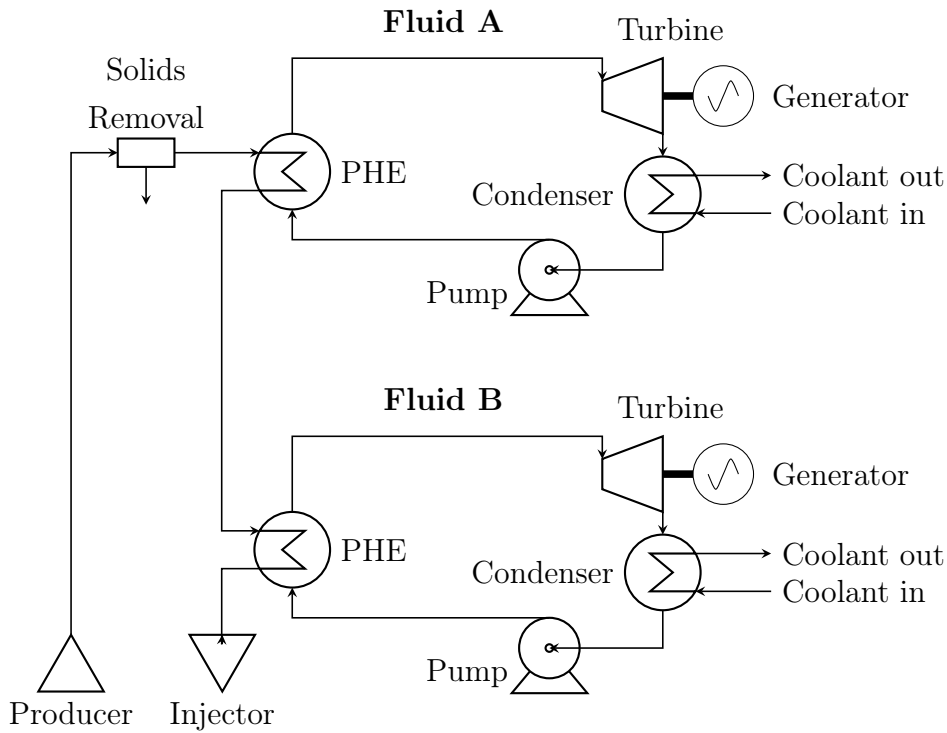


Figure 3.22: Schematic of a dual fluid binary ORC geothermal power plant. Adapted from [30]

Comparing the Temperature-Heat diagrams of a single fluid cycle (using n-Butane), Figure 3.15, and a dual fluid cycle (using n-Butane and n-Pentane), Figure 3.23, a closer temperature approach can be seen to be obtained.

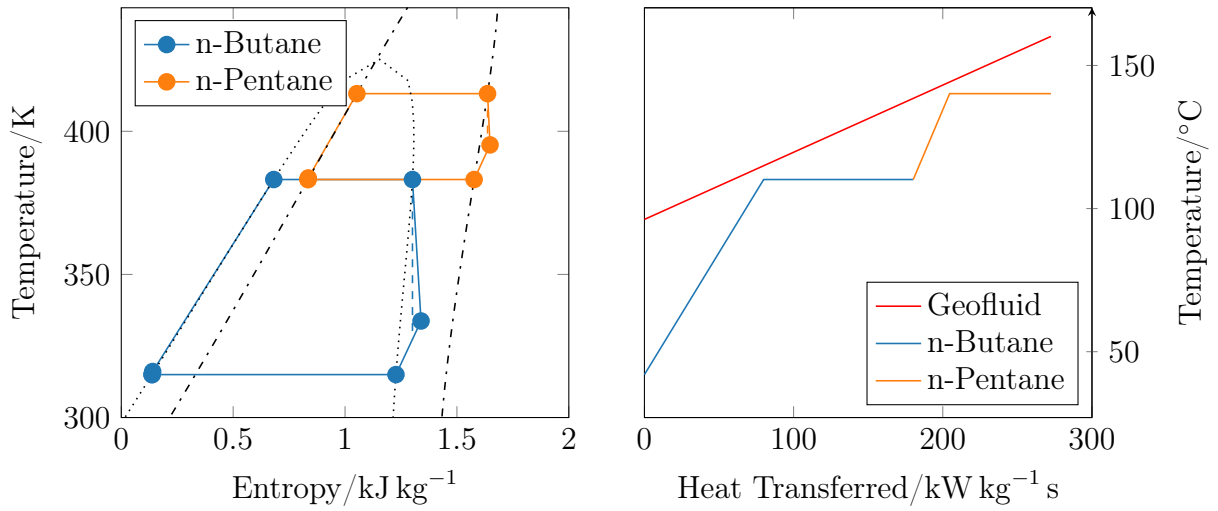


Figure 3.23: Temperature-Entropy and Temperature-Heat transfer diagrams of a dual fluid binary ORC geothermal power plant using n-Butane and n-Pentane as the working fluids for a saturated water-dominated geofluid at a temperature of 433 K (160 $^{\circ}\text{C}$) at the inlet. The cycle parameters were not optimised.

While a dual fluid configuration can improve the plant performance, it comes at a higher capital cost, due to requiring two separate cycles and also increases the complexity of the system. Perhaps for this reason, dual fluid cycles have seen only limited commercial use.

A prominent example of a dual fluid ORC is the Magmamax plant at East Mesa in the United States [30]. Here, a variation of the plant layout shown in Figure 3.22 is used, where the two fluid cycles interlock (or cascade), meaning that *left-over* heat from the hot cycle is transferred to the cold cycle, Figure 3.24.

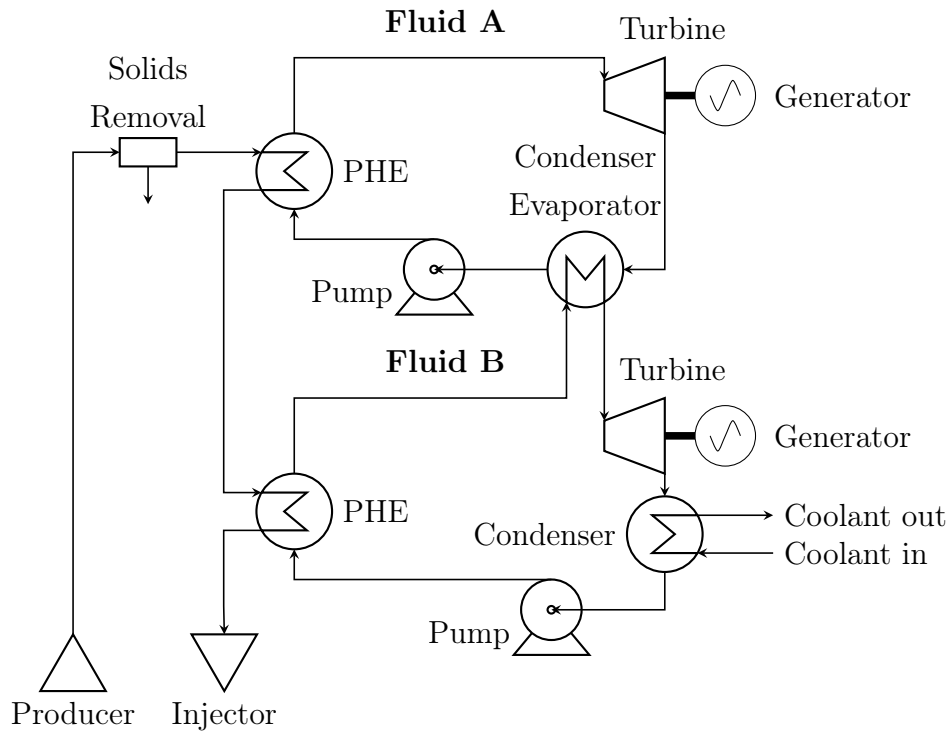


Figure 3.24: Schematic of an interlocking dual fluid binary ORC geothermal power plant. Adapted from [30]

Super-critical Cycle

In super-critical cycles, the working fluid is pressurised to super-critical pressures, before being heated to the desired temperature. Naturally, only working fluids can be used whose critical temperatures are below the source temperatures. ENEL in collaboration with Turboden and Politecnico di Milano built and tested a pilot plant near Livorno, Italy [9].

Due to its super-critical state, there is no discontinuous phase transition, allowing a closer match between the geofluid and working fluid heat profiles to be obtained, Figure 3.25. Moreover, supercritical cycles approximate the Lorenz or Triangular cycle, which as discussed in Section 3.2.6 is the ideal cycle for sensible heat dominated heat sources. However, the higher cycle pressures compared to sub-critical cycles result in higher pumping requirements, to re-pressurise the working fluid, as well as thicker pipework and sturdier joints to contain the fluid.

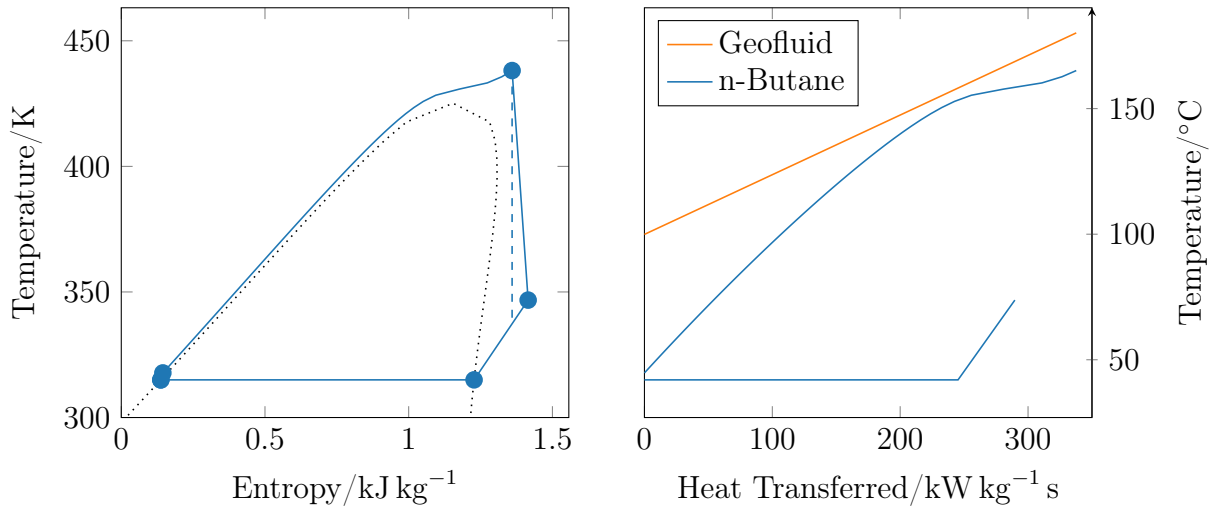


Figure 3.25: Temperature-Entropy and Temperature-Heat transfer diagrams of a supercritical binary ORC geothermal power plant using n-Butane as the working fluid for a saturated water-dominated geofluid at a temperature of 453 K (180 °C) at the inlet. The cycle parameters were not optimised.

Mixtures

While the phase transition of pure fluids from liquid to vapour at constant pressure occurs at a constant temperature, mixtures experience a temperature glide. This temperature glide could be exploited in ORCs to obtain a closer match in the geofluid and working fluid profile, Figure 3.26. In principle, this would allow the design engineers to tune the working fluid, specifically to the heat source (i.e. the geofluid).

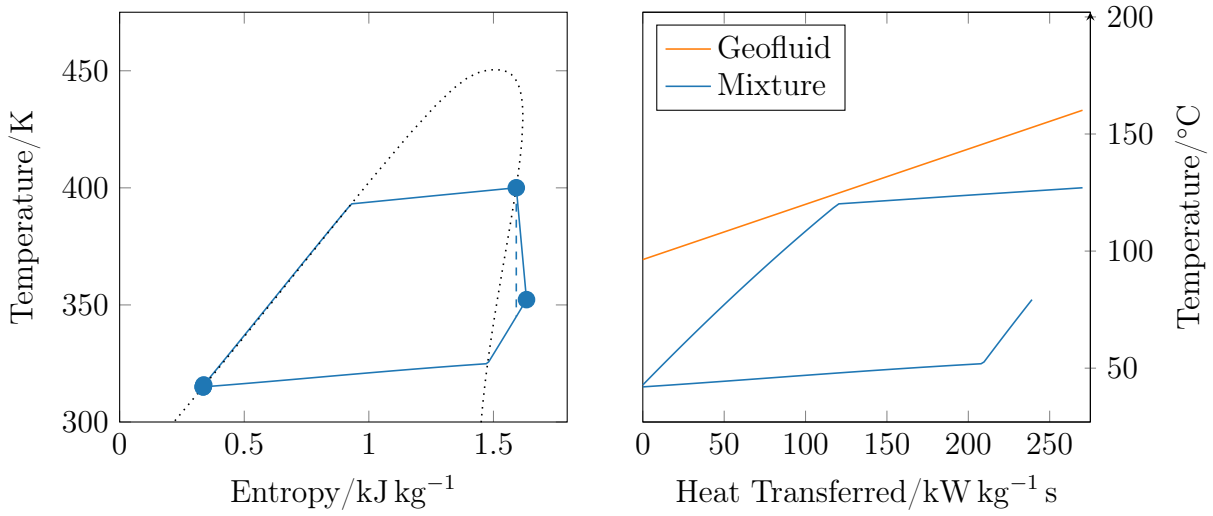


Figure 3.26: Temperature-Entropy and Temperature-Heat transfer diagrams of a binary ORC geothermal power plant using a 50:50 mixture of n-Butane and n-Pentane as the working fluid for a saturated water-dominated geofluid at a temperature of 433 K (160 °C) at the inlet. The cycle parameters and working fluid composition were not optimised.

However, mixtures also have a number of disadvantages, for instance, the temperature glide also occurs at when condensing the working fluid, and is generally more pronounced. As such, a compromise between a higher condensation pressure (and thus reduced turbine power) and closer approach temperatures in the condenser (and thus higher larger heat transfer area and cost) has to be found.

From an operational perspective, it is difficult to control the composition of the working fluid mixture - this can be attributed to lamination of the fluid in the evaporator/condenser, with heavier components collecting near the bottom and the lighter components collecting near the top of the pipes.

3.2.5. Optimisation

The optimisation of binary ORC geothermal power plants, primarily concerns choosing the optimum cycle parameters, such as the turbine inlet pressure and temperature as well as the condenser outlet pressure and temperature. As will be shown below, optimisation of the wellhead pressure (and in turn geofluid mass rate) for liquid dominated sources is trivial, but may require further consideration for two-phase sources.

Cycle Performance Optimisation

From a thermodynamic perspective, the choice of condensation conditions is trivial, i.e. the lowest possible condensation temperature/pressure, however, from an economic perspective, this also needs to be balanced against the cost of the condensing unit.

The turbine conditions present a trade-off, the higher the inlet temperature and pressure, the higher the turbine power, however the lower the working fluid mass rate, resulting in reduced geofluid utilisation.

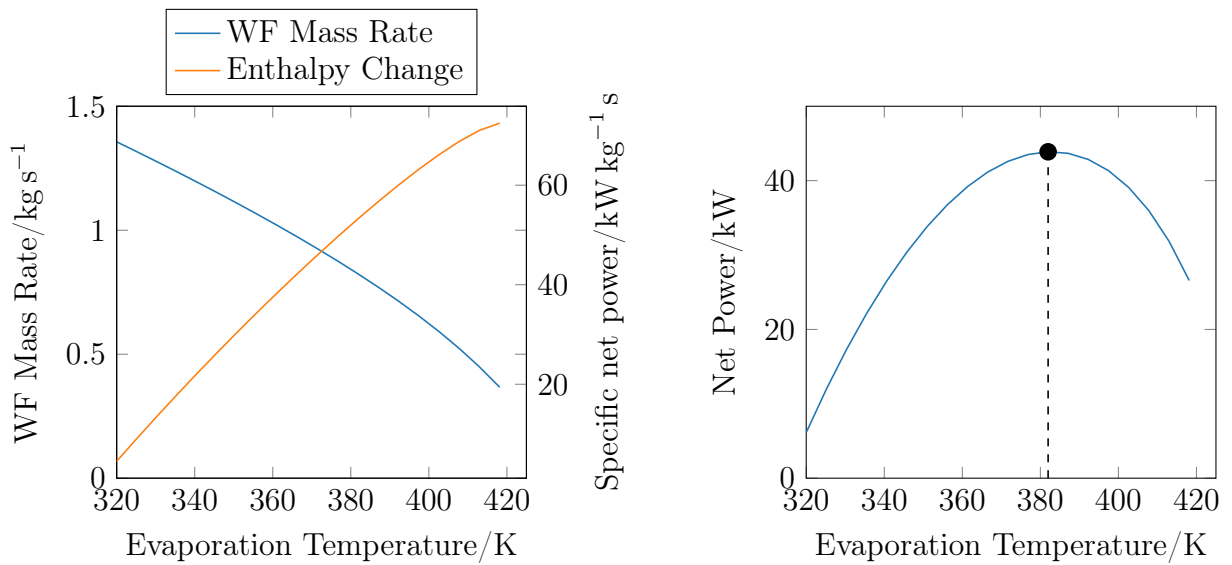


Figure 3.27: Left: The working fluid mass rate and the specific net power as a function of the evaporation temperature, assuming a saturated cycle. Right: The net power of the binary ORC using n-Butane as the working fluid for a unit mass rate (1 kg s^{-1}) of a saturated water-dominated geofluid at a temperature of 433 K (160°C) at the inlet.

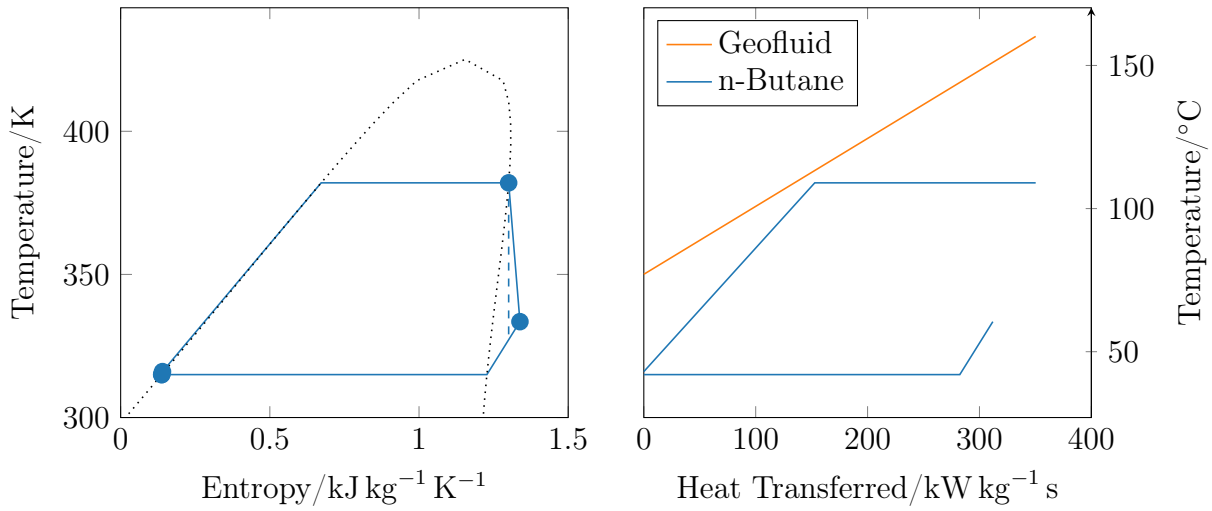


Figure 3.28: Temperature-Entropy and Temperature-Heat transfer diagrams of a binary ORC geothermal power plant using n-Butane as the working fluid for a saturated water-dominated geofluid at a temperature of 433 K (160 °C) at the inlet, assuming a saturated cycle. The evaporation temperature/pressure were optimised for maximum net cycle power.

Mass Rate Optimisation

For liquid-dominated sources, the optimisation of the mass flow rate of geofluid is somewhat trivial since the fluid temperature is only weakly dependent on the fluid pressure, Figure 3.29. As such, the plant net power is maximised by the maximum geofluid mass rate (i.e. WHP is as low as possible).

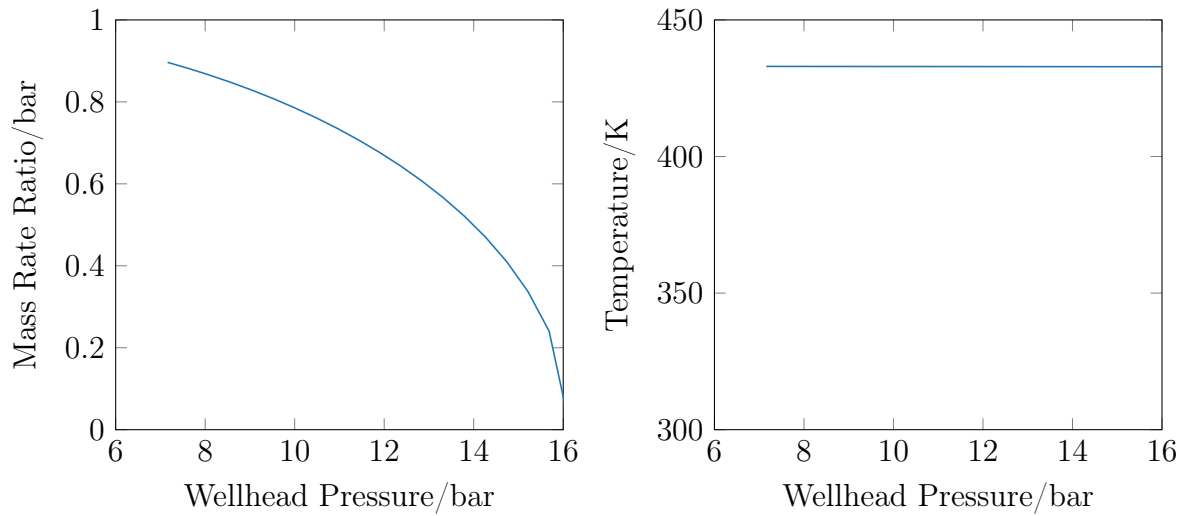


Figure 3.29: Left: The well performance curve, expressed as the mass rate ratio of geofluid (relative to the maximum mass rate) as a function of WHP. Right: The temperature of geofluid at the wellhead, about 433 K (160 °C), assuming constant enthalpy of around 570 kJ kg^{-1} along the wellbore, as a function of WHP.

However for artificially-lifted liquid-dominated sources, there maybe a trade-off between the net power of the cycle and the pumping requirements, if the frictional losses are significant. Ignoring frictional losses, the cycle and pumping power requirement are both directly proportional to the geofluid mass rate; as such the net plant power is maximised by the maximum geofluid mass rate (i.e. WHP is as low as possible).

For two-phase sources, the mass flow rate of geofluid must be optimised similar to DSCs, because the temperature is more strongly pressure dependent, Figure 3.30.

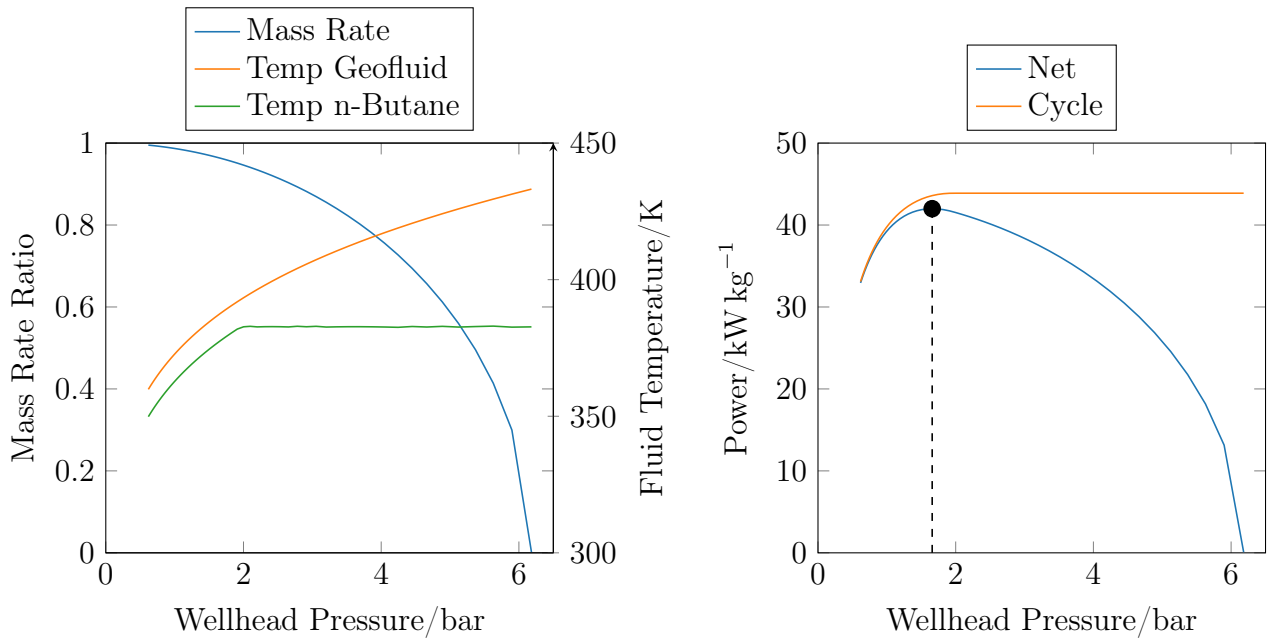


Figure 3.30: Left: The well performance curve, expressed as the mass rate ratio of geofluid (relative to the maximum mass rate) as a function of WHP. The temperature of geofluid at the wellhead, assuming constant enthalpy of around 570 kJ kg^{-1} along the wellbore, and the optimised working fluid (n-Butane) temperature, as a function of WHP. Right: The specific cycle power (relative to the geofluid mass rate) and the specific net power (relative to the maximum geofluid mass rate)

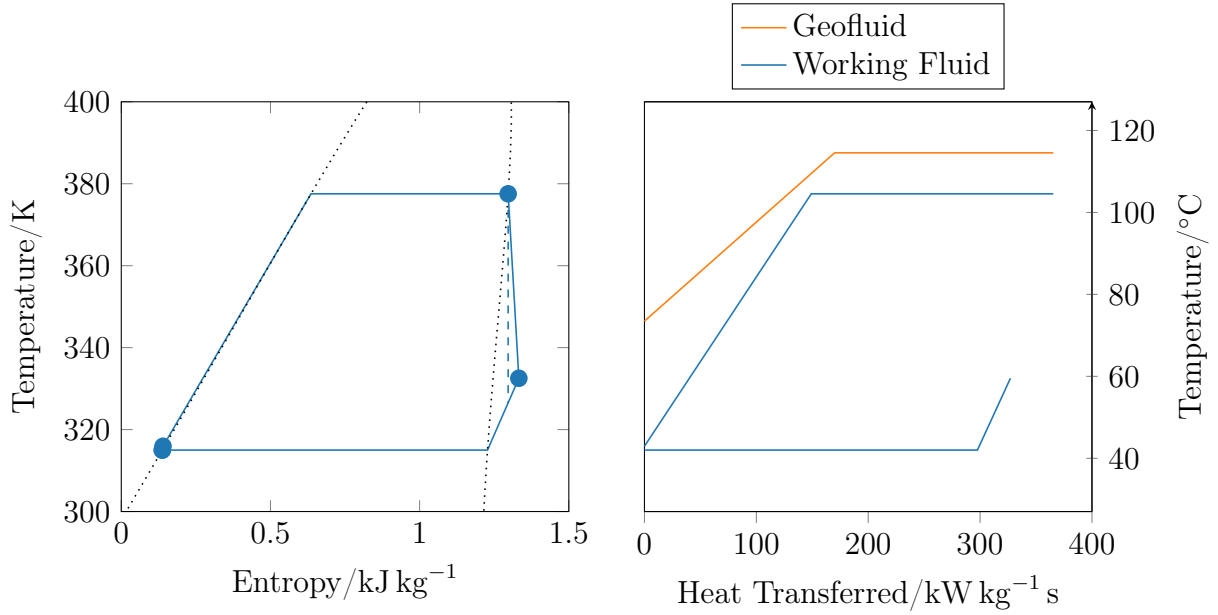


Figure 3.31: Temperature-Entropy and Temperature-Heat transfer diagrams of a binary ORC geothermal power plant using n-Butane as the working fluid for an optimised mass rate of a two-phase geofluid, assuming constant enthalpy of around 570 kJ kg^{-1} along the wellbore.

3.2.6. Intuitions for cycle and working fluid selection

While certain rules of thumb have been developed for choosing working fluids for single-phase heat sources, such as the critical temperature of the working fluid being well aligned with the source temperature [11], this section aims to explore whether these intuitions can also be applied to two-phase sources and what differences there may be.

A two-phase pure geofluid characterised by a vapour quality x , a temperature T_H , a latent heat Δh_{fg} and a constant specific heat capacity c_p of the condensed liquid is considered. The heat released by cooling the geofluid to a temperature T is thus given by Equation 3.3. Where \dot{Q} is the heat transferred, c_p is the specific heat capacity, T_H is the inlet temperature of the geofluid, T is the temperature to which the geofluid is cooled, x is the inlet vapour quality of the geofluid and Δh_{fg} is the latent heat of vaporisation of the geofluid.

$$\dot{Q} = c_p(T_H - T) + x\Delta h_{fg} \quad (3.3)$$

Two thermodynamic cycles are to be considered for exploiting the resource, Figure 3.32, a Rectangular cycle and a Triangular cycle, which can be seen as extreme instances of

ordinary Rankine cycles. For instance, the Rectangular cycle resembles a Rankine cycle using a working fluid with extremely large latent heat, whereas the Triangular cycle represents a Rankine cycle using a working fluid requiring no latent heat (e.g. a supercritical cycle).

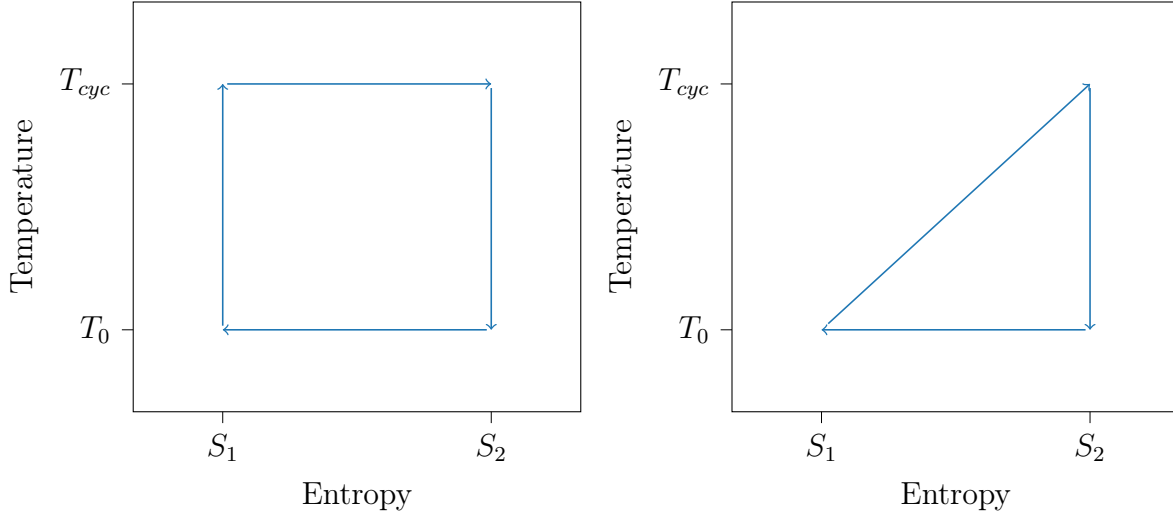


Figure 3.32: Temperature-Entropy diagram of the Rectangular cycle, left, and the Triangular cycle, right

The cycles are compared on the basis of the overall plant efficiency, Equation 3.4, which takes into account both the efficiency of the cycles themselves, as well as how well either cycle allows the available heat to be utilised. Moreover, the overall plant efficiency can also be used to choose the optimum cycle temperature T_{cyc} for each cycle considered. Where η_{plant} is the overall plant efficiency, η_{cycle} is the efficiency of the cycle, η_{recov} is the thermal recovery efficiency, \dot{W}_{net} is the net power generated by the heat engine, \dot{Q}_{in} and \dot{Q}_{out} are the heat transferred into and rejected from the heat engine.

$$\eta_{plant} = \frac{\dot{W}_{net}}{\dot{Q}_{max}} = \eta_{recov} * \eta_{cycle} \quad (3.4)$$

$$\eta_{recov} = \frac{\dot{Q}_{in}}{\dot{Q}_{max}} \quad (3.5)$$

$$\eta_{cycle} = \frac{\dot{W}_{net}}{\dot{Q}_{in}} \quad (3.6)$$

Rectangular Cycle

Figure 3.33 shows the temperature duty diagram for the heat source and the rectangular cycle. For a given cycle temperature T_{cyc} (in the range of T_H to T_0) there will always be a pinch point, preventing all of the heat to be extracted (i.e. \dot{Q}_{max}) - as a simplification, the minimum approach temperature is assumed to be zero. With this, two distinct regions emerge, Region 1 where the latent heat of condensation of the geofluid evaporates the working fluid, and Region 2 where the sensible heat of the geofluid evaporates the working fluid.

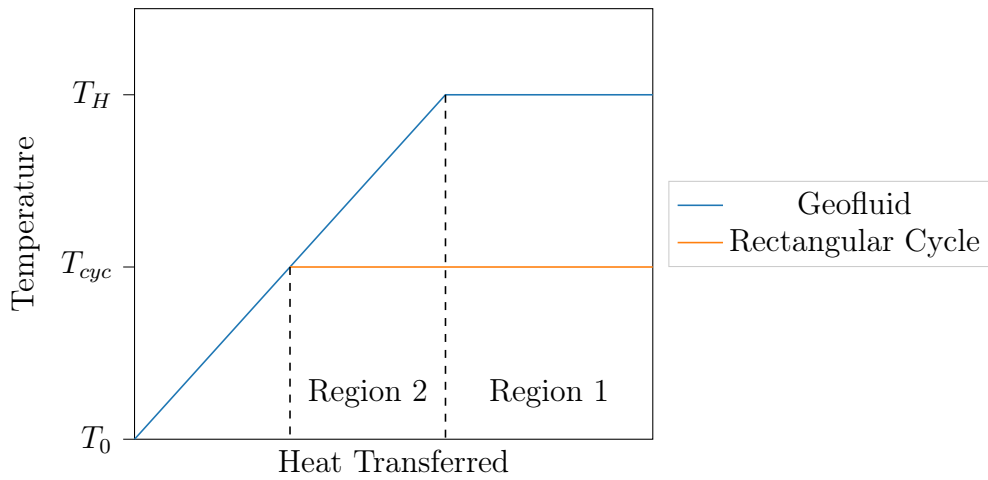


Figure 3.33: Temperature-Duty diagram of the geofluid and the rectangular cycle.

To obtain an expression for the cycle efficiency that accounts for all irreversibilities associated with the heat transfer, the enthalpy and entropy balances of the overall system, as well as each of the regions identified must be considered. Where \dot{m}_H is the mass rate of geofluid, h_{in}^H and h_{out}^H are the specific enthalpy of the geofluid at the inlet and outlet of the plant, s_{in}^H and s_{out}^H are the specific entropy of the geofluid at the inlet and outlet of the geofluid, \dot{S}_{gen}^{tot} is the entropy generated, and T_0 is the ambient temperature

Overall:

$$\dot{m}_H(h_{in}^H - h_{out}^H) - \dot{W}_{net} - \dot{Q}_{out} = 0 \quad (3.7)$$

$$\dot{m}_H(s_{in}^H - s_{out}^H) + \dot{S}_{gen}^{tot} - \frac{\dot{Q}_{out}}{T_0} = 0 \quad (3.8)$$

$$\frac{\dot{Q}_{out}}{\dot{Q}_{in}} = \frac{T_0(s_{in}^H - s_{out}^H) + \frac{T_0 \dot{S}_{gen}^{tot}}{\dot{m}_H}}{(h_{in}^H - h_{out}^H)} \quad (3.9)$$

For Region 1:

$$\dot{m}_H(h_{in}^H - h_{sat}^H) = \dot{m}_F(h_{out}^F - h_*^F) \quad (3.10)$$

$$\dot{m}_H(s_{in}^H - s_{sat}^H) - \dot{m}_F(s_{out}^F - s_*^F) + \dot{S}_{gen}^{Region1} = 0 \quad (3.11)$$

Where h_{sat}^H is the specific enthalpy of the geofluid at saturation, s_{sat}^H is the specific entropy of the geofluid at saturation, \dot{m}_F is the mass rate of working fluid, h_{out}^F and h_*^F are the specific enthalpy of the working fluid at the outlet of the heat exchanger and at the point where the geofluid reaches saturation, s_{out}^F and s_*^F are the specific entropy of the working fluid at the outlet of the heat exchanger and the point corresponding to saturation of the geofluid, and $\dot{S}_{gen}^{Region1}$ is the entropy generated in Region 1.

Combining Equations 3.11 and 3.10, recognising that evaporation/condensation of pure fluids occurs at constant temperature (at a given pressure), $\Delta s_{fg} = \frac{\Delta h_{fg}}{T}$, we obtain an expression for the entropy generation associated with the heat transfer in Region 1, Equation 3.12.

$$\dot{S}_{gen}^{Region1} = \dot{m}_H(h_{in}^H - h_{sat}^H) \left(\frac{1}{T_{cyc}} - \frac{1}{T_H} \right) \quad (3.12)$$

A similar expression can be obtained for Region 2, Equation 3.15.

$$\dot{m}_H(h_{sat}^H - h_{out}^H) = \dot{m}_F(h_*^F - h_{in}^F) \quad (3.13)$$

$$\dot{m}_H(s_{sat}^H - s_{out}^H) - \dot{m}_F(s_*^F - s_{in}^F) + \dot{S}_{gen}^{Region2} = 0 \quad (3.14)$$

$$\dot{S}_{gen}^{Region2} = \dot{m}_H(h_{sat}^H - h_{out}^H) \frac{1}{T_{cyc}} - \dot{m}_H(s_{sat}^H - s_{out}^H) \quad (3.15)$$

Where h_{in}^F is the specific enthalpy of the working fluid at the inlet of the heat exchanger, s_{in}^F is the specific entropy of the working fluid at the inlet of the heat exchanger, and $\dot{S}_{gen}^{Region2}$ is the entropy generated in Region 2.

Combining Equations 3.12 and 3.15, yields an expression for the total entropy generation across the system, Equation 3.17, assuming that heat engine is mechanically ideal and does not introduce any irreversibilities.

$$\frac{T_0 \dot{S}_{gen}^{tot}}{\dot{m}_H} = \frac{T_0 \dot{S}_{gen}^{Region1} + T_0 \dot{S}_{gen}^{Region2}}{\dot{m}_H} \quad (3.16)$$

$$\frac{T_0 \dot{S}_{gen}^{tot}}{\dot{m}_H} = (h_{in}^H - h_{out}^H) \frac{T_0}{T_{cyc}} - (h_{in}^H - h_{sat}^H) \frac{T_0}{T_H} - T_0(s_{sat}^H - s_{out}^H) \quad (3.17)$$

Equation 3.17 can then be substituted into Equation 3.9, which then simplifies to Equation 3.19 since then condensation of a pure fluid occurs at constant temperature and so $(s_{in}^H - s_{sat}^H) = \frac{(h_{in}^H - h_{sat}^H)}{T_H}$. Finally, the cycle efficiency is given by Equation 3.20. Where T_{cyc} is the cycle temperature.

$$\frac{\dot{Q}_{out}}{\dot{Q}_{in}} = \frac{T_0}{T_{cyc}} + \frac{(T_0(s_{in}^H - s_{sat}^H) - \frac{T_0}{T_H}(h_{in}^H - h_{sat}^H))}{(h_{in}^H - h_{out}^H)} \quad (3.18)$$

$$\frac{\dot{Q}_{out}}{\dot{Q}_{in}} = \frac{T_0}{T_{cyc}} \quad (3.19)$$

$$\eta_{cycle} = 1 - \frac{\dot{Q}_{out}}{\dot{Q}_{in}} = 1 - \frac{T_0}{T_{cyc}} \quad (3.20)$$

The thermal recovery or thermal utilisation efficiency η_{recov} is then obtained via the ratio of the heat extracted from the heat source (by cooling it to a temperature T_{cyc}) to the maximum heat that could be extracted (by cooling the geofluid to a temperature of T_0), Equation 3.22. Here $\tau = T_H + \frac{x\Delta h_{fg}}{c_p}$, representing an *effective* temperature of the geofluid at the inlet.

$$\eta_{recov} = \frac{\dot{Q}_{in}}{\dot{Q}_{in}^{max}} = \frac{h_{in}^H - h_{out}^H}{h_{in}^H - h_0^H} = \frac{c_p(T_H - T_{cyc}) + x\Delta h_{fg}}{c_p(T_H - T_0) + x\Delta h_{fg}} \quad (3.21)$$

$$\eta_{recov} = \frac{\tau - T_{cyc}}{\tau - T_0} \quad (3.22)$$

The overall plant efficiency for the two-phase geofluid and the rectangular cycle, Equation 3.23, is then obtained by combining Equations 3.20 and 3.22. This expression is valid for any heat source that can be parameterised by Equation 3.3.

$$\eta_{plant} = \frac{\tau - T_{cyc}}{\tau - T_0} * \left(1 - \frac{T_0}{T_{cyc}}\right) \quad (3.23)$$

The optimum cycle temperature T_{cyc}^{opt} can then be determined by finding the cycle temperature T_{cyc} , for which $\frac{d\eta_{plant}}{dT_{cyc}} = 0$, Equations 3.24 and 3.25. Equation 3.25 is valid up to $\frac{x\Delta h_{fg}}{c_p} = T_H \left(\frac{T_H}{T_0} - 1\right)$, above which, the optimum cycle temperature is equal to the temperature of the heat source T_H .

$$\frac{d\eta_{plant}}{dT_{cyc}} = -\frac{1}{\tau - T_0} + \frac{1}{\tau T_0} \frac{1}{T_{cyc}^2} \quad (3.24)$$

$$T_{cyc}^{opt} = \sqrt{\tau T_0} = \sqrt{T_0 * \left(T_H + \frac{x\Delta h_{fg}}{c_p} \right)} \quad (3.25)$$

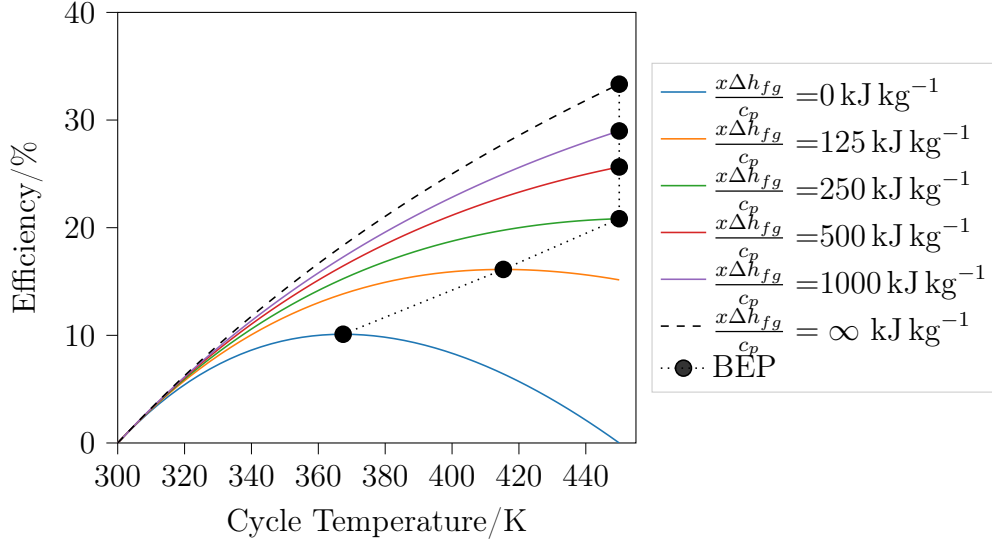


Figure 3.34: The overall plant efficiency as a function of the cycle temperature for a Rectangular cycle and a heat source characterised by a c_p of $4 \text{ kJ kg}^{-1} \text{ K}^{-1}$, a latent heat $x\Delta H_{fg}$ of 0 kJ kg^{-1} , an inlet temperature of 450 K and an ambient temperature of 300 K

Triangular Cycle

Assuming the specific heat capacity of the working fluid is constant over the range of temperatures of interest, Figure 3.35 shows the temperature duty diagram for the geofluid and the triangular cycle. Similarly to the rectangular cycle two distinct regions emerge, Region 1 where the latent heat of condensation of the geofluid provides sensible heat to the working fluid, and Region 2 where the sensible heat of the geofluid provides sensible heat to the working fluid.

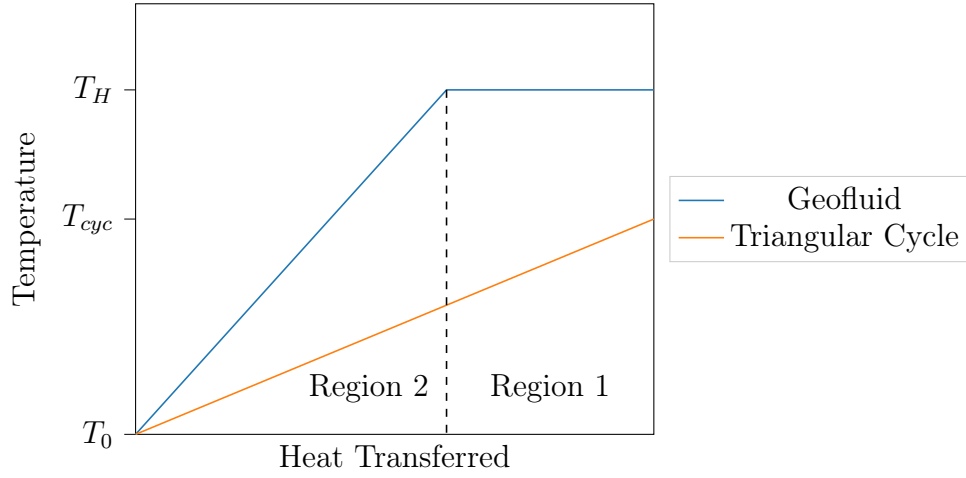


Figure 3.35: Temperature-Duty diagram of the geofluid and the triangular cycle.

To obtain an expression for the cycle efficiency that accounts for all irreversibilities associated with the heat transfer, the enthalpy and entropy balances of the overall system, as well as each of the regions identified must be considered. The nomenclature is used is consistent with that used in the previous chapter.

Overall:

$$\dot{m}_H(h_{in}^H - h_{out}^H) - \dot{W}_{net} - \dot{Q}_{out} = 0 \quad (3.26)$$

$$\dot{m}_H(s_{in}^H - s_{out}^H) + \dot{S}_{gen}^{tot} - \frac{\dot{Q}_{out}}{T_0} = 0 \quad (3.27)$$

$$\frac{\dot{Q}_{out}}{\dot{Q}_{in}} = \frac{T_0(s_{in}^H - s_{out}^H) + \frac{T_0 \dot{S}_{gen}^{tot}}{\dot{m}_H}}{(h_{in}^H - h_{out}^H)} \quad (3.28)$$

For Region 1:

$$\dot{m}_H(h_{in}^H - h_{sat}^H) = \dot{m}_F(h_{out}^F - h_*^F) \quad (3.29)$$

$$\dot{m}_H(s_{in}^H - s_{sat}^H) - \dot{m}_F(s_{out}^F - s_*^F) + \dot{S}_{gen}^{Region1} = 0 \quad (3.30)$$

Since condensation of pure fluids occurs at constant temperature (at a given pressure), $\Delta s_{fg} = \frac{\Delta h_{fg}}{T}$, this yields Equation 3.31 as an expression for the entropy generation associated with the heat transfer in Region 1.

$$\dot{S}_{gen}^{Region1} = \dot{m}_F(s_{out}^F - s_*^F) - \dot{m}_H \frac{(h_{in}^H - h_{sat}^H)}{T_H} \quad (3.31)$$

A similar expression can be obtained for Region 2, Equation 3.34.

$$\dot{m}_H(h_{sat}^H - h_{out}^H) = \dot{m}_F(h_*^F - h_{in}^F) \quad (3.32)$$

$$\dot{m}_H(s_{sat}^H - s_{out}^H) - \dot{m}_F(s_*^F - s_{in}^F) + \dot{S}_{gen}^{Region2} = 0 \quad (3.33)$$

$$\dot{S}_{gen}^{Region2} = \dot{m}_F(s_*^F - s_{in}^F) - \dot{m}_H(s_{sat}^H - s_{out}^H) \quad (3.34)$$

Combining Equations 3.31 and 3.34, yields an expression for the total entropy generation across the system, Equation 3.17, assuming that heat engine is mechanically ideal and does not introduce any irreversibilities.

$$\dot{S}_{gen}^{tot} = \dot{m}_F(s_{out}^F - s_*^F + s_*^F - s_{in}^F) - \dot{m}_H \frac{(h_{in}^H - h_{sat}^H)}{T_H} - \dot{m}_H(s_{sat}^H - s_{out}^H) \quad (3.35)$$

$$\frac{T_0 \dot{S}_{gen}^{tot}}{\dot{m}_H} = \frac{\dot{m}_F}{\dot{m}_H} T_0 (s_{out}^F - s_{in}^F) - (h_{in}^H - h_{sat}^H) \frac{T_0}{T_H} - T_0 (s_{sat}^H - s_{out}^H) \quad (3.36)$$

Substituting Equation 3.36 into Equation 3.28, yields an expression for the ration of the heat transferred out of and into the system. Since the condensation of the geofluid occurs at constant temperature ($s_{in}^H - s_{sat}^H = \frac{(h_{in}^H - h_{sat}^H)}{T_H}$), this then simplifies to Equation 3.38.

$$\frac{\dot{Q}_{out}}{\dot{Q}_{in}} = \frac{T_0(s_{in}^H - s_{out}^H - s_{sat}^H + s_{out}^H) - \frac{T_0}{T_H}(h_{in}^H - h_{sat}^H) + \frac{\dot{m}_F}{\dot{m}_H} T_0 (s_{out}^F - s_{in}^F)}{(h_{in}^H - h_{out}^H)} \quad (3.37)$$

$$\frac{\dot{Q}_{out}}{\dot{Q}_{in}} = \frac{\dot{m}_F}{\dot{m}_H} \frac{T_0 (s_{out}^F - s_{in}^F)}{(h_{in}^H - h_{out}^H)} \quad (3.38)$$

As the heat released by the geofluid is absorbed by the working fluid, the mass rate ratio $\frac{\dot{m}_F}{\dot{m}_H}$ is given by Equation 3.39. Moreover, assuming the working fluid has a constant specific heat capacity over the temperatures of interest, the difference in enthalpy and entropy are given by Equations 3.40 and 3.41 respectively. Combined they yield Equation 3.42, and in turn the cycle efficiency, Equation 3.43

$$\frac{\dot{m}_F}{\dot{m}_H} = \frac{(h_{in}^H - h_{out}^H)}{(h_{out}^F - h_{in}^F)} \quad (3.39)$$

$$h_{out}^F - h_{in}^F = c_p^F (T_{cyc} - T_0) \quad (3.40)$$

$$s_{out}^F - s_{in}^F = c_p^F \ln \frac{T_{cyc}}{T_0} \quad (3.41)$$

$$\frac{\dot{Q}_{out}}{\dot{Q}_{in}} = T_0 \frac{c_p^F \ln \frac{T_{cyc}}{T_0}}{c_p^F (T_{cyc} - T_0)} = \frac{T_0}{\frac{T_{cyc} - T_0}{\ln \frac{T_{cyc}}{T_0}}} = \frac{T_0}{T_{cyc}^{LM}} \quad (3.42)$$

$$\eta_{cycle} = 1 - \frac{\dot{Q}_{out}}{\dot{Q}_{in}} = 1 - \frac{T_0}{T_{cyc}^{LM}} \quad (3.43)$$

With regards to the thermal recovery (or utilisation) efficiency, unlike the rectangular cycle, the heat extracted from the heat source is not limited by the existence of a pinch point - assuming a minimum approach temperature difference of zero as a simplification. As such, the heat extracted from the geofluid is not a function of the cycle temperature, and the thermal recovery efficiency η_{recov} is 1, and the overall plant efficiency η_{plant} is only dependent on the cycle efficiency η_{cycle} of the triangular cycle.

In terms of the optimum cycle temperature, this is equal to the source temperature, as this minimises the magnitude of $\frac{\dot{Q}_{out}}{\dot{Q}_{in}}$.

$$T_{cyc}^{opt} = T_H \quad (3.44)$$

Direct Comparison

Comparing the overall plant efficiency of the Triangular and Rectangular cycle plants for different values of $\frac{x\Delta h_{fg}}{c_p}$, Triangular cycle can be seen to provide better overall plant efficiencies than the Carnot cycle plant for $\frac{x\Delta h_{fg}}{c_p}$ as high as 198 K, Figure 3.36. The critical ratio of latent heat to the specific heat capacity is given by Equation 3.45. For combinations of latent heat and specific heat capacity in excess of this critical point, the Rectangular cycle outperforms the Triangular cycle.

$$\frac{x\Delta H_{fg}}{C_p}_{crit} = \frac{T_H(T_{LM} - T_0)}{T_{LM} - T_H \left(\frac{T_{LM} - T_0}{T_H - T_0} \right)} \quad (3.45)$$

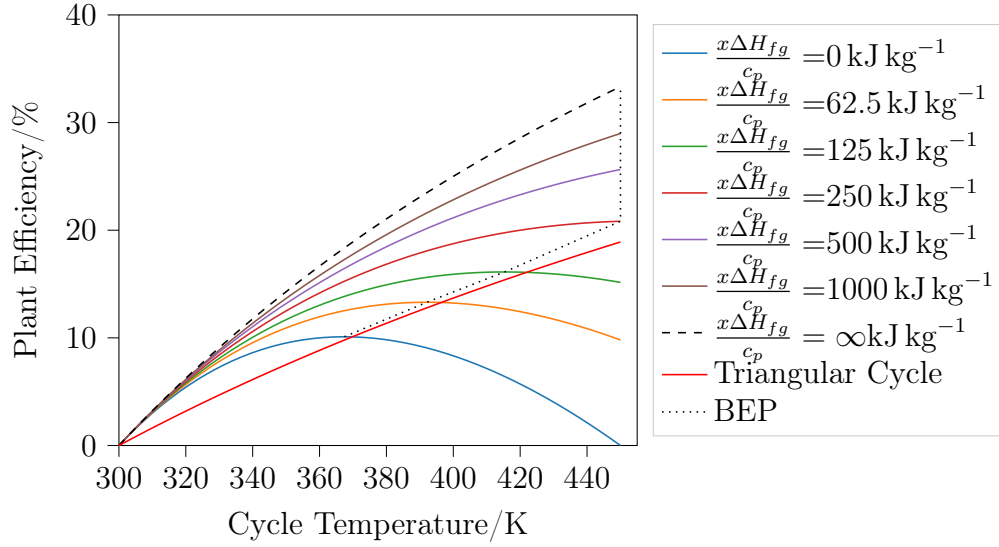


Figure 3.36: The overall plant efficiency as a function of the cycle temperature for a Rectangular cycle and a Triangular cycle for heat sources of different latent heat, a constant specific heat capacity C_p of $4 \text{ kJ kg}^{-1} \text{ K}^{-1}$, a geofluid inlet temperature of T_H of 450 K and an ambient temperature of 300 K.

In summary, the overall plant efficiency of a binary plant depends not only on the efficiency of the thermodynamic cycle but also on the efficiency of thermal recovery from the heat source. Even though triangular cycle, has a low cycle efficiency, it is best suited for single phase source or two-phase sources with low amounts of latent heat (relative to the specific heat capacity of the heat source), because of its high, and constant thermal recovery efficiency. The Rectangular cycle achieves higher cycle efficiencies, however, generally operates at lower thermal recovery efficiencies, which reduce the overall plant efficiency. In this respect, the Rectangular cycle is better suited for two-phase sources with large latent heat, due to the increased thermal recovery efficiency.

In the real world, this corresponds to working fluids with critical temperatures close to the temperature of the heat source being favourable for the exploitation of single-phase (or low quality) resources, because near the critical point the latent heat of vaporisation is diminishing, or is eliminated entirely, in the case of super-critical cycles. However, for two-phase heat sources, working fluids with large latent heat of vaporisation are favourable.

3.3. NCG Handling

The presence of NCG in geofluids can pose a number of issues for the operation of geothermal power plants. For instance, expelling the NCG liberated and expanded as part of

DSC geothermal power plants can be energy intensive and technically challenging. As most geothermal DSC power plants expand the geofluid to sub-atmospheric conditions, at a minimum the NCG must be re-pressurised to atmospheric conditions to allow the NCG to be vented to atmosphere.

Where the NCG contains harmful constituents such as mercury or hydrogen sulfide, further treatment of the NCG maybe required before it can be safely released into the environment. An example of this is the AMIS process designed by *ENEL* to remove mercury and hydrogen sulfide from the NCG effluent streams. During the AMIS process, mercury is removed using selenium or activated carbon adsorbents, and hydrogen sulfide is first catalytically oxidised to sulfur dioxide and then stripped using an alkaline solution (e.g. dilute ammonia or sodium hydroxide solution) [15, 63].

With regards to NCG with significant GWP, there are two schools of thought on whether venting to atmosphere is an option. On the one hand, venting NCG to atmosphere represents an obvious source of greenhouse gas emissions that should be prevented. In fact some geothermal power plants in Türkiye have carbon footprints as 900 kg MW^{-1} to 1400 kg MW^{-1} , which is comparable to coal-fired power stations.

On other hand, such emissions do also occur naturally in the absence of geothermal power plants, for example from surface features like fumaroles. In this respect, if the emissions of a geothermal power or heat plant reduce the natural emissions by the same amount, the overall emissions from the geothermal site are unchanged. That being said, tracking and quantifying emissions across a wide area is no trivial task, as illustrated from attempts tracking methane leakage from active as well as abandoned oil and gas wells [26]. While some countries, like Italy [109] and Türkiye [13], have taken the stance that geothermal power plants do not increase the overall emissions, this view is not shared universally and in, for instance, Iceland efforts are taken to actively reduce NCG emissions to reduce the carbon foot print [90].

At the Hellisheiði geothermal power plant in Iceland, *CarbFix* have trialled the dissolution, re-injection and sequestration of NCG using their *Carbfix* process[25]. At Hellisheiði, geothermal power is generated by means of a dual flash DSC from a geofluid with carbon dioxide and hydrogen sulfide impurities (the NCG comprises about 5 % of the steam mass flow rate [90]). Following the expansion and cooling the NCG is extracted using vacuum pumps. The NCG stream is then pressurised and fed to an absorption column (at a temperature of 293 K or 20 °C, and a pressure of 6 bar) [36] to dissolve in geofluid condensate. The left over NCG is vented the the atmosphere. The saturated gas-charged condensate is then injected at depth into the brine injection wellbore.

The basalt formations of the Hellisheiði field provide a natural mechanism for the long-term sequestration of carbon dioxide within the reservoir [25, 36]. That being said, it is important to ensure that mineralisation does not occur in close vicinity of the injection wells as this could result in clogging and reduce the injectivity in the long-term. Nevertheless, since 2014 the *CarbFix* project at Hellisheiði have injected over 100.000 t of carbon dioxide [25].

The main drawback from this approach is that the solubility of carbon dioxide in water at surface temperatures and pressures is low (at *CarbFix* the maximum mole fraction of carbon dioxide in the re-injected water phase is just 0.38 %). As the solubility of carbon dioxide increases with temperature and pressure, it is consequently not possible to dissolve and re-inject all of the produced carbon dioxide. In fact, this is already seen at *CarbFix*, where only around 35 % of the produced carbon dioxide is re-injected [90].

The main challenge to direct-injection of excess NCG is its low density compared to brines, which leads to extremely high WHPs being required to inject the NCG into the reservoir formation. For example, as a rough approximation, neglecting frictional losses and temperature changes, injecting 493 K (20 °C) into a static water column at a depth of just 500 m requires WHP in excess of 45 bar (assuming ideal gas behaviour of the carbon dioxide phase). This is investigated in further detail in Section 5.5.2.

$$P_{brine} = P_{wh, brine} + \rho_{brine} * g * h \quad (3.46)$$

$$P_{ncg} = P_{wh, ncg} * \exp \frac{M_r * g * h}{RT} \quad (3.47)$$

$$P_{wh, ncg} = (P_{wh, brine} + \rho_{brine} * g * h) * \exp - \frac{M_r * g * h}{RT} \quad (3.48)$$

$$P_{wh, ncg} = (1 * 10^5 + 1000 * 9.81 * 500) * \exp \left(- \frac{0.044 * 9.81 * 500}{8.314 * 293} \right) = 4.58 * 10^6 Pa \quad (3.49)$$

For reference, at these conditions the solubility has increased to 2.37 % on a mole fraction basis. In principle, this could be used to dissolve the remaining carbon dioxide at Hellisheiði. In fact Leontidis et al. [58] conducted steady-state and transient simulations on the re-injection of NCG into the reservoir considering various injection strategies, such as mixing of the NCG and brine at the surface (i.e. two-phase injection), co-axial injection through a central pipe and surrounding annular space, as well as co-axial injection with mixing at depth. While their results suggest that mixing at depth may be possible and an attractive strategy for reducing surface compression power, particularly for low NCG

content, the authors highlight the importance of the underlying thermophysical property models. However, given that the simulation tools used in this study (i.e. *PipeSim*, *OLGA*, etc.) were originally developed for the oil and gas industry and are therefore used out of context, further investigations into the role of the following items are required:

Flow Correlations The flow correlations used to determine the liquid-hold (e.g. Hagedorn & Brown [41]) have generally been developed for upward vertical flow. However, in this case the flow is vertically downwards, and as such the buoyancy forces are now opposed to the direction of motion, which could affect the phase distribution and thus the liquid hold-up. This is particularly important because of the tendency of gas bubbles tend to coalesce into large bubbles, reducing surface tension and increasing buoyancy effects.

Equilibration When mixing NCG and brine at depth, there may be significant barriers to mass transfer (e.g. due to limited interfacial area). As such, the common assumption of instantaneous equilibration (and hence dissolution of NCG) may no longer be valid, leading to an overestimation of the liquid hold-up within the wellbore. Further simulations assuming no dissolution of NCG in the brine even when in thermodynamic non-equilibrium could help assess the importance of these mass transfer effects.

Alternatively, owing to the low critical temperature, where the required wellhead pressure exceeds about 60 bar carbon dioxide could be liquefied at ambient temperatures. This has two advantages: 1) further compression requires significantly less power because liquid carbon dioxide is less compressible, 2) the higher density of liquid carbon dioxide adds significant static pressure in the wellbore, and 3) as the temperature and pressure increase, the liquid transitions to the supercritical state.

As an alternative to re-injecting the NCG into the reservoir, depending on the composition, it may be possible to upgrade the NCG to commercial products. For example, where carbon dioxide is the main constituent, NCG could be purified and converted to dry ice or used in beverages [13], provided there is a market and the capital investment is not prohibitive. There may also be niche applications, such as reusing carbon dioxide locally as an inhibitor to acidify the returns brine to prevent scale formation, as reported by Topcu et al. [101].

3.4. Scale Handling

The geofluids are created over geological timescales, during which surface water resides in the geothermal reservoir and chemically equilibrates with the surrounding formation, causing minerals to leach from the formation [30]. However, once the geofluid is produced from the reservoir and its temperature, pressure and composition are changed, this may cause the equilibrium to shift, causing minerals to precipitate. These mineral precipitates, commonly referred to as scales, can then deposit in the production system (i.e. wellbores, separators, heat exchange equipment) and impede the performance of the geothermal power plants. Calcite, Silica and sulphate scales are commonly encountered across the geothermal industry [61].

3.4.1. Calcite Scale

Calcite CaCO_3 is a common mineral in geofluids from carbonate reservoirs. Due to its negatively sloped solubility curve (with respect to temperature), temperature reduction induced scaling is not typically an issue in a geothermal setting, as the solubility increases as the temperature is reduced.

However, the solubility of calcite is also strongly dependent on the amount of carbon dioxide dissolved in the geofluid and the pH of the aqueous phase. Once the geofluid reaches its boiling point, or is flashed in the power plant, the resulting gas phase is enriched in carbon dioxide, which raises the pH and almost instantaneously causes calcite to precipitate. Such scaling is common carbonate fields, where the geofluids boils within the well-bores or surface, resulting in the thick calcite deposits that can incur significant pressure losses or even cause blockages[30]. Acidisation or mechanical cleaning maybe used to manage calcite scaling once deposits become significant.

3.4.2. Silica Scale

Silica SiO_2 is a common mineral found in geofluids, and exists in different crystalline structures, such as an amorphous state or as quartz in a highly crystalline state. While all forms of silica have a positively sloped solubility curve (with respect to temperature), the absolute solubility varies between the different forms, for example amorphous silica has a higher solubility in water than quartz[30]. This puts both binary ORC and DSC with flash geothermal power plants at risk from silica scaling. Reductions in temperature (e.g. in the PHE) or concentration of geofluid (e.g. steam removed by flashing) can result in the

geofluid becoming supersaturated in silica. Silica scaling prevention is simpler in binary plants, as the geofluid is not concentrated by flashing stages, meaning that by simply managing the re-injection temperature supersaturated conditions can be prevented.

In terms of mitigation, strategies are to either prevent supersaturation by raising the pH to above 7, or manage the kinetics of silica precipitation. For instance, reducing the speed of precipitation, may allow sufficient time for the geofluid to be re-injected into the reservoir, where any precipitate will eventually be dissolved. Kinetic inhibition could be achieved by pH control, by maintaining either low pH (<5.5) or high pH (>9.0) [30]. An alternative approach is to achieve a controlled precipitation by increasing the rate of precipitation, and to remove the excess silica, re-injecting under-saturated geofluid into the reservoir [30].

3.5. Turbines

Turbines are used to convert the thermal energy contained within the working fluid into mechanical energy. The following subsections aim to provide background on the working principle, internal configuration, and types of turbines.

3.5.1. Working Principle

Within the turbine, nozzles direct high velocity streams onto a solid element, called a blade, which deflects the fluid, Figure 3.37. The change in momentum (i.e. v_{in} to v_{out}) imparts a resultant force on the blade opposite in the direction of the change in momentum. The blades are attached to a central shaft, such that resultant force manifests as a torque, causing the shaft to rotate. This rotation can then be used to drive a generator [29, 91].

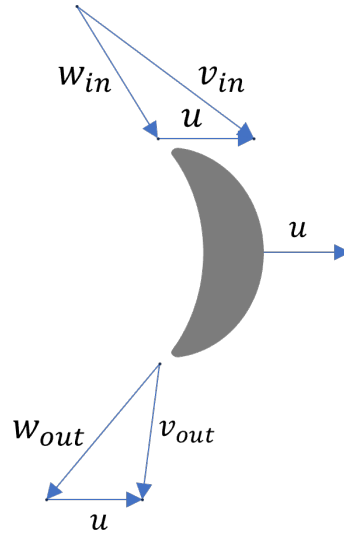


Figure 3.37: Fluid, blade and relative velocity vectors at the inlet and outlet of the blade.

The maximum work, \dot{w} generated by a turbine can be obtained from the Euler equation, Equation 3.50, or its alternate form, Equation 3.51, where v is the absolute fluid velocity, u is the tangential velocity of the blade, and w is the relative velocity from the perspective of the blade.

$$\dot{w} = \vec{u}_{in} \cdot \vec{c}_{in} - \vec{u}_{in} \cdot \vec{c}_{in} \quad (3.50)$$

$$\dot{w} = \frac{v_{in}^2 - v_{out}^2}{2} + \frac{u_{in}^2 - u_{out}^2}{2} - \frac{w_{in}^2 - w_{out}^2}{2} \quad (3.51)$$

Velocity triangles, Figure 3.38, summarise the inlet and outlet velocity vectors and are an important tool for and optimising the energy conversion.

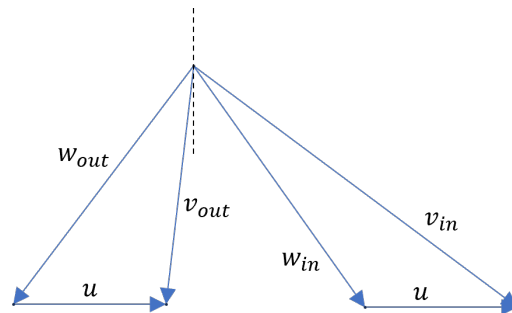


Figure 3.38: Velocity Triangles.

3.5.2. Impulse vs. Reaction Stages

To maximise the efficiency, the expansion is broken down into a number of stages, allowing the nozzles and blades to be specifically designed for the fluid and velocities at various stages of expansion. Each stage is comprised of a static stator, containing the nozzles, and the rotating rotor, containing the blades. There are two different types of turbine stages, impulse and reaction stages, the main difference being the mechanisms by which the fluid imparts the resultant force on the blades.

In an impulse stage, Figure 3.39a, the fluid is expanded in the stator nozzles, reducing the fluid pressure but increasing the volumetric flow rate and in turn the velocity of the fluid, Figure 3.39b. The fluid is then directed onto the blades, which deflect the fluid, and the change in momentum imparts the resultant force on the blade. In an ideal impulse stage, the fluid pressure in rotor section remains constant, such that only the kinetic energy is transferred to the blade/central shaft.

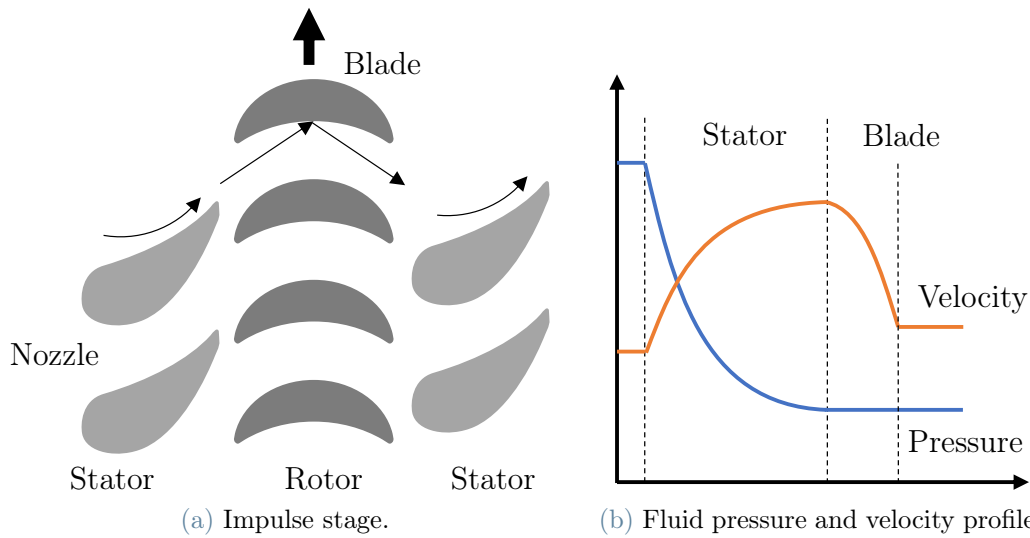


Figure 3.39: Configuration of an impulse turbine stage and the corresponding fluid pressure and velocity profiles. Adapted from [29, 91]

In a reaction stage, Figure 3.39a, the fluid is partially expanded in the stator nozzles and then directed onto the blades. Similarly to the impulse stage the fluid imparts some momentum on the blades, but is also expanded further, increasing its velocity, thus creating an area of low pressure on the back of the blades. This configuration allows both kinetic and pressure energy to be transferred to the shaft.

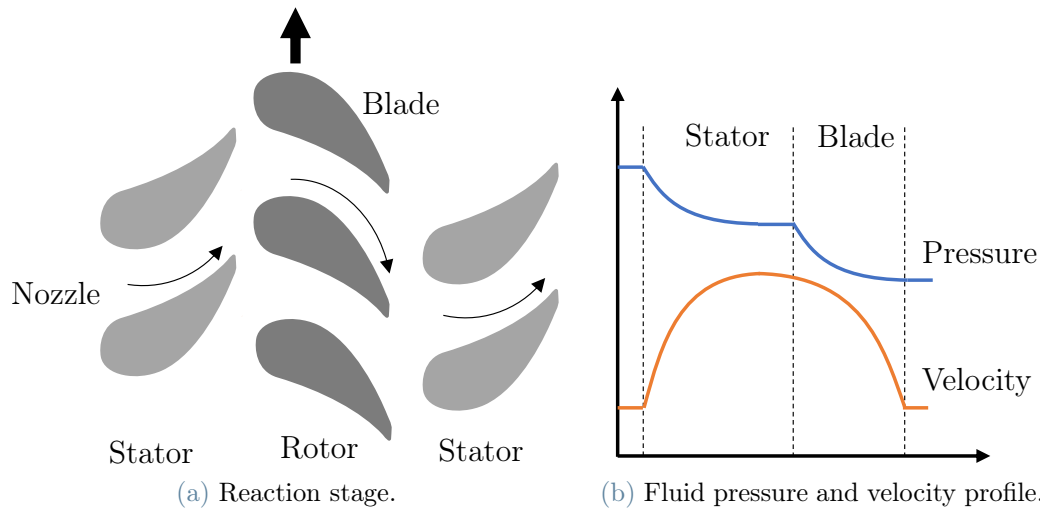


Figure 3.40: Configuration of a reaction turbine stage and the corresponding fluid pressure and velocity profiles. Adapted from [29, 91]

Impulse stages are typically used for small turbines or the high pressure stages of larger turbines. Reaction stages are used for low pressure and high through-put applications [91].

3.5.3. Types of Turbines

Axial Inflow, Axial Outflow

In axial turbines the fluid enters and exits the turbine parallel to the central axis, Figure 3.41. Many commercial steam turbines utilise this design, as it can be readily extended to accommodate a large number of stages. The lessons from many decades of steam turbine operation can also be translated to the significantly smaller ORC turbines, with this configuration being used extensively by ORC system manufactures like Turboden [93] and Ormat [24, 73].

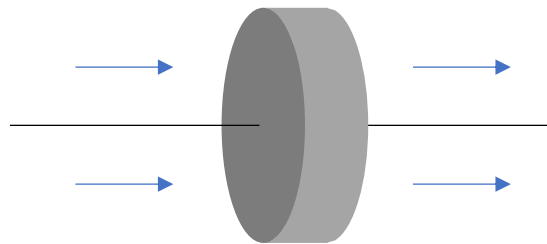


Figure 3.41: Inlet and outlet streams of an axial turbine.

Radial Inflow

In a radial inflow, the fluid enters the turbine perpendicular to the central shaft along the outer perimeter, similar to a centrifugal compressor in reverse flow [23]. Unlike axial turbines, where the tangential velocity of the blades is constant (i.e. $u_{in} = u_{out}$), in this configuration due to the decreasing radius the tangential blade velocity at the outlet is lower than at the inlet (i.e. $u_{in} > u_{out}$), allowing the second term of Equation 3.51 to be larger, leading to higher turbine efficiencies.

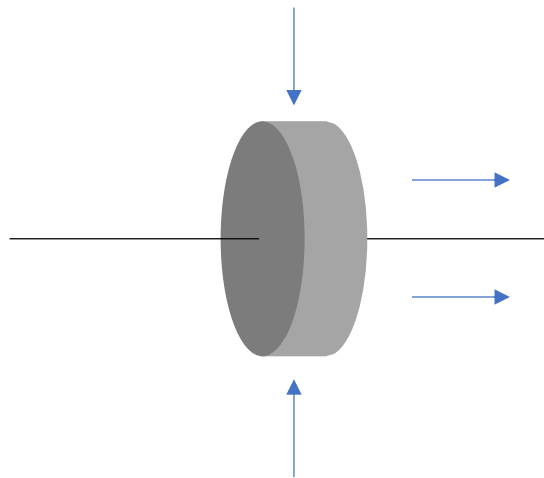


Figure 3.42: Inlet and outlet streams of a radial inflow turbine.

Radial Outflow

The Ljungström brothers [29] first proposed an axial inflow-radial outflow configuration, with the working fluid entering parallel to the central shaft, expanding radially through the turbine and then exiting perpendicular to the central shaft along the perimeter.

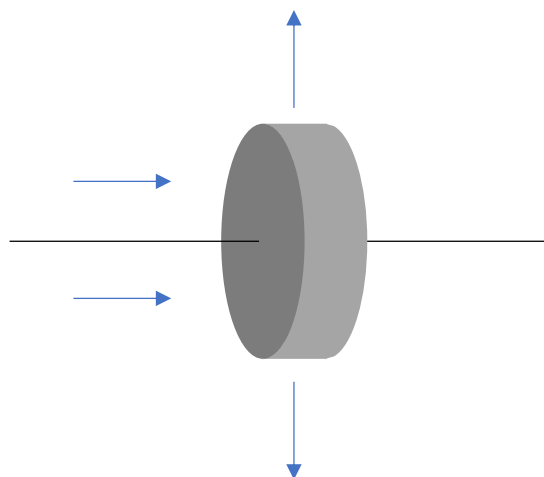


Figure 3.43: Inlet and outlet streams of a radial-outflow turbine.

An advantage of this design is that the flow area naturally increases as the fluid progresses radially through the turbine, thus, in principle allowing the turbine to be more compact. In axial turbines on the hand, the diameter must be increased along the length of the turbine to accommodate the increasing volume rate and prevent supersonic velocities. However, the increasing flowing radius also results in increasing blade velocities, which reduce the maximum work a given stage can extract, see Equation 3.51 where $u_{in} < u_{out}$.

This turbine configuration has not seen extensive use in steam expansion applications, as the increase in volumetric flow rate far exceeds the aforementioned increase in flow area, however Exergy International SRL [33] have used employed a related design in ORC applications where changes in fluid density and enthalpy are less significant

3.5.4. Wet Expansion

Unlike Rankine cycle power stations, where superheated or supercritical steam is expanded in turbines, guaranteeing a dry expansion, geothermal steam is typically saturated vapour or minimally super-heated. Consequently, due to the bell-shaped phase envelope of water in the temperature-entropy domain, two-phase condition during the expansion process are unavoidable. The formation of liquid droplets not only degrades the thermodynamic performance of the turbines but the droplets can also damage the turbine internals.

The mechanism for the formation of droplets is complex, involving meta-stable non-equilibrium fluid states and continues to be subject of research [86], but can broadly be divided into four phases: 1) Nucleation, 2) Droplet Growth, 3) Deposition and 4) Dispersion, see Figure 3.44.

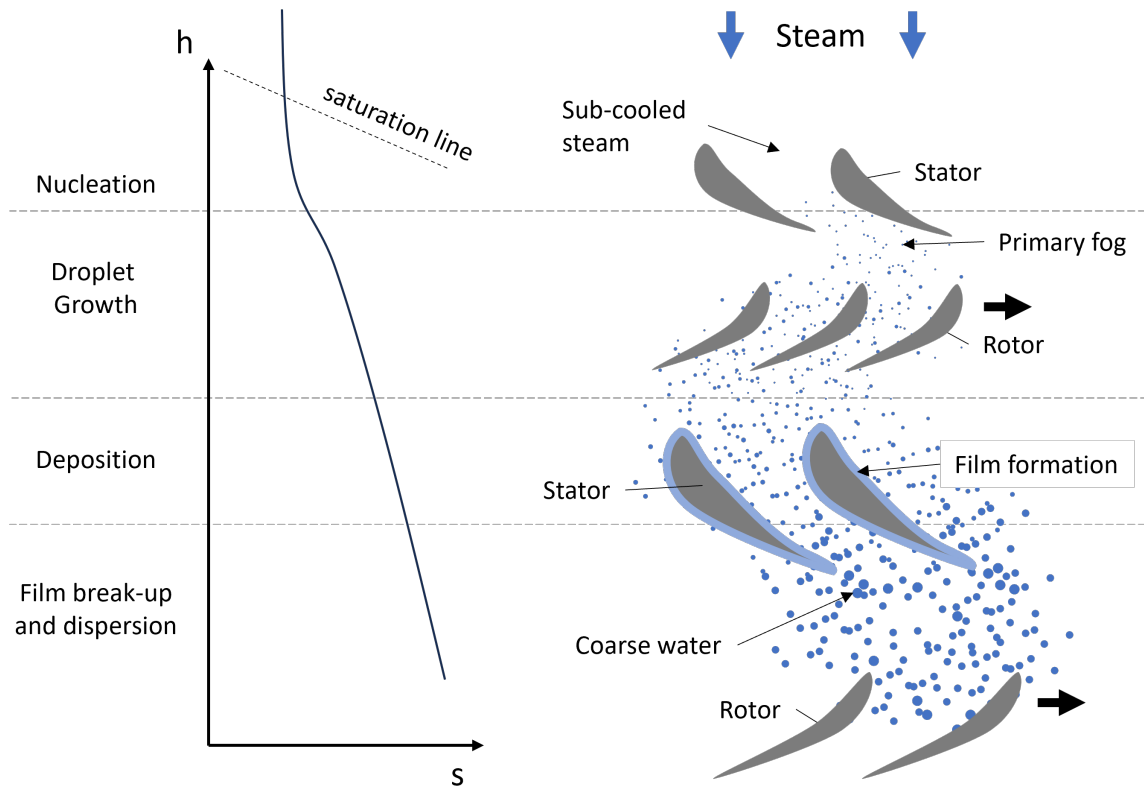


Figure 3.44: Mechanism for liquid formation in a steam turbine.

The condensation of liquid is not immediate, when the fluid is initially expanded to conditions below the saturation line. The reason for this is that for a pure fluid, the only pathway from an equilibrium vapour state to an equilibrium two-phase state is via drop-wise condensation¹, due to a lack of nucleation points and wettability. However, the formation of droplets poses a thermodynamic barrier (akin to an activation energy), as it increases the surface free energy due to interactions between the droplets and the vapour. For small droplet radii, the reduction in Gibbs free energy, which is proportional to the cube of the radius, is outweighed by the change in surface free energy, which is proportional to the square of the radius [64]. The Wilson point denotes the super-cooled conditions for which droplets are able to form spontaneously without explicit nucleation sites [12, 38, 64].

These initial droplets, typically between $0.01\ \mu\text{m}$ to $1\ \mu\text{m}$, continue to grow as the expansion progresses both due to continued condensation and coalescence with other droplets.

While the difference in vapour and droplet velocity, also called slip velocity, is minimal, as the droplets grow, sharp changes in fluid velocity can result in the deposition of a

¹Droplets of condensate do not wet surfaces/sites where they form and after growing expose the condensing surface/site without forming a film [91]

small fraction of droplets on rotor or stator surfaces. Shearing with the vapour phase, gravity and centrifuging, causes the liquid to accumulate and migrate towards the trailing edge of rotor blades or nozzles, from where it is stripped of by the high velocity vapour phase. The resultant coarse droplets, 10 μm to 500 μm , are much larger than the primary fog, exhibiting higher slip velocities and therefore pressure drops, but can also have a devastating effect on the downstream turbine internals [86].

However, condensation also impacts the energy conversion, reducing the apparent isentropic efficiency. The main phenomena responsible for these losses are [86]:

Thermal Relaxation Irreversible exchange of mass and heat between the vapour and the condensing droplets accounts for about 60 % to 90 % of losses, and is strongly droplet size dependent.

Coarse droplet & collected Water Coarse droplets impacting rotors and centrifuging of liquid films accounts for about 10 % to 40 % of losses.

Droplet Drag Increased frictional losses due to the presence of liquid droplets, typically, account for less than 5 % of losses. However, as the frictional losses depend on the slip velocity, which is small for the primary fog, higher losses can be anticipated where large or coarse droplets are more prevalent.

Baumann [16] first proposed a rule-of-thumb for capturing the efficiency degradation due to condensation in 1921, see Equation 3.52, where $\eta_{dry,turb}$ is the isentropic efficiency corresponding to a dry expansion and x_{in} and x_{out} are the steam quality at the inlet and outlet of the turbine. Equation 3.53, is a more modern and tunable formulation of the original Baumann rule, where α is the Baumann factor, typically between 0.4 and 2.5 or 1.0 for the original Baumann rule, and y_m is the average wetness across the turbine (sometimes weighted for dry stages) [86].

$$\eta_{isen,turb} = \eta_{dry,turb} * \frac{x_{in} + x_{out}}{2} \quad (3.52)$$

$$\eta_{isen,turb} = \eta_{dry,turb} * (1 - \alpha y_m) \quad (3.53)$$

However, it should be noted that the Baumann rule is entirely empirical, with the underlying source of thermodynamic losses being fluid, expansion, turbine geometry, and importantly *droplet size distribution* dependent. Despite a number of analytical approaches (e.g. for predicting the droplet nucleation and growth), to accurately predict the impact of condensation on turbine performance requires sophisticated CFD simulations or experimentation[86].

3.6. Heat Exchangers

Heat exchangers are used to facilitate the transfer of thermal energy from one fluid stream to another.

3.6.1. Working Principle

The rate of heat transfer \dot{Q} is driven by the overall heat transfer coefficient U (the inverse of the cumulative heat transfer resistances), the area A over which the heat transfer occurs, and the difference in temperature between the two streams ΔT , Equation 3.54.

$$\dot{Q} = U * A * \Delta T \quad (3.54)$$

Temperature Difference

The definition of the temperature difference depends on the heat exchange scenario. For instance, where transfer of heat does not change the temperature of either stream (e.g. exchange of latent heat), ΔT is simply the difference in temperature between the hot and cold stream. For idealised cases of counter-current or co-current heat exchange, the log-mean temperature difference ΔT_{lm} is used, see Equation 3.55, where ΔT_1 is the difference in temperature between the two streams at the inlet of the hot stream, and ΔT_2 is the difference in temperature between the two streams at the outlet of the hot stream [91].

$$\Delta T_{lm} = \frac{\Delta T_1 - \Delta T_2}{\ln \frac{\Delta T_1}{\Delta T_2}} \quad (3.55)$$

For real heat exchangers, where the heat transfer does not occur in a purely counter-current or co-current configuration (i.e. multiple tubing passes or shell passes in a shell and tube heat exchanger), ΔT is obtained by applying a correction factor f_T to the log-mean temperature difference ΔT_{lm} , Equation 3.56.

$$\Delta T = f_T * \Delta T_{lm} \quad (3.56)$$

The temperature correction factor is typically correlated based on two dimensionless numbers: the ratio of heat capacity flow rates R and thermal effectiveness of the heat exchanger P , which are calculated based on the inlet and outlet temperatures of the two streams, Equations 3.57 and 3.58 respectively. For simple geometries analytical solutions exist, for

example Equation 3.59 can be used to calculate the temperature correction factor for heat exchanger with one shell and two tubing passes (also referred to as a 1-2 heat exchanger). Correction factors for more complex geometries can be obtained from tables, graphical methods or simulations [91].

$$R = \frac{CP^{cold}}{CP^{hot}} = \frac{\dot{m}C_p^{cold}}{C_p^{hot}} = \frac{T_{in}^{hot} - T_{out}^{hot}}{T_{out}^{cold} - T_{in}^{cold}} \quad (3.57)$$

$$P = \frac{T_{out}^{cold} - T_{in}^{cold}}{T_{in}^{hot} - T_{in}^{cold}} \quad (3.58)$$

$$f_T^{1-2} = \begin{cases} \frac{\frac{\sqrt{2}P}{1-P}}{\ln \frac{2-P(2-\sqrt{2})}{2-P(2+\sqrt{2})}} & \text{if } R = 1 \\ \frac{\sqrt{R^2 + 1} \ln \frac{1-P}{1-RP}}{(R-1) \ln \frac{2-P(R+1-\sqrt{R^2+1})}{2-P(R+1+\sqrt{R^2+1})}} & \text{if } R \neq 1 \end{cases} \quad (3.59)$$

Overall Heat Transfer Coefficient

The overall heat transfer coefficient is a measure of the ease of heat transfer between the bulk hot stream and the bulk cold stream. For a shell & tube configuration, with the hot fluid on the shell side and the cold fluid on the tube side, the heat transfer can be broken down five stages, across the:

1. *Shell-side film*, Equation 3.60, where Q is the heat transferred, h_{ss} is the shell-side heat transfer coefficient, A_{ss} is the heat transfer area on the shell-side, and ΔT_{ss} is the temperature difference across the shell-side fluid film.

$$Q = h_{ss} A_{ss} \Delta T_{ss} \quad (3.60)$$

2. *Shell-side fouling layer*, Equation 3.61, where Q is the heat transferred, h_{ssf} is the shell-side fouling layer heat transfer coefficient, A_{ss} is the heat transfer area on the shell-side, and ΔT_{ssf} is the temperature difference across the shell-side fouling film. Fouling (i.e. the deposition of materials on surfaces, such as scales, biofilms, etc.) is a time dependent phenomenon, with complex mechanisms and multi variable dependencies, as such for design is usually performed with experienced based values

of fouling resistance after a reasonable period of operation [91].

$$Q = h_{ssf} A_{ss} \Delta T_{ssf} \quad (3.61)$$

3. *Tubing*, Equation 3.62, where Q is the heat transferred, k is the thermal conductivity of the tubing material, L is the length of the tubing, ΔT_{tw} is the temperature difference across the tubing wall, and d_{ss} and d_{ts} are the tubing diameter on the shell and tubing side respectively.

$$Q = \frac{2\pi k L}{\ln \frac{d_{ss}}{d_{ts}}} \Delta T_{tw} \quad (3.62)$$

4. *Tube-side fouling layer*, Equation 3.63, where Q is the heat transferred, h_{tsf} is the tube-side heat transfer coefficient, A_{ts} is the heat transfer area on the tube-side, and ΔT_{tsf} is the temperature difference across the tube-side fluid film.

$$Q = h_{tsf} A_{ts} \Delta T_{tsf} \quad (3.63)$$

5. *Tube-side film*, Equation 3.64, where Q is the heat transferred, h_{ts} is the tube-side heat transfer coefficient, A_{ts} is the heat transfer area on the tube-side, and ΔT_{ts} is the temperature difference across the tube-side fluid film.

$$Q = h_{ts} A_{ts} \Delta T_{ts} \quad (3.64)$$

Combining Equations 3.60 to 3.64, an expression for the overall heat transfer coefficient U can be obtained, Equation 3.65 (*Note*, this formulation is relative to the shell-side heat transfer area).

$$U = \left[\frac{1}{h_{ss}} + \frac{1}{h_{ssf}} + \frac{d_{ss} \ln \frac{d_{ss}}{d_{ts}}}{2\pi k L} + \frac{d_{ss}}{h_{tsf} d_{ts}} + \frac{d_{ss}}{h_{ts} d_{ts}} \right]^{-1} \quad (3.65)$$

An alternative, more generic formulation of the overall heat transfer coefficient U is given by Equation 3.66.

$$U = \left[\frac{1}{h_{int} \chi_{int} \frac{A_{int, pt}}{A_{ext, pt}}} + \frac{R_{int, f}}{\frac{A_{int, pt}}{A_{ext, pt}}} + R_m + \frac{R_{ext, f}}{\frac{A_{ext, t}}{A_{ext, pt}}} + \frac{1}{h_{ext} \chi_{ext} \frac{A_{ext, t}}{A_{ext, pt}}} \right]^{-1} \quad (3.66)$$

Here,

- h_{int} and h_{ext} are the internal and external film heat transfer coefficients. Exact values are not usually known until detailed design calculations have been performed. Astolfi [8] obtained typical values by performing regression analysis against overall heat transfer coefficient data, see Table 3.2.
- χ_{int} and χ_{ext} are the internal and external enhancement factor, with typical values ranging from 1 to 5. The enhancement factor accounts for improvement of the film heat transfer from turbulence/mixing promoting texturing of the heat transfer surface.
- $\frac{A_{int, pt}}{A_{ext, pt}}$ is the ratio of the internal to the external *plain* tubing area. It is usually around 0.87.
- $\frac{A_{ext, t}}{A_{ext, pt}}$ is the ratio of the external heat transfer area to the external plain tubing area. For plain tubes its value is 1, however for finned tubes its value can be as large as 14.
- $R_{int, f}$ and $R_{ext, f}$ are the heat transfer resistances the internal and external fouling layer. Typical values are shown in Table 3.3
- R_m is the resistance of the material. Due to the high thermal conductivity of the materials used, the material resistance is small and can be neglected.

Table 3.2: Film heat transfer coefficients for different fluids [8].

Fluid	$h/W \text{ m}^{-2} \text{ K}^{-1}$
Water (liquid)	7500
Water (boiling)	7000
Water (condensing)	10000
Water (vapour LP)	125
Water (vapour HP)	800
Organic (liquid)	1900
Organic (boiling)	1900
Organic (condensing)	2500
Organic (vapour LP)	125
Organic (vapour HP)	600
Air	125

Table 3.3: Fouling resistances for different fluids [98]. ^aSodium Chloride or Calcium Chloride solutions in TEMA standard ^b Refrigerant in TEMA standard

Fluid	$R_f/10^{-5} \text{ m}^2 \text{ K W}^{-1}$
Steam	8.81
Water	8.81
Brine ^a	52.83
Organic ^b (vapour)	35.22
Organic ^b (liquid)	17.61
Air	17.61

3.6.2. Shell & Tube Heat Exchangers

In shell and tube heat exchangers, one fluid flow through a collection of tubes, which are contained within an outer shell. The other fluid flows through the interspace between the tubes and the shell, Figure 3.45. On the shell side, baffles are used not only to hold tubes in place and reduce vibrations, but also to ensure even flow across all tubes and prevent short-circuiting [46].

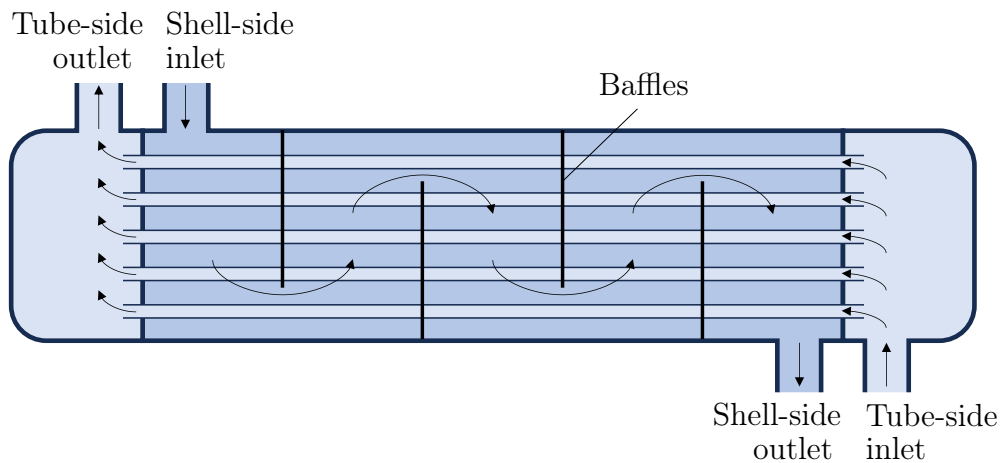


Figure 3.45: Shell & Tube heat exchanger. Adapted from [46]

Shell and tube heat exchangers can be divided into three core components, 1) the front end, 2) the shell and 3) the rear end, with many possible configurations being available for each component [98]. This versatility has made shell and tube heat exchangers popular across many industries, with Tubular Exchangers Manufacturers Association (TEMA) providing standards for their design and operation since as early as 1939 [99].

For *dirty* fluids, such as scaling-prone geofluids, TEMA recommend confining the fluid to the tube-side reduce maintenance costs (compared to the shell-side), and to avoid U-bends, as these may make it impossible to clean the U-bend section of the tubing, which may lead to high pressure losses and in the worst case clogging.

3.7. Equipment Costs

3.7.1. Steam Turbines

Steam turbines have not only been installed in many power plants across the globe but also for many decades, yielding significant experience in their design, manufacture and operation. Some cost correlations, in terms of the fluid power \dot{W} , i.e. work done by the fluid, (or similar) are shown in Table 3.4.

The *genGEO* steam turbine cost model suggested by Adams et al. [6] is a development of a cost model from *GETEM* [68], where the specific cost has been matched against cost data of coal-fired power stations reported by National Energy Technology Laboratory (NETL) between 2007 and 2019. This also explains the similarity in specific cost predicted by either model, see Figure 3.46.

Table 3.4: Steam turbine cost correlations. \dot{W} is the fluid power in kW, \dot{W}_s is the shaft power in kW, and \dot{W}_e is the electrical power in kW. ^aFitted against data from Thermoflex, $R^2 = 0.9994$

Cost Correlation	Min/kW	Max/kW	Currency	Reference
$C_{turb, gen} = 2830 \cdot \dot{W}_e^{0.745} + 3685 \cdot \dot{W}_e^{0.617}$	-	-	€2002	[68]
$C_{turb, gen} = 0.67 \cdot (2830 \cdot \dot{W}_e^{0.745} + 3680 \cdot \dot{W}_e^{0.617})$	-	-	€2002	[6]
$\log C_{turb, gen} = 2.6259 + 1.4398 \log \dot{W}_s - 0.1776(\log \dot{W}_s)^2$	70	7500	€2001	[103]
$C_{turb, gen} = 10^3 \cdot \exp(-0.0408 \ln^2 \dot{W}_e + 1.3039 \ln^2 \dot{W}_e - 0.1583)$	500	70000	€2021	[100] ^a

However, although steam turbines share the same working fluid, there are some stark differences in the expansion processes used in coal-fired and geothermal power stations. As discussed in Section 3.5.4, wet expansion is unavoidable in geothermal DSC power plants and reduces the isentropic efficiency of the turbine. In turn, this should lead to higher specific costs for geothermal steam turbines.

With this in mind, a wet expansion turbine was simulated in *Thermoflex* [100] for a range of operating conditions, analogous to a geothermal DSC and different mass rates. The combined turbine and generator costs predicted by *Thermoflex* were then correlated against the turbine power.

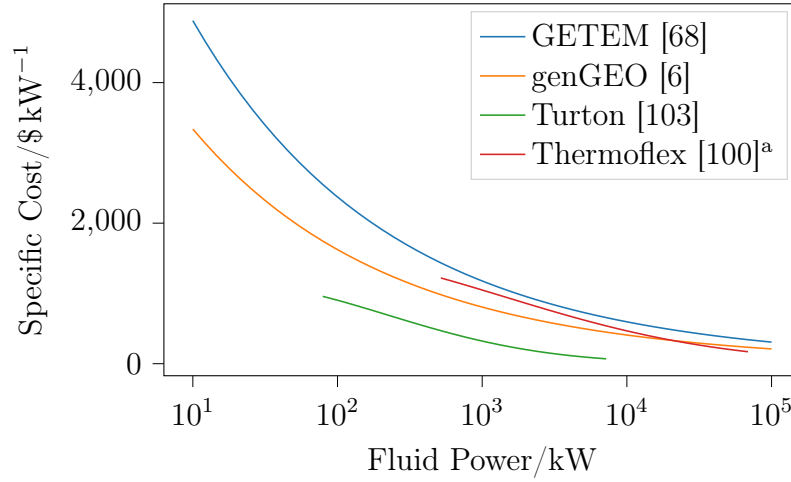


Figure 3.46: Steam turbine specific cost correlations. ^aFitted against data from Thermoflex, $R^2 = 0.9994$

While the cost model developed in *Thermoflex* incorporates the turbine efficiency reduction into the cost estimate, more practical consideration such as material allowances to handle the effects of liquid formation within the turbine are not captured. Moreover, given that geothermal fluids are not pure water, additional allowances could be made to incorporate the increased vapour volumetric flow rate when NCG is present, corrosion- and erosion-resistant materials to handle the presence of minerals and NCG in the geofluid.

3.7.2. ORC Turbines

For ORC turbines there are two types of cost models, ones that correlate the cost to the turbine power (similar to steam turbines), and the ones correlating costs with the number of stages and the size parameter SP . For ORC turbines, the latter approach is preferred as it allows the effect of different working fluids and expansion processes on the turbine cost to be captured. A number of ORC turbine cost models are shown in Table 3.5.

Table 3.5: ORC turbine cost correlations. \dot{W} is the fluid power in kW, \dot{W}_s is the shaft power in kW, and \dot{W}_e is the electrical power in kW.

Cost Correlation	Min/kW	Max/kW	Currency	Reference
$C_{turb, gen} = 7400 \cdot \dot{W}_e^{0.6} + 1800 \cdot \dot{W}_e^{0.67}$	-	11000	€2002	[68]
$C_{turb, gen} = -1.4 \cdot 10^4 + 1900 \cdot W^{0.75}$	100	20000	\$2010	[102]
$\log C_{turb, gen} = 2.7051 + 1.4398 \log \dot{W} - 0.1776(\log \dot{W})^2$	100	7500	€2001	[103]
$C_{turb} = 1.23 \cdot 10^6 \cdot \frac{n}{2}^{0.5} \cdot \frac{SP}{0.18}^{1.1}$	-	-	€2014	[11]
$n = \left\lceil \max \left(\frac{\Delta h_{isen}^{tot}}{\Delta h_{stage}^{max}}, \frac{V_{r,isen}^{tot}}{V_{r,stage}^{max}} \right) \right\rceil$				
$SP = \frac{\sqrt{\dot{V}_{isen}}}{\sqrt[4]{\frac{\Delta h_{isen}^{tot}}{n_{stages}}}}$				
$C_{gen} = 2 \cdot 10^5 \cdot (W_e/5000)^{0.67} \cdot S_{gear}$	-	-	€2014	[11]

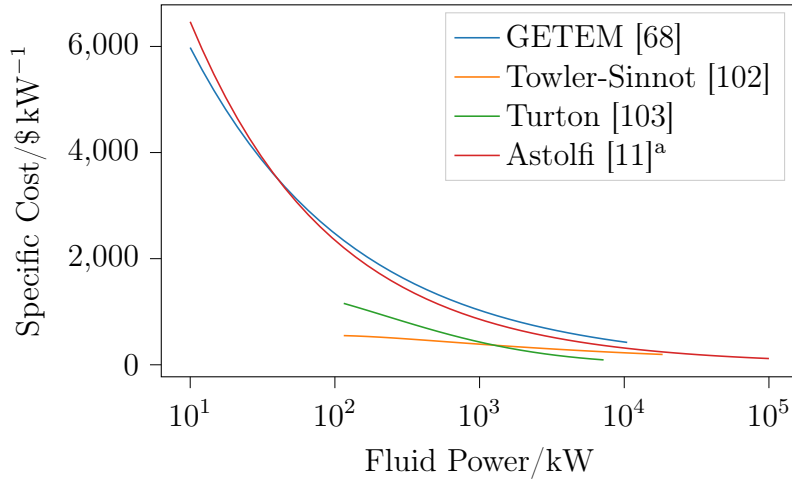


Figure 3.47: ORC turbine specific cost correlations. ^aAssuming n-Butane as the working fluid, 3 turbine stages, $\Delta h = 78.74$ kW, and an outlet vapour density of 10.45 kg m^{-3}

From Figure 3.47 it can be seen that the generic model from *GETEM* and the *Similitude* approach yield comparable costs estimates over a wide range of turbine capacities. However, for other fluids or expansion processes agreement between the two approaches may differ.

3.7.3. Shell & Tube Heat Exchangers

Shell and Tube heat exchangers are common process equipment that have been in use for many decades, resulting in extensive design, manufacturing and operational experience. As a result, cost correlations have been published in a number of reference text books, see Table 3.6, the main challenge being to accurately update the purchasing costs to today's cost levels.

Table 3.6: Cost correlations for shell and tube heat exchangers. A is the heat transfer area in m^2 . ^aFloating head ^bFixed head ^cFixed or floating head ^dKettle boiler ^ePrimary heat exchanger ^fRecuperator

Cost Correlation	Min/ m^2	Max/ m^2	Currency	Reference
$C = 3.28 \cdot 10^4 * \left(\frac{A}{80}\right)^{0.68}$	80	4000	\$2000	[91]
$C = 239 * A + 13400$	-	-	\$2002	[6, 76] ^a
$C = 181 * A + 3320$	-	-	\$2002	[6, 76] ^b
$C = 235 * A + 17900$	-	-	\$2002	[6, 60] ^c
$\log C = 4.3247 - 0.3030 \log A + 0.1634(\log A)^2$	10	1000	\$2001	[103] ^a
$\log C = 4.8306 - 0.8509 \log A + 0.3187(\log A)^2$	10	1000	\$2001	[103] ^b
$\log C = 4.4646 - 0.5277 \log A + 0.3955(\log A)^2$	10	100	\$2001	[103] ^d
$C = 1500 * \left(\frac{UA}{4000}\right)^{0.9} * 10^{f_P}$	-	-	€2014	[11] ^e
$f_P = 0.03881 - 0.11272 * \log P + 0.08183 * \log^2 P$	-	-	€2014	[11] ^f
$C = 260 * \left(\frac{UA}{650}\right)^{0.9} * 10^{f_P}$	-	-	€2014	[11] ^f
$f_P = -0.00164 - 0.00627 * \log P + 0.0123 * \log^2 P$	-	-	€2014	[11] ^f

As can be seen from Figure 3.48 the different correlations yield remarkably similar results over a wide range of heat transfer areas. Owing to most the majority of the cost models scaling linearly to the heat transfer area, the specific cost for heat exchangers larger than 10 m^2 remains fairly constant at around $225 \$ \text{m}^{-2}$.

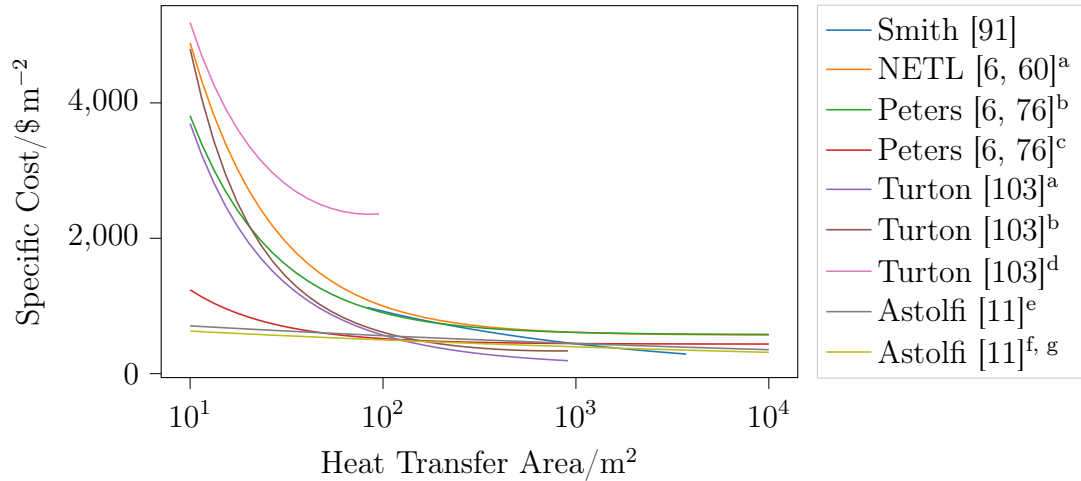


Figure 3.48: Shell and tube specific cost correlations. ^aFloating head ^bFixed head ^cFixed/floating head ^dKettle boiler ^eAssuming an overall heat transfer coefficient of $1000 \text{ W m}^{-2} \text{ K}^{-1}$ ^fPHE ^gRecuperator.

3.7.4. Condensers

A number of condenser cost models were considered, see Table 3.7, however it was noticed that there appears to be some disagreement in the cost scaling between the different correlations, see Figure 3.49. For instance, the correlations from Smith [91] and Turton [103], are at opposite ends of the spectrum, possibly indicating that they represent different cooling systems architectures or mechanisms. The remaining correlations, taken from *GETEM* [68] and Astolfi et al. [11], agree more closely and form a middle ground.

Table 3.7: Cost correlations for condensers. A is the heat transfer area in m^2 . ^avia [6]
^bNCG condenser

Cost Correlation	Min/ m^2	Max/ m^2	Currency	Reference
$C = 1.56 \cdot 10^5 * \left(\frac{A}{200}\right)^{0.89}$	200	2000	\$2000	[91]
$\log C = 4.0336 + 0.2341 \log A + 0.0497(\log A)^2$	10	10000	\$2001	[103]
$C = 1.56 \cdot 10^5 * \left(\frac{A}{200}\right)^{0.89}$	200	2000	\$2000	[91]
$C = 768 * A^{0.85}$	-	-	\$2002	[68] ^a
$C = 1780 * A^{0.72}$	-	-	\$2002	[68] ^{a, b}
$C = 5.3 \cdot 10^5 * \left(\frac{A}{3563}\right)^{0.9}$	-	-	€2014	[11]
$U = -9.84 * 10^3 * \delta^2 + 3.61 * 10^3 * \delta + 9.72 * 10^2$ $\delta = \frac{\Delta T_{min}}{\Delta T_{cold inlet}}$				

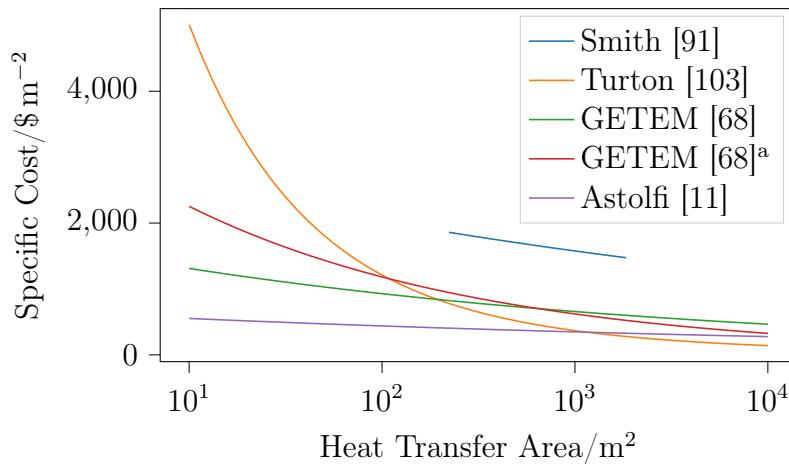


Figure 3.49: Condenser specific cost correlations. ^aNCG condenser.

3.7.5. Pumps

From the pump cost models considered, Table 3.8, no clear conclusions on suitability. The models from Turton [103] and Astolfi et al. [11] are in good agreement for pump sizes

greater than 10 kW, Figure 3.50, whereas the models from Smith [91] and *GETEM* [68] provide significantly higher costs but agree well with each other.

Table 3.8: Cost correlations for pumps. \dot{W} is the pump power in kW.

Cost Correlation	Min/kW	Max/kW	Currency	Reference
$C_{pump} = 1.051 \cdot 10^4 * \left(\frac{\dot{W}}{4}\right)^{0.55}$	4	700	\$2000	[91]
$C_{pump} = 1185 * S_{mat} * (1.34 * \dot{W})^{0.767}$			\$2002	[68]
$\log C_{pump} = 3.3892 + 0.0536 \log \dot{W}_s + 0.1538(\log \dot{W}_s)^2$	1	300	\$2001	[103]
$C_{pump} = 1.4 \cdot 10^4 * \left(\frac{\dot{W}_{elec}}{200}\right)^{0.67}$	-	-	€2014	[11]

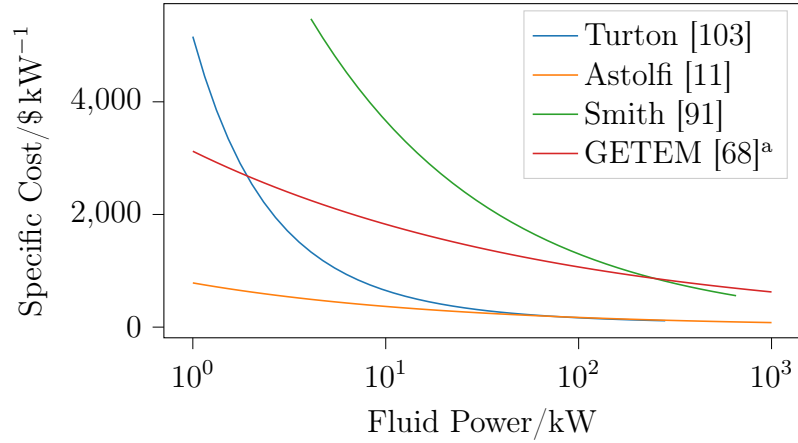


Figure 3.50: Pump specific cost correlations. ^a S_{mat} is 1 corresponding to carbon steel.

3.7.6. Compressors

There are significant differences in the specific cost predicted by the correlations investigated. While the correlations by Turton [103] and Smith [91], appear to be in good agreement at high capacities, the model by Duc et al. [32] has been used in a similar context (i.e. CO₂ compression) in the original paper as well as *genGeo* [6].

Table 3.9: Cost correlations for compressors. \dot{W} is the fan power in kW.

Cost Correlation	Min/kW	Max/kW	Currency	Reference
$\log C_{comp} = 2.2897 + 1.3604 \log \dot{W} - 0.1027(\log \dot{W})^2$	1	300	\$2001	[103]
$C_{comp} = 7248 * (1.34 * \dot{W})^{0.82}$	-	-	\$2005	[32]
$C = 9.84 \cdot 10^4 * \left(\frac{\dot{W}}{250}\right)^{0.46}$	250	10000	\$2000	[91]

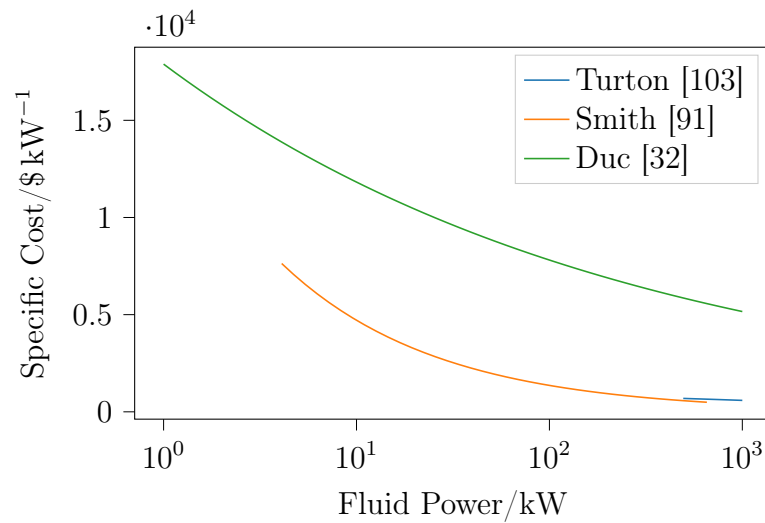


Figure 3.51: Compressor specific cost correlations. Citations in order of appearance [103], [91], and [32].

3.7.7. Fans

The fan models considered are not in close agreement, and the model by Turton [103] provides unrealistic cost estimates for capacities exceeding 8 kW, as the specific cost begins to increase with capacity.

Table 3.10: Cost correlations for fans. \dot{V} is the volumetric flow rate in $\text{m}^3 \text{s}^{-1}$ and \dot{W} is the fan power in kW.

Cost Correlation	Min/kW	Max/kW	Currency	Reference
$\log C_{fan} = 3.5391 - 0.3533 \log \dot{V} + 0.4477 (\log \dot{V})^2$	1	100	\$2001	[103]
$C_{fan} = 1.23 \cdot 10^4 * \left(\frac{\dot{W}}{50}\right)^{0.76}$	50	200	\$2000	[91]

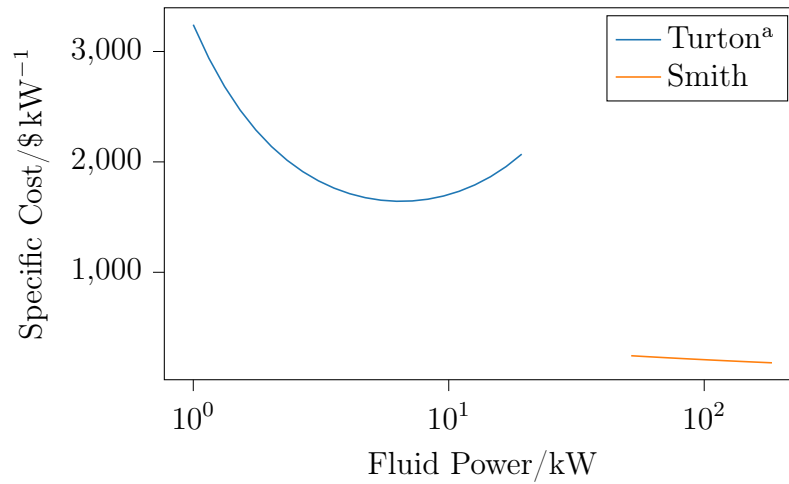


Figure 3.52: Fan specific cost correlations. Citations in order of appearance [103], [91].

^aAssuming a pressure drop of 120 Pa, an fan efficiency of 60 %, resulting in a air enthalpy of 0.16 kJ kg^{-1} and a density of 1.18 kg m^{-3} .

3.7.8. Power Plants

GEOPHIRES-X [17] is a useful reference for comparing the cost of binary ORC and DSC geothermal power plants. As can be seen from Figure 3.53 the absolute cost of both types of power plant decrease with temperature, resulting in lower specific costs, Figure 3.54. Binary ORCs scale almost linearly with plant, indicating fewer economies of scale compared to DSCs, whose specific costs decrease more significantly with plant capacity.

However this approach has a number of drawbacks. For instance the geofluid temperature is not the sole discriminator between binary and DSC geothermal power plants, but the steam quality also plays an important role, particularly for DSCs. Moreover, the binary ORC is generic and does not differentiate between different working fluids.

Comparing the cost estimates from *GEOPHIRES-X* against costs derived in a study by Astolfi et al. [11] it can be seen that there is a significant discrepancy of almost 50 %.

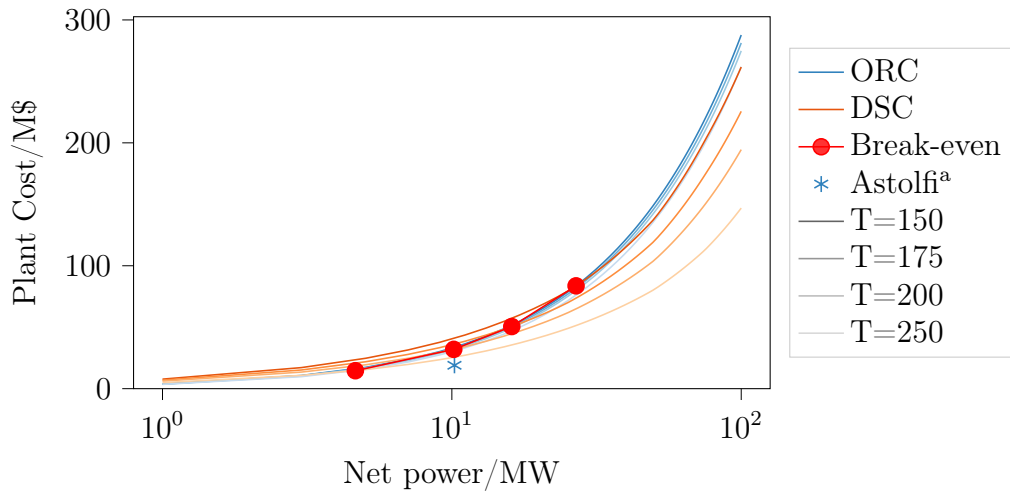


Figure 3.53: Cost correlations of a sub-critical binary ORC and a single flash DSC for different geofluid inlet temperatures [17, 18, 84]. ^a Super-critical ORC with R134a as the cycle working fluid. Geofluid inlet temperature of 150°C and mass rate of 200 kg s^{-1} [11]

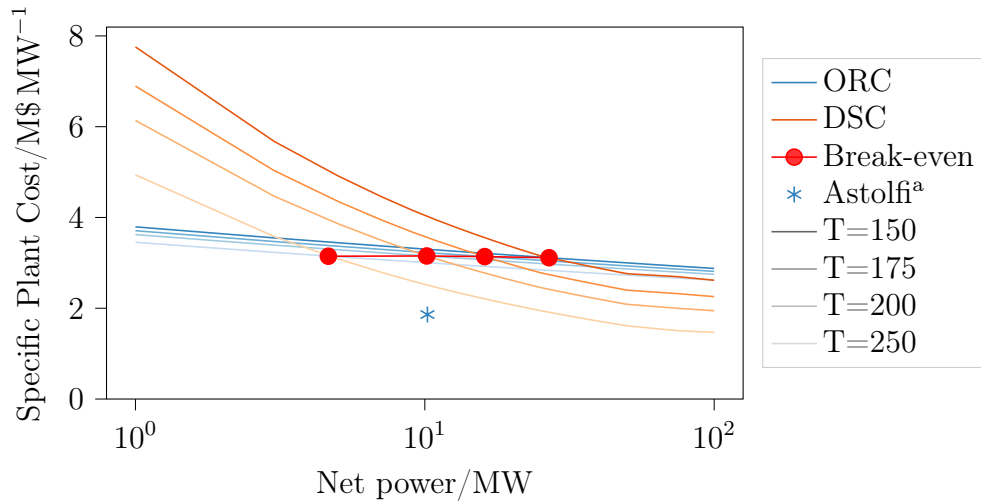


Figure 3.54: Specific cost cost correlations of a sub-critical binary ORC and a single flash DSC for different geofluid inlet temperatures [17, 18, 84].

4 | Power Plant Modelling

The following section seeks to outline the governing equations used within *PowerCycle*, which was inspired by Lorenzo Galieti's codebase *wopycle* [34].

4.1. Architecture

At its core *PowerCycle* is comprised of a fluid properties calculation engine and power plant equipment models, see Section 4.2 and 4.3, which form the building blocks of the power plant. The thermodynamic and techno-economic performance of the power plant can then be calculated for a given set of boundary conditions, and process parameters can be optimised to maximise the thermodynamic or techno-economic performance, see Figure 4.1.

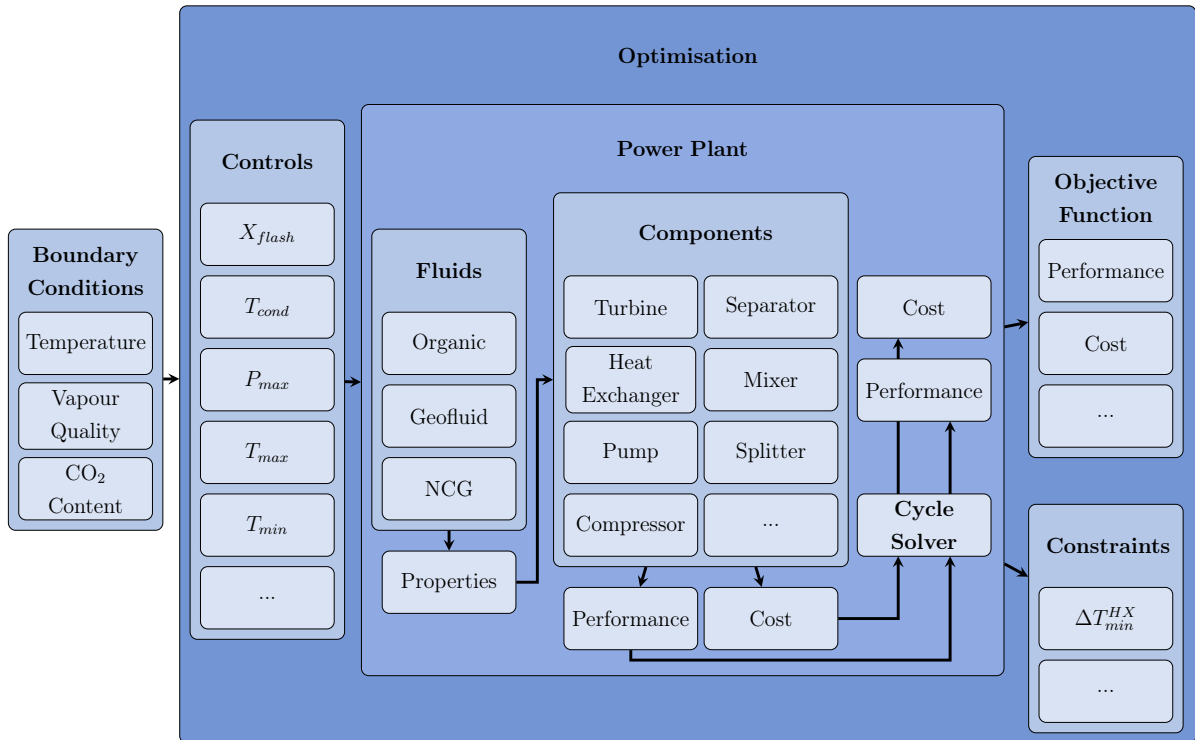


Figure 4.1: Component diagram of *PowerCycle*

4.2. Fluid Properties

Underlying to all power plant component calculations are the thermophysical properties of the fluid(s) a given component is handling. However, as previously discussed in Thermophysical Property Modelling, different fluids require different modelling approaches.

For example, pure fluids like idealised geofluids (i.e. water) or binary ORC working fluids (i.e. hydrocarbons and refrigerants) are best modelled with dedicated EOS, such as the WP HEOS for pure water. Such fluids can be modelled using calculation frameworks like *CoolProp*, *REFPROP*, *FluidProp*, etc. On the other hand, geofluids, which are complex mixtures of water, minerals and NCG, require more flexible modelling approaches, such as *GeoProp*.

From a modelling perspective, this poses a logistical problem because each calculation engine follows a unique syntax and workflow for obtaining and reporting thermophysical properties, and it is impractical to generate calculation engine specific component models. An alternative approach is the use of an unified fluid property modelling interface for the component models to interact with.

The following section aims to provide details of the implementation of such a unified fluid property modelling interface and an overview of the calculation engines used in this work.

4.2.1. Architecture

The unified fluid property modelling interface is comprised of three key components: 1) the calculation engines, 2) the engine interfaces and 3) the front-end, which is accessible to the user.

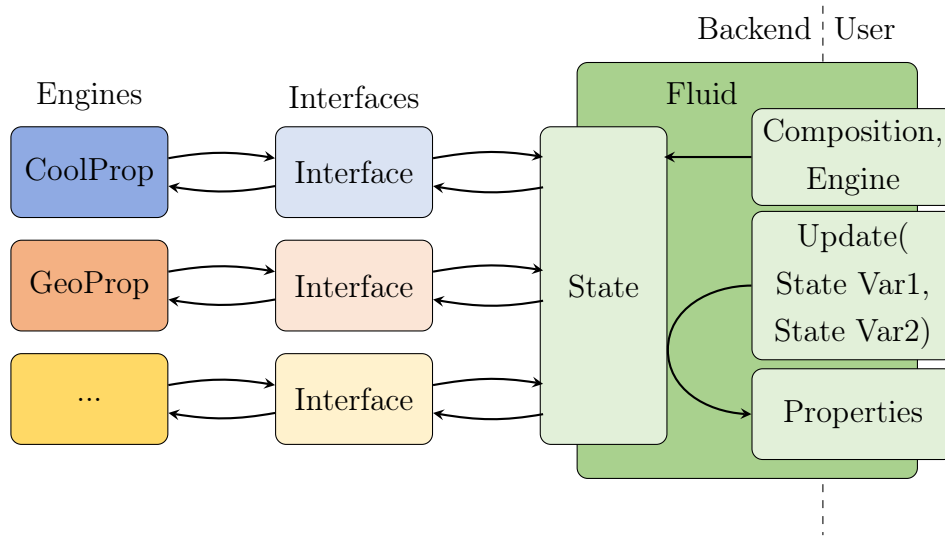


Figure 4.2: Architecture of the fluid properties module

The user creates a *Fluid* by specifying the composition and the desired calculation engine to be used for the property calculations. Internally, this then creates a *State*, which represents the thermodynamic state of the *Fluid*. To obtain the properties of a given *State*, the user provides the defining state variable pairs, e.g. pressure and specific enthalpy.

The *State* then sends a request to the corresponding engine *interface*, which parses the instructions for updating the state to a format accepted by the underlying calculation *engine*. The *engine* then performs the required calculations and the *interface* then aggregates the fluid properties and returns them to the *State* and in turn to the *Fluid*, where they can then be accessed by the user.

In principle, this plug-in architecture, allows the collection of calculation engines to be extended to any number of models. The only requirement for adding additional *engines*, is the creation of a corresponding *interface* script.

4.2.2. Calculation Engines

To date, three calculation engines can be used:

CoolProp: For modelling pure fluids, such as pure water geofluids and coolant, pure component hydrocarbons and refrigerants for use as working fluid in binary ORCs and air as coolant.

Note. *CoolProp* supports most state variable pairs for updating the fluid state of single component fluids. However, for mixtures only three calculation modes

are available: pressure-temperature, pressure-vapour quality and temperature-vapour quality, other calculation modes have to be performed by iteration using the base modes.

GeoProp: For modelling geofluids, in particular mixtures of water and carbon dioxide. In its default configuration the SP2009 model is used for the partition and the thermophysical properties are determined using *CoolProp* and *ThermoFun*.

Note. Natively, *GeoProp* only supports pressure-temperature calculations, meaning that other calculation modes (e.g. pressure-enthalpy or pressure-entropy) are calculated by iteration.

Note. The SP2009 model is only valid for pressures between 1 bar and 600 bar, and as such to handle expansions to sub-atmospheric conditions, *CoolProp* is used for pressures below 1 bar, see Figure 4.3.

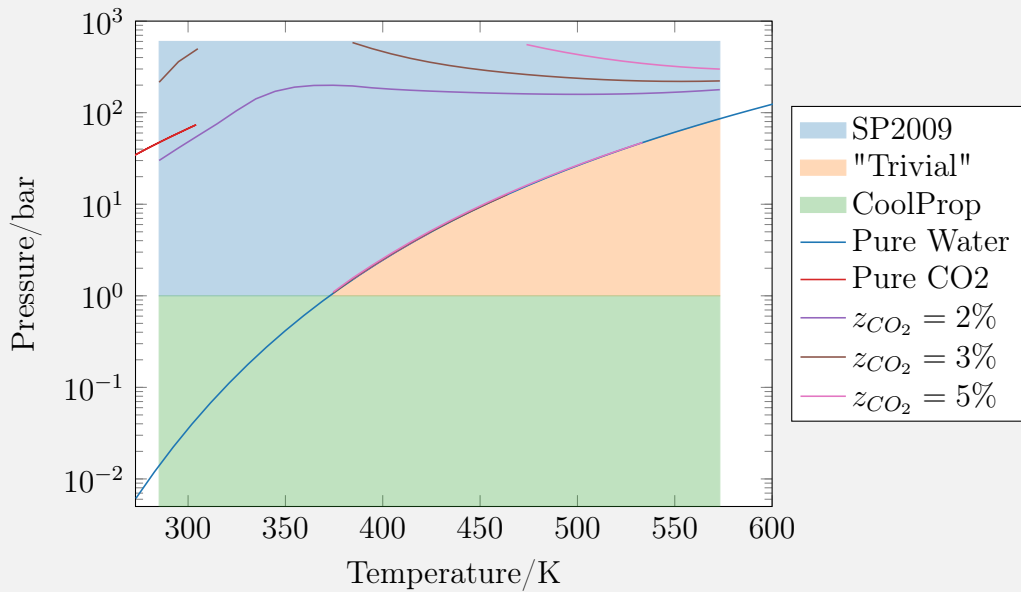


Figure 4.3: The calculation regions when using GeoProp. The *Trivial* region covers the temperature and pressure conditions for which the SP2009 is used, but because the natural state of water is gaseous, the fluid as a whole is considered gaseous.

LookUpTables: Allow the user to use pre-generated data tables of fluid properties in order to reduce calculation time.

4.2.3. Stream

The material stream is a collection of a mass rate \dot{m} and a composition \mathbf{z} , as well as the properties associated with a given state of the fluid. The state of fluid can be defined based on the state variable pairs shown in Table 4.1:

Table 4.1: State variable pairs.

Variable 1	Variable 2	Note
Pressure	Specific Enthalpy	
Pressure	Specific Entropy	
Pressure	Temperature	Only outside the two-phase region (pure fluids)
Pressure	Quality	Only inside the two-phase region
Temperature	Quality	Only inside the two-phase region

4.3. Base Components

The base components are the building blocks that make up any power plant, such as turbines, heat exchangers, pumps, compressors, etc. The following section sees to outline the different base components that can be modelled within PowerCycle, and how their performance, exergy loss and cost is calculated.

The notation convention for the expressions of the exergetic losses follows that presented in Exergy Analysis.

4.3.1. Turbine

The turbine component can be used to expand a stream from a high to a low pressure, thereby providing the rotational power to drive a generator and generate electrical power, see Figure 4.4.

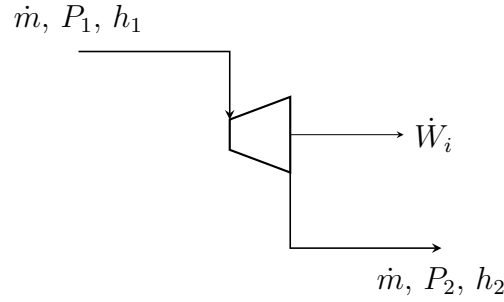


Figure 4.4: The process streams entering and exiting a turbine

Considering a stream of mass rate \dot{m} , pressure P_1 , and specific enthalpy h_1 , the work done by the fluid on the turbine, \dot{W}_{turb} , in lowering the stream pressure to, P_2 , where $P_1 > P_2$, can be calculated using Equation (4.1).

Note. By convention the work done by the fluid is negative, while work done on the fluid is positive.

$$\dot{W}_{turb} = \dot{m} * (h_2 - h_1) \quad (4.1)$$

The specific enthalpy of the stream at the turbine outlet, h_2 , can be determined from the definition of the isentropic efficiency, η_{turb}^{isen} , see Equation (4.2), where $h_{2,isen}$ corresponds to the outlet specific enthalpy assuming an isentropic expansion (i.e. the specific entropy at the inlet and outlet are equal, $s_2 = s_1$). Combining Equations 4.1 and 4.2 yields an expression for the turbine work, Equation 4.3. The electrical power can then be determined by assuming an efficiency for the generator, η_{gen} , see Equation 4.4. By default the isentropic efficiency of the turbine and the efficiency of the generator are assumed to be 85 % and 95 % respectively [30].

$$\eta_{turb}^{isen} = \frac{h_2 - h_1}{h_{2,isen} - h_1} \quad (4.2)$$

$$\dot{W}_{turb} = \dot{m} * \eta_{turb}^{isen} * (h_{2,isen} - h_1) \quad (4.3)$$

$$\dot{W}_{turb}^{elec} = \eta_{gen} * \dot{W}_{turb} \quad (4.4)$$

In case of wet expansion, i.e. the expansion crosses the phase envelope, the Baumann rule is used to correct the isentropic efficiency for the vapour *wetness*, Equation 4.5. Where $\eta_{turb}^{isen,dry}$ is the isentropic efficiency of a dry expansion, and x_1 and x_2 are the vapour quality at the inlet and outlet of the turbine, defined on a mole basis.

$$\eta_{turb}^{isen} = \eta_{turb}^{isen,dry} * \frac{x_1 - x_2}{2} \quad (4.5)$$

Note. While the definition of the vapour quality on a mass or mole basis is irrelevant when dealing with pure working fluids, for mixtures, such as water and NCG, a distinction has to be made. In this work, the mole-based vapour quality is used as it underestimates the isentropic turbine efficiency compared to a mass-based vapour quality, see Figure 4.5. For outlet mole-based vapour qualities of 0.7 mol mol^{-1} the difference in isentropic turbine efficiency is at most 10 %.

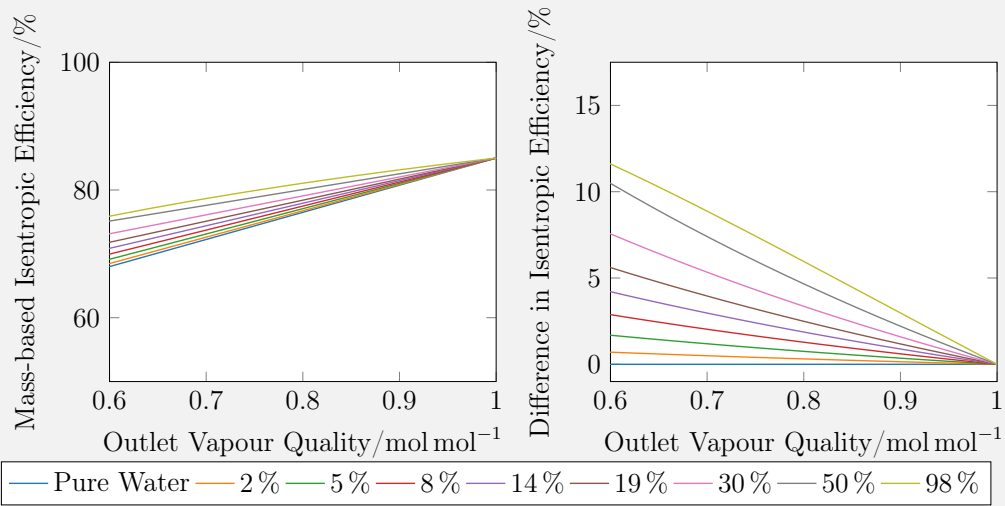


Figure 4.5: Comparing the Baumann-corrected isentropic turbine efficiency as calculated from mole- or mass-based vapour quality for geofluids of different CO₂ content. The fluid was partitioned by assuming that CO₂ only exists in the vapour phase, i.e. the liquid phase is pure water. The line corresponding to pure water is used as the reference, since for pure fluids mole- and mass-based vapour quality are equal.

Note. The Baumann rule is a purely empirical correlation, but does not captures the underlying processes, see Section Turbines. In this respect, it is unclear whether the Baumann rule holds for water-NCG mixtures, nevertheless, it is used in this work to capture the anticipated drying effect of NCG.

The exergetic loss, see Appendix C for derivations, across the turbine is calculated from the difference in exergy between the turbine inlet and outlet and the work done by the fluid on the turbine, see Equation 4.6. Similarly, the brute-force and functional efficiencies can be calculated as shown in Equations 4.7 and 4.8.

$$\Delta \dot{E}_{loss} = \dot{m} * (e_1 - e_2) - \dot{E}_W \quad (4.6)$$

$$\eta_{bf}^{II} = \frac{\dot{E}_W + \dot{m}_2 * e_2}{\dot{m}_1 * e_1} \quad (4.7)$$

$$\eta_{f_{unc}}^{II} = \frac{\dot{E}_W}{\dot{m} * (e_1 - e_2)} \quad (4.8)$$

Depending on the power plant configuration two different cost models are used, one binary ORCs and another for DSCs.

For ORC turbines, a cost correlation presented by Astolfi et al. [11] is used, Equation 4.9, which correlates the turbine cost $C_{turb,ORC}$ to the number of stages n_{stages} , Equation 4.10 and the size parameter SP , Equation 4.11 of the turbine, which are analogous to the turbine length and diameter respectively. The cost of the accompanying generator, $C_{gen,ORC}$, was taken from the same work, Equation 4.12.

$$C_{turb,ORC} = 1.23 \cdot 10^6 * \left(\frac{n_{stages}}{2} \right)^{0.5} \left(\frac{SP}{0.18} \right)^{1.1} \quad \text{€2013} \quad (4.9)$$

$$n_{stages} = \left\lceil \max \left(\frac{\Delta h_{isen}^{tot}}{\Delta h_{stage}^{max}}, \log_{V_{r,stage}^{max}} V_{r,isen}^{tot} \right) \right\rceil \quad (4.10)$$

$$SP = \frac{\sqrt{V_{isen}}}{\sqrt[4]{\frac{\Delta h_{isen}^{tot}}{n_{stages}}}} \quad (4.11)$$

$$C_{gen,ORC} = 0.2 \cdot 10^6 * \left(\frac{\dot{W}_{turb}^{elec}}{5 \cdot 10^6} \right)^{0.67} \quad \text{€2013} \quad (4.12)$$

For DSCs, the cost of the turbine and generator, $C_{turb+gen,DSC}$ is calculated from a correlation based on cost data from *THERMOFLEX v31* [100] for a steam turbine with wet expansion, see Equation 4.13.

$$C_{turb+gen,DSC} = a_0 * \exp \left(a_1 \ln^2 \frac{\dot{W}_{elec}}{1000} + a_2 \ln^2 \frac{\dot{W}_{elec}}{1000} + a_3 \right) * f_{mix} * f_{mat} \quad \text{€2021} \quad (4.13)$$

$$a_0 = 1000 \quad a_1 = -0.0408229 \quad a_2 = 1.303859 \quad a_3 = -0.158304$$

f_{mix} is a correction to account for the difference in volumetric flow rate of water-NCG mixtures compared to pure water for the same turbine power. The correction is based on the turbine size parameter SP (analogous to the turbine width), assuming that the specific enthalpy change and number of stages are constant, as well as near ideal gas behaviour of outlet vapour, Equation 4.14.

$$f_{mix} = \left(\frac{SP^{mix}}{SP^{H_2O}} \right) \Rightarrow \left(\frac{\dot{V}_{isen}^{H_2O+NCG}}{\dot{V}_{isen}^{H_2O}} \right)^{0.55} \Rightarrow \left(\frac{1}{1 - z_{NCG}} \right)^{0.55} \quad (4.14)$$

f_{mat} is a material correction factor to account for more expensive non-corrosive materials and more durable turbine internals (e.g. blades).

4.3.2. Heat Exchanger

The heat exchanger component allows two streams to exchange heat along a temperature gradient, see Figure 4.6. Besides the cost calculations, no assumptions of the heat exchanger dimensions are made, other than the two streams being contacted indirectly, i.e. separated by an impermeable barrier.

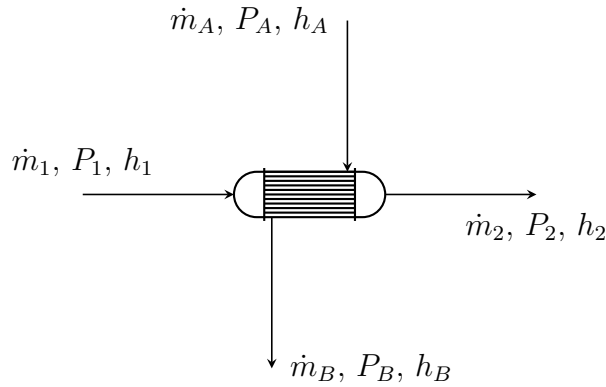


Figure 4.6: The process streams entering and exiting a heat exchanger

Assuming negligible changes in kinetic and potential energy for each stream, the heat exchanger duty can be calculated from Equation (4.15), provided four out of five variables (i.e. R -the ratio of mass rate $\frac{\dot{m}_{cold}}{\dot{m}_{hot}}$, $h_{hot,in}$, $h_{hot,out}$, $h_{cold,in}$, $h_{cold,out}$) are known.

$$\dot{m}_1 * (h_1 - h_2) = \dot{m}_A * (h_B - h_A) \quad (4.15)$$

It is also possible to determine the heat exchanger duty for cases where only three out of five variables are known by ensuring a pre-defined minimum approach temperature.

The minimum approach temperature is an important design parameter and, less the heat transfer area be infinite, must be strictly larger than zero (i.e. $T_{hot}(z) > T_{cold}(z)$). The choice of minimum approach temperature difference is ultimately a compromise between cost and performance - a larger minimum approach temperature difference reduces heat transfer area required but increases the exergetic losses in the heat exchanger.

The exergetic loss across the heat exchanger is calculated from the difference in exergy between the inlet and outlet streams, see Equation 4.16. Similarly, the brute-force and functional efficiencies can be calculated as shown in Equations 4.17, 4.18, and 4.19.

$$\Delta \dot{E}_{loss} = \dot{m}_1 * (e_1 - e_2) + \dot{m}_A * (e_A - e_B) \quad (4.16)$$

$$\eta_{bf}^{II} = \frac{\dot{m}_2 * e_2 + \dot{m}_B * e_B}{\dot{m}_1 * e_1 + \dot{m}_A * e_A} \quad (4.17)$$

$$\eta_{func,1}^{II} = \frac{\dot{m}_C * (e_4 - e_3)}{\dot{m} * (e_1 - e_2)} \quad (4.18)$$

$$\eta_{func,2}^{II} = \frac{\dot{m}_C * (e_4 - e_3)}{\dot{m} * e_1} \quad (4.19)$$

Depending on the type of heat exchanger different cost correlations are used.

The cost of recuperators, C_{rec} , is calculated from the UA of the recuperator, Equation 4.20 [11], with a correction factor for the fluid pressure, to account for the increased wall thickness required to contain the fluids, Equation 4.21.

$$C_{rec} = 2.60 \cdot 10^5 * \frac{UA}{6.5 \cdot 10^5}^{0.9} * 10^{f_P} \quad \text{€2013} \quad (4.20)$$

$$f_P = a_1 + a_2 \cdot \log_{10} \frac{P}{10^5} + a_3 \cdot \log_{10}^2 \frac{P}{10^5} \quad (4.21)$$

UA is determined by discretising the heat exchanger into $N + 1$ points, yielding N segments of equal duty Q^i , and the fluid temperature on the hot and cold side were calculated at each point – this allows the log-mean temperature, ΔT_{lm}^i , for each of the N intervals to be determined Equation 4.22, where ΔT_{in}^i and ΔT_{out}^i are the differences in temperature between the hot and cold side at the inlet and outlet of interval i respectively. Subsequently, the UA is calculated using Equation 4.23, where Q^i is the heat transferred in interval i .

Note. Where $\Delta T_{in}^i = \Delta T_{out}^i$, ΔT_{lm}^i is assumed to be ΔT_{in}^i .

$$\Delta T_{lm}^i = \frac{\Delta T_{in}^i - \Delta T_{out}^i}{\log \frac{\Delta T_{in}^i}{\Delta T_{out}^i}} \quad (4.22)$$

$$UA = \sum_{i=0}^N UA^i = \sum_{i=0}^N \frac{Q^i}{\Delta T_{lm}^i} \quad (4.23)$$

For all other heat exchangers the cost is estimated from the heat transfer area A . The cost of pre-heater, evaporators and superheaters $C_{Pre-H,eva,SH}$, is evaluated using Equation 4.24 [76]. The cost of air-cooled condensers C_{cond} is calculated from Equation 4.25 [68].

$$C_{preh,evap,sh} = 239 * A + 1.34 \cdot 10^4 \quad \$2002 \quad (4.24)$$

$$C_{cond} = 768 * A^{0.85} \quad \$2002 \quad (4.25)$$

To calculate the heat exchange area A , similarly to above, the heat exchanger was discretized into $N + 1$ points, yielding N segments of equal duty, and the temperature and vapor quality on the hot and cold side as well as the log-mean temperature difference, Equation 4.22 were calculated for each point. The vapor qualities, x_{in}^i and x_{out}^i at the inlet and outlet of interval i , were used to detect any phase changes as well as determine the dominant phase on the hot and cold side of the heat exchanger, see Equation 4.26, allowing the appropriate heat transfer coefficient, U^i , to be selected from Table 4.2 and Table 4.3. The heat transfer area is then calculated using Equation 4.27.

$$Fluid\ Type = \begin{cases} boiling & x_{out}^i - x_{in}^i > 0 \\ condensing & x_{out}^i - x_{in}^i < 0 \\ liquid & x_{in}^i \\ vapour & x_{in}^i \end{cases} \quad (4.26)$$

$$A = \sum_{i=0}^N A^i = \sum_{i=0}^N \frac{Q^i}{\Delta T_{lm}^i U^i} \quad (4.27)$$

Table 4.2: Estimated overall heat transfer coefficients U , $\text{W m}^{-2} \text{K}^{-1}$, in the PHE and recuperator for different combinations of fluids and states. The values were derived using values from Tables 3.2 and 3.3 and Equation 3.66. R_m was assumed to be zero; A_r was assumed to be 0.87 for liquid and condensing water as well as LP organic vapour, 1 for liquid or boiling organic fluid and 3.7 for HP water vapour or HP organic vapour; χ was assumed to be 1 for all fluids but condensing water, for which a value of 4 was used [8].

Hot Side		Cold Side		
		Organic		
		Liquid	Boiling	Vapor
Water	Liquid	1038	1038	1323
	Condensing	1193	1193	1584
	Vapor	936	936	1161
Organic	Vapour	99	-	-

Table 4.3: Estimated overall heat transfer coefficients U , $\text{W m}^{-2} \text{K}^{-1}$, in air-cooled condensers for different combinations of fluids and states. The values were derived using values from Tables 3.2 and 3.3 and Equation 3.66. R_m was assumed to be zero; A_r was assumed to be 0.87 for water and organic fluids and 14 for air; χ was assumed to be 4 for water and organic fluids and 1 for air [8].

Cold Side		Hot Side					
		Organic			Water		
		Liquid	Condensing	Vapor	Liquid	Condensing	Vapor
Air	Vapor	1048	1089	322	1355	1372	333

4.3.3. Pump & Compressor

The turbine component can be used to expand a stream from a high to a low pressure, thereby providing the rotational power to drive a generator and generate electrical power, see Figure 4.7.

The pump and compressor component can be used to compress a stream from a low to a high pressure. The performance calculations for pumps and compressors are identical, the only difference being the fluid phase they can handle - pumps are used for liquids, while compressors are used for gases. Two-phase compression is generally avoided as it can be damaging to the pump/compressor internals (e.g. bubbles causing cavitation or liquid droplets colliding with fast moving blades).

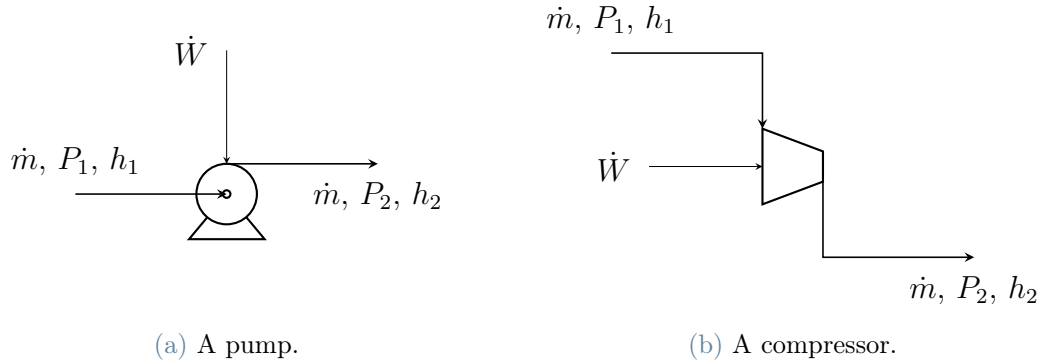


Figure 4.7: The process streams entering and exiting a pump and compressor

Considering a stream of mass rate \dot{m} , pressure P_1 and specific enthalpy h_1 , the work done by a pump/compressor in raising the pressure to P_2 , where $P_2 > P_1$, can be calculated as follows, see Equation (4.28).

Note. By convention the work done by the fluid is negative, while work done on the fluid is positive.

$$\dot{W}_{pump,comp} = \dot{m} * (h_2 - h_1) \quad (4.28)$$

The specific enthalpy at the outlet h_2 can be determined from the definition of the isentropic efficiency $\eta_{isen}^{pump,comp}$, see Equation (4.29), where $h_{2,isen}$ corresponds to the outlet specific enthalpy assuming an isentropic compression (i.e. specific entropy at the inlet and outlet are equal, $s_2 = s_1$). Combining Equations 4.28 and 4.29 yields an expression for the pump/compressor work, Equation 4.30. The electrical power can then be determined by assuming an efficiency of the motor, η_{motor} , see Equation 4.31. By default the isentropic efficiency of pumps, compressors and fans are assumed to be 75 %, 70 % and 60 % respectively and an efficiency of the motor of 95 %.

$$\eta_{isen}^{pump,comp} = \frac{h_{2,isen} - h_1}{h_2 - h_1} \quad (4.29)$$

$$\dot{W}_{pump,comp} = \dot{m} * \frac{h_{2,isen} - h_1}{\eta_{isen}^{pump,comp}} \quad (4.30)$$

$$\dot{W}_{pump,comp}^{elec} = \frac{\dot{W}_{pump,comp}}{\eta_{motor}} \quad (4.31)$$

The exergetic losses across the pump/compressor is calculated from the difference in

exergy between the inlet and outlet streams, see Equation 4.32. Similarly, the brute-force and functional efficiencies can be calculated as shown in Equation 4.33 and 4.34.

$$\Delta \dot{E}_{loss} = \dot{m} * (e_1 - e_2) + \dot{E}_W \quad (4.32)$$

$$\eta_{bf}^{II} = \frac{\dot{m}_2 * e_2}{\dot{m}_1 * e_1 + \dot{E}_W} \quad (4.33)$$

$$\eta_{func}^{II} = \frac{\dot{m} * (e_2 - e_1)}{\dot{E}_W} \quad (4.34)$$

The cost of pumps is calculated from the pump electrical power using Equations 4.35 [11]. The cost of fans is calculated from the fan electrical power using Equation 4.36 [91], where the total fan power is between 20 kW and 200 kW, outside these limits the specific cost is kept constant.

$$C_{pump} = 14000 * \left(\frac{\dot{W}}{200000} \right)^{0.67} \text{ €2013} \quad (4.35)$$

$$C_{fan} = 1.31 \cdot 10^4 * \left(\frac{\dot{W}_{elec}}{50000} \right)^{0.76} \text{ €2005} \quad (4.36)$$

4.3.4. Multi-Stage Compressor

Compressing gases through large compression ratios can result in excessive heating (i.e. $\frac{P_{out}}{P_{in}} \propto \frac{T_{out}}{T_{in}}$ from the ideal gas law). Compression work can be reduced by cooling the fluid, thus reducing its compressibility. This can be achieved by dividing the compression processes into multiple compression stages with cooling between each compression stage, see Figure 4.8.

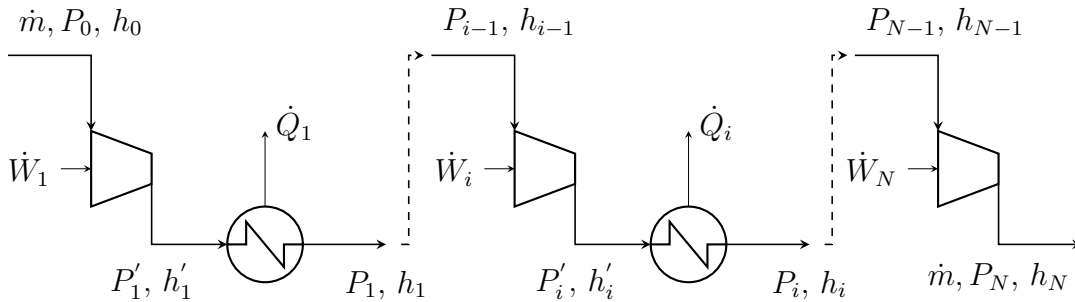


Figure 4.8: The process streams entering and exiting a stage of a multi-stage compressor

Considering a stream of mass rate \dot{m} , pressure P_1 and specific enthalpy h_1 , the compression is split into N stages of equal compression ratio. The work done by each compression stage is determined using Equation 4.37, assuming an isentropic efficiency of 70 %. The inter-stage cooling reduces the fluid temperature to a pre-defined temperature, by default 298 K (25 °C), the heat removed from the fluid is calculated via Equation 4.38.

The number of stages is determined iteratively to avoid outlet temperatures above 473 K (200 °C).

$$\dot{W}_i = \dot{m} * \frac{h'_{i,isen} - h_{i-1}}{\eta_{isen}^{comp}} \quad (4.37)$$

$$\dot{Q}_i = \dot{m} * (h'_i - h_i) \quad (4.38)$$

$$h_i = h(P'_i, T_{ambient}) \quad (4.39)$$

The exergetic losses across the multi-stage compressor is calculated from the difference in exergy between the inlet and outlet streams, the work done on the fluid and the heat removed from the fluid, see Equation 4.40. Similarly, the brute-force and functional efficiencies can be calculated as shown in Equation 4.41 and 4.42.

$$\Delta \dot{E}_{loss} = \dot{m} * (e_{in} - e_{out}) + \sum_{i=1}^N \dot{E}_{W_i} + \sum_{i=1}^{N-1} \left(1 - \frac{T_0}{T_i}\right) * Q_i \quad (4.40)$$

$$\eta_{bf}^{II} = \frac{\dot{m} * e_{out} + \sum_{i=1}^{N-1} \left(1 - \frac{T_0}{T_i}\right) * Q_i}{\dot{m} * e_{in} + \sum_{i=1}^N \dot{E}_{W_i}} \quad (4.41)$$

$$\eta_{func}^{II} = \frac{\dot{m} * (e_2 - e_1)}{\sum_{i=1}^N \dot{E}_{W_i}} \quad (4.42)$$

The cost of multi-stage compressors is calculated from the component's electrical power using Equations 4.43 [32].

$$C_{comp} = 6950 * \left(\frac{1.34 * \dot{W}_{elec}}{1000} \right)^{0.82} \quad \text{€2005} \quad (4.43)$$

4.3.5. Mixer and Joint

Mixers and joints can be used to combine various streams into a single outlet stream, see Figure 4.9. These do not have to represent explicit mixing units but can also be points in the system where two or more streams are joined.

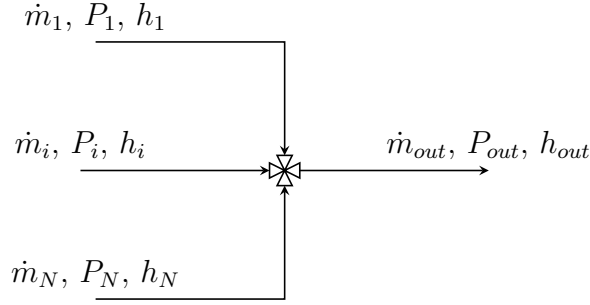


Figure 4.9: The process streams entering and exiting a mixer

To calculate the mixer performance, the combined mass and enthalpy rates of the inlet streams must be conserved, see Equations (4.44) and (4.45). The outlet pressure is assumed to be the minimum pressure of the mixed streams.

$$\dot{m}_{out} = \sum_{i=1}^N \dot{m}_i \quad (4.44)$$

$$h_{out} = \frac{\sum_{i=1}^N \dot{m}_i * h_i}{\sum_{i=1}^N \dot{m}_i} \quad (4.45)$$

The exergetic losses across the mixer are calculated from the difference in exergy between the inlet and outlet streams, see Equation 4.46. The brute-force is using Equation 4.47.

$$\Delta \dot{E}_{loss} = \sum_{i=1}^N \dot{m}_i * e_i - \dot{m}_{out} * e_{out} \quad (4.46)$$

$$\eta_{bf}^{II} = \frac{\dot{m}_{out} * e_{out}}{\sum_{i=1}^N \dot{m}_i * e_i} \quad (4.47)$$

As the mixers are mostly used for simply blending streams, their cost is assumed to be negligible when compared to the other power plant components.

4.3.6. Separator

Separators are used to split two-phase streams into their constituent phase streams. They have one inlet and two outlet streams, see Figure 4.10.

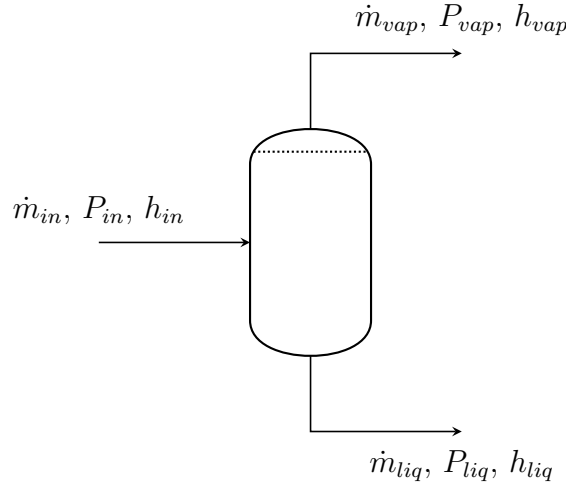


Figure 4.10: The process streams entering and exiting a separator

The performance calculations ensure that the inlet stream is equilibrated and that the combined mass and enthalpy flows at the inlet and outlet are equal, see Equation 4.48 and 4.49, although this is implicitly achieved as part of the equilibration and partitioning of the fluid.

$$\dot{m}_{in} = \dot{m}_{vap} + \dot{m}_{liq} \quad (4.48)$$

$$h_{in} = \frac{\dot{m}_{vap} * h_{vap} + \dot{m}_{liq} * h_{liq}}{\dot{m}_{vap} + \dot{m}_{liq}} \quad (4.49)$$

The exergetic losses across the mixer are calculated from the difference in exergy between the inlet and outlet streams, see Equation 4.50. The brute-force is using Equation 4.51.

$$\Delta \dot{E}_{loss} = \dot{m}_{in} * e_{in} - \dot{m}_{vap} * e_{vap} + \dot{m}_{liq} * e_{liq} \quad (4.50)$$

$$\eta_{bf}^{II} = \frac{\dot{m}_{vap} * e_{vap} + \dot{m}_{liq} * e_{liq}}{\dot{m}_{in} * e_{in}} \quad (4.51)$$

The cost of the separator is assumed to be negligible compared to the other power plant components.

4.4. Economic Model

The total plant costs are split into three categories, the primary equipment cost (i.e., the main components of the direct and binary cycle), the secondary equipment (i.e., minor components like mixers and separators as well as piping, wiring, control system), and construction. The primary equipment costs are evaluated from equipment specific cost correlations. The secondary equipment is assumed to be 40 % of the primary equipment cost, and construction costs are around 70 % of the total equipment cost[11].

The total plant construction cost is calculated using Equation 4.52, where the secondary equipment and construction costs are determined from Equation 4.53 and Equation 4.54, with $X_{sec}=40\%$ and $X_{constr}=70\%$.

$$C_{total} = C_{primary} + C_{secondary} + C_{construction} \quad (4.52)$$

$$C_{secondary} = X_{sec} * C_{primary} \quad (4.53)$$

$$C_{constr} = X_{constr} * (C_{primary} + C_{secondary}) \quad (4.54)$$

The primary equipment cost is calculated as the sum of the primary equipment in the reference year (assumed to be 2023 in this study) and currency (assumed to be USD), see Equation 4.55.

$$C_{primary} = \sum_{i=1}^N f_{PPI} * f_{currency} * C_i \quad (4.55)$$

As the individual cost correlations have been developed at different points in time and in currencies, the calculated cost must be corrected to the reference year and currency. By convention, the currency is converted to the reference currency in the year of publication of the correlation, Equation 4.56 and then corrected for inflation using the ratio of the Producer Price Index (PPI) of the corresponding equipment in the reference and publication year, Equation 4.57. The USD-EUR exchange rate and PPI values are shown in Figure 4.11 and 4.12.

$$f_{currency} = \frac{USD(year_{pub})}{EUR(year_{pub})} \quad (4.56)$$

$$f_{PPI} = \frac{PPI(year_{ref})}{PPI(year_{pub})} \quad (4.57)$$

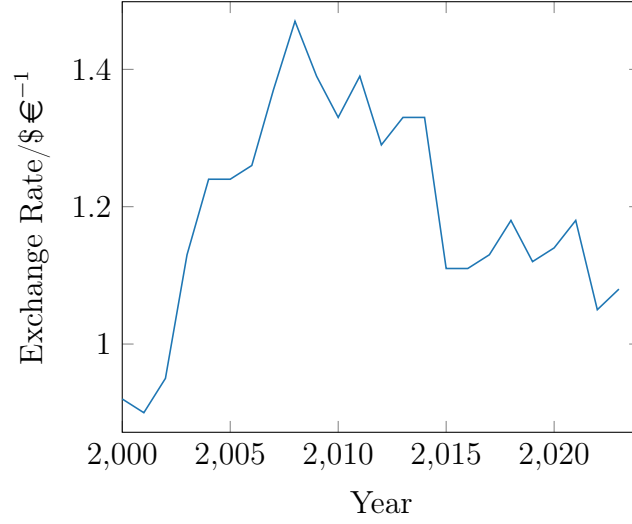


Figure 4.11: USD-EUR exchanger rate between 2002 and 2023 [59]

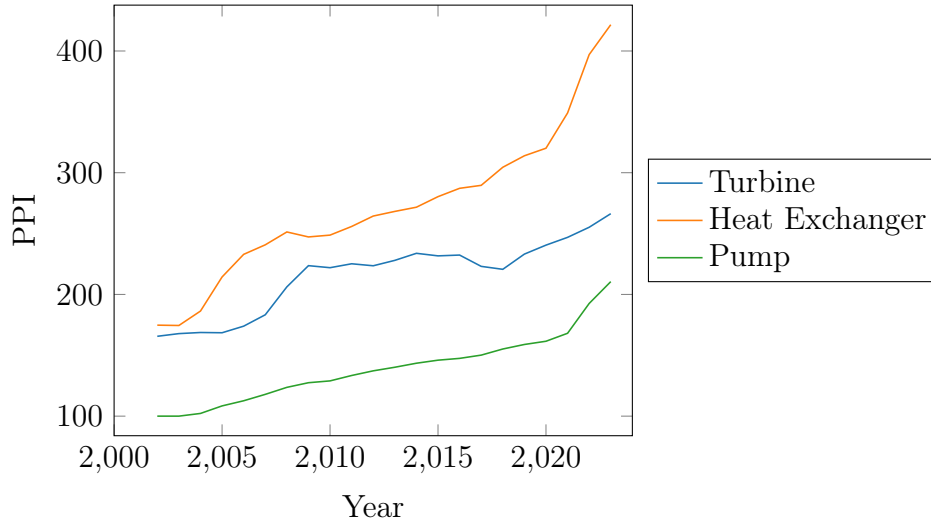


Figure 4.12: PPI for turbines (WPU1197), heat exchangers (WPU1075) and pumps/compressors (PCU33391-33391) between 2002 and 2023 [72]

The net present value (NPV) can then be calculated using Equation 4.58, where C_{rev_i} and C_{op_i} are the revenue and operating costs, calculated using Equations 4.59 and 4.60, in year i . f_{tax} is the tax rate, by default set at 20%, $f_{disc\ rate}$ is the discount rate, by default set at 0.1, f_{price} is the electricity price, by default set at 0.4 \$/kWh⁻¹, and f_{inf} is the year on year rate of inflation, assumed to be 3%. C_{op_0} is the operating cost in year zero, which assumed to be 5% of the total plant cost C_{total} .

$$NPV = -C_{total} + \sum_{i=1}^N * \frac{(1 - f_{tax}) * (C_{rev_i} - C_{op_i})}{(1 + f_{disc\ rate})^i} \quad (4.58)$$

$$C_{rev_i} = 8.76 * \dot{W}_{elec} \cdot f_{price} \quad (4.59)$$

$$C_{op_i} = C_{op_0} * (1 + f_{inf})^i \quad (4.60)$$

Additional economic performance metrics are also calculated. The levelised cost of electricity (LCOE) is obtained by iteratively determining the price of electricity f_{price} for which the NPV becomes zero. Similarly, the internal rate of return (IRR) is found by determining the discount rate $f_{disc\ rate}$ for which the NPV becomes zero.

4.5. Optimisation

The system performance can also be optimised. Here, a process metric (*Objective Function*) is maximised/minimised, by adjusting process variables (*Controls*), while ensuring that all process variables, parameters and metrics remain within their allowable range (*Constraints*). In principle, any *Objective Function*, *Control* and *Constraint* can be defined within *PowerCycle*.

The optimisation is performed using *pymoo* [21], an open-source framework for performing single and multi objective optimisation, and its Genetic Algorithm (GA). While Newton and gradient-based optimisation algorithms, generally have a higher rate of convergence, requiring fewer iterations, obtaining derivatives can be computationally expensive, and require the *Objective Function* to be calculable over the entire solution space, which may not be the case. GAs on the other hand only require individual evaluations of the *Objective Function*, allowing these to be parallelised, and non-calculable cases do not prevent the algorithm from proceeding.

4.6. Validation

The following section provides a description of the validation of the various component models against their respective counterparts in *Aspen Plus v11*. Validations for additional equipment is included in Appendix E.

4.6.1. Fluid Properties

The thermophysical properties calculations were validated by calculating relevant thermophysical properties (i.e. enthalpy, entropy and density) for a range of temperatures and pressures for several fluids. In *Aspen Plus v11* this was achieved using an inlet stream, initialised to 298 K and 101 325 Pa, and a heater element to heat the fluid to the desired temperature and pressure, Figure 4.13. *REFPROP* was used as the property model for all fluids. A corresponding calculation was configured in *PowerCycle*, see Listing 4.1.

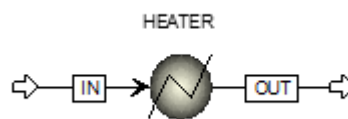


Figure 4.13: Process diagram of the *Aspen Plus v11* simulation used to calculate the enthalpy, entropy and density of different fluids

Listing 4.1 Configuration of a fluid properties calculation in *PowerCycle* for water at a given temperature T and pressure P

```

1  from FluidProperties.fluid import Fluid
2
3  fluid = Fluid(["water", 1])
4  fluid.update("PT", P, T)
5
6  props = fluid.properties
7  H, S, D = props.H, props.S, props.D

```

From Figure 4.14 it can be seen that the thermophysical properties calculated by *Aspen Plus* and *PowerCycle* are in close agreement, without any noticeable differences. Similar validation plots for n-butane and n-pentane, can be found in Power Cycle Validation.

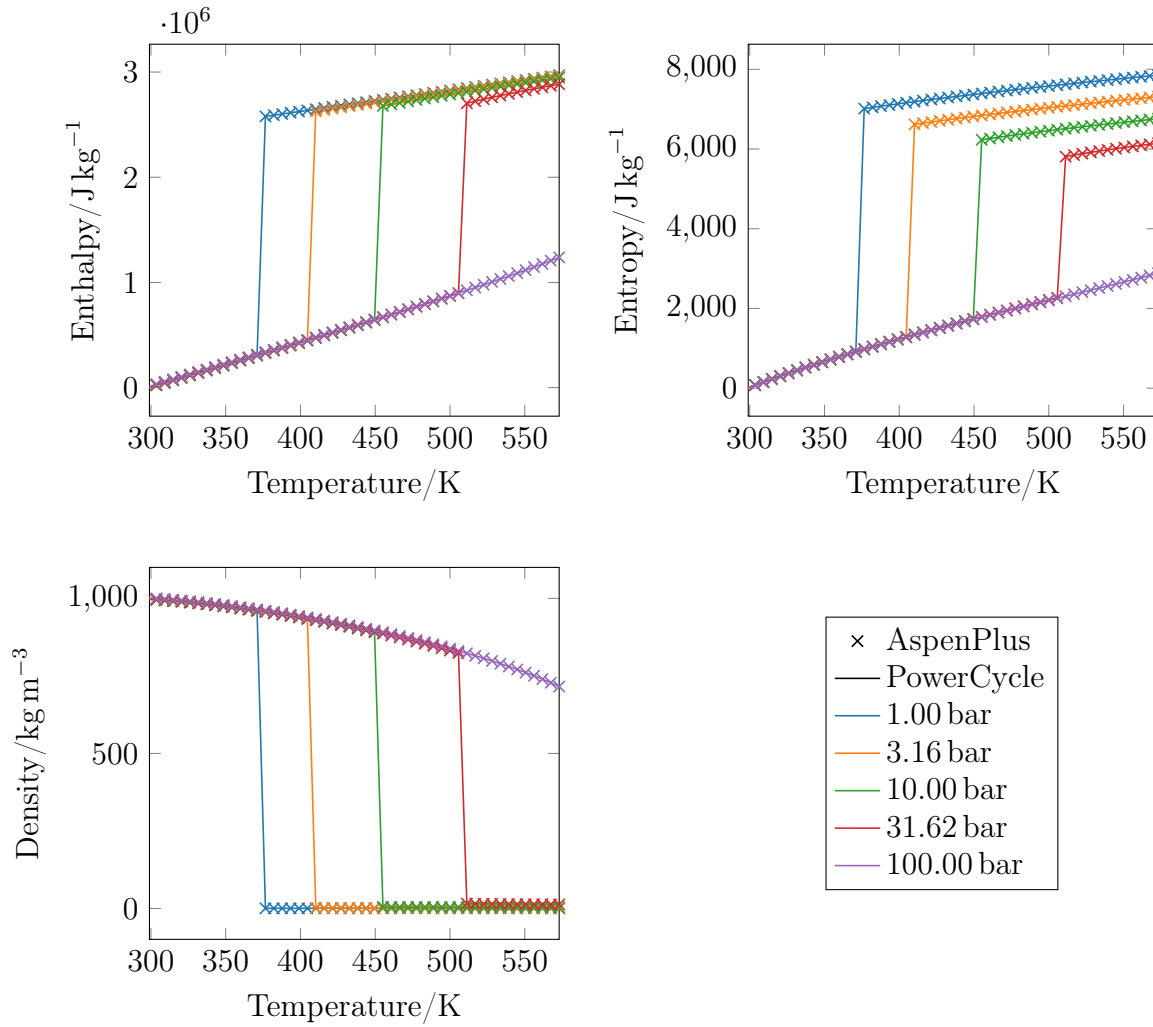


Figure 4.14: Comparison of the thermophysical properties of water calculated by *Aspen Plus* and *PowerCycle*. The enthalpy and entropy are reported relative to 298 K and 101 325 Pa

4.6.2. Turbine

A stream of saturated steam at a temperature of 473 K (200°C) was expanded in a turbine to a discharge pressure of 0.1 bar. The expansion process is assumed to be dry (i.e. wetness effects are negligible), with the isentropic efficiency of the turbine being 85 % and the efficiency of the generator being 95 % respectively, see Table 4.4.

Table 4.4: The boundary conditions for the turbine performance validation calculations for a dry expansion

Parameter	Units	Value
Fluid	-	Water
\dot{m}	kg s^{-1}	1
T_{in}	K	473
Q_{in}	kg kg^{-1}	1
P_{out}	bar	0.1

Models for each scenario were then formulated in *AspenPlus v11* and *PowerCycle*, Figure 4.15 and Listing 4.2 respectively.

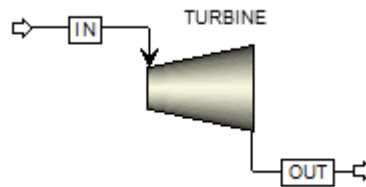


Figure 4.15: Process diagram of the *Aspen Plus v11* simulation used to calculate the performance of a turbine, assuming dry expansion

Listing 4.2 Configuration of a turbine performance calculation in *PowerCycle* for saturated steam at temperature T assuming dry expansion

```

1  import Simulator
2  from Simulator.streams import MaterialStream
3  from FluidProperties.fluid import Fluid
4
5  inlet = Fluid(["water", 1])
6  inlet = MaterialStream(inlet, m=1)
7  inlet.update("TQ", Tin, Qin)
8
9  pump = Simulator.turbine(0.85, mech_eff=0.95)
10 pump.set_inputs(inlet, Pout)
11 outlet = pump.calc()

```

The calculation results are in close agreement, with negligible differences, see Table 4.5. A similar validation was also performed for a wet expansion process, however as this

is not captured by the native functionality in *Aspen Plus v11*, this has been moved to Appendix E.

Table 4.5: The turbine performance calculation results for *Aspen Plus v11* and *PowerCycle* for a dry expansion process

Parameter	Units	Aspen Plus v11	Power Cycle	Difference/%
T_{out}	K	318.96	318.96	0.00
\dot{W}	kW	-642.88	-642.88	-0.00
\dot{W}_{elec}	kW	-610.73	-610.73	-0.00

4.6.3. Heat Exchanger

For validating the heat exchanger calculations, two calculation modes were considered: 1) fixed mass rate ratio of the hot and cold streams, known inlet conditions of the hot stream and known inlet and outlet conditions of the cold stream - here the outlet conditions of hot stream and the minimum temperature approach are to be determined; and 2) known inlet conditions of the hot stream, known inlet and outlet conditions of the cold stream, and fixed minimum temperature approach - here the outlet conditions of the hot stream and the mass rate ratio of the hot and cold stream are to be determined.

Fixed Mass Rate Ratio

The hot inlet stream, water, was initialised to a temperature of 453 K (180 °C) and vapour quality of 5 %, the cold inlet stream, n-Butane, was initialised to a temperature of 298 K and is assumed to be super-heated by 10 K at the outlet. The validation was repeated for three different pressures of the cold stream, 20 bar, 32 bar, and 45 bar, Table 4.6.

Corresponding models were formulated in *Aspen Plus v11* and *PowerCycle*, see Figure 4.16 and Listing 4.3.

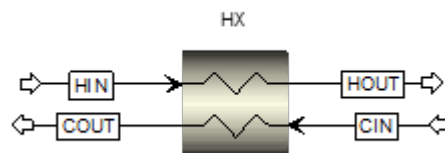


Figure 4.16: Process diagram of the *Aspen Plus* simulation used to calculate the performance of a heat exchanger for a fixed mass rate ratio, and hot inlet, cold inlet and cold outlet stream conditions

Table 4.6: The boundary conditions for the heat exchanger performance calculation validation for scenario 1

Parameter	Units	Value
Hot Fluid	-	Water
\dot{m}^{hot}	kg s ⁻¹	1
T_{in}^{hot}	K	453
Q_{in}^{hot}	%	0.05
Cold Fluid	-	n-Butane
\dot{m}^{cold}	kg s ⁻¹	1
T_{in}^{cold}	K	298
T_{out}^{cold}	K	397.5
P^{cold}	bar	20, 30, 45

Listing 4.3 Configuration of a heat exchanger performance calculation in *PowerCycle* for a fixed mass rate ratio, and hot inlet, cold inlet and cold outlet stream conditions

```

1  import Simulator
2  from Simulator.streams import MaterialStream
3  from FluidProperties.fluid import Fluid
4
5  hot_in = Fluid(["water", 1])
6  hot_in = MaterialStream(hot, m=1)
7  hot_in.update("TQ", Tin_H, Qin_H)
8
9  cold_in = Fluid(["butane", 1])
10 cold_in = MaterialStream(cold_in, m=1)
11 cold_in = cold_in.update("PT", Pin_C, T_in_C)
12
13 cold_out = cold_in.copy()
14 cold_out.update("PQ", Pin_C, 1)
15 Tsat_C = cold_out.properties.T
16 cold_out.update("PT", Pin_C, Tsat_C + 10)
17
18 HX = Simulator.heat_exchanger(deltaP_hot=0, deltaP_cold=0)
19 HX.set_inputs(Inlet_hot=hot_in, Inlet_cold=cold_in, Outlet_cold=cold_out)
20 hot_out, cold_out = HX.calc()

```

For the cases where the pressure of the cold fluid is 20 bar and 45 bar, *PowerCycle* and *Aspen Plus v11* are in close agreement, Figure 4.17. Minor discrepancies are observed

near the bubble and dew-points, because unlike *Aspen Plus v11* *PowerCycle* does not add an additional point at saturation. Nevertheless, with sufficient discretisation, differences can be minimised.

For the case where the pressure of the cold fluid is 32 bar, near the critical pressure of n-Butane, some differences are observed, Figure 4.17:

- The phase transition occurs at a higher temperature compared to *Power Cycle*
- There is a discontinuity in the TQ profile (at 45 kW)

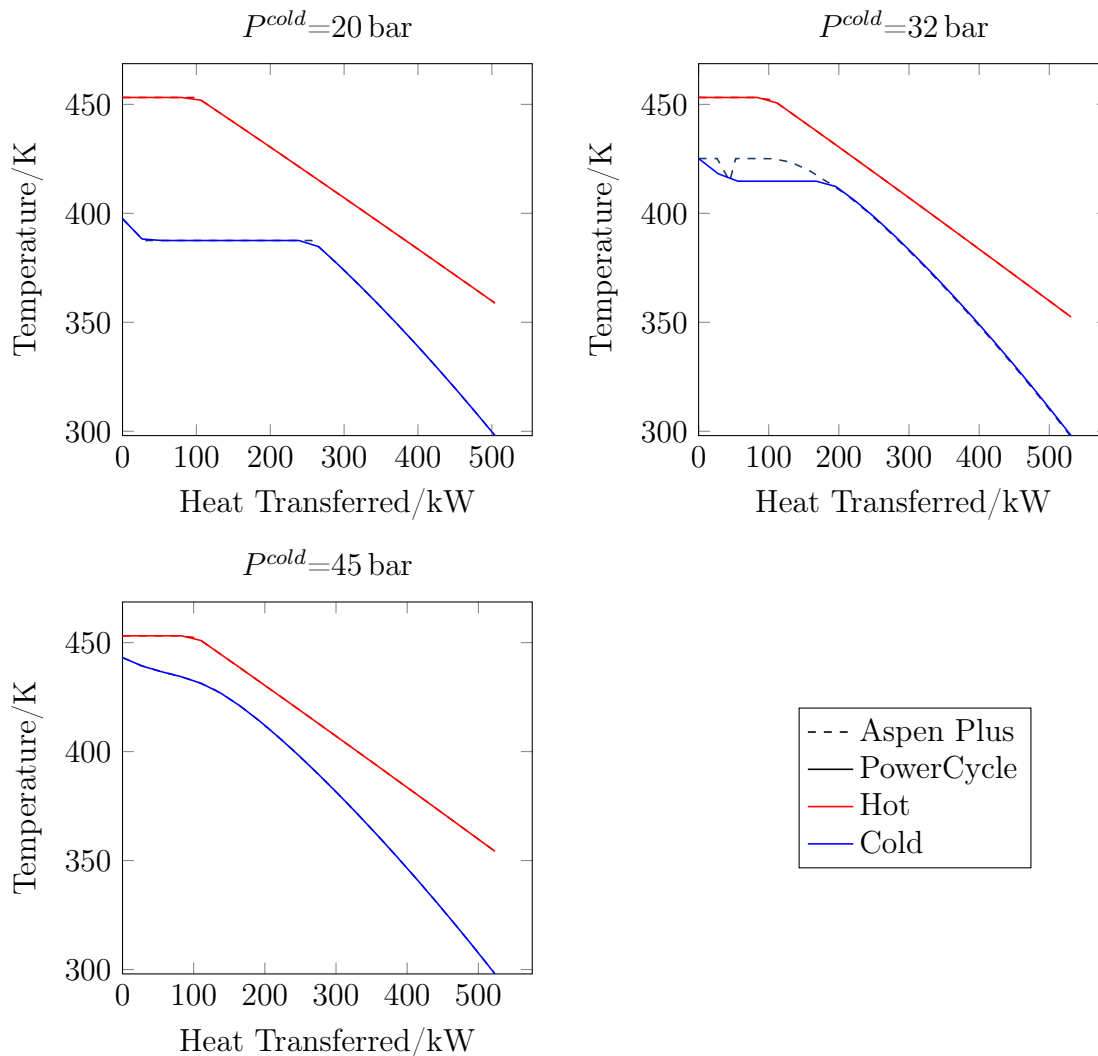
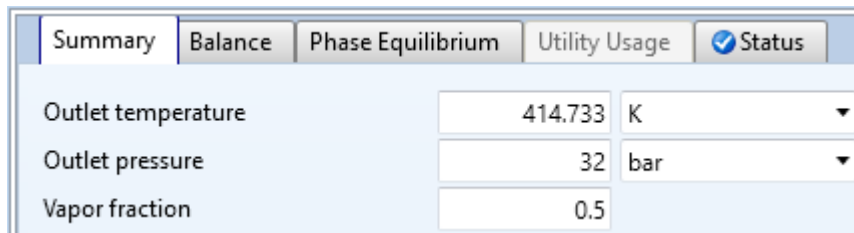


Figure 4.17: Comparison of the temperature duty profiles calculated in *Aspen Plus* and *PowerCycle* for scenario 1.

The apparent saturation temperature of 425 K (compared to about 415 K calculated by *PowerCycle*) is inconsistent with the validation of the fluid properties performed in Section 4.6.1 (also see AppendixE). Recalculating the saturation temperature of n-Butane at

a pressure of 32 bar using a heater element, it can be seen to be consistent with *PowerCycle*, Figure 4.18.

Moreover, the *Aspen Plus* results are also inconsistent with the boundary conditions imposed, as the cold fluid at the outlet of the heat exchanger is not super-heated by 10 K. That being said, no convergence issues, calculation warnings or errors were raised for this calculation in *Aspen Plus*, and as such the cause of the observed behaviour remains unclear.



Summary	Balance	Phase Equilibrium	Utility Usage	Status
Outlet temperature	414.733	K		
Outlet pressure	32	bar		
Vapor fraction	0.5			

Figure 4.18: The saturation temperature of n-butane at 32 bar in *Aspen Plus* using a Heater element

Despite the above, the calculated hot stream outlet temperature and the minimum temperature difference between the hot and cold stream are in good agreement, Table 4.7.

Table 4.7: The heat exchanger performance calculation results for *Aspen Plus v11* and *PowerCycle* for scenario 1

Parameter	Units	Aspen Plus v11	Power Cycle	Difference/%
P_{cold}	bar	20		-
T_{out}^{hot}	K	358.89	358.80	0.03
DT_{min}	K	29.86	30.48	-2.06
P_{cold}	bar	32		-
T_{out}^{hot}	K	352.84	352.41	0.12
DT_{min}	K	19.41	19.11	1.54
P_{cold}	bar	45		-
T_{out}^{hot}	K	354.33	354.24	0.03
DT_{min}	K	10.0	10.0	0.00

Fixed Minimum Approach Temperature Difference

The hot inlet stream, water, was initialised to a temperature of 453 K (180 °C), the cold inlet stream, n-butane, was initialised to a temperature of 298 K, a pressure of 20 bar

at the outlet the cold stream is to be super-heated by 10 K, corresponding to an outlet temperature of 397.5 K. Three vapour qualities were considered: 0 %, 5 % and 15 %, see Table 4.8.

Table 4.8: The boundary conditions for the heat exchanger performance calculation validation for scenario 2

Parameter	Units	Value
Hot Fluid	-	Water
\dot{m}^{hot}	kg s^{-1}	1
T_{in}^{hot}	K	453
Q_{in}^{hot}	%	0, 5, 15
Cold Fluid	-	n-Butane
P^{cold}	bar	20
T_{in}^{cold}	K	298
T_{out}^{cold}	K	397.5

Corresponding models were formulated, in *Aspen Plus v11* this was achieved using a *Design Spec* to iterate on the mass rate of the cold stream to achieve the desired minimum approach temperature, in this case 5 K, Figure 4.19. The corresponding *PowerCycle* model can be seen in Listing 4.4.

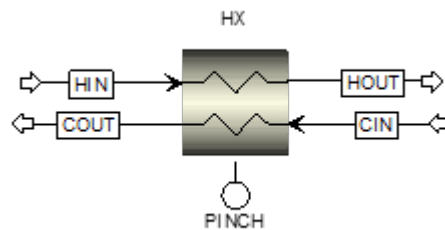


Figure 4.19: Process flow diagram of the *Aspen Plus v11* simulation used to calculate the performance of a heat exchanger

The calculated hot stream outlet temperatures and mass rate ratios can be seen to be in close agreement, Table 4.9. The location of the minimum temperature approach within the heat exchanger (by cumulative heat transferred) correlate well, Figure 4.20, and the observed differences can explained by differences in the discretisation of the heat exchanger when calculating the approach temperature differences.

Listing 4.4 Configuration of a heat exchanger performance calculation in *PowerCycle* for a fixed mass rate ratio, and hot inlet, cold inlet and cold outlet stream conditions

```

1  import Simulator
2  from Simulator.streams import MaterialStream
3  from FluidProperties.fluid import Fluid
4
5  hot_in = Fluid(["water", 1])
6  hot_in = MaterialStream(hot, m=1)
7  hot_in.update("TQ", Tin_H, Qin_H)
8
9  cold_in = Fluid(["butane", 1])
10 cold_in = MaterialStream(cold_in, m=1)
11 cold_in = cold_in.update("PT", Pin_C, T_in_C)
12
13 cold_out = cold_in.copy()
14 cold_out.update("PQ", Pin_C, 1)
15 Tsat_C = cold_out.properties.T
16 cold_out.update("PT", Pin_C, Tsat_C + 10)
17
18 HX = Simulator.heat_exchanger(deltaP_hot=0, deltaP_cold=0)
19 HX.set_inputs(MassRatio=-1, Inlet_hot=hot_in, Inlet_cold=cold_in, Outlet_cold=cold_out)
20 hot_out, cold_out = HX.calc()

```

Table 4.9: The heat exchanger performance calculation results for *Aspen Plus v11* and *PowerCycle* for scenario 2

Parameter	Units	Aspen Plus v11	Power Cycle	Difference/%
Q_{in}^{hot}	%	0		-
T_{out}^{hot}	K	332.37	331.16	0.36
R	kg kg ⁻¹	1.021	1.030	-0.90
Q_{in}^{hot}	%	5		-
T_{out}^{hot}	K	310.79	310.64	0.05
R	kg kg ⁻¹	1.400	1.400	-0.01
Q_{in}^{hot}	%	15		-
T_{out}^{hot}	K	303.15	302.96	0.06
R	kg kg ⁻¹	1.863	1.863	-0.01

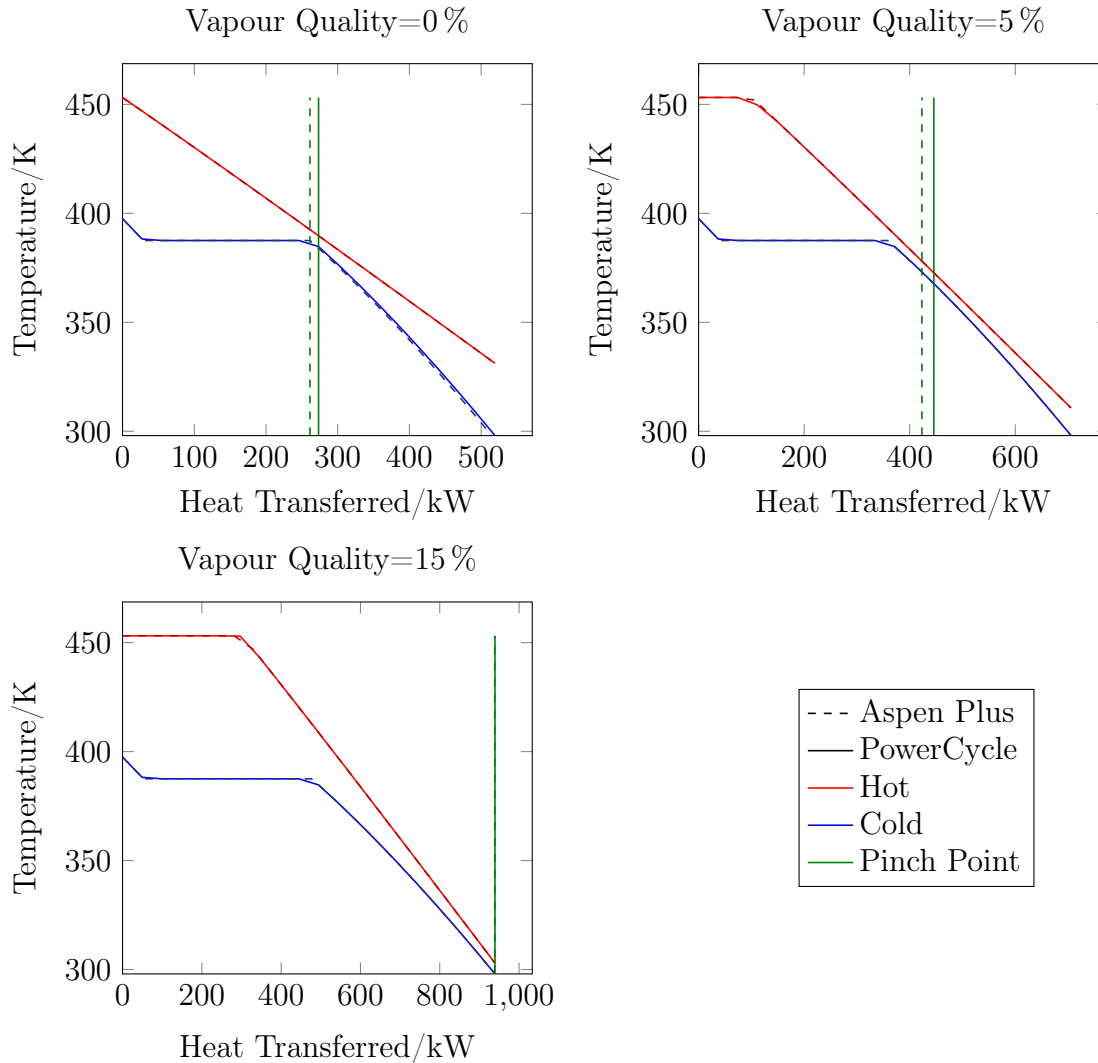


Figure 4.20: Comparing the heat exchanger performance calculations between PowerCycle and Aspen Plus v11

4.6.4. Direct Steam Cycle

The geofluid stream, water, was initialised to a temperature of 453 K (180°C) and a vapour quality of 10 %, and is assumed to be expanded to 0.1 bar in a dry expansion process. The coolant, water, was initialised to a temperature of 298 K and a pressure of 1.0325 bar. Following expansion and condensation, the condensate is re-pressurised to the inlet pressure and then returned to the reservoir. The inputs are summarised in Table 4.10.

Table 4.10: The boundary conditions for the direct steam cycle performance calculation validation

Parameter	Units	Value
Geofluid	-	Water
\dot{m}^{geo}	kg s^{-1}	1
T_{in}^{geo}	K	473
Q_{in}^{geo}	kg kg^{-1}	1
P_{cond}^{geo}	bar	0.1
Coolant	-	Water
\dot{m}^{cool}	kg s^{-1}	100
P_{in}^{cool}	bar	1.013 25
T_{in}^{cool}	K	298

Corresponding models were formulated in *Aspen Plus v11* and *PowerCycle*, Figure 4.21 and Listing 4.5. The performance calculation results were found to be in good agreement, Table 4.11.

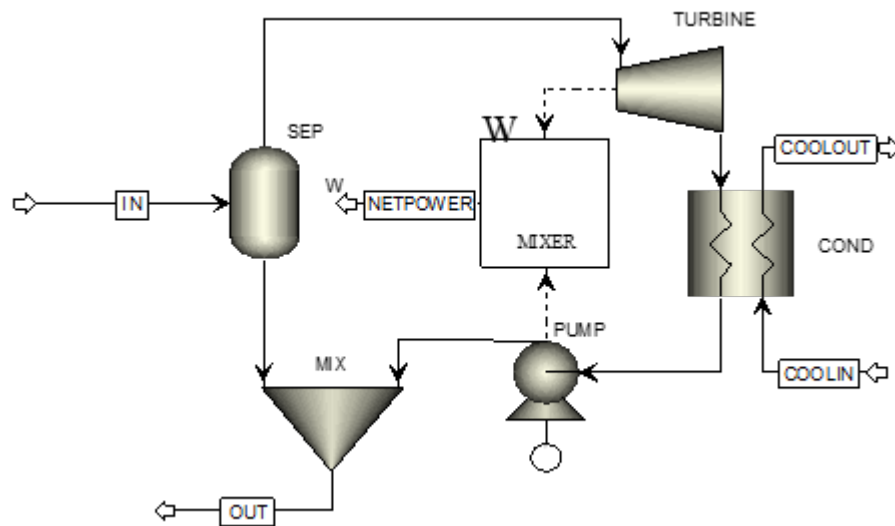


Figure 4.21: Process diagram of the *Aspen Plus* simulation used to calculate the performance of a direct steam cycle

Listing 4.5 Configuration of a direct steam cycle performance calculation in *PowerCycle*

```

1  from FluidProperties.fluid import Fluid
2  import Simulator
3  from Simulator.streams import MaterialStream
4
5  geo_in = Fluid(["water", 1])
6  geo_in = MaterialStream(geo_in, m=m_geo)
7  geo_in.update("TQ", T_geo_in, Q_geo_in)
8
9  cool_in = Fluid(["water", 1])
10 cool_in = MaterialStream(cool_in, m=m_cool)
11 cool_in.update("PT", P_cool_in, T_cool_in)
12
13 sep = Simulator.separator()
14 sep.set_inputs(geo_in)
15 liq, vap = sep.calc()
16
17 turbine = Simulator.turbine(0.85, mech_eff=0.95)
18 turbine.set_inputs(vap, P_cond)
19 vap = turbine.calc()
20
21 condensate_ = vap.copy()
22 condensate_.update("PT", P_cond, T_cond)
23
24 cond = Simulator.heat_exchanger(deltaP_hot=0, deltaP_cold=0)
25 cond.set_inputs(Inlet_hot=vap, Inlet_cold=cool_in, Outlet_hot=condensate_)
26 condensate, cool_out = cond.calc()
27
28 pump = Simulator.pump(0.85, mech_eff=0.95)
29 pump.set_inputs(condensate, geo_in.properties.P)
30 condensate = pump.calc()
31
32 mixer = Simulator.mixer()
33 mixer.set_inputs(liq, condensate)
34 geo_out = mixer.calc()
35
36 net_work = turbine.work + pump.work
37 net_power_elec = turbine.power_elec + pump.power_elec

```

Table 4.11: The single flash DSC performance calculation results for *Aspen Plus v11* and *PowerCycle*

Parameter	Units	Aspen Plus v11	Power Cycle	Difference/%
\dot{W}	kW	-128.21	-128.21	-0.00
\dot{W}_{elec}	kW	121.76	-121.76	-0.00
DT_{min}^{cond}	K	5.15	5.15	0.00

4.6.5. Binary ORC

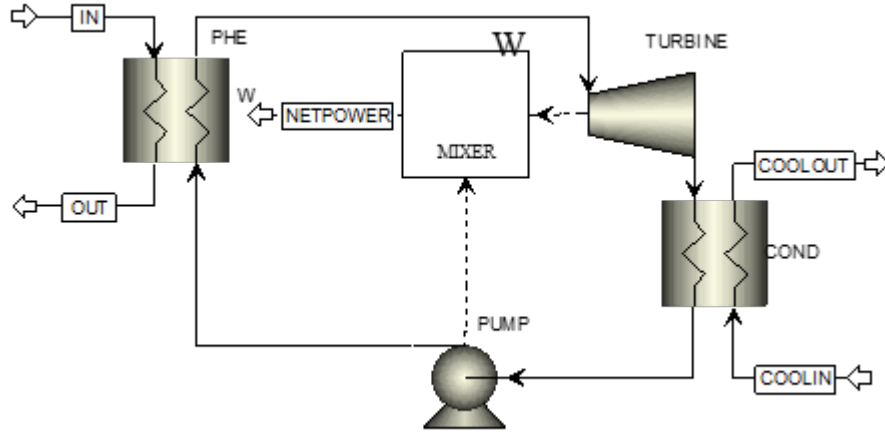
The geofluid stream, water, was initialised to a temperature of 473 K (180 °C) and a vapour quality of 0 %. The working fluid, n-Butane, is to be evaporated at a pressure of 20 bar and condensed at a pressure of 3 bar. The coolant, water, was initialised to a temperature of 298 K and a pressure of 1.0325 bar. The boundary conditions are summarised in Table 4.12.

Table 4.12: The boundary conditions for the direct steam cycle performance calculation validation

Parameter	Units	Value
Geofluid	-	Water
\dot{m}^{geo}	kg s ⁻¹	1
T_{in}^{geo}	K	473
Q_{in}^{geo}	kg kg ⁻¹	0
Coolant	-	Water
\dot{m}^{cool}	kg s ⁻¹	100
P_{in}^{cool}	bar	1.013 25
T_{in}^{cool}	K	298
Working Fluid	-	n-Butane
\dot{m}^{wf}	kg s ⁻¹	1
P_{evap}^{wf}	bar	20
Q_{evap}^{wf}	kg kg ⁻¹	1
P_{cond}^{wf}	bar	3
Q_{cond}^{wf}	kg kg ⁻¹	0

Corresponding models were formulated in *Aspen Plus v11* and *PowerCycle*, Figure 4.22 and Listing 4.6. The performance calculation results were found to be in good agreement,

Table 4.13.

Figure 4.22: Process diagram of the *Aspen Plus* simulation used to calculate the performance of a binary ORCTable 4.13: The binary ORC performance calculation results for *Aspen Plus v11* and *PowerCycle*

Parameter	Units	Aspen Plus v11	Power Cycle	Difference/%
\dot{W}	kW	-63.19	-63.19	-0.01
\dot{W}_{elec}	kW	-59.66	-59.67	-0.015
DT_{min}^{PHE}	K	13.60	13.01	4.31
DT_{min}^{cond}	K	6.07	6.22	-2.55

Listing 4.6 Configuration of a binary ORC performance calculation in *PowerCycle*

```

1  from FluidProperties.fluid import Fluid
2  import Simulator
3  from Simulator.streams import MaterialStream
4
5  geo_in = Fluid(["water", 1])
6  geo_in = MaterialStream(geo_in, m=m_geo)
7  geo_in.update("TQ", T_geo_in, Q_geo_in)
8
9  cool_in = Fluid(["water", 1])
10 cool_in = MaterialStream(cool_in, m=m_cool)
11 cool_in.update("PT", P_cool_in, T_cool_in)
12
13 wf = Fluid(["butane", 1])
14 wf = MaterialStream(wf, m=m_wf)
15
16 wf_pump_in = wf.copy()
17 wf_pump_in.update("PQ", P_cond, Q_cond)
18
19 pump = Simulator.pump(0.85, mech_eff=0.95)
20 pump.set_inputs(wf_pump_in, P_evap)
21 wf_PHE_in = pump.calc()
22
23 wf_turb_in_ = wf.copy()
24 wf_turb_in_.update("PQ", P_evap, Q_evap)
25
26 PHE = Simulator.heat_exchanger(deltaP_hot=0, deltaP_cold=0, N_discretisation=25)
27 PHE.set_inputs(Inlet_hot=geo_in, Inlet_cold=wf_PHE_in, Outlet_cold=wf_turb_in_)
28 geo_out, wf_turb_in = PHE.calc()
29
30 turbine = Simulator.turbine(0.85, mech_eff=0.95)
31 turbine.set_inputs(wf_turb_in, P_cond)
32 wf_cond_in = turbine.calc()
33
34 cond = Simulator.heat_exchanger(deltaP_hot=0, deltaP_cold=0)
35 cond.set_inputs(Inlet_hot=wf_cond_in, Inlet_cold=cool_in, Outlet_hot=wf_pump_in)
36 wf_pump_in_, cool_out = cond.calc()
37
38 net_work = turbine.work + pump.work
39 net_power_elec = turbine.power_elec + pump.power_elec

```

5 | Power Plant Simulations

5.1. Commercial Software

5.1.1. Objectives

Refine the application range of DSCs with flash and binary ORC geothermal power plants for two-phase sources, which are currently predominantly exploited via DSCs.

5.1.2. Geothermal Sources

Primarily two-phase geothermal sources were considered, with wellhead temperatures ranging between 100 °C and 200 °C and vapour quality ranging between 0 % to 50 %. In the context of this study the vapour quality is exclusively defined as the ratio of the mass of water in the vapour phase to the total mass of water, Equation 5.1. The brine salinity, defined in terms of NaCl and relative to the total mass of water, Equation 5.2, ranges between 0.0 kg kg⁻¹ to 0.3 kg kg⁻¹. The NCG content, defined in terms of CO₂ and relative to the total mass of water, Equation 5.3, ranges between 0.00 kg kg⁻¹ to 0.03 kg kg⁻¹. Heat losses between the wellhead and the plant inlet were assumed to be insignificant and therefore neglected.

$$x = \frac{\dot{m}_{H_2O}^V}{\dot{m}_{H_2O}^V + \dot{m}_{H_2O}^L} \quad (5.1)$$

$$s_{NaCl} = \frac{\dot{m}_{NaCl}}{\dot{m}_{H_2O}^V + \dot{m}_{H_2O}^L} \quad (5.2)$$

$$s_{NCG} = \frac{\dot{m}_{NCG}}{\dot{m}_{H_2O}^V + \dot{m}_{H_2O}^L} \quad (5.3)$$

While a unit geofluid mass rate could be considered for the power plant simulations, this has the undesirable effect of artificially reducing the power plants' performance as the effective inlet heat rate is lower due to the lower specific heat capacities of salinity and

NCG compared to water. Instead, the combined mass rate of liquid water and steam is assumed to be 1 kg s^{-1} (i.e. $\dot{m}_{H_2O}^V + \dot{m}_{H_2O}^L = 1 \text{ kg s}^{-1}$) for the following calculations, to which the mass rates of salinity and NCG are added, see Equation 5.4.

$$\dot{m} = \dot{m}_{H_2O}^V + \dot{m}_{H_2O}^L + \dot{m}_{NaCl} + \dot{m}_{NCG} \quad (5.4)$$

5.1.3. Power Plant Configurations

Two power plant configurations are considered, 1) a direct single flash steam cycle and 2) a binary ORC. In a DSC only the vapour portion of the geofluid is utilised and subsequently expanded in a turbine, see Figure 5.1. On the other hand, in a binary ORC the geofluid merely serves as a heat source to vaporise a secondary fluid, which is then expanded in a turbine similarly to the DSC, see Figure 5.3. This allows exploiting the heat contained within both the vapour as well as the liquid phase.

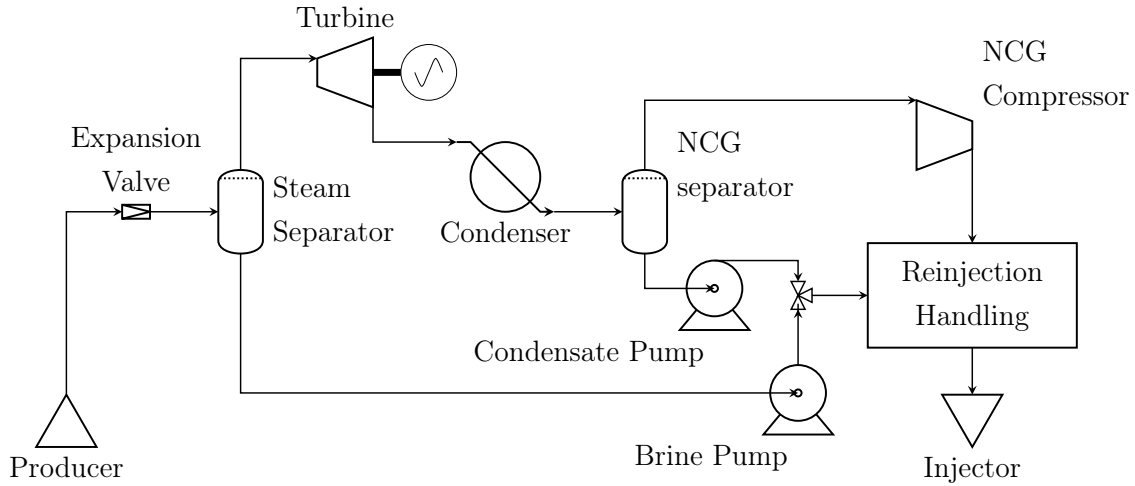


Figure 5.1: DSC geothermal power plant.

Both power plants are subject to the same boundary conditions:

- Geofluid composition, inlet temperature, pressure and steam quality
- Heat is rejected into the surrounding environment at a temperature of 25°C
- Geofluid enters and exits the power plant at the same pressure – this is to penalise for NCG handling to ensure that it is not released into the atmosphere but instead re-injected into the formation.
- Geofluid re-injection temperature is not constraint, as scaling is assumed to be negligible.

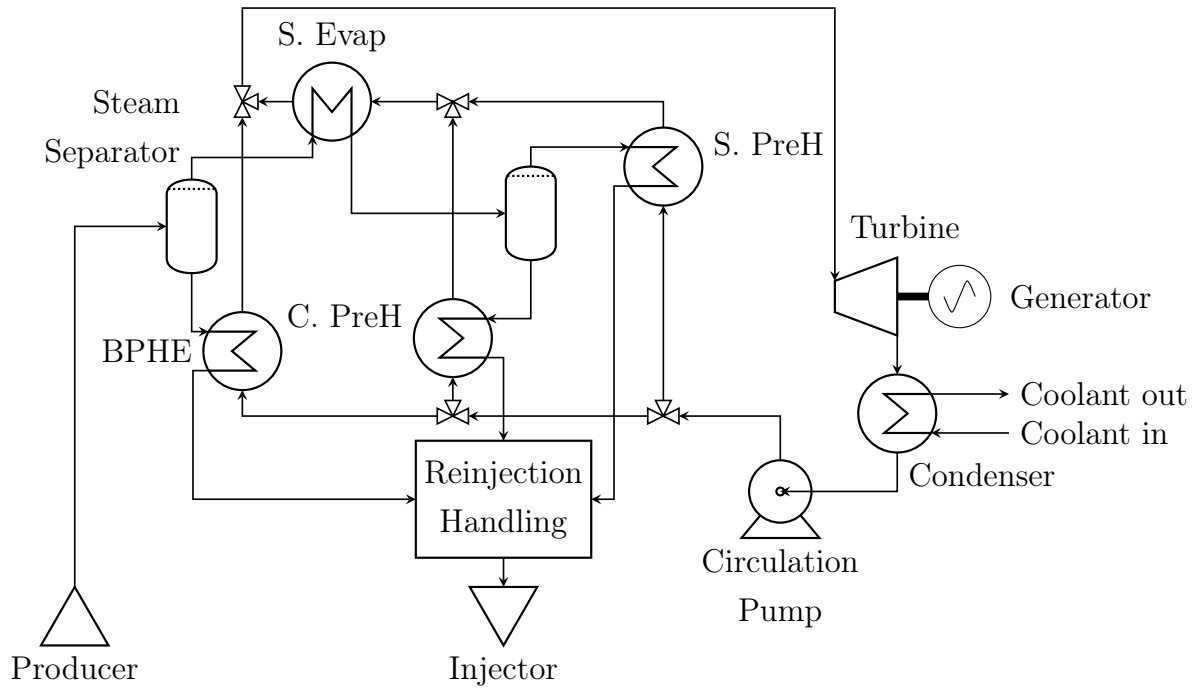


Figure 5.2: Binary ORC geothermal power plant.

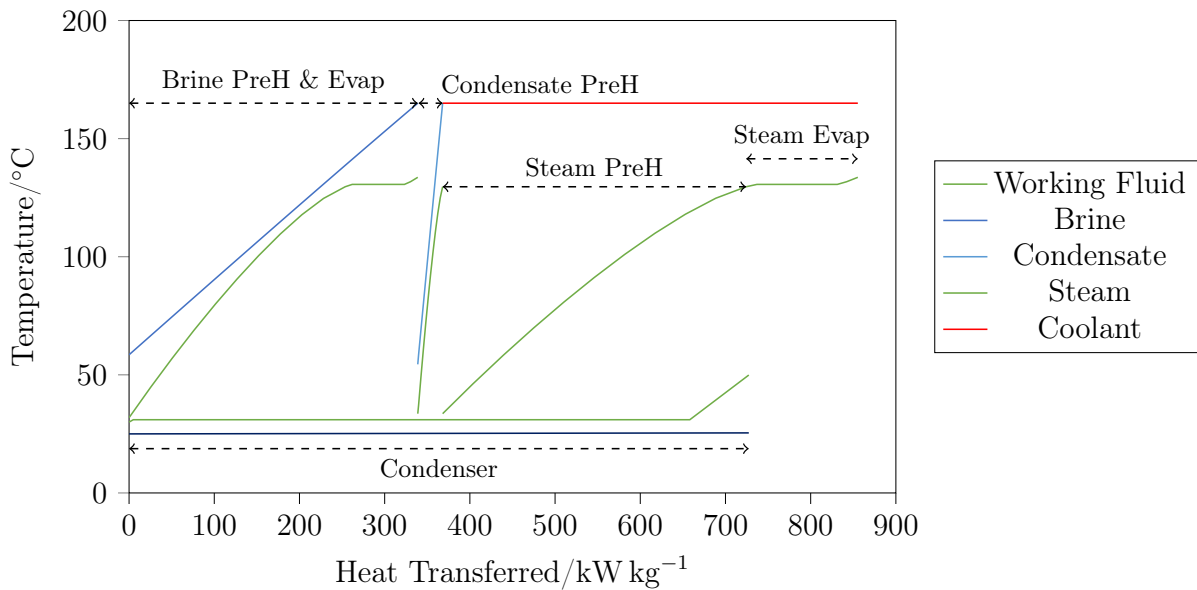


Figure 5.3: Temperature Heat Transferred diagram for the Binary ORC geothermal power plant shown in Figure 5.3. For an inlet temperature of 165 °C and a vapour quality of 25 %.

The specific net power output from the power plant, defined in Equation 5.5, will be used to judge which performs better for a set of boundary condition. This definition was chosen with the simulations of real geofluids, containing NCG and salinity, in mind because the

presence of impurities diminishes the heat flow into the power plant. As such, the mass rate of the main heat-carrying constituent of the real geofluid (i.e. water) was chosen as a reference.

$$\dot{w}_{net} = \frac{\dot{W}_{turb} - \dot{W}_{pump} + \dot{W}_{repr}}{\dot{m}_{H_2O}^V + \dot{m}_{H_2O}^L} \quad (5.5)$$

5.1.4. Model Description

For the DSC:

- The net power is optimised by adjusting the flash temperature/pressure, increasing the vapour mass rate while sacrificing specific enthalpy drop across the turbine; the pressure of the liquid fraction is consequently also decreased by the flash process.
- The stream exiting the turbine is then cooled to 30 °C, partially condensing the stream, before separating it into a liquid stream and a NCG stream. All outlet streams, i.e. the liquid stream from the flash chamber, the condensate stream and the NCG stream, must then be re-pressurised to the inlet pressure so that they can be re-injected into the reservoir.
- Given the bell-shaped vapour dome of water in the T-s (temperature-specific entropy) diagram, the turbine efficiency is corrected for liquid drop out using the empirical Baumann Rule, Equation 5.6, where η_{turb}^{wet} is the turbine wet efficiency, η_{turb}^{dry} is the turbine dry efficiency, assumed to be 85 % [30], and x_{in} and x_{out} are the mole-based vapour fraction at the turbine inlet and outlet respectively.

$$\eta_{turb}^{wet} = \eta_{turb}^{dry} * \left(\frac{x_{in} + x_{out}}{2} \right) \quad (5.6)$$

For the binary ORC:

- The incoming geofluid is split into a liquid and vapour stream with each stream being used to pre-heat and evaporate the cycle working fluid. The vapour stream is further split into a vapour and condensate following the vapour powered evaporator.
- The net power is optimised by adjusting evaporation and condensation temperature/pressure and the working fluid mass flow rates, while ensuring that the minimum approach temperatures do not fall below 5 °C in liquid dominated and 10 °C in vapour dominated heat exchangers. Moreover, the vapour quality at the vapour evaporator outlet should be above 75 % to avoid excessive conditions of simultane-

ous condensation on the hot-side and evaporation on the cold-side, which may be difficult to find a suitable heat exchanger design for¹.

- Iso-butane, n-butane, iso-pentane, n-pentane and cyclopentane were considered as ORC working fluids.

The simulations were run in *Aspen Plus V11*.

5.1.5. Case 1: Pure Water

To establish a base case, the two power plants were simulated in *Aspen Plus V11* for a geofluid modelled as pure water for inlet temperatures and steam quality ranging between 100 °C to 200 °C and 0 % to 50 % respectively. The results are shown in Figure 5.4. Figures 5.5 and 5.6 are constant vapour quality and constant temperature slices of Figure 5.4 showing all working fluids considered. The key observations are:

- The investigated ORC configurations thermodynamically outperform the DSCs at any temperature for saturated liquid sources. For inlet temperatures above 150 °C, the ORC configurations begin to outperform the DSCs at increasingly higher steam quality.
- All ORC working fluids perform similarly poorly at lower temperatures (up to 150 °C), which can likely be attributed to the critical temperatures of the selected working fluids being too high. Isobutane and n-butane appear to be the most favourable working fluids for the conditions studied.
- Cross-over of isobutane and n-butane in Figure 5.5 can be attributed to the vapour heated branch becoming vapour fraction constraint (i.e. the vapour quality in the vapour evaporator outlet reaches the limit of 75 %), limiting the amount of working fluid that can be evaporated.

¹Private communication: This constraint may be unnecessary, as there is at least one example of a binary ORC geothermal power plant, where condensing steam is used to evaporate the working fluid. In any case, a heat transfer fluid could be used to facilitate the heat transfer, to first condense the steam, heating the heat transfer fluid, and then evaporate the working fluid, cooling the heat transfer fluid. The main disadvantage of this approach is the pumping cost of the heat transfer fluid and the cost of an additional heat exchanger.

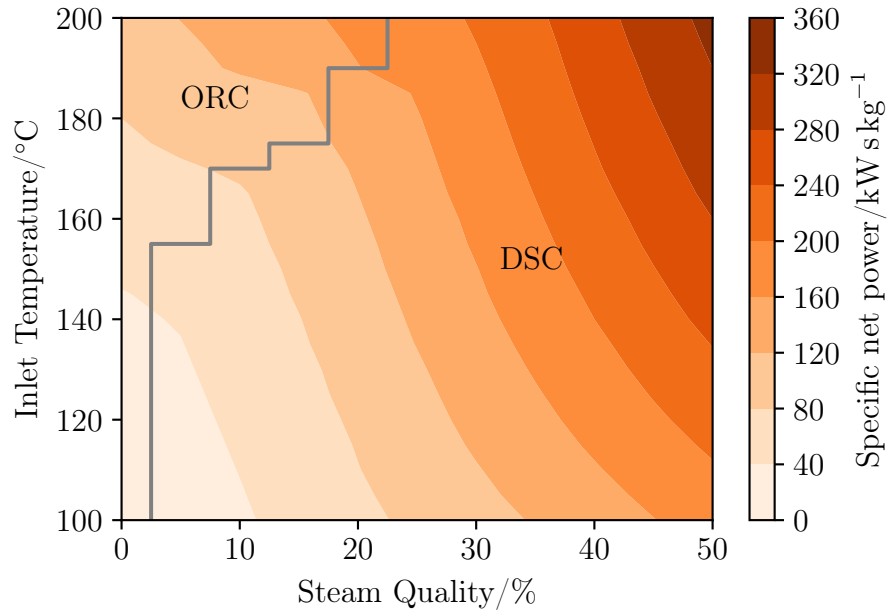


Figure 5.4: Maximum specific net power from a geofluid of pure water as a function of inlet temperature and steam quality. The grey line indicates the performance boundary between binary ORC and DSCs.

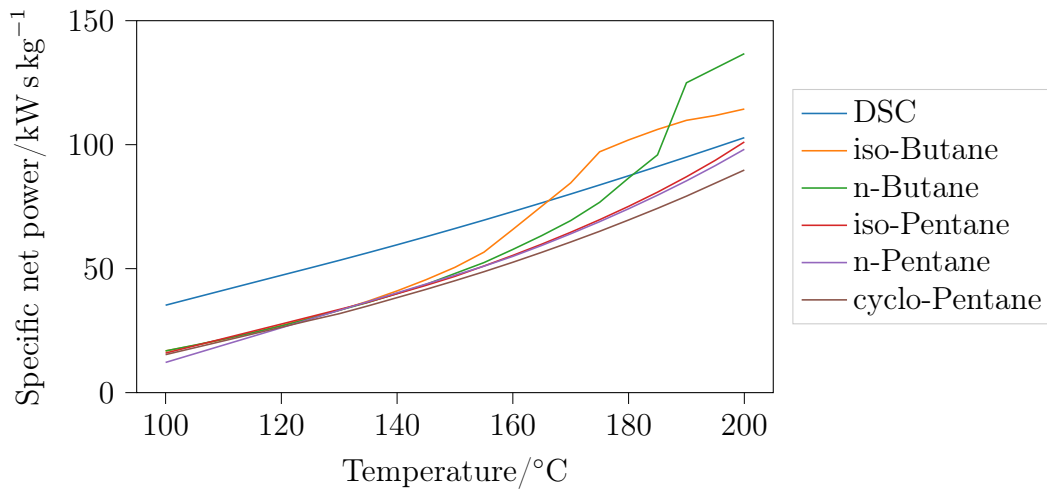


Figure 5.5: Specific net power from a geofluid of pure water as a function of inlet temperature and a steam quality of 25 % for a DSC and binary ORC plant using various working fluids.

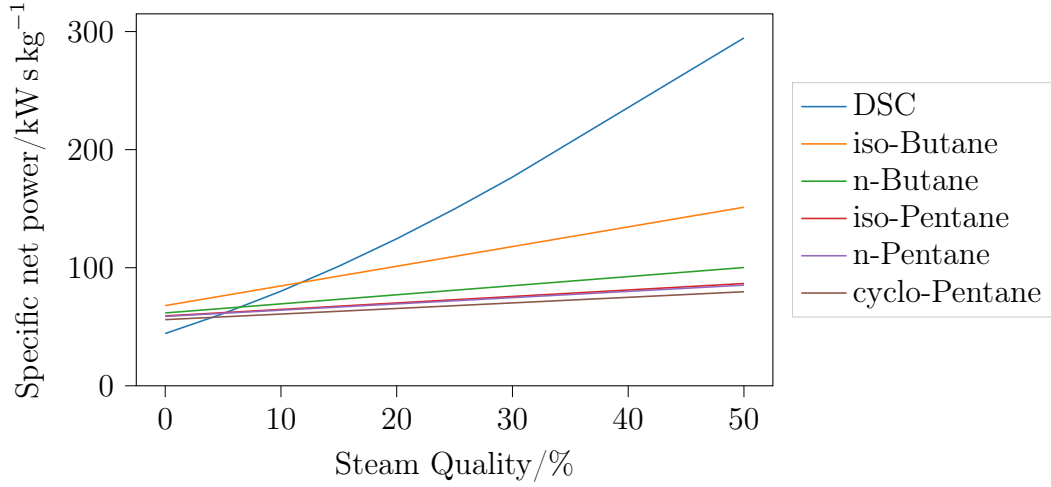


Figure 5.6: Specific net power from a geofluid of pure water as a function of steam quality and an inlet temperature of 165 °C for a DSC and binary ORC plant using various working fluids.

5.1.6. Role of Salinity and NCG

In reality geofluids are not only comprised of pure water, but may also carry dissolved minerals and NCG. The presence of such impurities alters the geofluid's phase behaviour and thermophysical properties compared to pure water, the magnitude of deviations being strongly related to the effective salinity, Equation 5.7, and effective NCG content, Equation 5.8, and has implications for the performance of direct steam and binary ORC power plants.

$$s_{NaCl}^{eff} = \frac{\dot{m}_{NaCl}}{\dot{m}_{H_2O}^L} \quad (5.7)$$

$$s_{NCG}^{eff} = \frac{\dot{m}_{NCG}}{\dot{m}_{H_2O}^V} \quad (5.8)$$

Perhaps most consequential is their effect on the geofluid saturation pressure. Considering a geofluid comprised of $H_2O(aq)$, $Na^+(aq)$, $Cl^-(aq)$ and $H_2O(g)$, the presence of the $Na^+(aq)$, $Cl^-(aq)$ causes a reduction in chemical potential of the $H_2O(aq)$, meaning that mixture prefers to be in the liquid state and thus the saturation pressure is reduced, see Figure 5.7. Similarly, for a geofluid comprised of $H_2O(aq)$, $H_2O(g)$ and $CO_2(g)$, the fluid prefers to be in the gaseous state and hence the saturation pressure increases.

The change in saturation pressure is particularly important for DSCs, as, for example in the case of high salinity, impedes the ability to optimise flash temperature/pressure and

reduces net power. Specifically, a geofluid with an effective salinity of 0.3 kg kg^{-1} of NaCl, the saturation pressure is reduced from 10 bar to 8 bar.

Salinity and NCG also affect the geofluid's thermophysical properties, such as the specific enthalpy or specific heat capacity. Changes can primarily be attributed to both salts and NCG having far lower heat capacity than pure water and to a smaller extent to the reduction in species chemical potential, although this is more significant for higher concentrations of salts and NCG. That being said, the heat flow is relatively unchanged compared to pure water, see Figure 5.8. This suggests that, assuming the total mass rate scales with the mass rate of impurities, the performance of the binary ORC is only weakly affected.

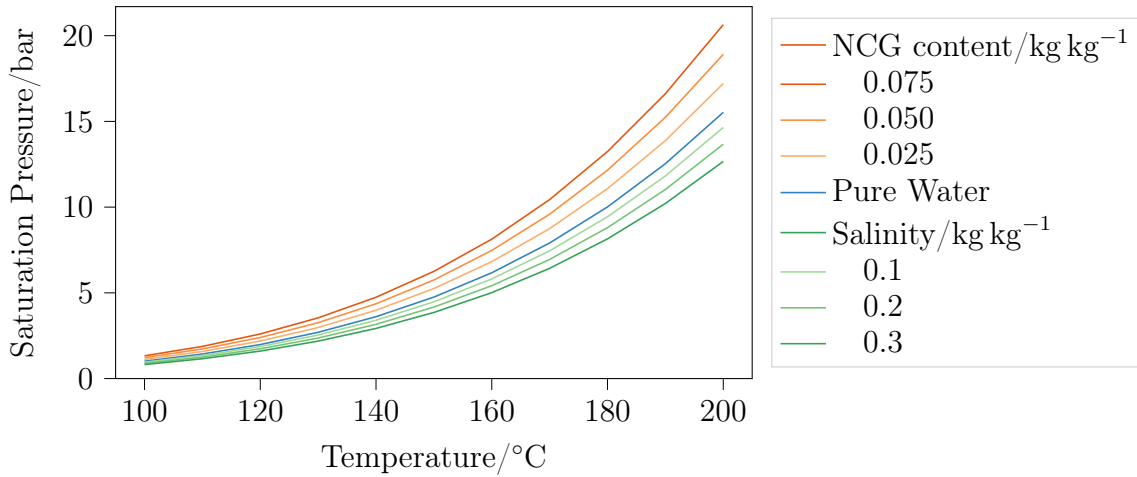


Figure 5.7: Geofluid saturation pressure as a function of temperature for a range of effective salinity and NCG content.

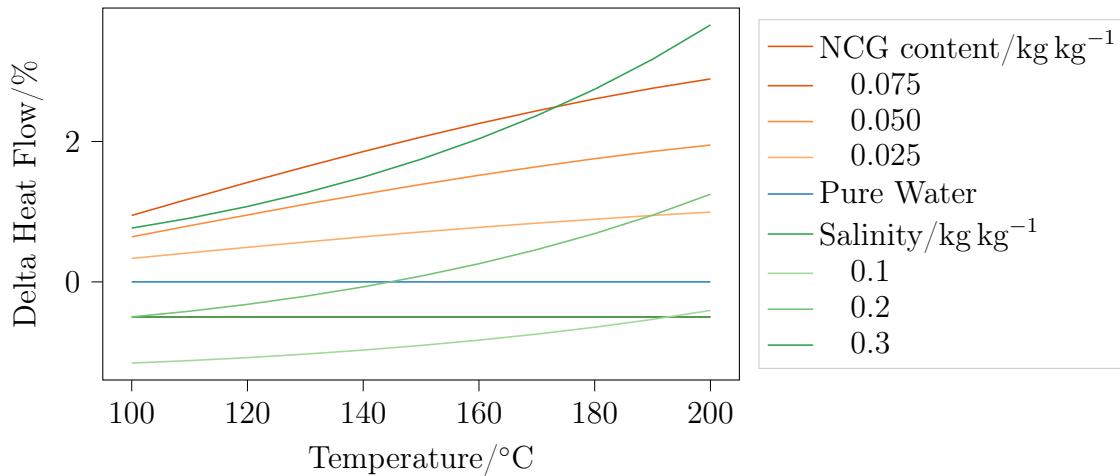


Figure 5.8: Deviation of liquid and vapour heat flow from pure water/steam for a range of effective salinity and NCG content, at a steam quality of 10 %, as a function of temperature. The reference conditions are 25°C and 1 bar.

5.1.7. ELECNRTL vs. SP2009

Within *Aspen Plus v11*, the ELECNRTL model has so far been used to capture the phase behaviour of water, sodium chloride and carbon dioxide mixtures. Given the particular focus of this work on the thermophysical properties and phase behaviour of the geofluid, it was important to compare the ELECNRTL model against other available models, such as SP2009.

To compare the mutual solubilities of water and carbon dioxide from the ELECNRTL model, a simple process was modelled in *Aspen Plus v11*. Two streams of pure water and carbon dioxide are mixed, then taken to the desired temperature and pressure in the Heater element. Finally the mixture is partitioned into a vapour and liquid phase in the Separator, see Figure 5.9.

The methodology above relies on a two-phase mixture to exist at the desired temperature and pressure, such that both the liquid and vapour phase are considered saturated. For conditions, where only a single phase exists, water or carbon dioxide, would need to be added until mixture becomes saturated, however, this procedure is difficult to implement in *Aspen Plus v11*. In this respect, the ratio of water to carbon dioxide at the inlet was set to 1 to 10 on a mole basis as this was found to yield a two-phase mixture over a wide range of conditions.

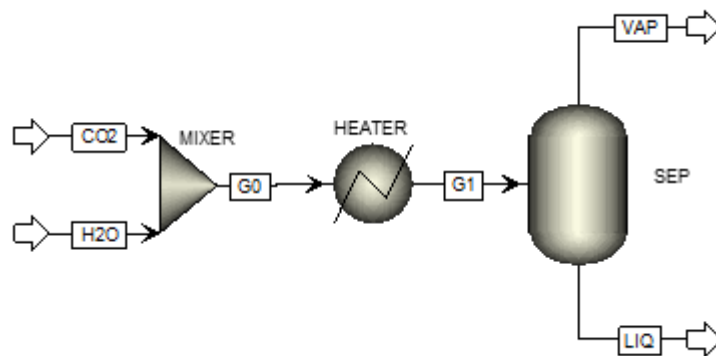


Figure 5.9: Process flow diagram of the *Aspen Plus v11* simulation used to calculate the mutual solubilities of water and carbon dioxide

Comparing the equilibrium mole fraction of water in the vapour/carbon dioxide-rich phase, see Figures 5.10, it can be seen that the ELECNRTL model generally provides higher estimates than the SP2009 model. The deviations from SP2009's estimates increase with decreasing temperature; from a ratio of 1.31 at 250 °C and 600 bar to 2.20 at 60 °C and 600 bar.

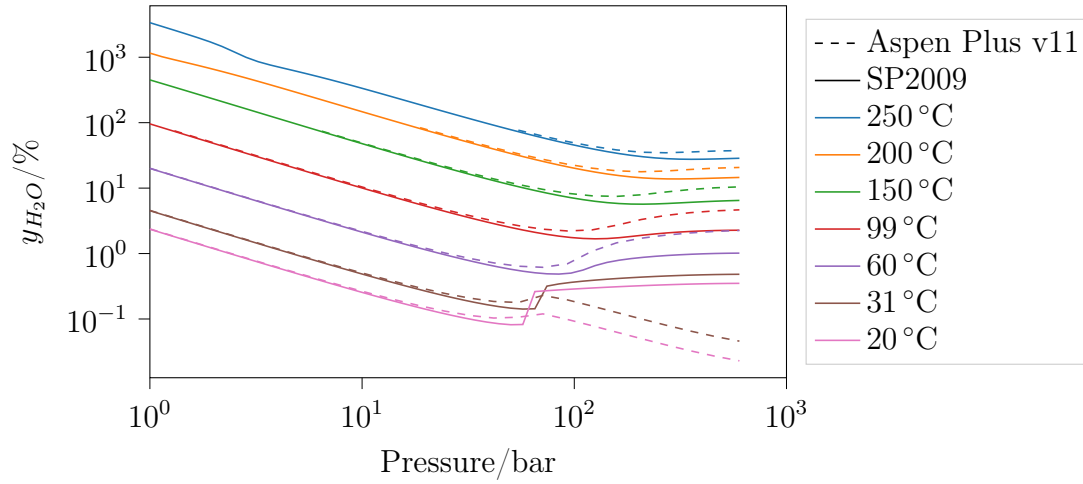


Figure 5.10: The equilibrium mole fraction of water in a carbon dioxide-rich phase as a function of temperature and pressure, as calculated using the ELECNRTL model in *Aspen Plus v11* and the SP2009 model

The observed deviations at temperatures below 60 °C can in part be explained by phase change of the carbon dioxide-rich phase from vapour to liquid, visible as the discontinuities of the lines corresponding to temperatures of 31 °C and 20 °C. This phase change does not appear to be captured within the ELECNRTL model in *Aspen Plus v11*.

As for the equilibrium mole fraction of carbon dioxide in a water-rich phase, while the ELECNRTL and SP2009 models show good agreement at low temperatures, they deviate considerably at higher temperatures, see Figures 5.11 and 5.12. As described above, the low-temperature and high-pressure behaviour of the ELECNRTL model can likely be attributed to the phase change from vapour to liquid carbon dioxide not being captured.

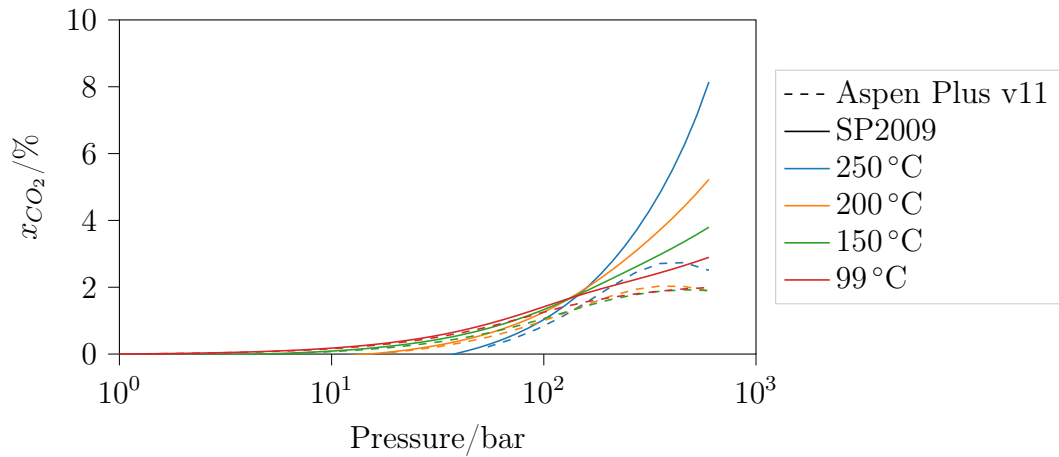


Figure 5.11: The equilibrium mole fraction of carbon dioxide in a water-rich phase as a function of temperature and pressure, as calculated using the ELECNRTL model in *Aspen Plus v11* and the SP2009 model

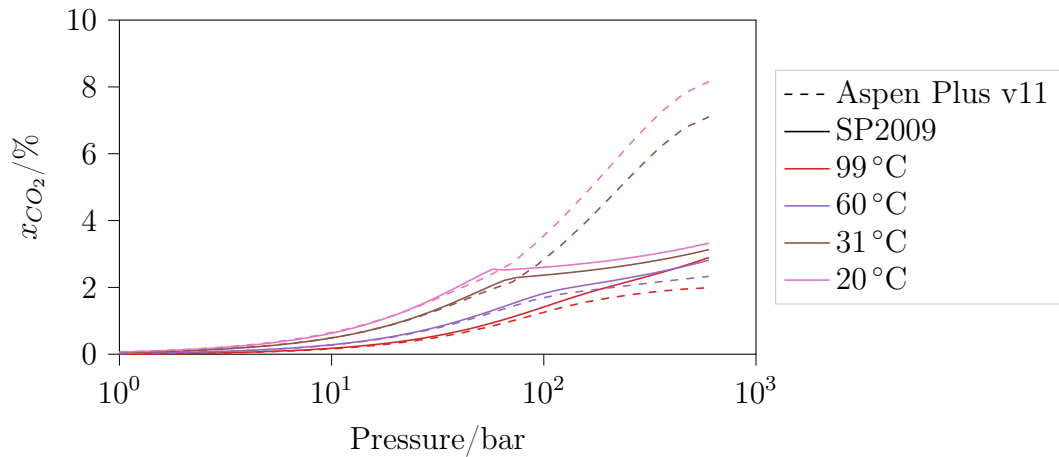


Figure 5.12: The equilibrium mole fraction of carbon dioxide in a water-rich phase as a function of temperature and pressure, as calculated using the ELECNRTL model in *Aspen Plus v11* and the SP2009 model

Another factor to consider when comparing these results is nature of the phases considered by each model: *Aspen Plus v11* differentiates between a vapour, liquid and solid phase, whereas SP2009 considers a water-rich and a carbon dioxide-rich phase. For the vast majority of conditions these definitions are congruent, however below the critical temperature of carbon dioxide (about 31 °C) carbon dioxide can exist in its liquid state, provided pressures are sufficiently high. For our investigation it is unclear, whether the ELECNRTL model makes this distinction, nevertheless, *Aspen Plus v11* still reports carbon dioxide in the vapour phase at these conditions, see Figure 5.13.

	Units	G1	VAP	LIQ
Description				
From		HEATER	SEP	SEP
To		SEP		
Stream Class		CONVEN	CONVEN	CONVEN
Maximum Relative Error				
– MIXED Substream				
Phase			Vapor Phase	Liquid Phase
Temperature	C	20	19.9993	19.9993
Pressure	bar	100	100	100
– Mole Fractions				
H2O		0.909078	0.00092591	0.964617
CARBO-01		0.0908984	0.999074	0.0353576
H3O+		1.17873e-05	0	1.25124e-05
HCO3-		1.17873e-05	0	1.25124e-05
CO3--		3.93503e-13	0	4.17993e-13
Molar Vapor Fraction		0.0576329	1	0
Molar Liquid Fraction		0.942367	0	1

Figure 5.13: Reported stream composition with the ELECNRTL model in *Aspen Plus v11* for supercritical conditions

In summary, at low pressures (less than 100 bar) mutual solubilities predicted by ELECNRTL and SP2009 compare well, though for the vapour phase deviations increase with increasing temperature, while for the liquid phase deviations increase with decreasing temperature. In this respect, the ELECNRTL model can be used to model the inlet two-phase geofluid and partition it into a vapour and liquid phase. However, given the large deviations at low temperatures for the liquid phase, care should be taken when investigating re-injection scenarios involving the re-dissolution of carbon dioxide in brine similar to the *CarbFix* process.

5.1.8. Case 2: Salinity and NCG

To investigate the effect of impurities, the two power plants were simulated in *Aspen Plus V11* for an inlet temperature of 150 °C and steam quality of 10 % for geofluids with salinity between 0.0 kg kg⁻¹ to 0.2 kg kg⁻¹ of NaCl and NCG content ranging between 0.00 kg kg⁻¹ to 0.03 kg kg⁻¹ of CO₂ respectively, see Figures 5.14 and 5.15. The key observations were:

- Salinity does not significantly affect the performance of DSCs or ORCs.

- NCG content primarily impacts the performance of DSCs due to the additional compression requirements to reinject the NCG.
- ORCs begin to thermodynamically outperform DSCs at about 0.025 kg kg^{-1} of CO_2 for any salinity studied.

NCG content primarily impacts the performance of DSCs due to the additional compression requirements to reinject the NCG.

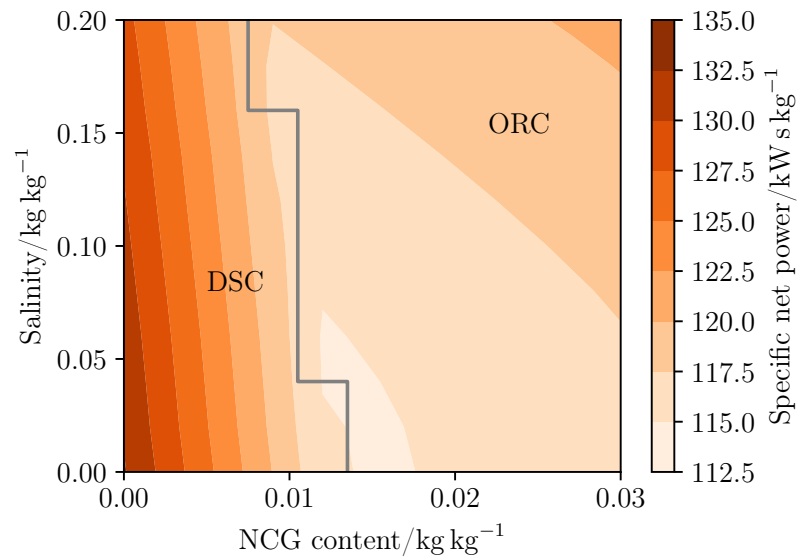


Figure 5.14: Maximum specific net power from a DSC or a binary ORC as a function of salinity and NCG content. Inlet temperature is 150°C and a steam quality of 10 %

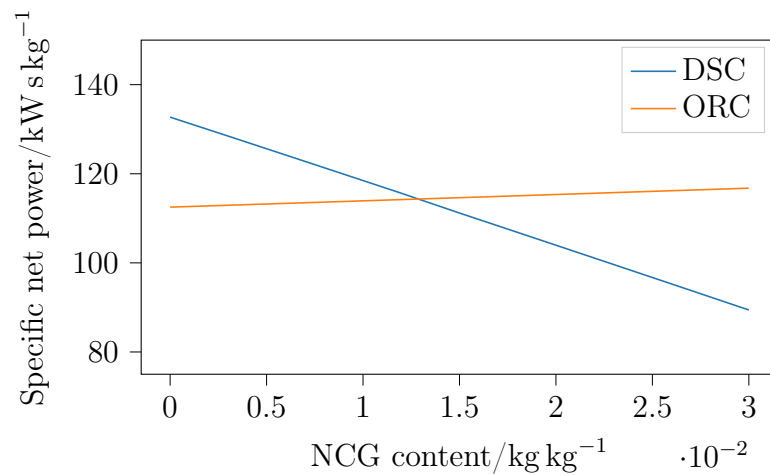


Figure 5.15: Specific net power as a function of NCG content. Inlet temperature is 150°C and steam quality is 10 %

5.1.9. Observations

Simulations of geothermal power plants showed that ORCs can thermodynamically outperform DSCs for inlet steam quality as high as 30 %, provided an appropriate working fluid has been selected - iso-butane and n-butane were found to be thermodynamically promising working fluids. The presence of impurities in the geofluid such as salts and NCG does not significantly affect the heat flow entering the power plant, and in turn the turbine power. That being said, NCG compression for re-injection reduced the net power of DSCs significantly, rendering binary ORCs thermodynamically favourable for NCG content as low as 0.025 kg kg^{-1} of CO_2 .

From a practical perspective, *Aspen Plus v11* represents a black box to the user, meaning that any troubleshooting of potential issues (e.g. model assumptions/implementation, calculation convergence, solver order or crashes) is limited to outputs provided by the tool (e.g. error, warning and debug messages) or the user guides.

Formulating stable optimisable power plant models for a wide range of inlet conditions without expert knowledge in this black-box environment proved to be a challenging task, resulting in a number of unresolved issues to be encountered:

- Achieving consistent initialisation of individual cases between a standalone and sensitivity calculation
- Unoptimised solver order leading to unnecessary iterations and runtime
- Difficulty in tracing severity of warnings and errors in sensitivity calculations, undermining reliability of results
- Small model modifications (e.g. enabling/disabling the recuperator, or super-critical vs. sub-critical ORC) require separate model templates
- Connectivity to non-standard third party applications/models
- Reproducible and non-reproducible (random) system crashes

5.2. Thermodynamic Optimisation

The following section aims to investigate the performance of thermodynamically optimised single flash DSC and binary ORC geothermal power plants for two-phase geothermal heat sources.

5.2.1. Plant Configurations

Single Flash DSC

The hot geofluid is expanded via an expansion valve and then passed through a separator to split the liquid brine and vapor phases, Figure 5.16, into two streams. The vapour is then expanded in a turbine connected to an electrical generator, producing electricity, before being condensed. The brine and condensate streams are re-pressurised, by means of pumps, and re-injected. The model parameters used are summarised in Table 5.1

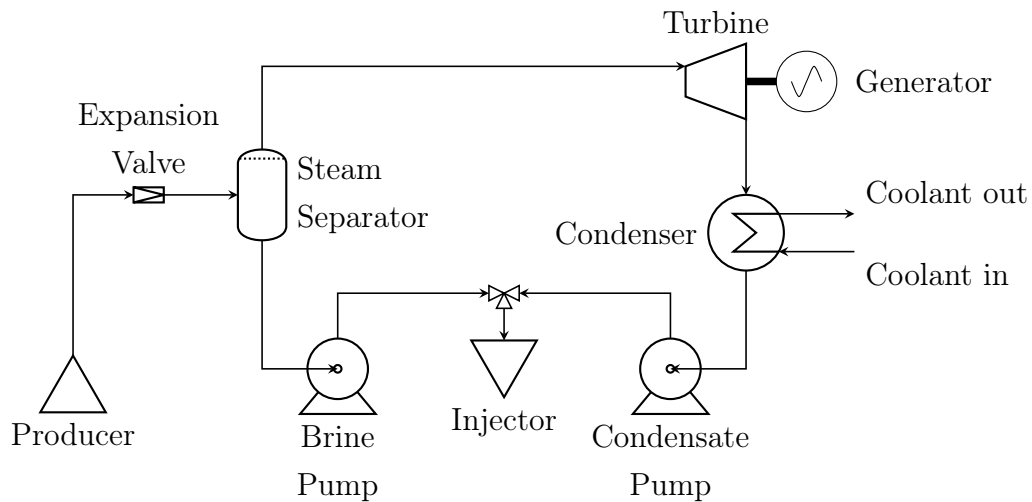


Figure 5.16: Single flash DSC geothermal power plant.

Table 5.1: The model parameters used for the single flash DSC component models.

Parameter	Unit	Value
$\eta_{dry, turb}$	%	85
η_{gen}	%	95
$\eta_{pump, brine}$	%	75
$\eta_{pump, condensate}$	%	75
η_{fan}	%	60
η_{motor}	%	95
ΔT_{cond}^{min}	K	5
ΔT_{sc}^{min}	K	3

Binary ORC

The hot geofluid heats and evaporates a secondary high-pressure low-boiling point fluid, Figure 5.17. The resulting high-pressure vapor is expanded in a turbine which drives an alternator, generating electricity. The expanded vapor is then condensed, re-pressurised and returned to the pre-heater. The cold geofluid is re-pressurized and re-injected. The model parameters used are summarised in Table 5.2

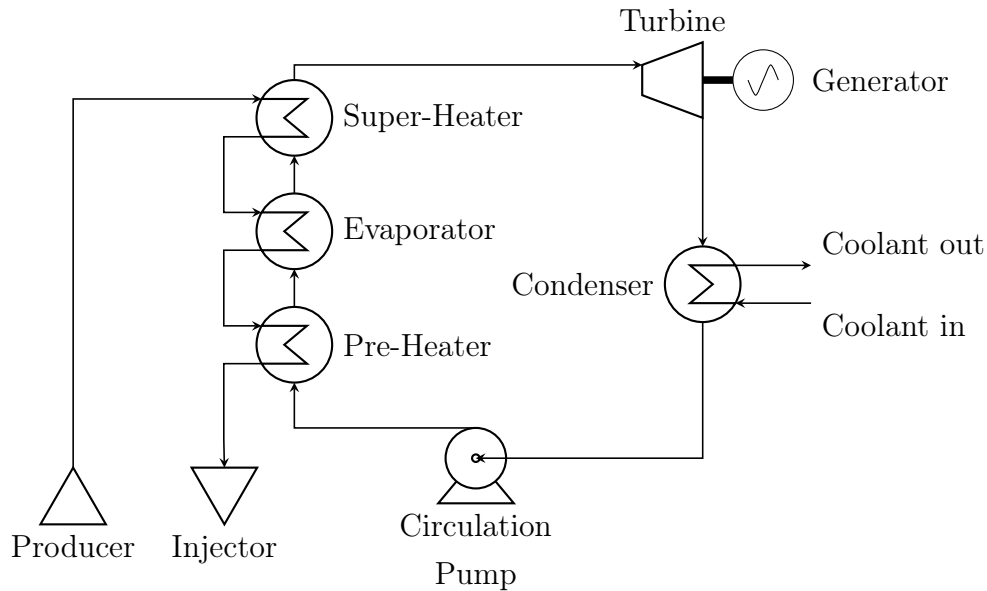


Figure 5.17: Binary ORC geothermal power plant.

Table 5.2: The model parameters used for the binary ORC component models.

Parameter	Unit	Value
$\eta_{dry, turb}$	%	85
η_{gen}	%	95
η_{pump}	%	75
η_{fan}	%	60
η_{motor}	%	95
ΔT_{preh}^{min}	K	5
ΔT_{evap}^{min}	K	10
ΔT_{suph}^{min}	K	10
ΔT_{cond}^{min}	K	5
ΔT_{sc}	K	3
ΔT_{sh}	K	5

n-Propane, Cyclopropane, Isobutane, n-Butane, Isopentane, Isohexane, Cyclopentane and n-Heptane were chosen as candidate cycle working fluids based on their critical temperatures covering the full range of geothermal source temperatures to be considered. Vendor safety sheets [7] suggest that all fluids are dangerous, with hazards including flammability, explosiveness, toxicity to aquatic life, and may cause irritation on contact or inhalation.

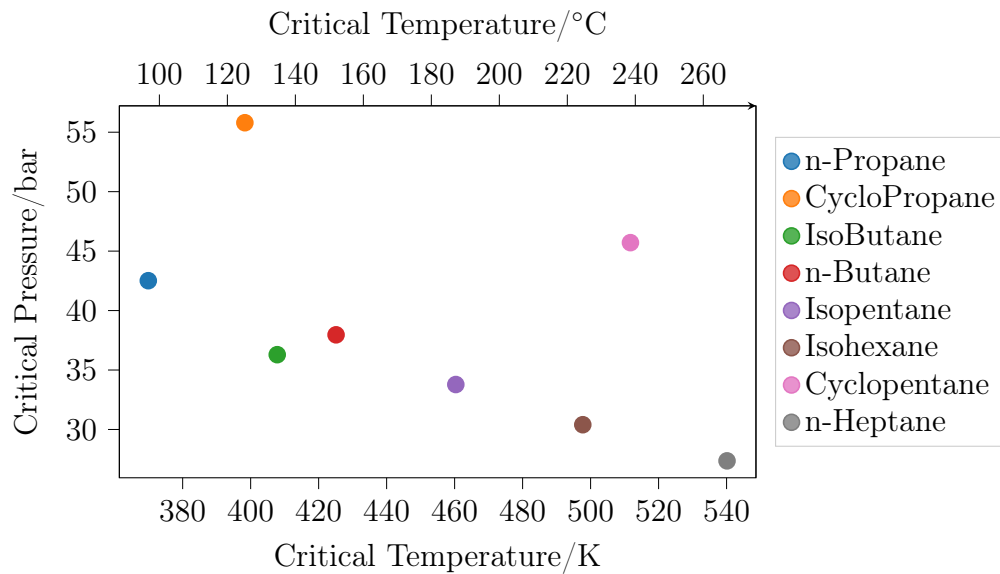


Figure 5.18: The critical temperature and pressure of the ORC working fluids considered.

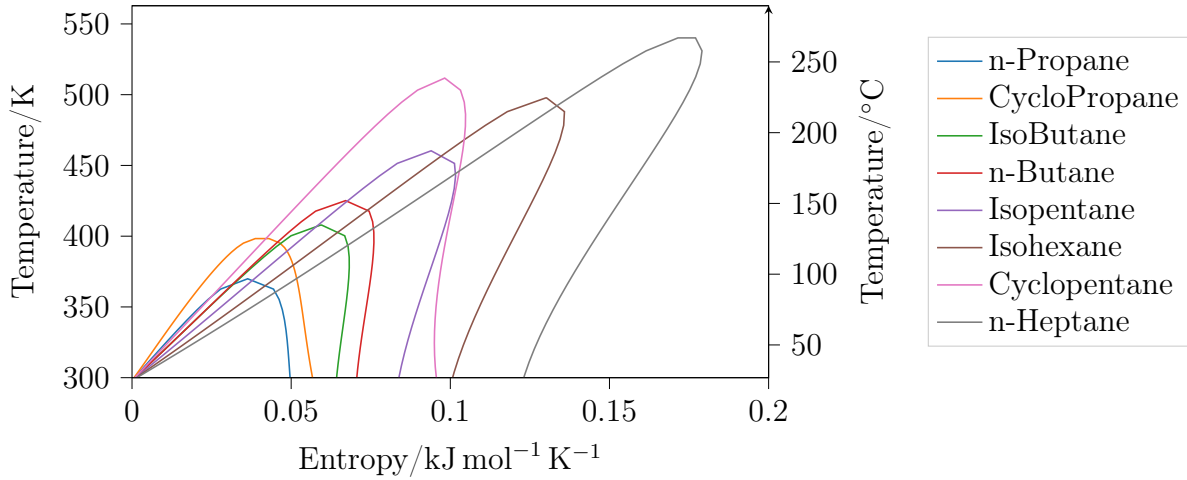


Figure 5.19: The phase envelopes in the temperature-entropy domain of the ORC working fluids considered.

5.2.2. Boundary Conditions

The geofluid is assumed to be pure water, arriving at the wellhead at a temperature between 423 K and 548 K (150 °C and 275 °C respectively) and a steam quality between 0 % (saturated liquid) and 100 % (saturated vapour). The geofluid inlet pressure is back-calculated from the inlet temperature and steam quality. The mass rate of geofluid is fixed at 50 kg s⁻¹.

Table 5.3: The boundary conditions used for the single flash DSC and the binary ORC geothermal power plants.

Condition	Values
Inlet Temperature	$423 \text{ K} \leq T_{geo, in} \leq 548 \text{ K}$
Inlet Steam Quality	$0 \% \leq x_{geo, in} \leq 100 \%$
Inlet Pressure	calculated
Outlet Pressure	$P_{geo, out} = P_{geo, in}$

5.2.3. Optimisation Configuration

The performance of the power plants is optimised based on the net electrical power generated, while ensuring that the approach temperatures in the heat exchangers (i.e. condenser, pre-heater, evaporator and super-heater) do not exceed the defined minimum values, Table 5.4, by adjusting the process variables. For the DSC plant, the flash pressure and the condensation pressure adjusted; for the binary ORC plant, the evaporation

pressure, the degree of super-heating and the condensation temperature are adjusted.

Table 5.4: The optimisation parameters used for the single flash DSC and the binary ORC geothermal power plants.

	Single Flash DSC	Binary ORC
Objective Function	$W_{net, elec}$	$W_{net, elec}$
Constraints	$\Delta T_{cond}^{min} \geq 5K$	$\Delta T_{cond}^{min} \geq 5K$ $\Delta T_{preh}^{min} \geq 5K$ $\Delta T_{evap}^{min} \geq 10K$ $\Delta T_{sh}^{min} \geq 10K$
Controls	$0.1 \text{ bar} \leq P_{cond} \leq 5.0 \text{ bar}$ $0.3 \leq \frac{P_{flash}}{P_{in}} \leq 1.0$	$303 \text{ K} \leq T_{cond} \leq 400 \text{ K}$ $0.2 \leq \frac{P_{evap}}{P_{crit}} \leq 0.8$ $3 \text{ K} \leq \Delta T_{sh} \leq 15 \text{ K}$

5.2.4. Performance Analysis: DSC

The net power produced by the DSC geothermal power plant increases with both steam quality, due to the higher steam mass rate, and temperature, due to the higher heat content of the vapour, Figure 5.20. The gains in net power with temperature appear to be diminishing, which can be attributed to the shape of the phase envelope in the pressure-enthalpy domain, Figure 5.22, where with increasing temperature (or pressure) the gradient of the dew-point line becomes vertical for temperatures higher than around 500 K.

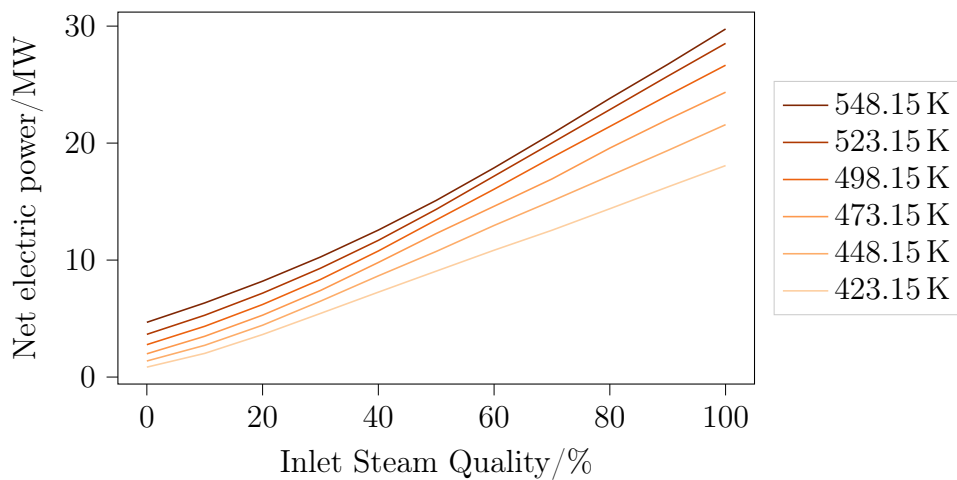


Figure 5.20: The net electrical power of the single flash DSC geothermal power plant as a function of inlet steam quality at different inlet temperatures.

The sensitivity study indicates that, the lower condensation pressures are favoured, Figure 5.21. In fact, for all inlet conditions considered, the optimised condensation pressure is equal to the minimum condensation pressure of 0.1 bar. This indicates that even lower condensation pressures would be favoured, the lower limit being the saturation pressure at the ambient temperature plus the required minimum approach temperature in the condenser.

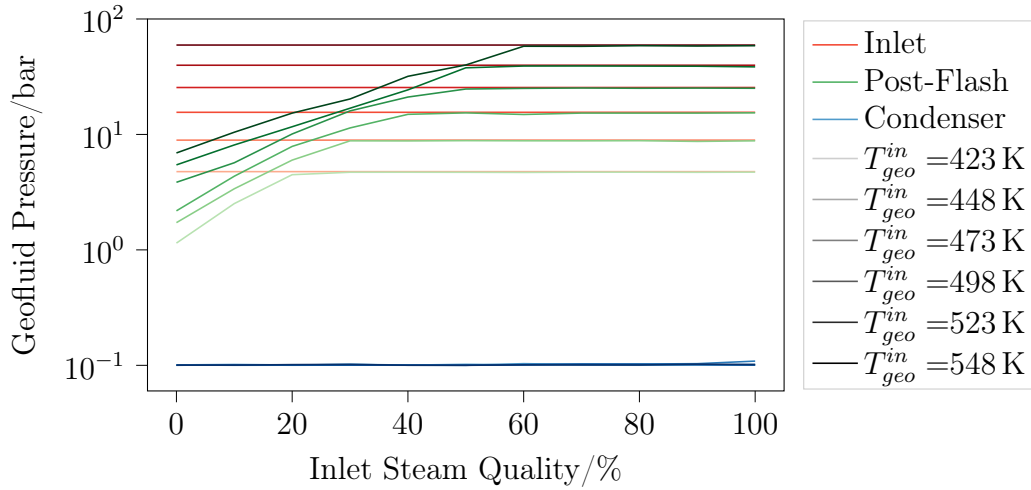


Figure 5.21: The geofluid inlet pressure and optimised flash and condensation pressures for the single flash DSC geothermal power plant as a function of inlet steam quality at different inlet temperatures.

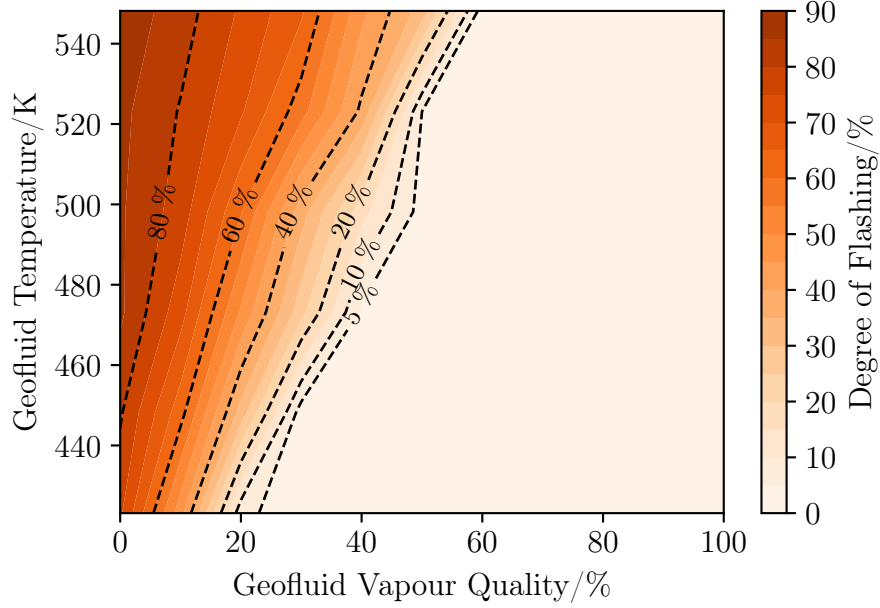


Figure 5.22: The degree of flashing X_{flash} for a single flash DSC geothermal power plant as a function of geofluid inlet temperature and vapour quality.

The optimum degree of flashing X_{flash} (i.e. $X_{flash} = 1 - \frac{P_{flash}}{P_{in}}$) decreases with increasing geofluid inlet steam quality, Figure 5.22, which can be attributed to the lines of equal vapour quality in the pressure-enthalpy domain becoming more vertical, Figure 5.23, and as such flashing liberates less additional vapour. For instance, flashing a geofluid arriving at 423 K and an inlet vapour quality of 15 % by 50 % (i.e. $P_{flash} = 0.5 * P_{in}$), raises the vapour quality to 19 %. Considering a geofluid at the same temperature and an inlet vapour quality of 70 %, the same flash only raises the vapour quality to 72 %.

Similarly, the optimum degree of flashing increases with geofluid temperature, as the lines of equal vapour quality are more curved, Figure 5.23, and thus larger amounts of vapour can be liberated for the same degree of flashing. For instance, flashing a geofluid arriving at 548 K and an inlet vapour quality of 15 % by 50 % (i.e. $P_{flash} = 0.5 * P_{in}$), raises the vapour quality to 25 %. Considering a geofluid at 423 K, the same flash only raises the vapour quality to 19 %.

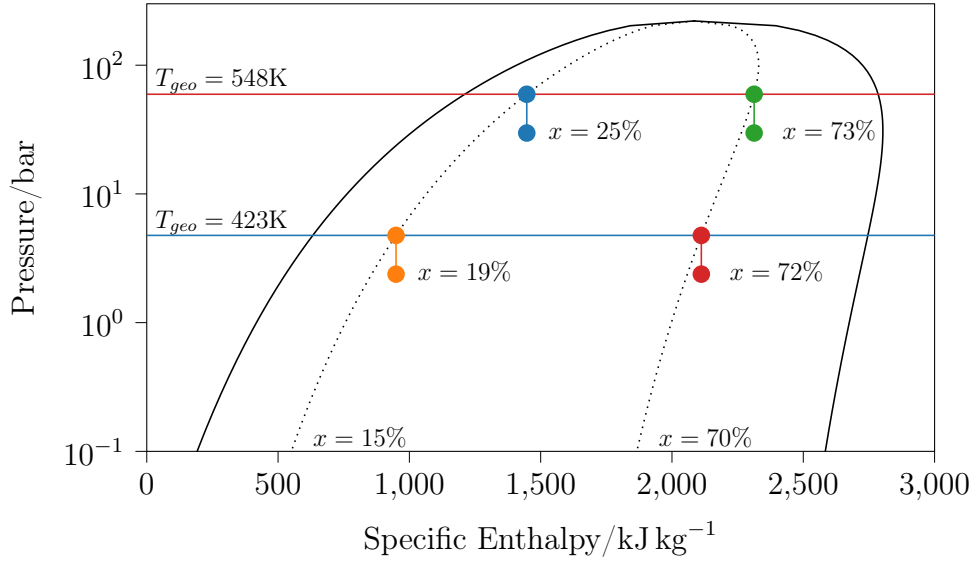


Figure 5.23: The inlet geofluid vapour quality and the resultant vapour quality following a 50 % flash.

With regards to the cost, four main cost components can be identified for the single flash DSC; the turbine, the condenser, secondary equipment and construction, Figure 5.24. By definition, see Section 4.4, the combined construction and secondary equipment cost amount to about 45 % of total plant cost, with the remainder being roughly evenly split between the turbine and the condenser. The increasing cost share of the condenser relative to the turbine with geofluid inlet vapour quality, Figure 5.24, can be attributed to the scaling of the respective cost correlations, and can more generally be observed with increasing power plant capacity. Re-pressurisation is not a significant cost component, owing to the low power requirements, as the geofluid is virtually in-compressible. The specific costs calculated in this study, Figure 5.25, are about 50 % lower than cost estimates from *GEOPHIRES-X* [17], see Section 3.7.8.

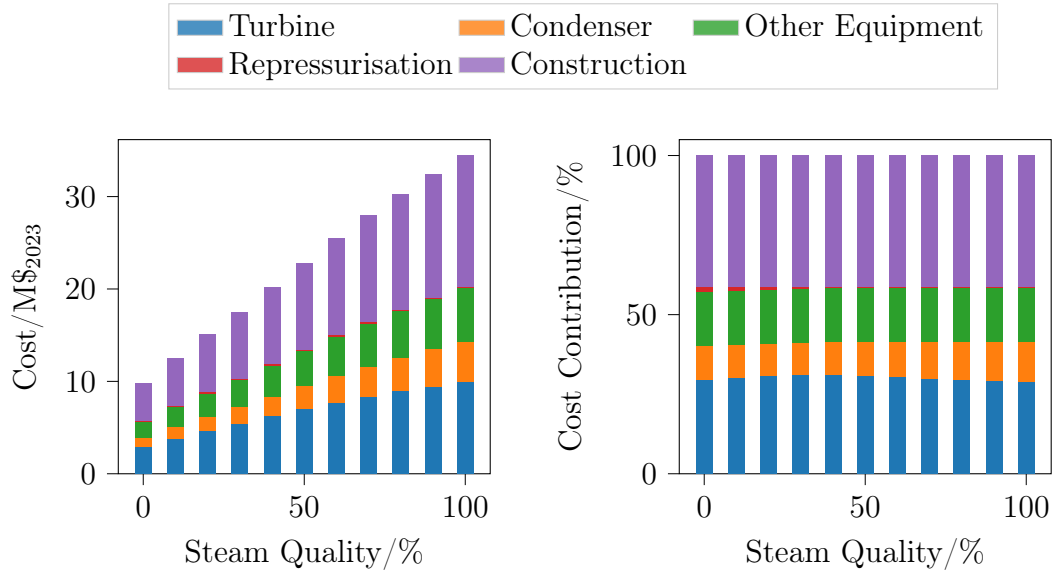


Figure 5.24: The absolute cost (left) and relative cost (right) of plant components of a single flash DSC geothermal power plant for a geofluid inlet temperature of 523 K (225 °C) as a function of inlet steam quality.

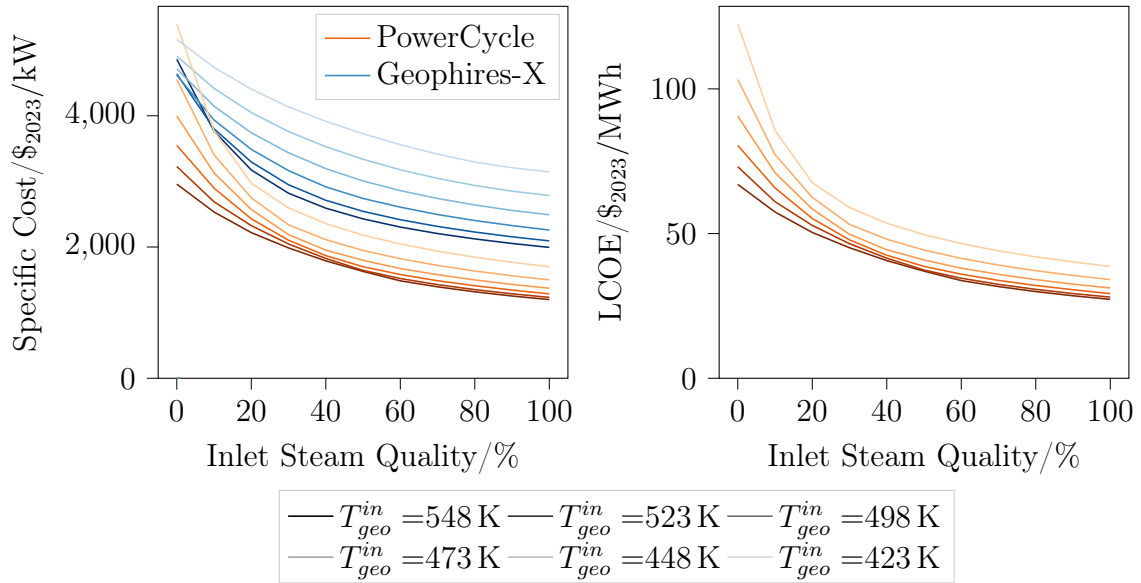


Figure 5.25: The specific plant cost (left) and the LCOE (right) of a single flash DSC geothermal power plant as a function of inlet steam quality at different inlet temperatures.

5.2.5. Performance Analysis: Binary ORC

The net power of binary ORC geothermal power plants increases with geofluid inlet temperature and steam quality, Figure 5.26, due to the higher heat flow entering the power plant. Similarly to the performance of the DSC plant, with increasing geofluid inlet

temperature, the increases in net power diminish, as a result of the dew-line undergoing an inflection in the temperature-enthalpy domain at temperatures above 473 K (200 °C). Consequently, the heat flow entering the power plant is almost constant with temperature as $\frac{\partial H}{\partial T}$ is close to zero.

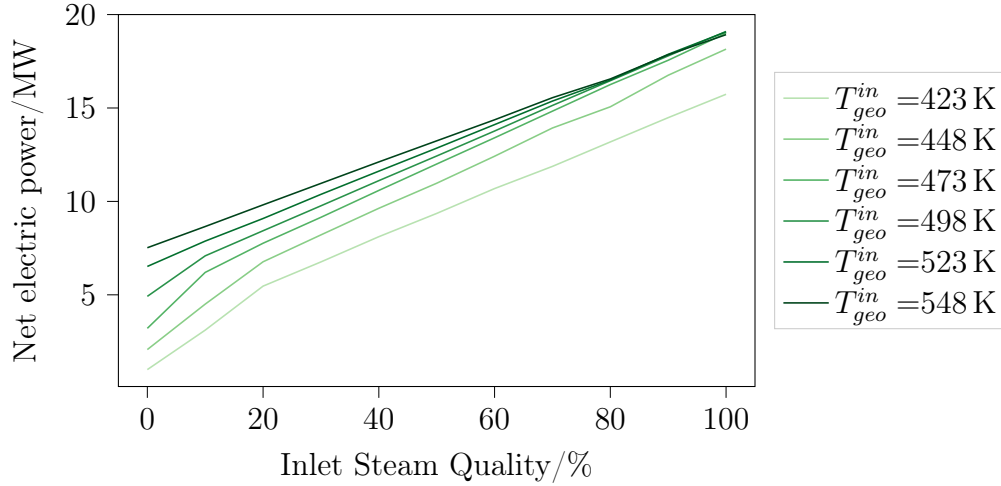


Figure 5.26: The net electrical power for a binary ORC using IsoPentane as the working fluid as a function of inlet steam quality at different inlet temperatures.

As can be seen in Figure 5.26, the dependency of the net power on the geofluid inlet steam quality follows two distinct slopes, which can be attributed to a shift in the location of the pinch-point from the outlet of the pre-heater (on the working fluid side) to its inlet, Figure 5.27.

Considering a binary ORC using Isopentane as the working fluid, for saturated liquid geofluids (i.e. $x_{geo}^{in} = 0\%$) the pinch-point is located at the pre-heater outlet (on the working fluid side). The cycle parameters (i.e. P_{max} and ΔT_{sh}) are chosen such that the cycle net power is optimised. For two-phase geofluids with small inlet steam qualities, the additional heat content of the steam, allows the pinch-point to occur at a higher temperature (and in turn maximum cycle pressure P_{max}). Once the maximum cycle pressure is reached, for any higher geofluid inlet qualities, the pinch-point is then pushed inside the pre-heater, and the cycle power can now only be maximised by raising the degree of super-heating ΔT_{sh} . For high enough steam qualities (in this case about 20%), the pinch-point is located at the pre-heater inlet (on the working fluid side). Up until this point, the increase in cycle power is driven by 1) the increase in heat flow entering the plant, thus increasing the working fluid mass rate and 2) increasingly favourable operating parameters for the ORC.

At even higher geofluid inlet steam qualities, the cycle operating parameters remain un-

changed, either because they have reached their upper bound or because the optimum parameters with respect to the source temperature have been determined. As such, the subsequent increase in net power with geofluid inlet steam quality are now simply a result of the increased heat flow.

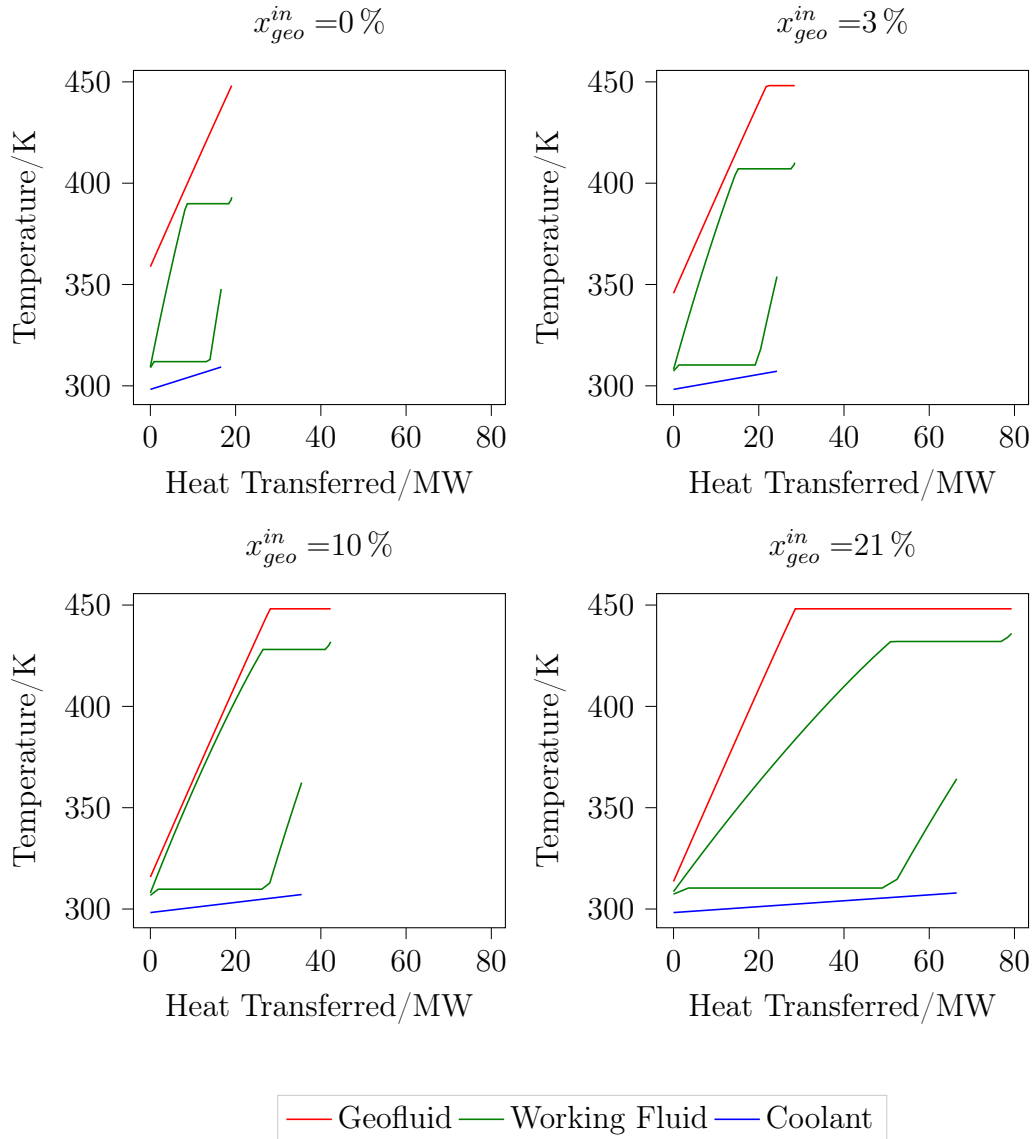


Figure 5.27: Temperature-Heat transferred diagrams for a binary ORC using Isopentane as the working fluid for different geofluid steam qualities.

At even higher geofluid inlet steam qualities, the cycle operating parameters remain unchanged, either because they have reached their upper bound or because the optimum parameters with respect to the source temperature have been determined. As such, the subsequent increase in net power with geofluid inlet steam quality are now simply a result of the increased heat flow.

A similar behaviour can also be observed with respect to the geofluid inlet temperature, where for higher geofluid inlet temperatures, the pinch-point shifts towards the pre-heater inlet (on the working fluid side), Figure 5.28

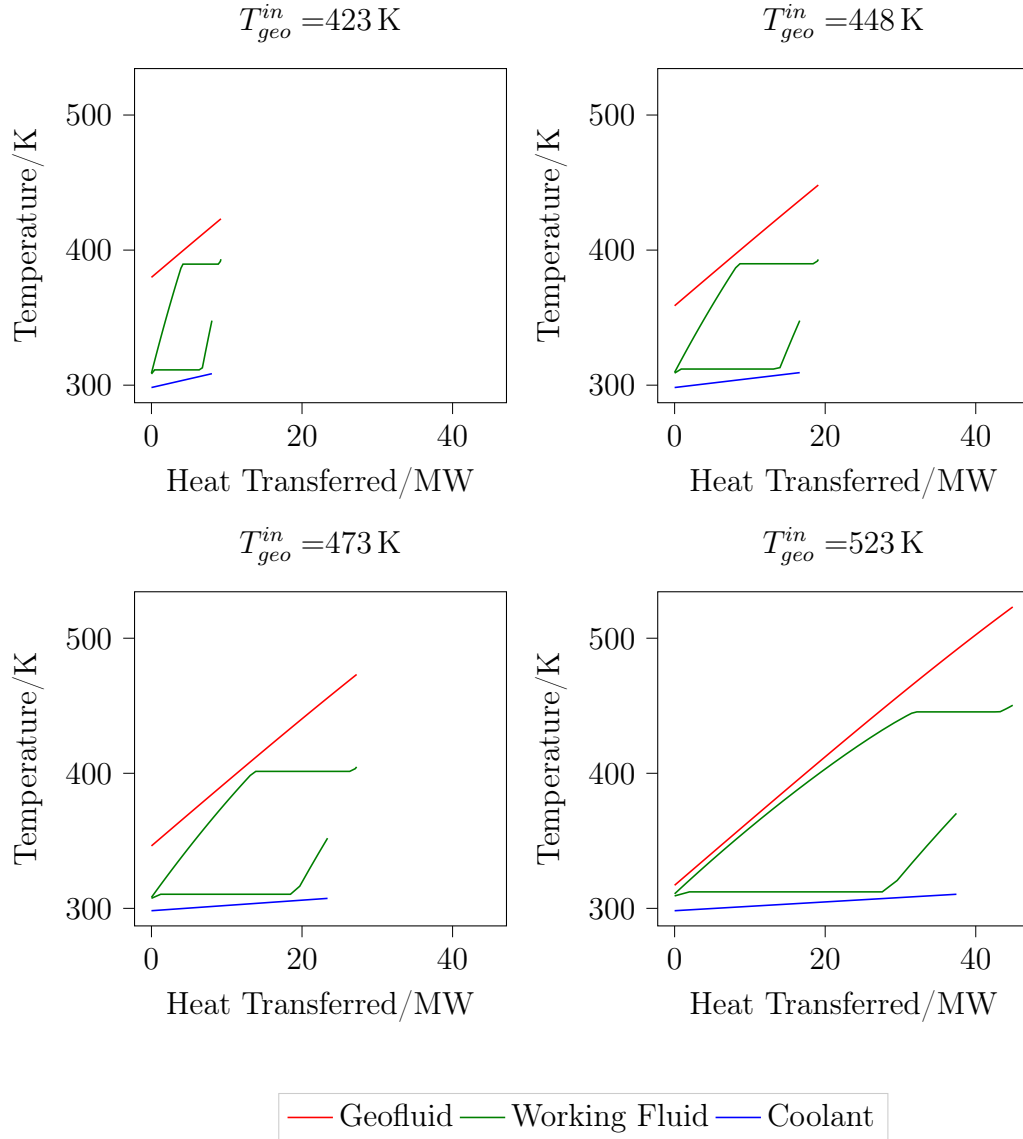


Figure 5.28: Temperature-Heat transferred diagrams for a binary ORC using Isopentane as the working fluid for different geofluid inlet temperatures.

Regarding the optimisation of process variables, the following trends can be identified:

- The reduced pressure P_r increases with both geofluid inlet temperature and pressure as a result of the pinch-point shifting towards the pre-heater inlet, Figure 5.29.

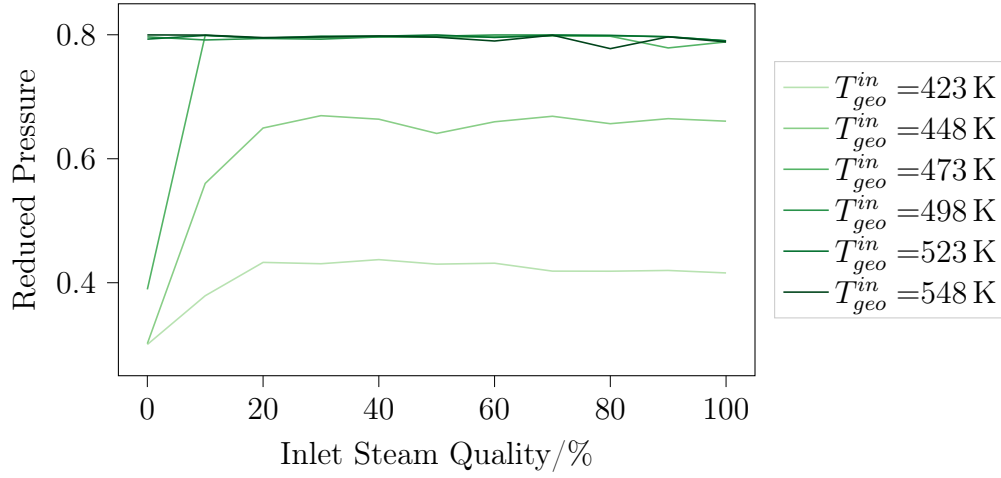


Figure 5.29: The optimised reduced pressure P_r for a binary ORC using Isopentane as the working fluid as a function of inlet steam quality at different inlet temperatures.

- The minimum temperature T_{min} is virtually independent of the geofluid inlet temperature and steam quality, Figure 5.30, and assumes values close to the specified lower bound value of 303 K (30 °C). As such, the condensation pressure for each working fluid is essentially fixed for all geofluid inlet conditions and may therefore be omitted as an optimisation variable. Instead, the minimum cycle temperature T_{min} , could be estimated based on the ambient temperature T_{amb} and the minimum approach temperature in the condenser ΔT_{cond}^{min} .

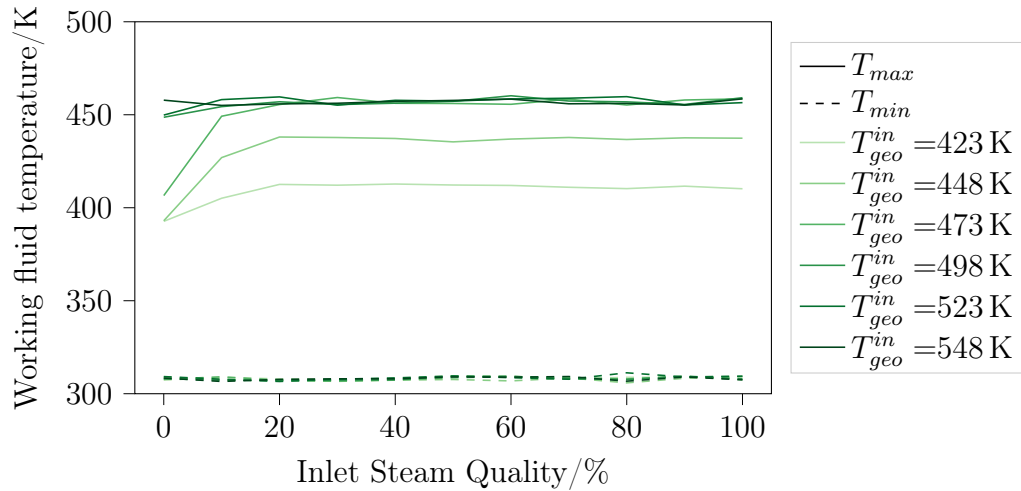


Figure 5.30: The minimum cycle temperature T_{min} and the maximum cycle temperatures T_{max} for a binary ORC using Isopentane as the working fluid as a function of inlet steam quality at different inlet temperatures.

- The degree of super-heating ΔT_{sh} generally only begins to increase once the maxi-

imum cycle temperature can no longer be increased by raising the reduced pressure P_r , Figure 5.31.

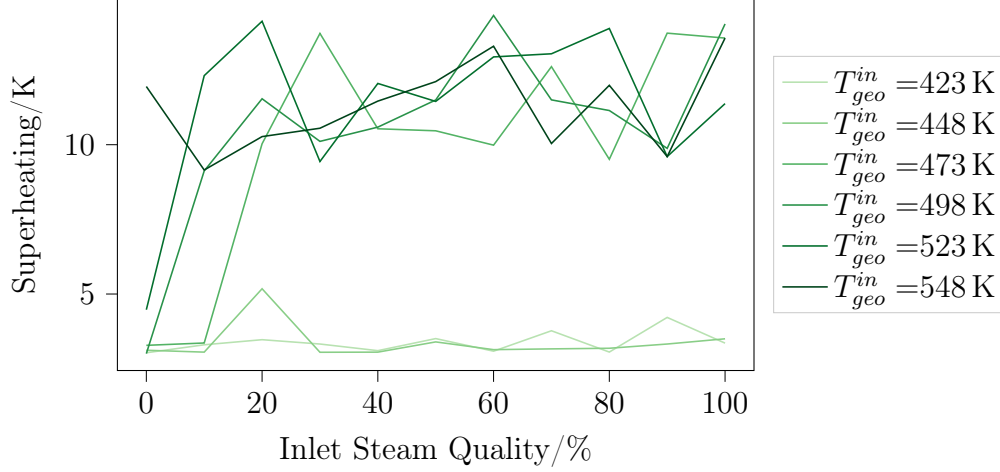


Figure 5.31: The degrees of super-heating ΔT_{sh} for a binary ORC using Isopentane as the working fluid as a function of inlet steam quality at different inlet temperatures.

The *noisiness* of the optimisation variables (e.g. the degrees of super-heating) with respect to the geofluid inlet conditions, can be attributed to degeneracy of the optimisation problem. As such there may be multiple (or even infinite) combinations of the optimisation variables that yield the same value (or similar values) of the objective function.

For example, considering a binary ORC using IsoPentane as the working fluid, operating on a geofluid inlet temperature of 473 K (200 °C) and steam quality of 20 %, the normalised objective function (i.e. $\frac{W_{net,elec}}{W_{max,elec}}$) was calculated for the full range of optimisation variables (i.e. P_r and DT_{sh}). For simplicity, the minimum cycle temperature T_{min} was fixed at 308 K (35 °C), Figure 5.32.

As can be seen from Figure 5.32, there are many combinations of the reduced pressure P_r and the degrees of super-heating ΔT_{sh} that yield a normalised objective function value of 0.99. Nevertheless, the optimisation has converged satisfactorily (i.e. the average value of the objective function across all *species* is within 1 % of the best *species* encountered, Figure 5.33. In principle the *noisiness* could be reduced by lowering the convergence tolerance for the optimisation (set at 1 % for this study), however this comes at the expense of increased model runtime, however even with the default tolerance, the optimisation comes within 0.1 % of the global optimum value of the objective function as determined via the brute-force approach.

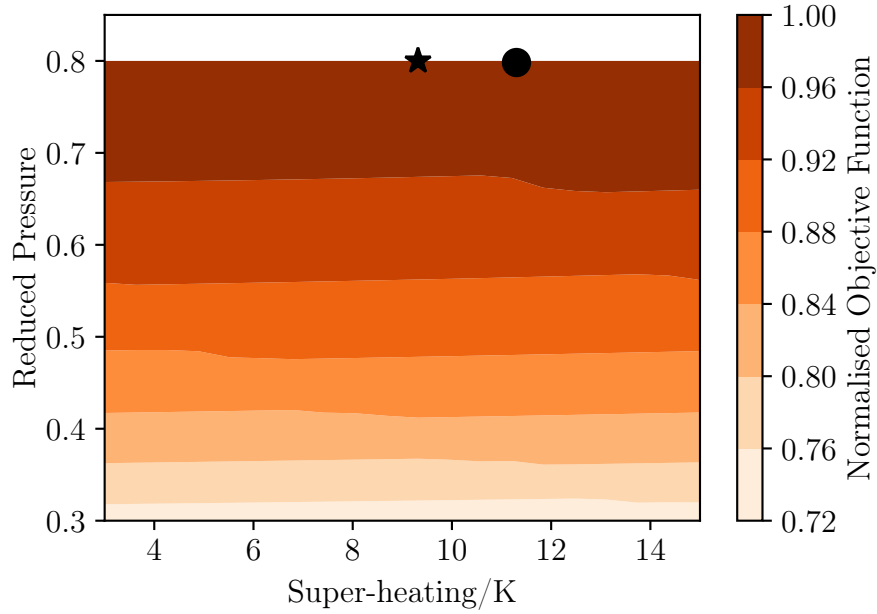


Figure 5.32: The normalised objective function space (i.e. $\frac{W_{net,elec}}{W_{net,elec}^{max}}$) for a binary ORC using IsoPentane as the working fluid, operating on a geofluid temperature of 473 K (200 °C) and steam quality of 20 %. The minimum cycle temperature T_{min} is fixed at 308 K (35 °C). The black star indicates the global optimum point; the black circle indicates the optimum operating conditions found in *PowerCycle*.

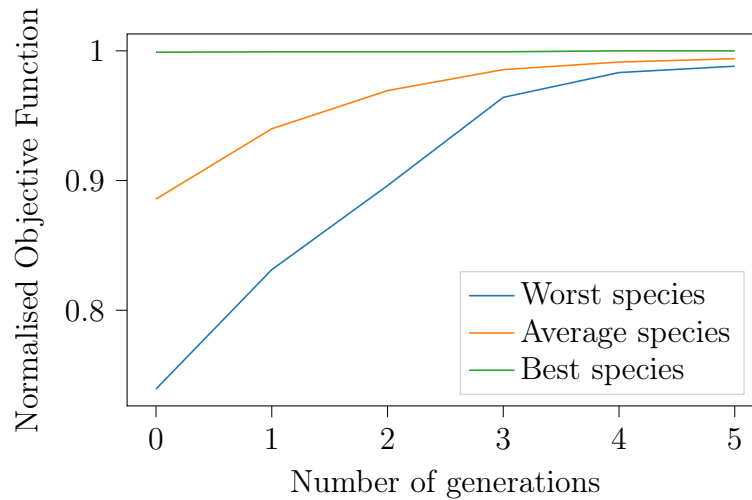


Figure 5.33: The normalised objective function (i.e. $\frac{W_{net,elec}}{W_{net,elec}^{max}}$) as a function of the optimiser iterations for a binary ORC using IsoPentane as the working fluid, operating on a geofluid temperature of 473 K (200 °C) and steam quality of 20 %. The minimum cycle temperature T_{min} is fixed at 308 K (35 °C). The black star indicates the global optimum point; the black circle indicates the optimum operating conditions found in *PowerCycle*.

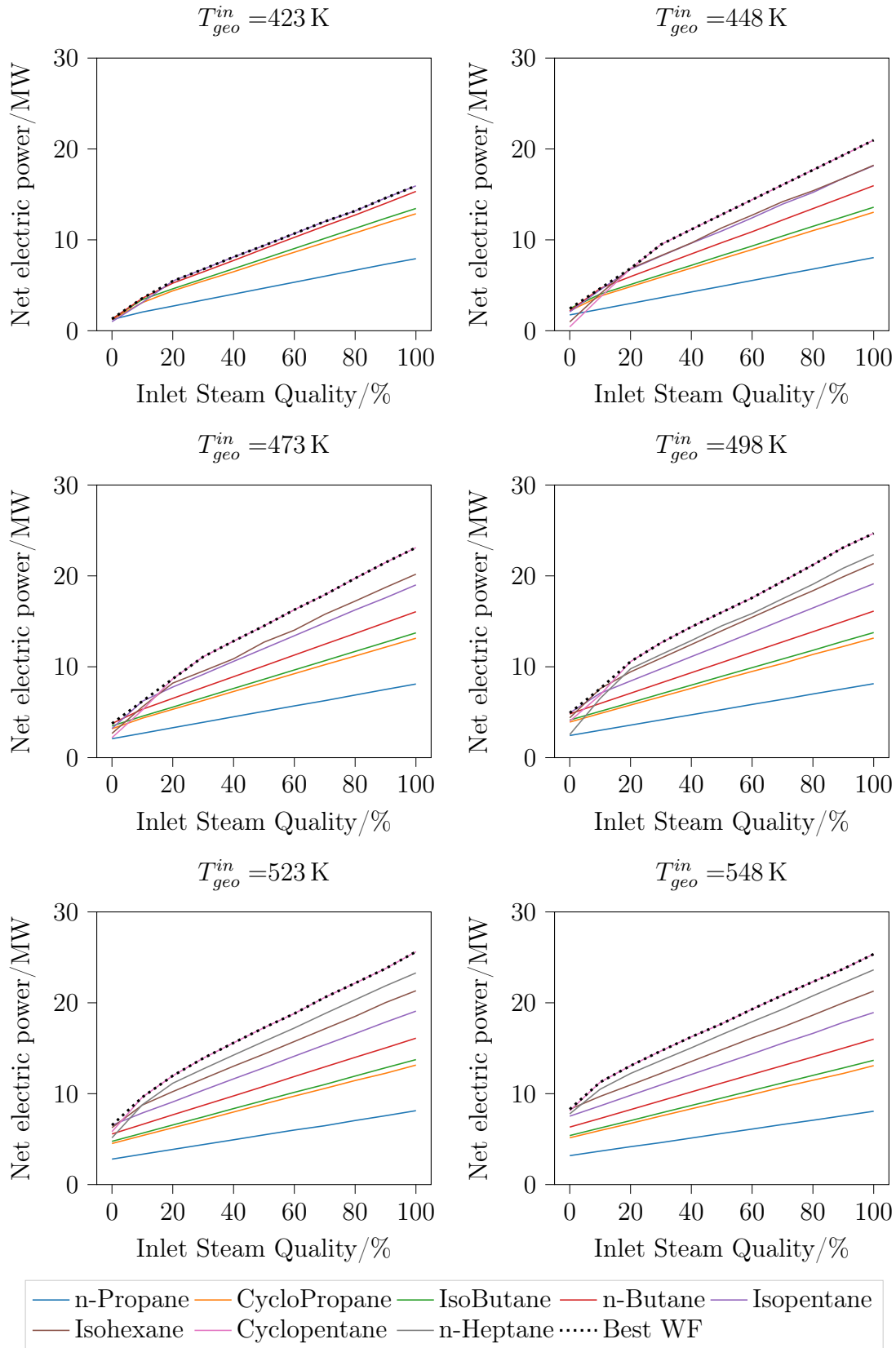


Figure 5.34: The net electrical power as a function of inlet steam quality at different inlet temperatures for a range of working fluids. The best performing working fluid is indicated by the dotted black line

Comparing the performance of the different working fluids considered, Figure 5.34, several working fluids can be seen to dominate at different geofluid inlet conditions. Overall, CycloPentane appears to be the best performing working fluid, yielding the highest net power for virtually all geofluid inlet steam qualities and temperatures greater than or equal to 448 K. n-Butane and Isopentane can be seen to perform well at lower temperatures and low steam qualities.

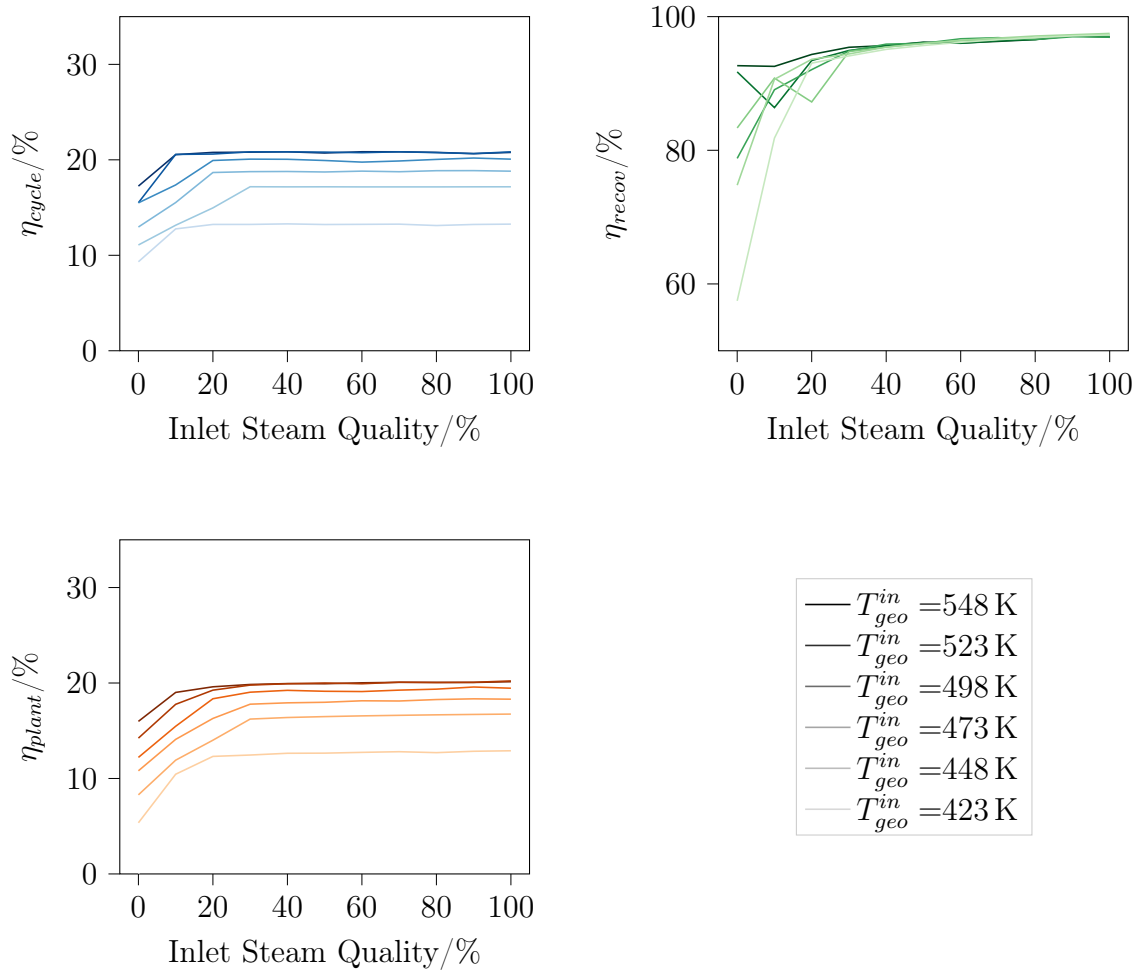


Figure 5.35: The maximum 1st law plant efficiency (bottom left) and corresponding cycle (top left) and thermal recovery (top right) efficiencies of the binary ORC plant across all working fluids as a function of inlet steam quality at different inlet temperatures for a range of working fluids.

The 1st law plant efficiency for two-phase heat sources is higher than that of single-phase sources, Figure 5.35. The cycle efficiency increases with geofluid inlet vapour quality (up to a threshold) because the pinch point in the PHE is shifted towards to the working fluid inlet, allowing for higher cycle temperatures. For the same reason the thermal recovery efficiency increases with geofluid inlet vapour quality, reaching values as high as 97%,

irrespective of geofluid inlet temperature, for saturated vapour sources. Consequently, the plant efficiency approaches the cycle efficiency. Two-phase sources can reach plant efficiencies almost twice as high as single-phase liquid heat sources, though the effect diminished with source temperature. These trends are in keeping with what was previously identified from a theoretical perspective in section 3.2.6.

The maximum net power and the corresponding specific plant cost across all working fluids for the different geofluid inlet conditions is shown in Figure 5.36. The specific cost is compared against estimates from *GEOPHIRES-X* [17], though while the specific costs are of similar magnitude, overall agreement is poor. This could be the result of a number of factors, such as the *GEOPHIRES-X* cost model being intended for at most saturated geofluids and geofluid temperatures below 473 K, as well as in this case the binary ORC being optimised solely on net power.

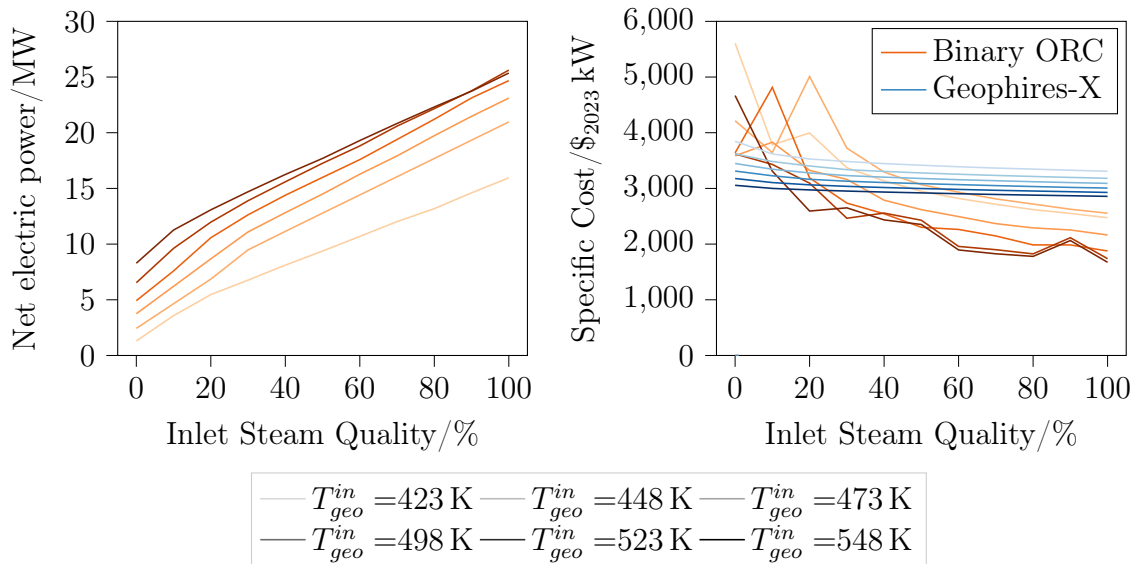


Figure 5.36: The net electrical power (left) and the corresponding specific plant cost (right) for the best performing working fluid.

The above being said, the thermodynamically best performing working fluids can be seen to be less favourable from a specific cost perspective. Particularly CycloPentane achieves specific costs about $1000\ \$_{2023}\text{ kW}^{-1}$ higher than the minimum specific cost observed across all working fluids considered, Figure 5.37. Although this gap closes at higher temperatures, and for some geofluid inlet vapour qualities at inlet temperatures exceeding 523 K, CycloPentane actually achieves the lowest specific cost across all working fluids.

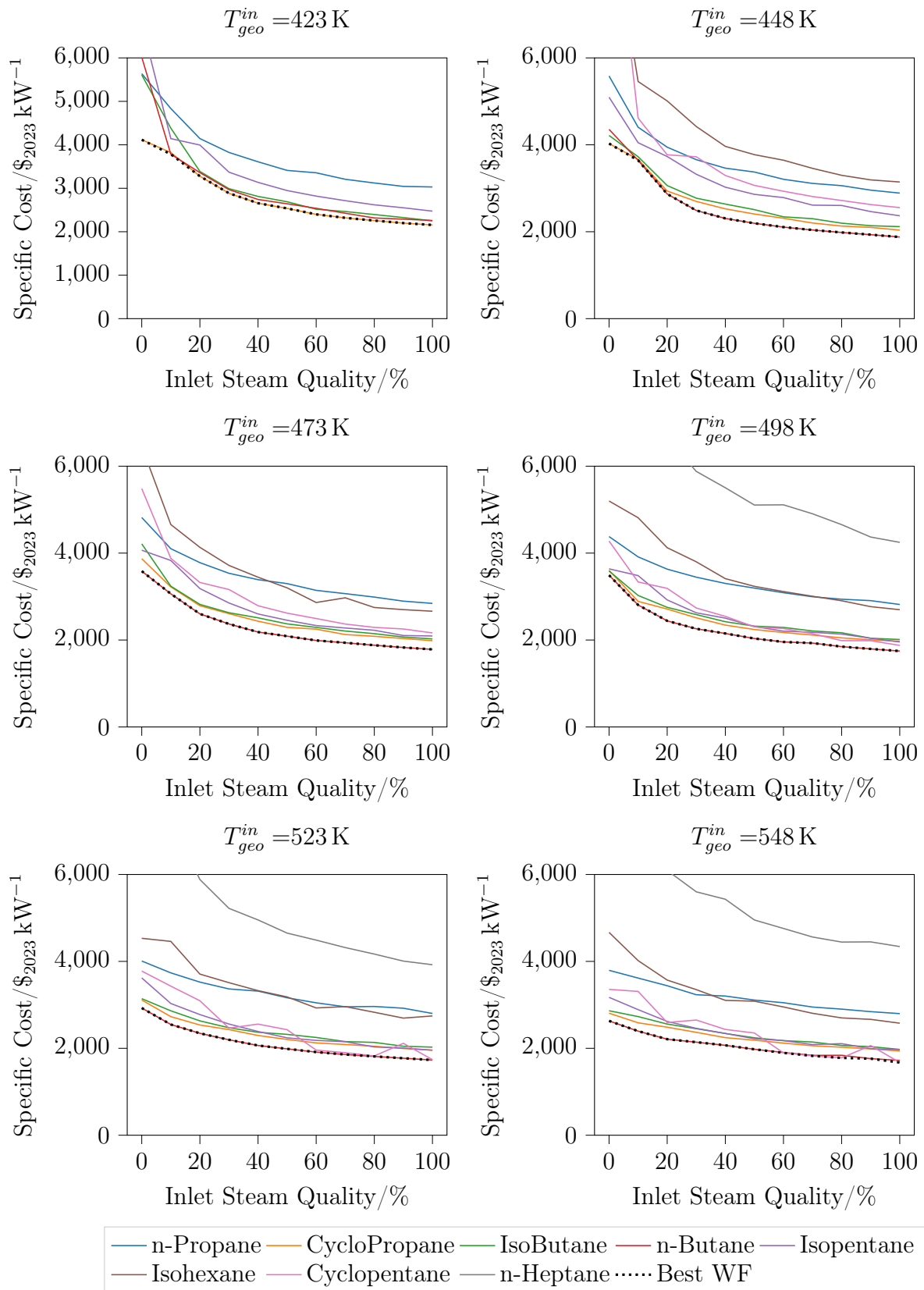


Figure 5.37: The specific plant cost as a function of inlet steam quality at different inlet temperatures for a range of working fluids. The best performing working fluid is indicated by the dotted black line

CycloPropane produces the lowest specific cost for geofluid inlet temperatures of 423 K and n-Butane produces the lowest cost for virtually all other inlet conditions investigated, see Figure 5.37. The minimum specific cost and the corresponding net electrical power across all working fluids for the different geofluid inlet conditions is shown in Figure 5.38. For saturated geofluids, better agreement between the specific cost calculated in PowerCycle and *GEOPHIRES-X* can be observed.

Note. The *oscillations* in the net power between geofluid inlet vapour qualities of 60 % to 100 %, Figure 5.38, are a result of the working fluid with the lowest specific cost switching from n-Butane to CycloPentane (and vice versa), Figure 5.37

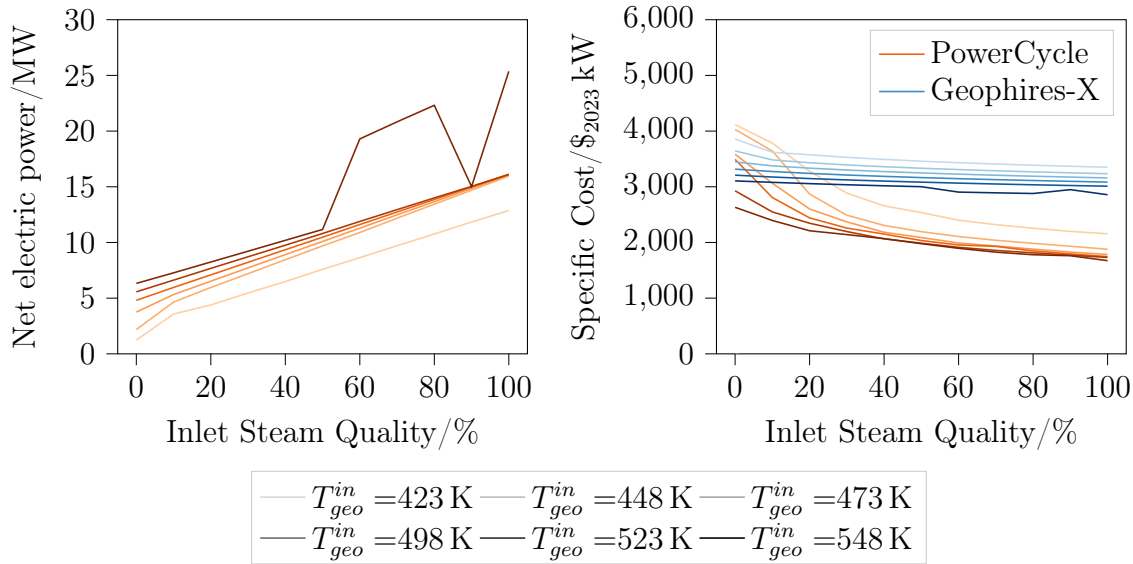


Figure 5.38: The specific plant cost (left) and the corresponding net power (right) for the best performing working fluid.

Besides the construction and secondary equipment costs, the main cost components of the binary ORC geothermal power plant are the turbine, condenser and PHE. Construction and secondary plant equipment, by definition (Section 4.4), make up 41.2 % and 16.8 % of the total plant cost respectively. Depending on the working fluid, the turbine represents between 11.5 % and 37.7 %, the condenser accounts for between 4.1 % and 25.2 %, with the remainder (between 0.6 % to 6.7 %) being attributable to the PHE, Figure 5.39. The cost of the circulation pump is negligible.

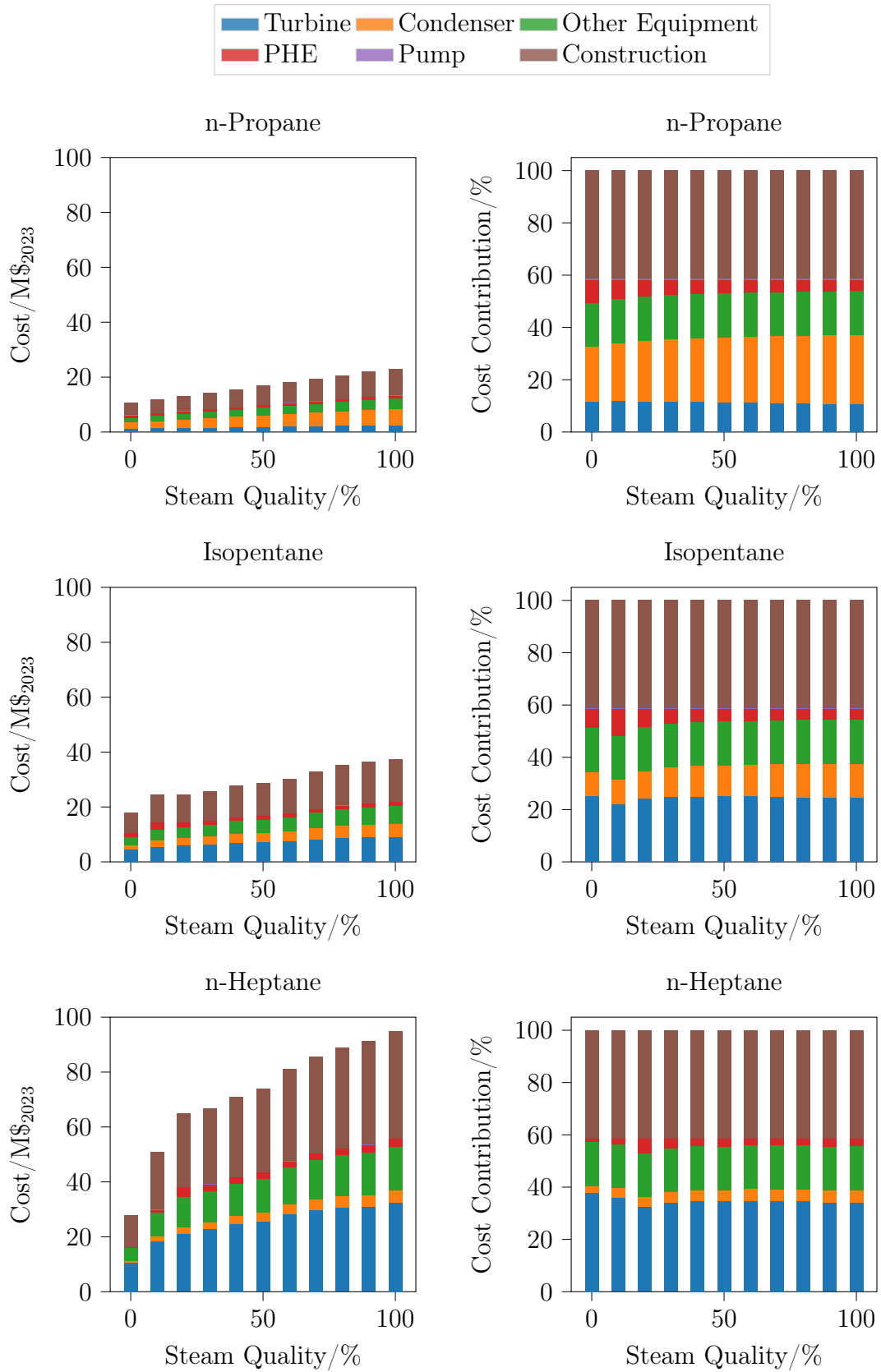


Figure 5.39: The absolute cost (left) and relative cost (right) of plant components of binary ORC geothermal power plants operating on different working fluids for a geofluid inlet temperature of 523 K (225 °C) as a function of inlet steam quality.

The cost contribution of the turbine is primarily dependent on the working fluid with lighter less complex working fluids like Propane yielding cheaper turbines than more complex working fluids such as n-Heptane, see Figure 5.40. This can be attributed to the latter requiring a larger number of stages and having a higher size parameter SP , Figure 5.41.

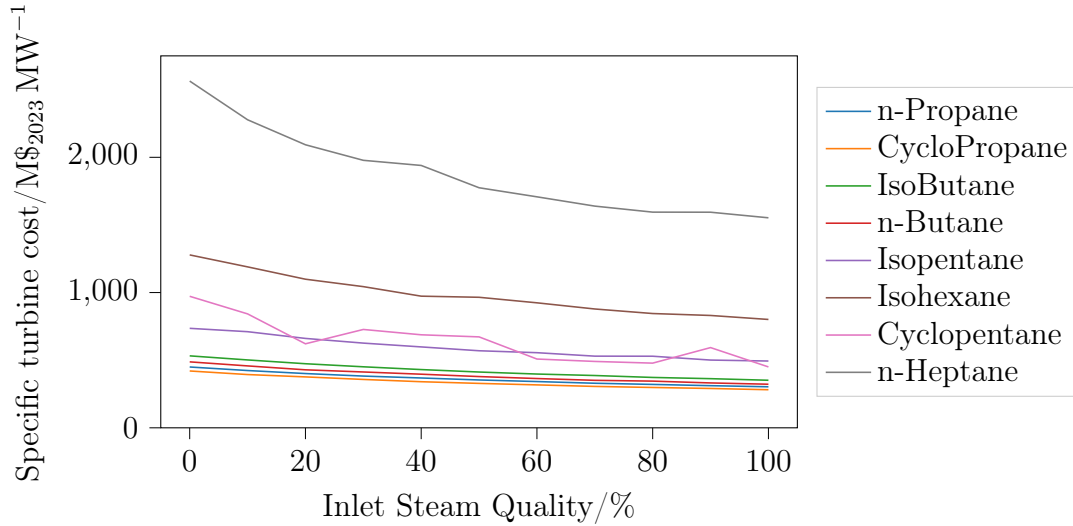


Figure 5.40: The turbine cost fluid normalised by the plant power by working for a geofluid inlet temperature of 548 K as a function of inlet vapour quality.

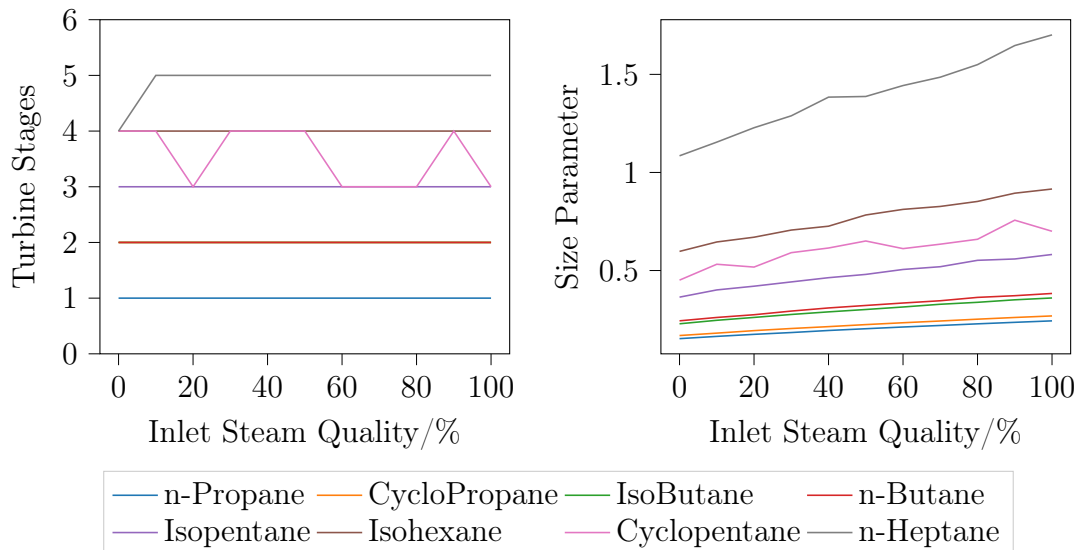


Figure 5.41: The turbine stages and size parameter SP by working fluid for a geofluid inlet temperature of 548 K as a function of inlet vapour quality.

Note. The *oscillations* in the specific turbine cost and the number of stages that can be observed for Cyclopentane, Figures 5.40 and 5.41 are a result of how the number of stages are calculated from the overall change in specific enthalpy and volume across the turbine, Equation 4.10, see Section 4.3.1. In this particular case, the minimum number of stages is numerically close to 3.0, meaning that if the value is found to be less than 3.0 it is rounded up to 3 stages, but if it is just above 3.0 it is rounded up to 4 stages.

$$n_{stages} = \left\lceil \max \left(\frac{\Delta h_{isen}^{tot}}{\Delta h_{stage}^{max}}, \log_{V_{r,stage}^{max}} V_{r,isen}^{tot} \right) \right\rceil \quad (4.10)$$

Similarly to the turbine, the specific cost of the condenser is dependent on the working fluid, with lighter less complex working fluids like Propane requiring more expensive condensers (per unit net plant power) than heavier more complex fluids like n-Heptane, Figure 5.42. This can be primarily attributed to the differences in net plant power, as the absolute condenser costs only demonstrate slight variability with working fluid. The general reduction in specific condenser cost with geofluid inlet vapour quality is a result of the increased cooling duty, and in turn heat transfer area, leading to lower specific equipment costs.

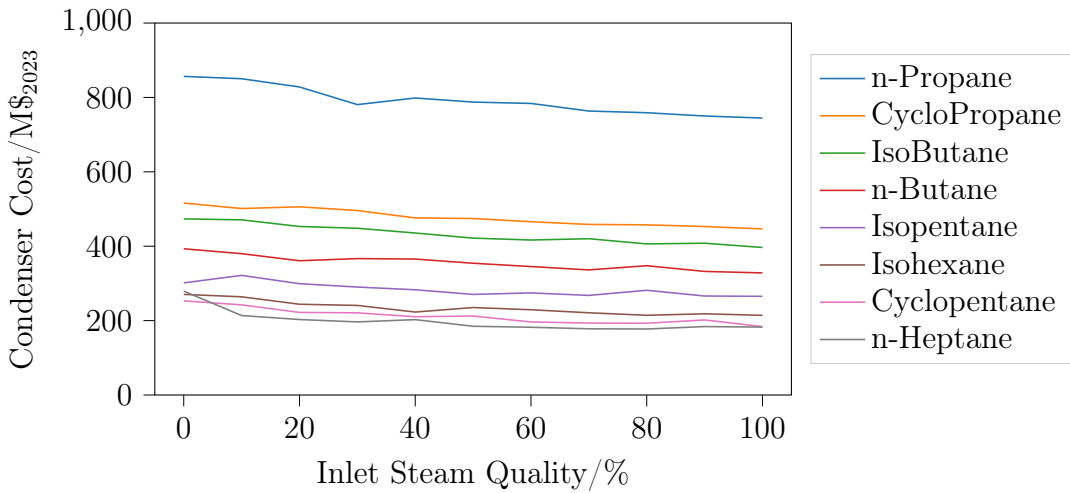


Figure 5.42: The condenser cost fluid normalised by the plant power by working for a geofluid inlet temperature of 548 K as a function of inlet vapour quality.

5.2.6. Direct Comparison

To draw a direct comparison between the single flash DSC and the binary ORC geothermal power plants, a suitable metric must first be chosen to select the optimum binary ORC

configuration amongst the configurations considered (in this case the different working fluids investigated).

For instance, if net electrical power is considered the most important, then the for each geofluid inlet condition studied, the binary ORC configuration(s) yielding the maximum net electrical power should be selected, Figure 5.43. For further comparison of plant metrics, such as the specific plant cost, the values corresponding to the selected binary ORC configuration(s) should be considered.

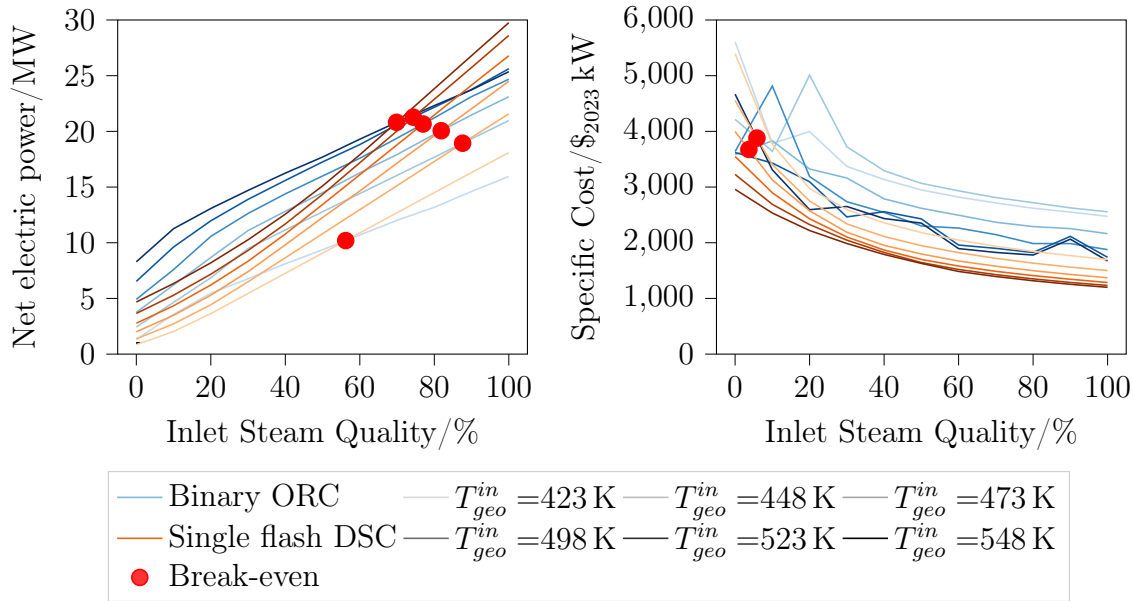


Figure 5.43: The net electrical power (left) and the corresponding specific cost (right) of the single flash DSC and the binary ORC geothermal power plants. For the binary ORC, the net electrical power is the maximum across all working fluids.

From a second law efficiency perspective, the break-even in brute-force efficiencies closely matches the break-even in net electrical power at geofluid inlet vapour qualities between around 55 % and 85 %. By contrast, for the functional efficiency the break-even is less dependent on the geofluid inlet vapour quality and occurs at around 45 %, see Figure 5.44. Combined, the two technologies generate electricity at second law efficiencies in excess of 50 % for temperatures above 200 K irrespective of the geofluid inlet vapour quality.

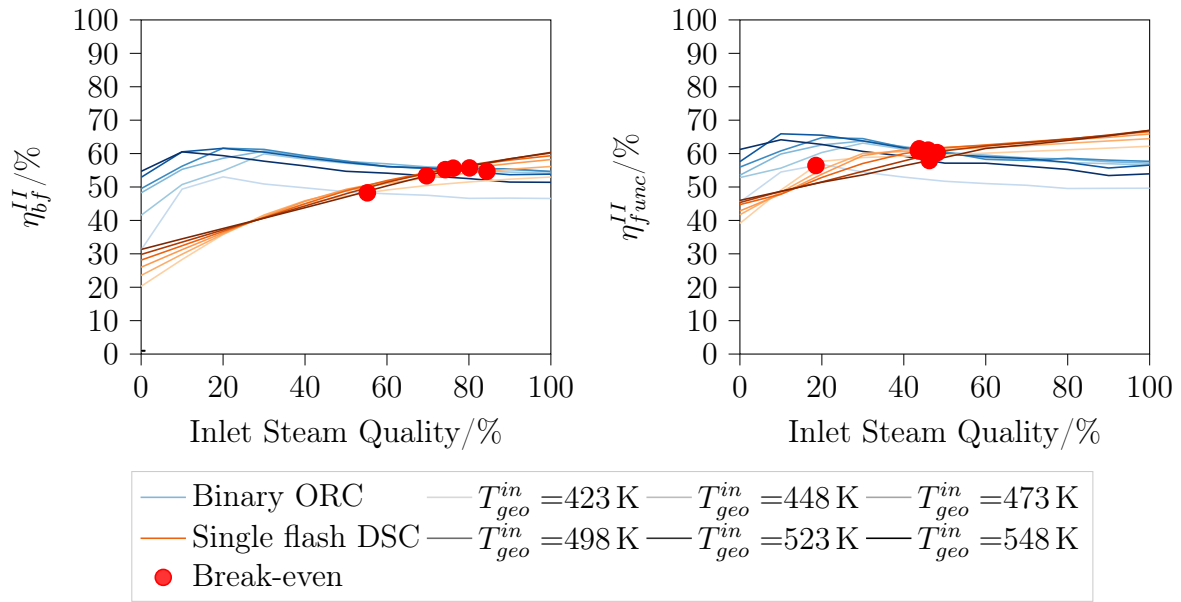


Figure 5.44: The brute-force (left) and functional (right) second law efficiency of the single flash DSC and the binary ORC geothermal power plants. For the binary ORC, the maximum efficiency across all working fluids is shown.

Plotting the geofluid inlet conditions for which the single flash DSC and binary ORC reach parity, then allows feasibility regions to be identified, Figure 5.45. Three regions can be identified:

Region 1 Left of the yellow line (representing parity in specific plant cost), where the binary ORC produces more net electrical power and at a lower specific plant cost compared to the single flash DSC.

Region 2 Between the blue line (representing parity of net electrical power) and yellow line, where the binary ORC produces more net electrical power than the single flash DSC, albeit at a higher specific cost.

Region 3 Right of the blue line, where the single flash DSC produces more net electrical power and at a lower specific plant cost than the binary ORC.

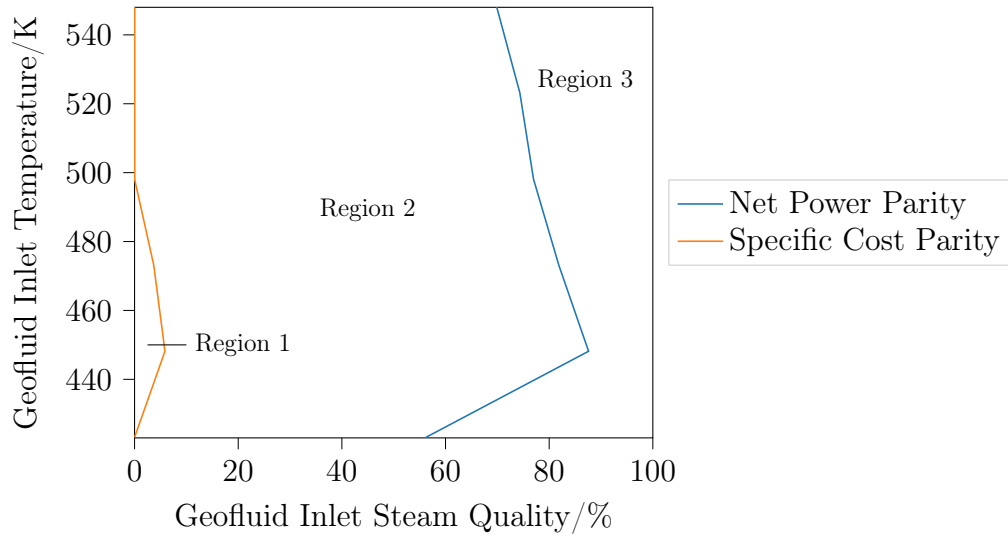


Figure 5.45: The geofluid inlet conditions for which the binary ORC and single flash DSC geothermal power plants deliver equal net electrical power and have equal specific plant cost. For the binary ORC, the net electrical power is the maximum across all working fluids.

Note. The *kink* in *Net Power Parity* line in Figure 5.45 can be attributed a change in working fluid. While the upper part of the line follows the net power parity inlet conditions of Cyclopentane, at the lowest temperature considered (423 K) Cyclopentane is not a viable working fluid, as such the next best viable working fluid, Isohexane, is selected, see Figure 5.46.

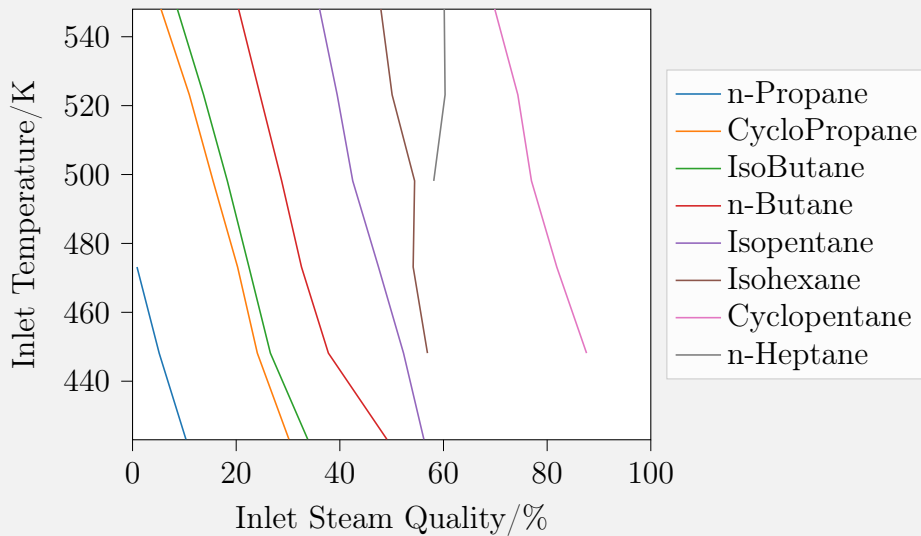


Figure 5.46: The geofluid inlet conditions for which the binary ORC and single flash DSC geothermal power plants deliver equal net electrical power by working fluid.

Similarly, if the specific cost is considered the most important metric, then the for each

geofluid inlet condition studied, the binary ORC configuration(s) yielding the minimum specific plant cost should be selected, Figure 5.47. The same three region are observed, however their spread is reduced, and Region 1 extends to higher geofluid inlet vapour qualities for all temperatures (about 20 %).

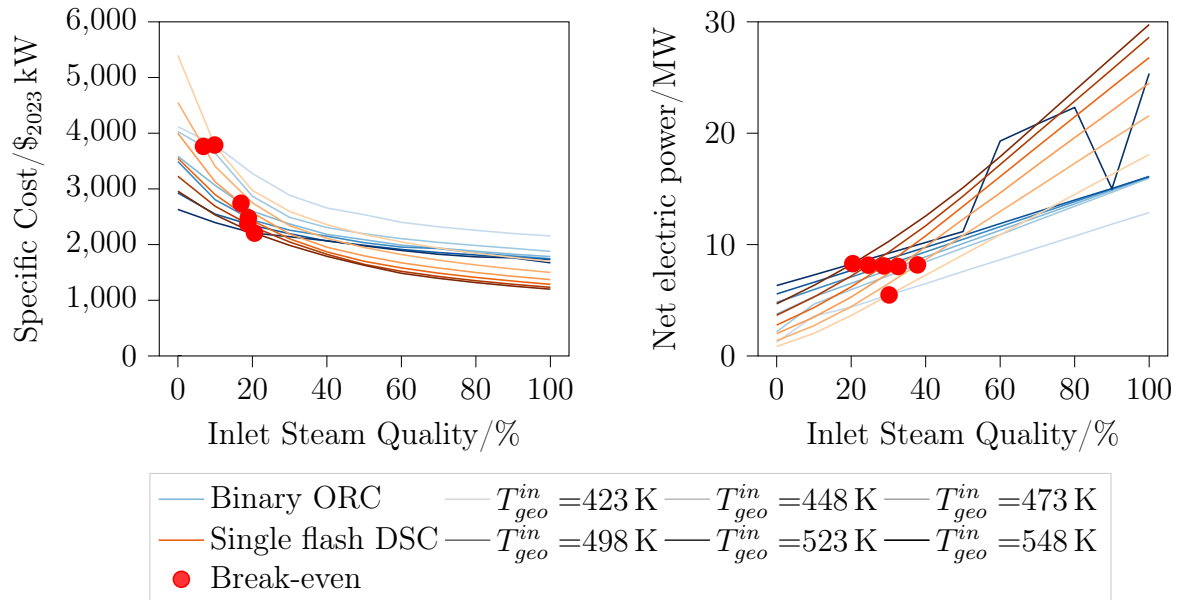


Figure 5.47: The specific plant cost (left) and the corresponding net electrical power (right) of the single flash DSC and the binary ORC. For the binary ORC, the specific plant cost is the minimum across all working fluids considered.

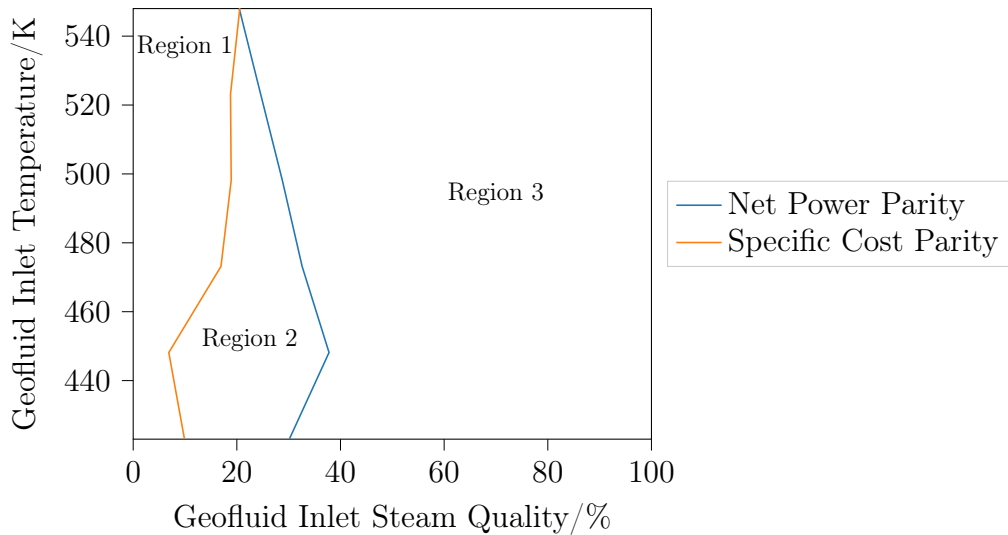


Figure 5.48: The geofluid inlet conditions for which binary ORC and single flash DSC geothermal power plants deliver equal net electrical power and have equal specific plant costs. For the binary ORC, the specific plant cost is the minimum across all working fluids considered.

5.2.7. Conclusions

Binary ORCs can thermodynamically outperform DSC geothermal power plants for a wide range of geofluid inlet conditions. However from a cost perspective, the application envelope of such thermodynamically optimised binary ORCs is limited to low geofluid inlet vapour qualities.

With the turbine and condenser being the main cost components, their size optimisation represents the largest potential for cost reductions. For instance, the size and cost of the condenser could be reduced by enforcing a larger approach temperature, at the expense of turbine power, or the use of a recuperator to improve the overall heat transfer coefficient for the cooling of the super-heating turbine outlet vapour (i.e. vapour-liquid contacting in the recuperator versus vapour-vapour contacting in the condenser).

5.3. Techno-Economic Optimisation

The following section aims to investigate the performance of techno-economically optimised single flash DSC and binary ORC geothermal power plants for two-phase geothermal heat sources.

5.3.1. Plant Configurations

The power plant configurations used for the techno-economic optimisation are the same as those used for the thermodynamic optimisation, see Section 5.2.1.

5.3.2. Boundary Conditions

The boundary conditions used for the techno-economic optimisation are the same as those used for the thermodynamic optimisation, see Section 5.2.3.

5.3.3. Optimisation Configuration

The performance of the power plants is optimised based on the specific plant cost, by adjusting the process variables. For the DSC plant, the flash pressure and the condensation pressure, as well as the minimum temperature in the condenser are adjusted; for the binary ORC plant, the evaporation pressure, the degree of super-heating and the condensation temperature, as well as the minimum approach temperature differences in the pre-heater, evaporator, super-heater and condenser are adjusted, Table 5.5, .

Table 5.5: The optimisation parameters used for the single flash DSC and the binary ORC geothermal power plants.

	Single Flash DSC	Binary ORC
Objective Function	C_{plant}	C_{plant}
Controls	$0.1 \text{ bar} \leq P_{cond} \leq 5.0 \text{ bar}$	$303 \text{ K} \leq T_{cond} \leq 400 \text{ K}$
	$0.3 \leq \frac{P_{flash}}{P_{in}} \leq 1.0$	$0.2 \leq \frac{P_{evap}}{P_{crit}} \leq 0.8$
	$2 \text{ K} \leq \Delta T_{cond}^{min} \leq 30 \text{ K}$	$3 \text{ K} \leq \Delta T_{sh} \leq 15 \text{ K}$
		$2 \text{ K} \leq \Delta T_{preh}^{min} \leq 30 \text{ K}$
		$2 \text{ K} \leq \Delta T_{evap}^{min} \leq 30 \text{ K}$
		$2 \text{ K} \leq \Delta T_{suph}^{min} \leq 30 \text{ K}$
		$2 \text{ K} \leq \Delta T_{cond}^{min} \leq 30 \text{ K}$

5.3.4. Performance Analysis: DSC

The techno-economic optimisation of the DSC geothermal power plant reduces the specific plant costs by between 7 % and 10 %, Figure 5.49, at the expense of between 10 % to 35 % of net plant power, Figure 5.50.

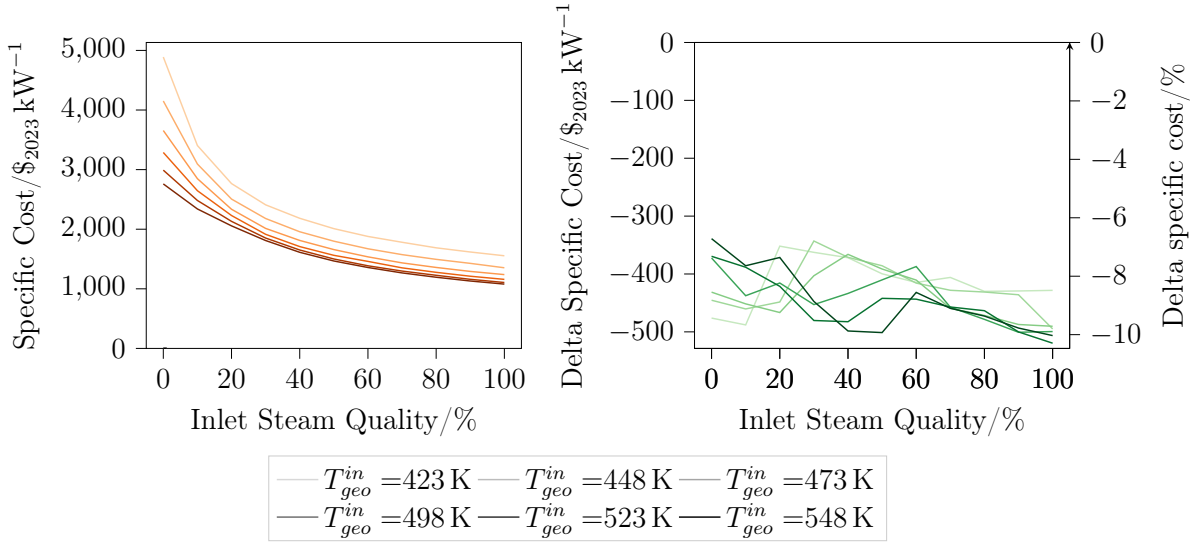


Figure 5.49: Left: the specific plant cost of the techno-economically optimised single flash DSC. Right: the change in specific plant cost compared to the thermodynamically optimised single flash DSC.

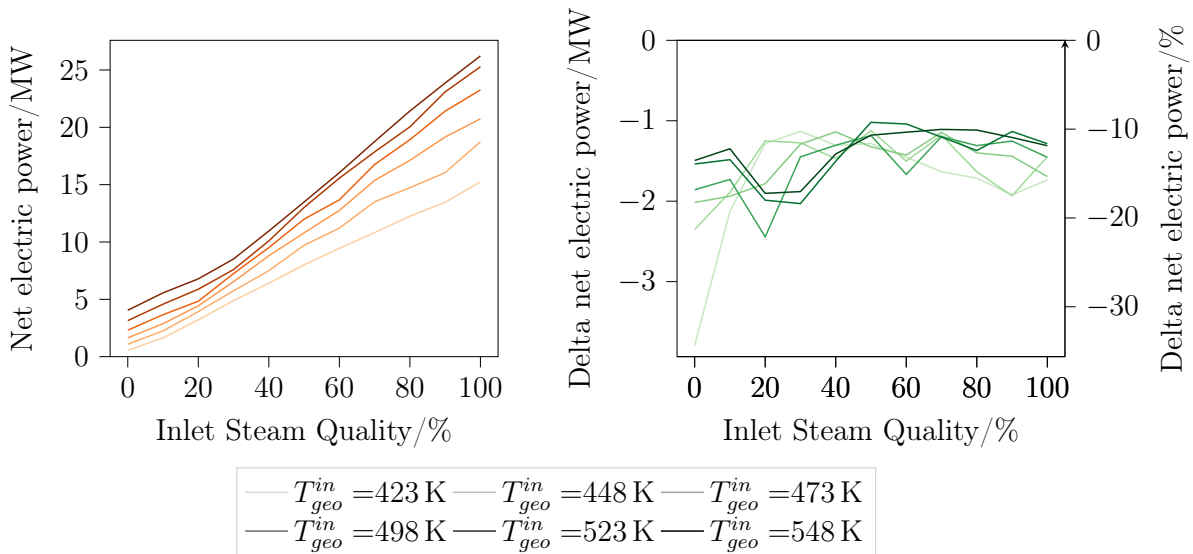


Figure 5.50: Left: the net electrical power of the techno-economically optimised single flash DSC. Right: the change in net electrical power compared to the thermodynamically optimised single flash DSC.

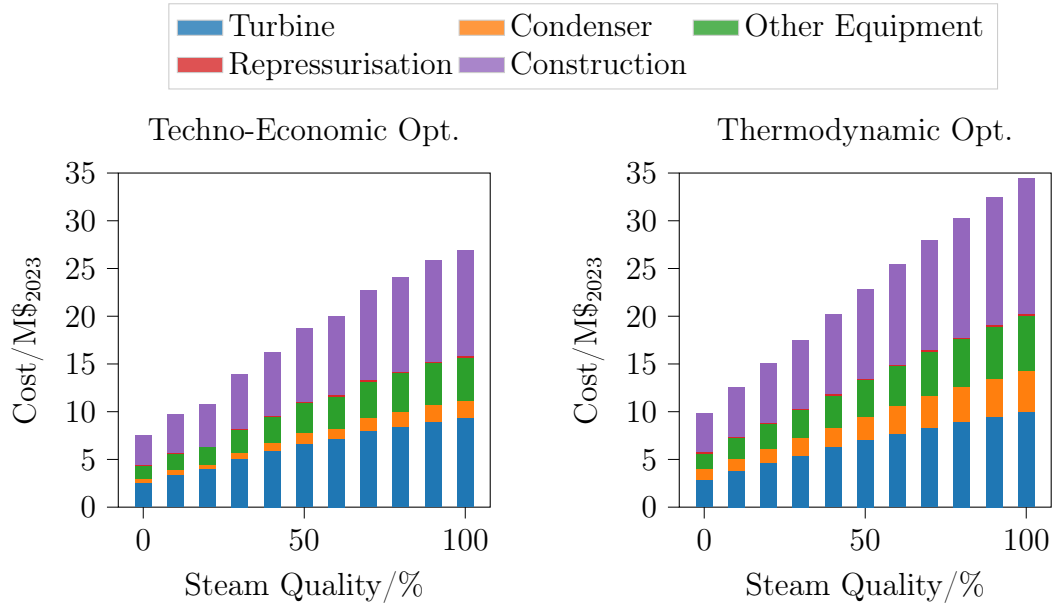


Figure 5.51: The absolute cost of plant components for techno-economically optimised (left) and thermodynamically optimised single flash DSC geothermal power plant. The geofluid inlet temperature is 523 K (225 °C).

The reduction in specific cost is primarily driven by the decrease in the cost of the condenser. Compared to the thermodynamically optimised single flash DSC, the specific cost of the condenser (relative to the net electrical power) is between 40 % to 60 % lower for the techno-economically optimised power plant. This is achieved by raising the minimum approach temperature difference in the condenser and the condensation pressure/temperature, Figure 5.52, as well as reducing the degree of flashing, compared to the thermodynamically optimised case, Figure 5.53.

Raising the minimum approach temperature difference, has the effect of providing a greater driving force for the heat transfer in the condenser, thus allowing the heat transfer area to be reduced. This in turn requires the condensation temperature to be raised to allow for the greater temperature difference, but decreases the turbine power. Reducing the degree of flashing maintains a higher turbine inlet pressure, thus providing a greater driving force for the expansion, and by virtue of reducing the vapour mass rate also reduces the duty, and thus the size of the condenser.

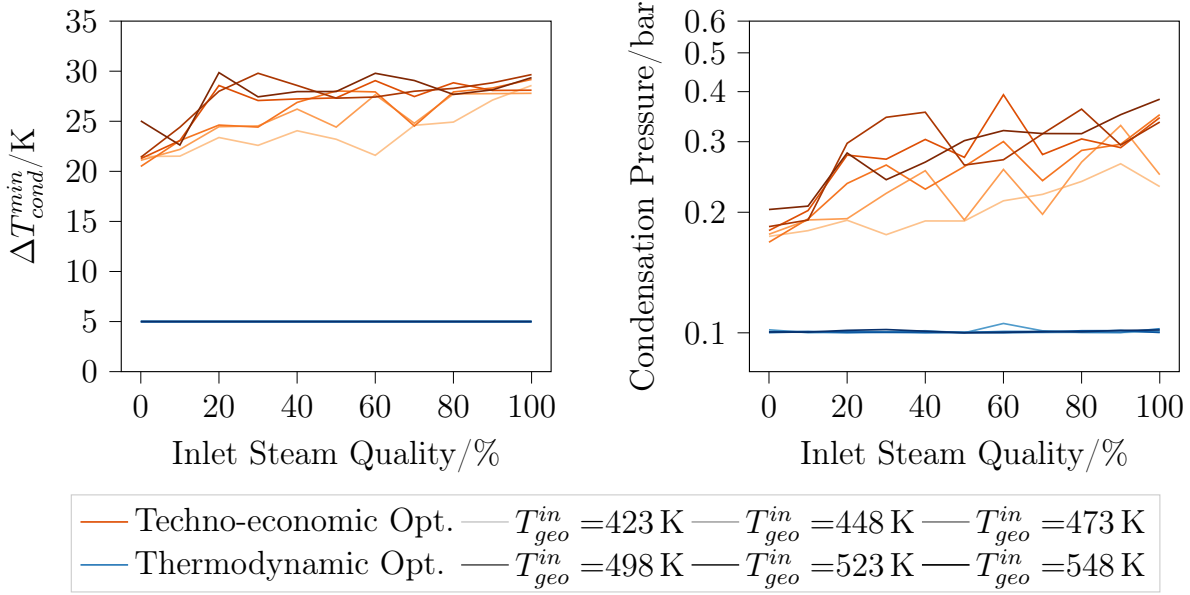


Figure 5.52: The minimum approach temperature in the condenser T_{cond}^{min} (left) and the condensation pressure (right) for a techno-economically and a thermodynamically optimised single flash DSC geothermal power plant.

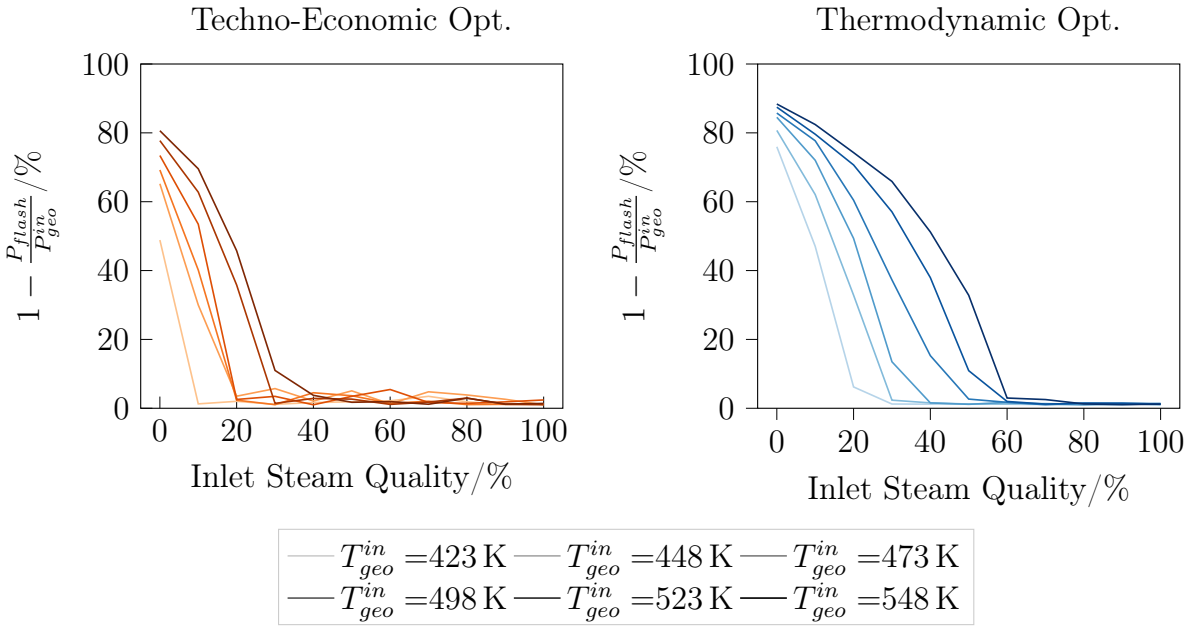


Figure 5.53: The degree of flashing X_{flash} a techno-economically (left) and a thermodynamically (right) optimised single flash DSC geothermal power plant.

5.3.5. Performance Analysis: ORC

The techno-economic optimisation of the binary ORC geothermal power plant reduces the specific plant cost by between about 20 % to 30 %, Figure 5.54, at the expense of 40 %

to 65 % of net electrical power, Figure 5.55.

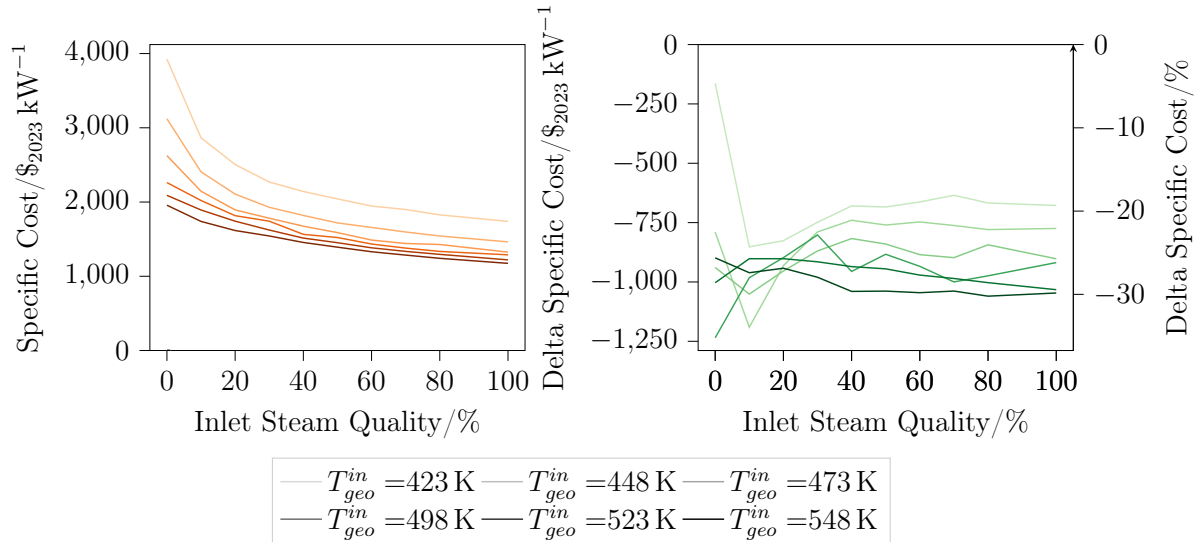


Figure 5.54: Left: the minimum specific cost of the techno-economically optimised binary ORC. Right: the difference to the minimum specific cost obtained for the thermodynamically optimised binary ORC.

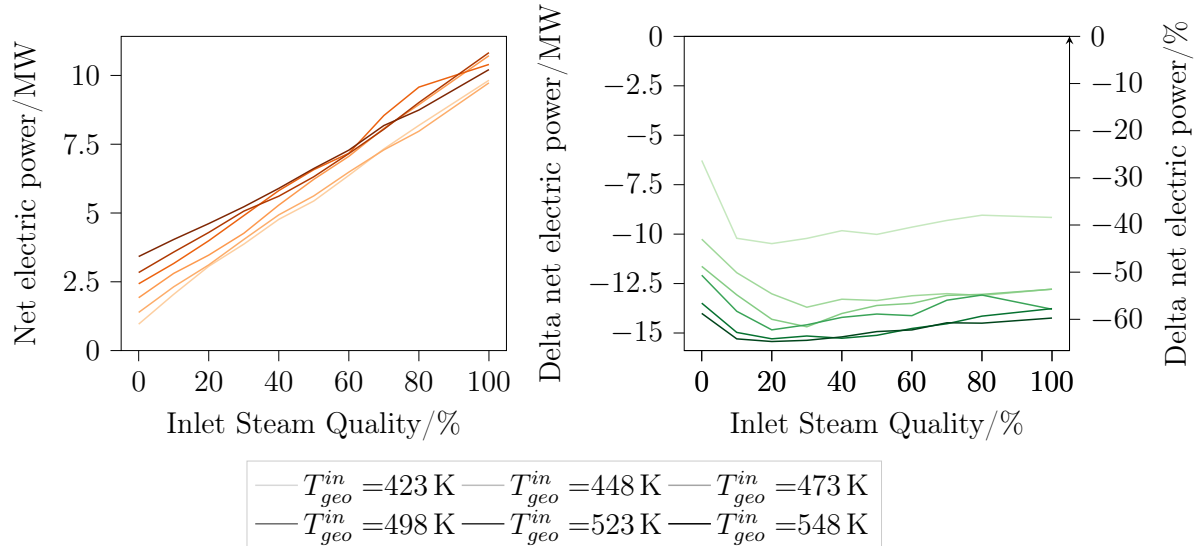


Figure 5.55: Left: the maximum net electrical power of the techno-economically optimised binary ORC. Right: the difference to the maximum net electrical power obtained for the thermodynamically optimised binary ORC.

The reduction in specific plant cost is primarily driven by the miniaturisation of the turbine and the condenser, Figure 5.56. The cost of the condenser is reduced irrespective of working fluid, while the cost of the turbine is only reduced for heavier more complex working fluids like Isopentane or n-Heptane.

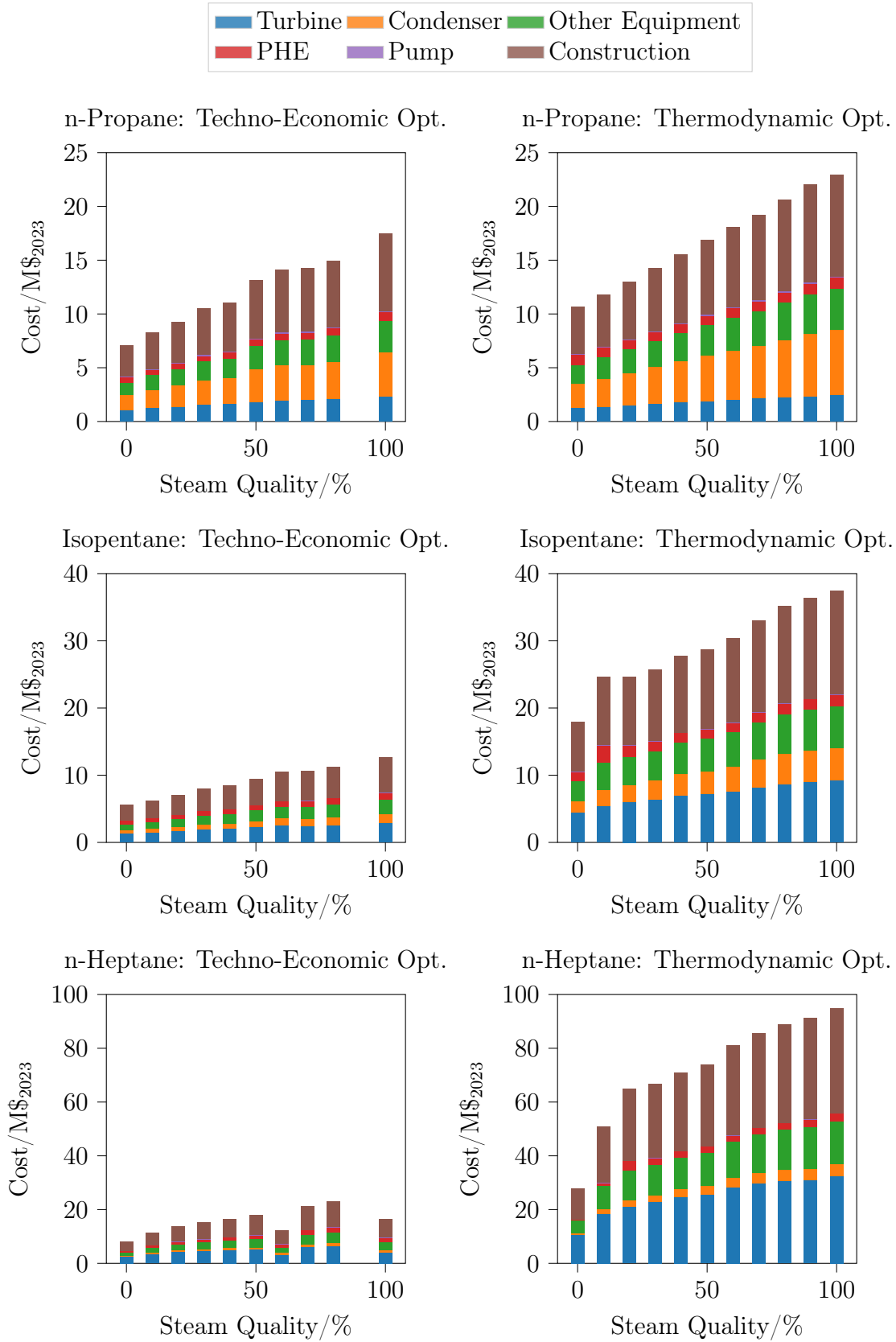


Figure 5.56: The absolute cost of plant components for techno-economically optimised (left) and thermodynamically optimised binary ORC geothermal power plants operating for different working fluids. The geofluid inlet temperature is 523 K (225 °C).

Compared to the thermodynamically optimised binary ORC, the specific cost of the turbine (relative to the net electrical plant power) is between 25% to 55% lower for the techno-economically optimised power plant. This can be attributed to significantly smaller turbines, both in terms of number of stages, Figure 5.57, and the size parameter, Figure 5.58.

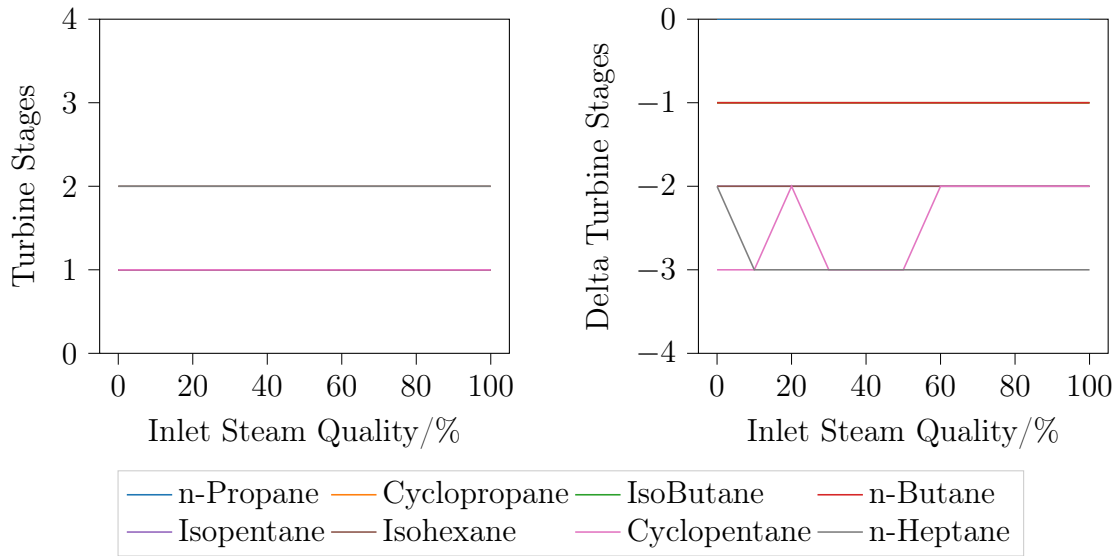


Figure 5.57: Left: the number of turbine stages of the techno-economically optimised binary ORC. Right: the change in the number of turbine stages compared to the thermodynamically optimised binary ORC.

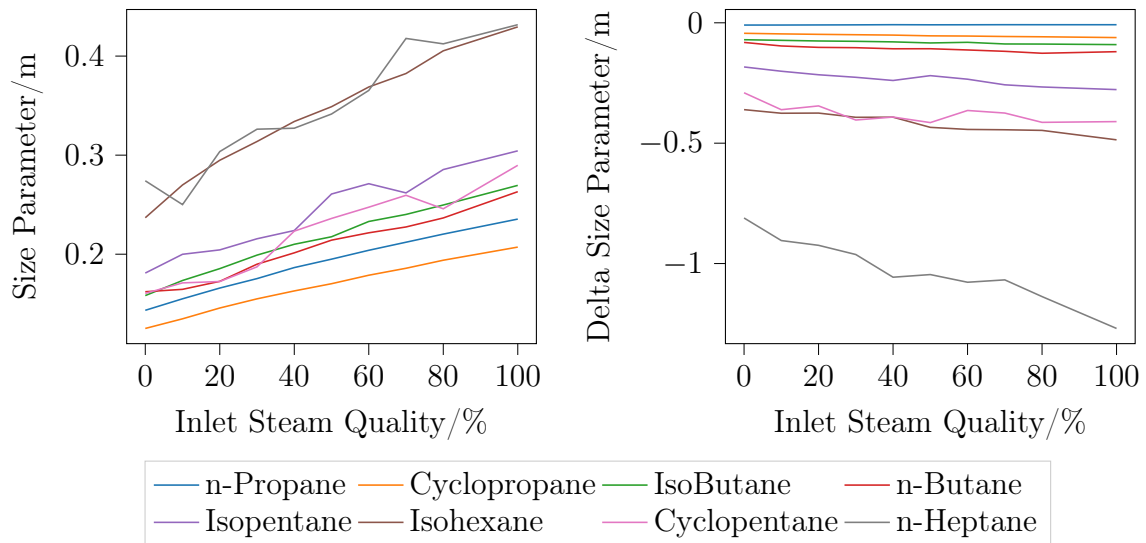


Figure 5.58: Left: the turbine size parameter of the techno-economically optimised binary ORC. Right: the change in the turbine size parameter compared to the thermodynamically optimised binary ORC.

The number of turbine stages are reduced by opting for lower evaporation pressures, thereby decreasing the expansion ratio and in turn the volume ratio across the turbine, Figure 5.59. For most working fluids, except n-Heptane, this allows the expansion to be performed with just a single stage, Figure 5.57.

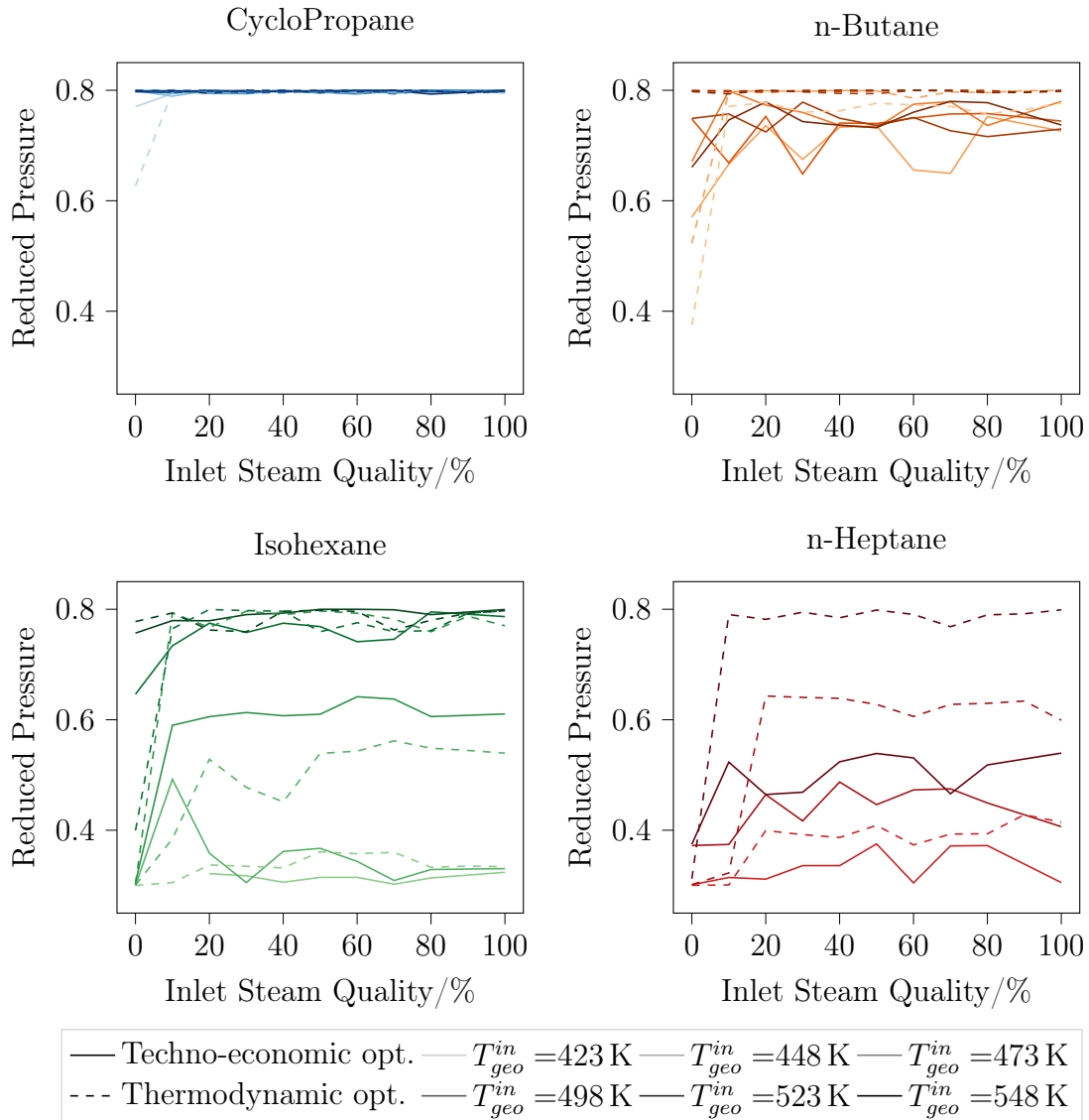


Figure 5.59: The techno-economically and thermodynamically optimised reduced pressure for some working fluids.

The size parameter SP , Equation 4.11, is reduced by raising the turbine exhaust pressure (i.e. the condensation pressure) thereby reducing the volumetric rate. In practice this is achieved by raising the minimum cycle temperature (i.e. the condensation temperature), Figure 5.60.

$$SP = \frac{\sqrt{\dot{V}_{isen}}}{\sqrt[4]{\frac{\Delta h_{isen}^{tot}}{n_{stages}}}} \quad (4.11)$$

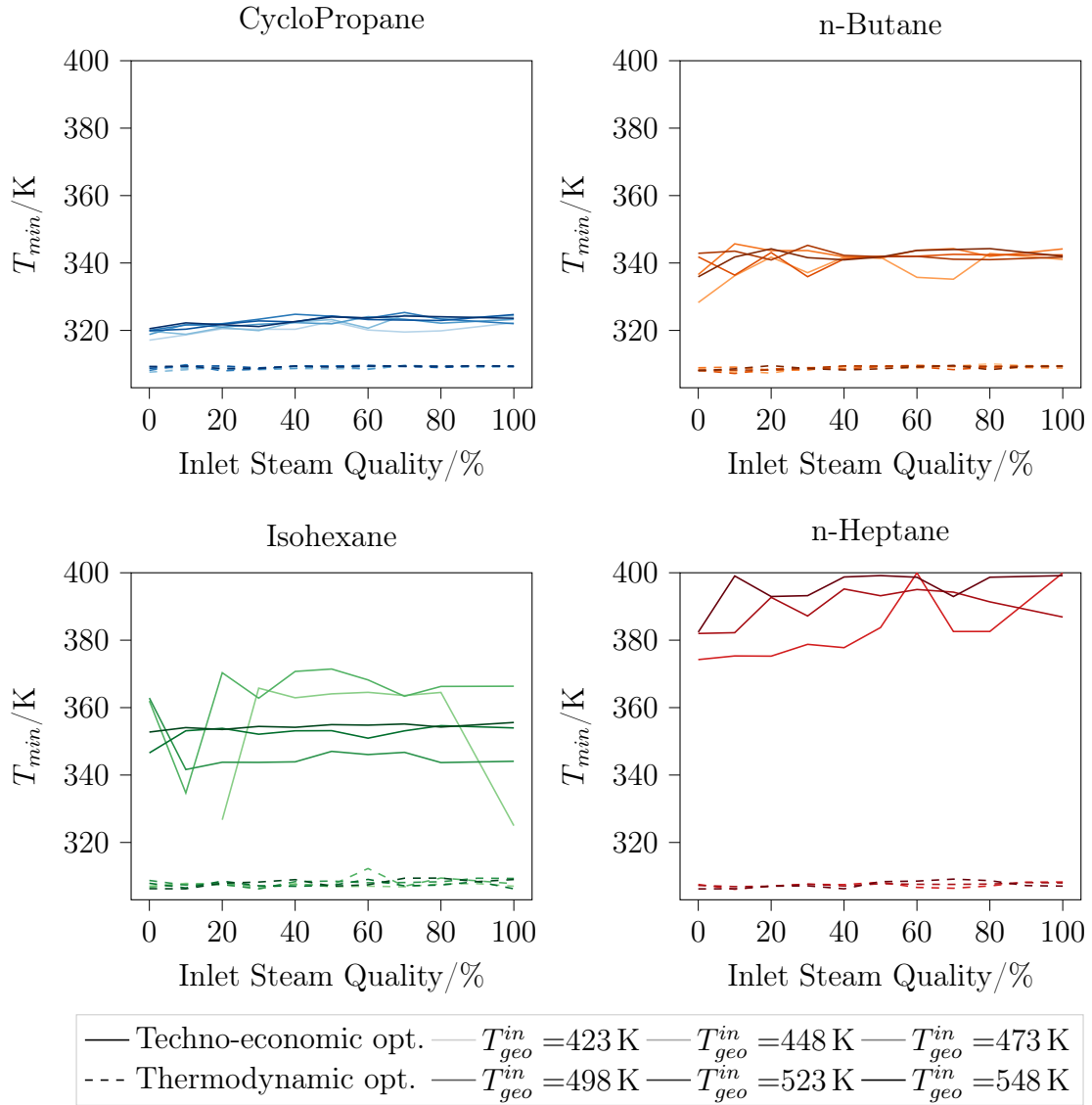


Figure 5.60: The techno-economically and thermodynamically optimised minimum cycle temperature for some working fluids.

Similarly to the single flash DSC, the condenser cost is minimised by increasing the minimum approach temperature difference, Figure 5.61, thus providing a larger driving force to the heat transfer, reducing the required heat transfer area.

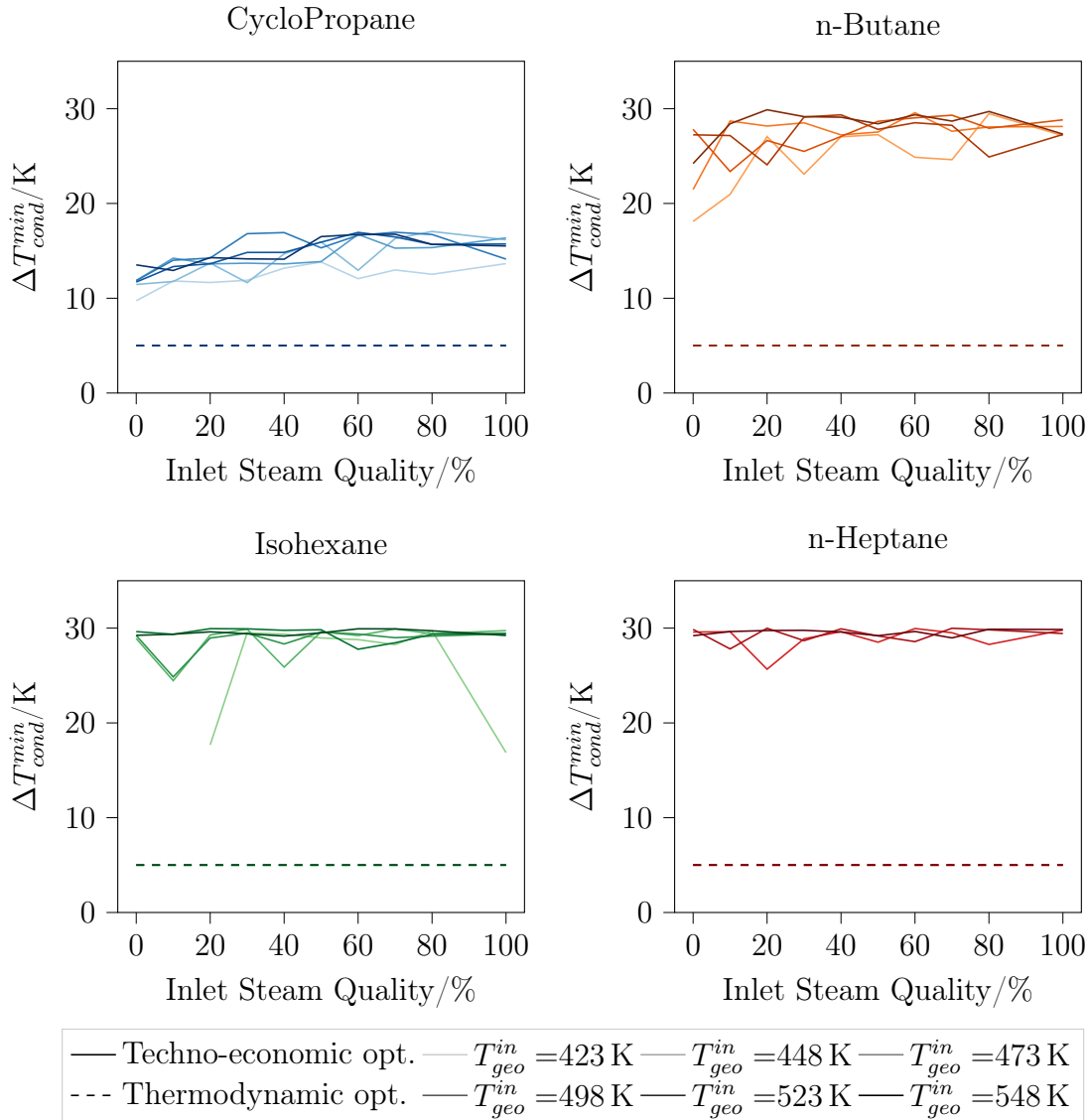


Figure 5.61: The techno-economically and thermodynamically optimised condenser minimum approach temperature difference for some working fluids.

Increasing the minimum approach temperature difference in the pre-heater, Figure 5.62, not only increases the driving force for heat transfer in the PHE, reducing the heat transfer area required, but also reduces the duty of the condenser by decreasing the working fluid mass rate. However this comes at the expense of the net electrical power generated by the power plant.

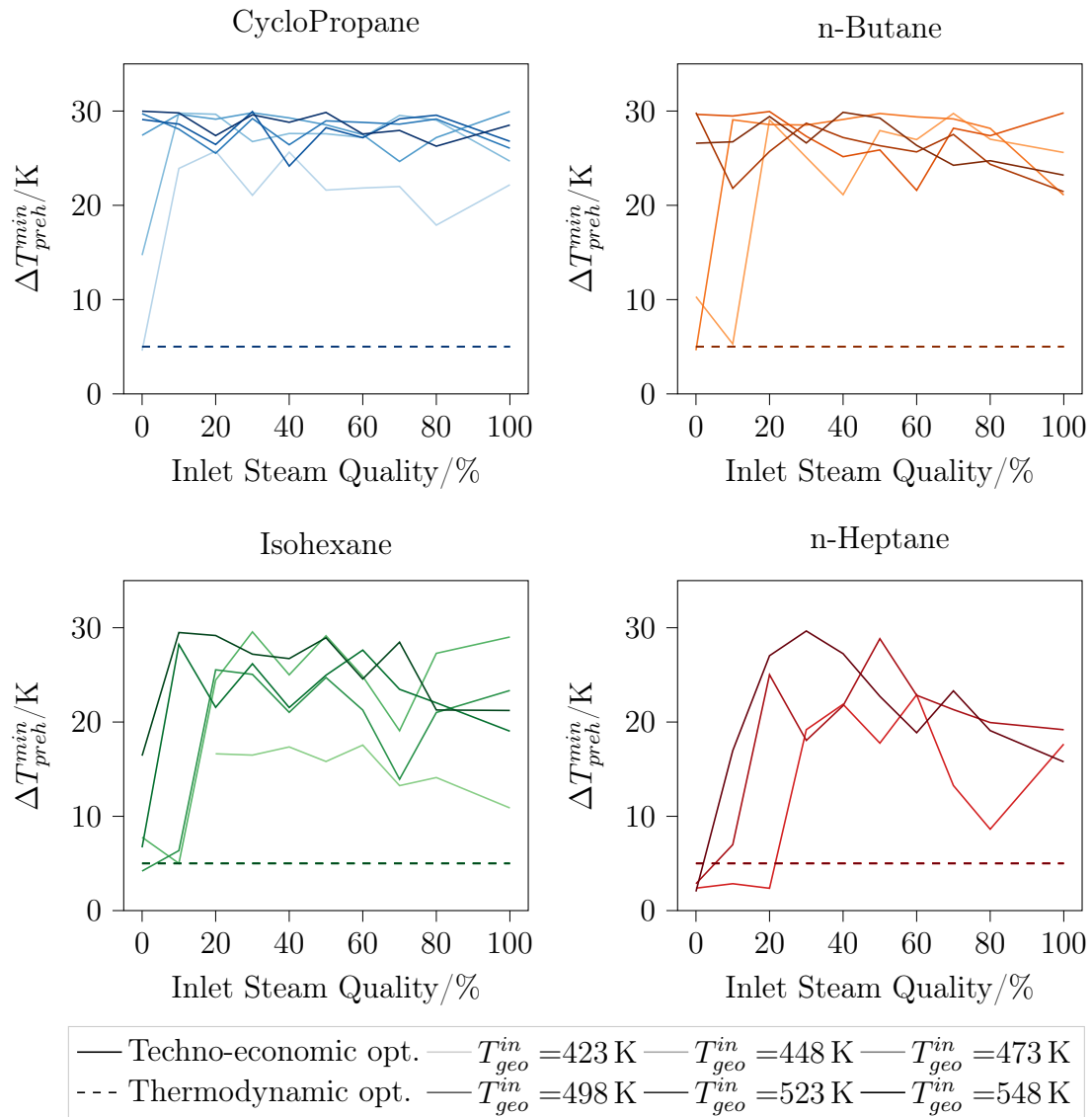


Figure 5.62: The techno-economically and thermodynamically optimised pre-heater minimum approach temperature difference for some working fluids.

Given that the pinch-point occurs within the pre-heater for most conditions investigated, the minimum approach temperature differences in the evaporator and the super-heater have no effect on the objective function.

Note:. As discussed in Section 5.2.5, the *noisiness* of the optimised variables can be attributed to the *shape* of the objective function. For example, the objective function for the techno-economic optimisation is discontinuous (e.g. the cost of the turbine), whereas the objective function for the thermodynamic optimisation is continuous. As such, changes in the optimisation variables does not necessarily translate into a change of the objective function.

5.3.6. Direct Comparison

Similarly to Section 5.2.6, a direct comparison between the single flash DSC and the binary ORC, requires the selection of a suitable metric to select the optimum binary ORC plant configuration. Based on the specific plant cost, it can be seen that binary ORC can compete up to geofluid inlet vapour qualities of 60 % to 80 %, Figure 5.63, although the net electrical power is significantly below that of the single flash DSC.

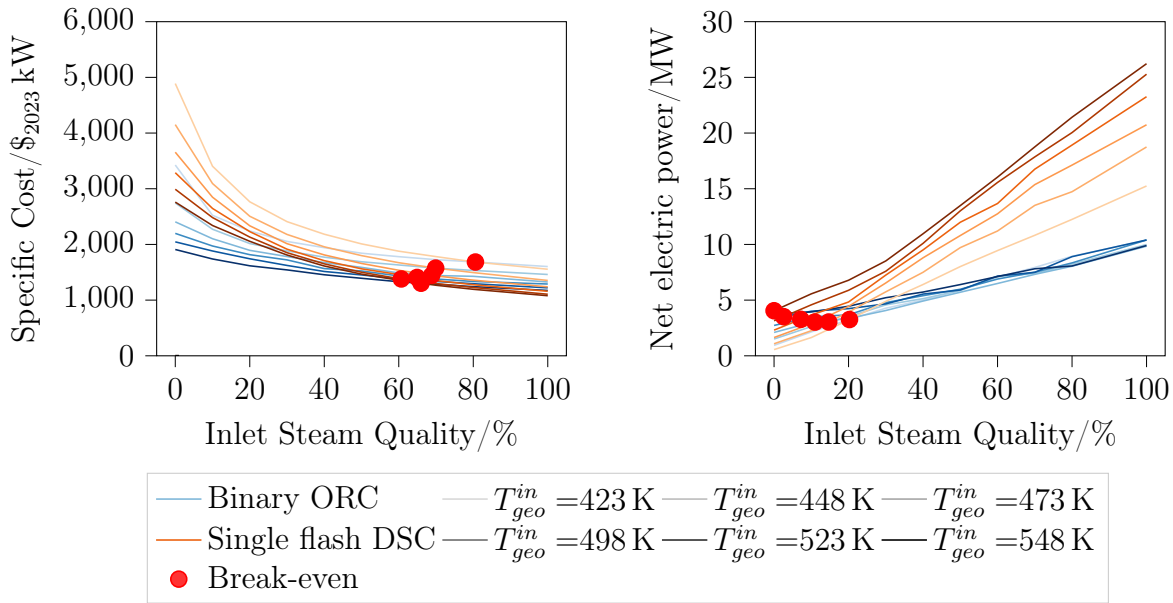


Figure 5.63: The specific plant cost (left) and the corresponding net electrical power (right) of the single flash DSC and the binary ORC. For the binary ORC, the specific cost is the minimum across all working fluids considered.

From a geofluid inlet conditions perspective, three feasibility regions can be identified:

Region 1 Left of the blue line (representing parity in net power), where the binary ORC produces more net electrical power and at a lower specific plant cost compared to the single flash DSC.

Region 2 Between the blue line and the yellow line (representing parity of specific plant cost), where the binary ORC produces less net electrical power than the single flash DSC, albeit at a lower specific cost.

Region 3 Right of the yellow line, where the single flash DSC produces more net electrical power and a lower specific plant cost than the binary ORC.

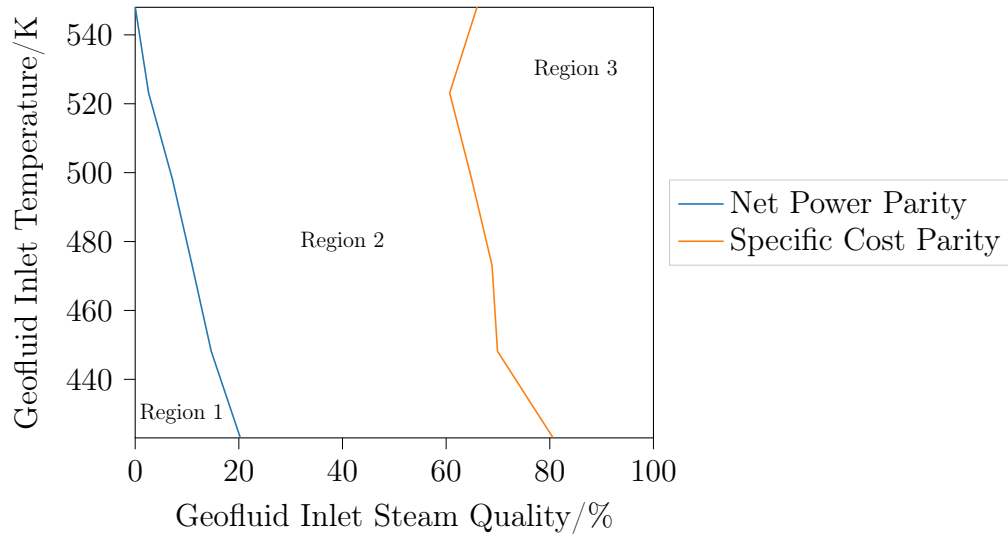


Figure 5.64: The geofluid inlet conditions for which the binary ORC and single flash DSC geothermal power plants deliver equal net electrical power and have equal specific plant costs. For the binary ORC, the specific plant cost is the minimum across all working fluids considered.

Alternatively, based on the net electrical power, it can be seen that the binary ORC can compete up to geofluid inlet vapour qualities of 10 % to 30 %, Figure 5.65 and at similar specific plant costs to the single flash DSC.

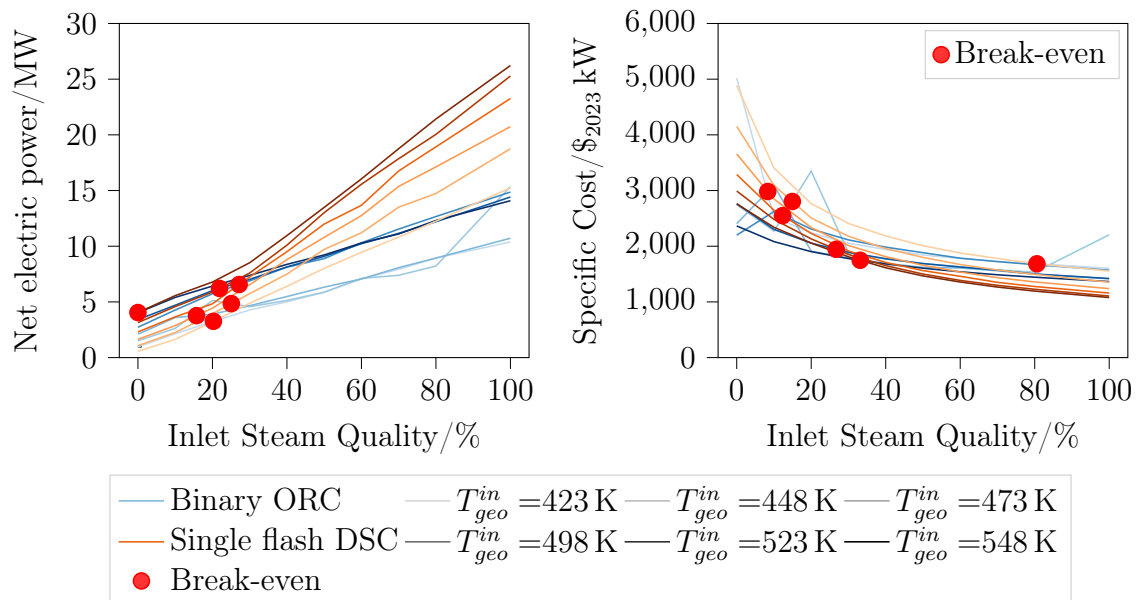


Figure 5.65: The net electrical plant power (left) and the corresponding specific plant cost (right) of the single flash DSC and the binary ORC. For the binary ORC, the net power is the maximum across all working fluids considered.

From a geofluid inlet conditions perspective, four feasibility regions can be identified:

Region 1 Left of the blue line (representing parity in net power) and left of the yellow line (representing parity in specific plant cost), where the binary ORC produces more net electrical power and at a lower specific plant cost compared to the single flash DSC.

Region 2a Right of the blue line and left of the yellow line, where the binary ORC produces less net electrical power than the single flash DSC, albeit at a lower specific cost.

Region 2b Left of the blue line and right of the yellow line, where the binary ORC produces more net electrical power than the single flash DSC, but at a higher specific cost.

Region 3 Right of the yellow line, where the single flash DSC produces more net electrical power and at a lower specific plant cost than the binary ORC.

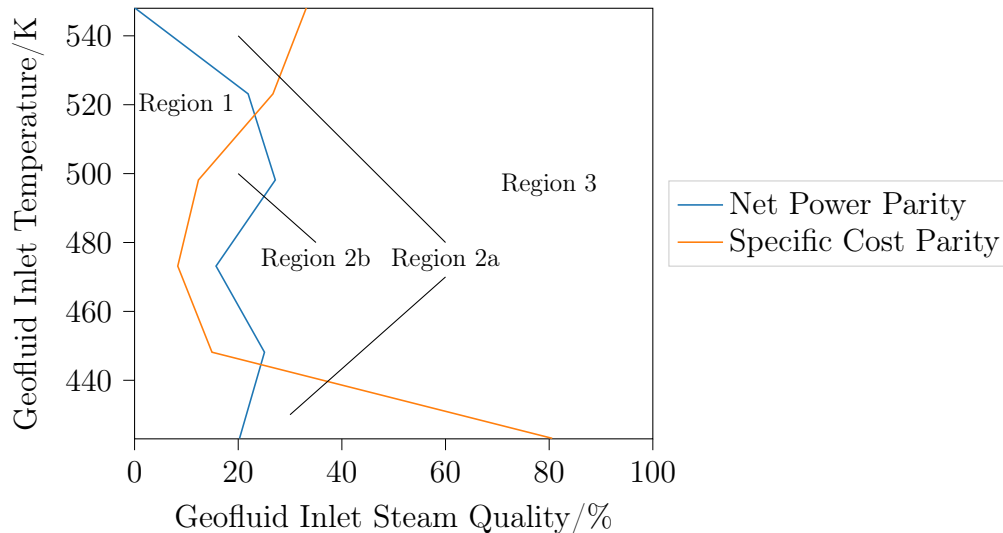


Figure 5.66: The geofluid inlet conditions for which the binary ORC and single flash DSC geothermal power plants deliver equal net electrical power and have equal specific plant costs. For the binary ORC, the net electrical power is the maximum across all working fluids considered.

5.3.7. Conclusions

For the single flash DSC, specific cost reductions of about 6 % to 10 %, at the expense of around 10 % to 20 % of net electrical power were observed. The cost reductions are almost entirely a result of a reduction in condenser size, by raising the minimum approach

temperature difference and condensation temperature. For the binary ORC, larger cost reductions of about 20 % to 30 % were observed, at the expense of up to 65 % net electrical power. For all fluids the condenser costs are reduced by raising the minimum approach temperature difference and condensation temperature, for the heavier working fluids simultaneously reducing the number of turbine stages from a maximum of 5 to a minimum of 1. Nevertheless, n-Butane achieves the lowest specific net electrical power across a broad range of geofluid inlet conditions.

From a specific cost perspective, techno-economically optimised binary ORCs can compete with single flash DSCs to geofluid inlet vapour qualities as high as 80 %, but produce significantly less power. Here, the envelope for competitive specific power and net electrical power reduces from a geofluid inlet vapour quality of 20 % at a geofluid inlet temperature 423 K to 0 % at 548 K.

5.4. Impact of Drilling Costs

The following section aims to investigate the impact of drilling costs on the design of single flash DSC and binary ORC geothermal power plants.

5.4.1. Boundary Conditions

The geofluid is assumed to be pure water, arriving at the wellhead at a temperature of 473 K (200 °C) and a steam quality 20 %. The geofluid inlet pressure is back-calculated from the inlet conditions. The mass rate of geofluid is fixed at 50 kg s⁻¹. The working fluid is assumed to be n-Butane.

Table 5.6: The boundary conditions used for the single flash DSC and the binary ORC geothermal power plants.

Condition	Values
Inlet Temperature	473 K
Inlet Steam Quality	20 %
Inlet Pressure	calculated
Outlet Pressure	$P_{geo, out} = P_{geo, in}$
Working Fluid	n-Butane

5.4.2. Optimisation Configuration

Three optimisations were considered: a thermodynamic optimisation (i.e. maximising the net electrical power) and two techno-economic optimisations (i.e. maximising the specific plant cost), and excluding and the other including the drilling cost.

For all optimisations the evaporation pressure, the degree of super-heating and condensation temperature could be adjusted by the optimiser. For the thermodynamic optimisation, the minimum approach temperature differences in the pre-heater, evaporator, super-heater and condenser are treated as constraints, whereas for the techno-economic optimisations they are adjusted by the optimiser, Table 5.7

Table 5.7: The optimisation parameters used for the single flash DSC and the binary ORC geothermal power plants.

	Thermodynamic	Techno-economic	
		incl. drilling cost	excl. drilling costs
Objective Function	W_{elec}^{net}	$\frac{C_{plant} + C_{drilling}}{W_{elec}^{net}}$	$\frac{C_{plant}}{W_{elec}^{net}}$
Controls	$303 \text{ K} \leq T_{cond} \leq 400 \text{ K}$	$303 \text{ K} \leq T_{cond} \leq 400 \text{ K}$	$303 \text{ K} \leq T_{cond} \leq 400 \text{ K}$
	$0.2 \leq \frac{P_{evap}}{P_{crit}} \leq 0.8$	$0.2 \leq \frac{P_{evap}}{P_{crit}} \leq 0.8$	$0.2 \leq \frac{P_{evap}}{P_{crit}} \leq 0.8$
	$3 \text{ K} \leq \Delta T_{sh} \leq 15 \text{ K}$	$3 \text{ K} \leq \Delta T_{sh} \leq 15 \text{ K}$	$3 \text{ K} \leq \Delta T_{sh} \leq 15 \text{ K}$
		$5 \text{ K} \leq \Delta T_{preh}^{min} \leq 30 \text{ K}$	$5 \text{ K} \leq \Delta T_{preh}^{min} \leq 30 \text{ K}$
		$10 \text{ K} \leq \Delta T_{evap}^{min} \leq 30 \text{ K}$	$10 \text{ K} \leq \Delta T_{evap}^{min} \leq 30 \text{ K}$
		$10 \text{ K} \leq \Delta T_{suph}^{min} \leq 30 \text{ K}$	$10 \text{ K} \leq \Delta T_{suph}^{min} \leq 30 \text{ K}$
		$5 \text{ K} \leq \Delta T_{cond}^{min} \leq 30 \text{ K}$	$5 \text{ K} \leq \Delta T_{cond}^{min} \leq 30 \text{ K}$
Constraints	$5 \text{ K} \leq \Delta T_{preh}^{min} \leq 30 \text{ K}$		
	$10 \text{ K} \leq \Delta T_{evap}^{min} \leq 30 \text{ K}$		
	$10 \text{ K} \leq \Delta T_{suph}^{min} \leq 30 \text{ K}$		
	$5 \text{ K} \leq \Delta T_{cond}^{min} \leq 30 \text{ K}$		

5.4.3. Results

The power plant was optimised for drilling costs ranging between zero to 60 M\$₂₀₂₃, Figure 5.67. The specific plant cost obtained from the thermodynamic and simple techno-economic optimisation, are by definition, independent of the drilling cost and form an upper and lower bound for the specific plant cost.

When the drilling cost is included in the objective function, the specific plant cost tends towards the upper bound determined from the thermodynamic optimisation. This is a result of the contribution of the plant costs towards the total cost diminishing with increasing drilling costs. As such, greater reductions in specific total plant cost can be achieved by maximising the net electrical power, instead of reducing the cost the power plant, which also tends to reduce net electrical power. The significance of this effect also depends on the working fluid, see Figure 5.68 for CycloPentane for comparison.

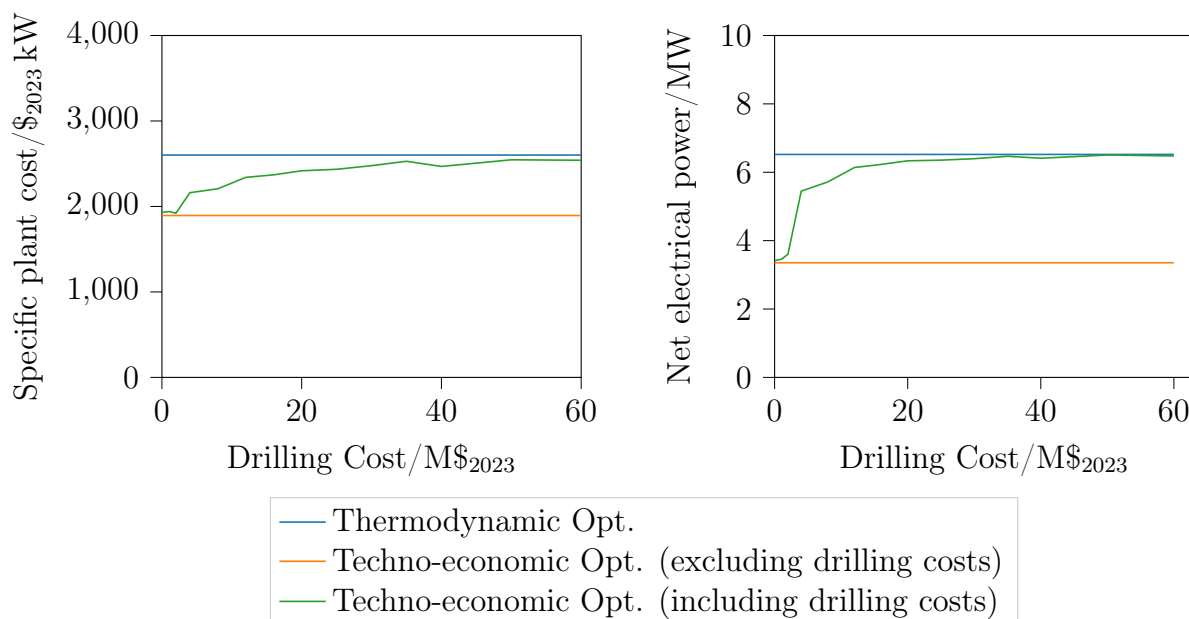


Figure 5.67: The specific plant cost (excl. drilling costs) (left) and the net electrical power (right) as obtained from the thermodynamic and techno-economic optimisations as a function of the drilling cost. The working fluid is n-Butane

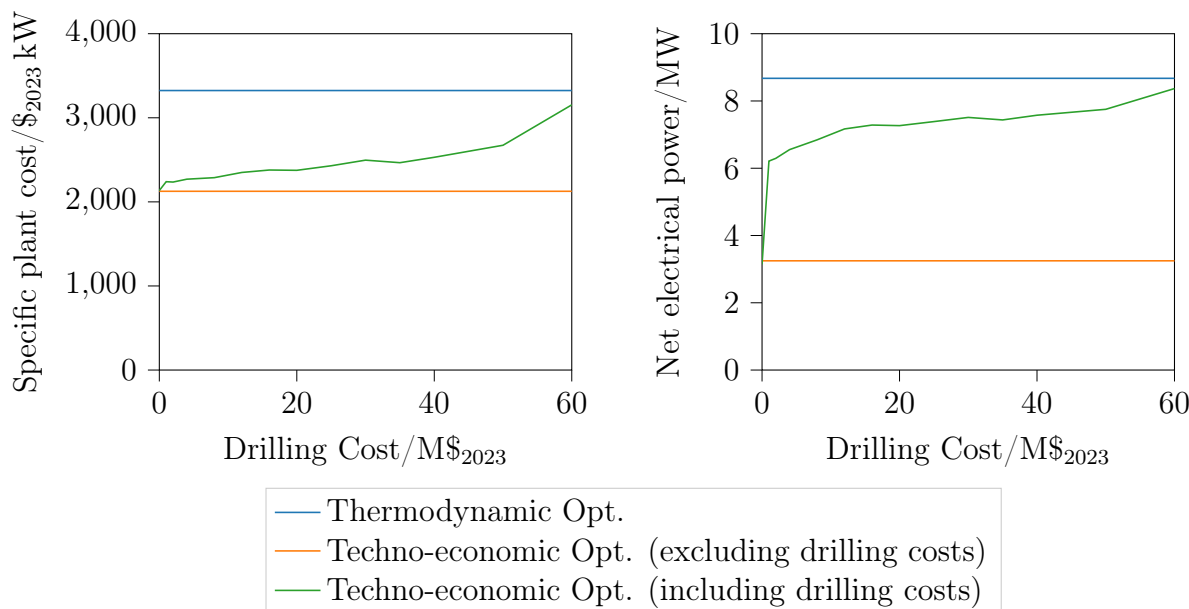


Figure 5.68: The specific plant cost (excl. drilling costs) (left) and the net electrical power (right) as obtained from the thermodynamic and techno-economic optimisations as a function of the drilling cost. The working fluid is CycloPentane

5.5. Impact of NCG handling

The presence of impurities like NCG in the geofluid represents a challenge for the operation of geothermal power plants, as they can not only be harmful and toxic, but may also pose a global warming potential. Harmful and toxic substances maybe removed by means of scrubbing the NCG stream (e.g. AMIS or CarbFix process), however species like carbon dioxide and methane are mostly released into the environment.

The following chapter focuses on the latter constituents of NCG (i.e. CO_2 and CH_4), and aims to investigate the impact of the presence of NCG in the geofluid on the performance of the power plant, as well as various options for their disposal.

5.5.1. NCG Venting

To prevent the build of NCG with the power plant, NCG must be released from the power plant. Venting to the atmosphere (following the removal of harmful constituents) represents a low-effort solution, but raises the carbon-foot print of the power plant.

Nevertheless, venting still represents a challenge to DSC geothermal power plants, as the vapour is typically expanded to sub-atmospheric conditions, see Section 5.2.4, and as such the NCG must be re-pressurised to atmospheric pressure to be vented. Binary ORCs do not face this challenge as the pressure losses within the PHE are comparatively low, and so the NCG remains about atmospheric pressure and can be vented without issue.

Plant Configurations

The DSC plant used for the thermodynamic, see Section 5.2.1 is modified to include an NCG separator following the condenser, as well as compressor and a pump to repressurise the NCG and condensate streams to atmospheric pressure (if required, Figure 5.69).

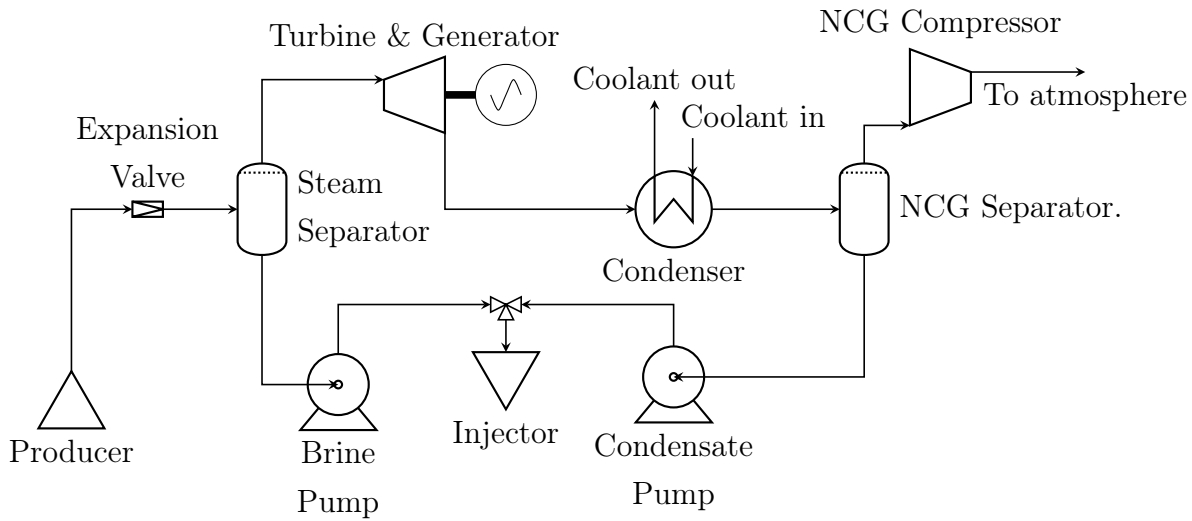


Figure 5.69: Single flash DSC geothermal power plant with NCG re-pressurisation to atmospheric pressure to allow venting.

Besides a NCG separator, the binary ORC does not required any modifications to facilitate the venting of NCG to the atmosphere, Figure 5.70.

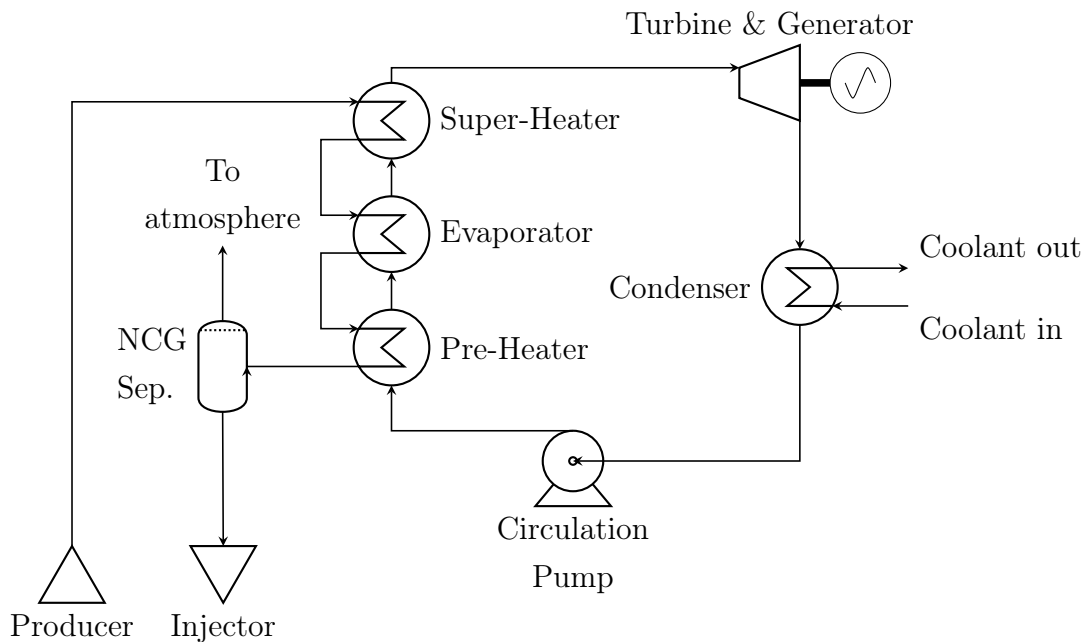


Figure 5.70: Binary ORC geothermal power plant with NCG venting to atmosphere.

Boundary Conditions and Assumptions

Unlike the previous investigations, the geofluid is assumed to be a mixture of water and carbon dioxide, ranging between pure water and up to 12 mol% CO_2 (corresponding to 30 mass% (CO_2)). The working fluid used in the binary ORC is n-Butane.

The geofluid inlet temperature and vapour quality were chosen to be 473 K (200 °C) and 20 % respectively, such that for the pure water case the binary ORC and single flash DSC have a similar net electrical power and specific cost, Figure 5.71.

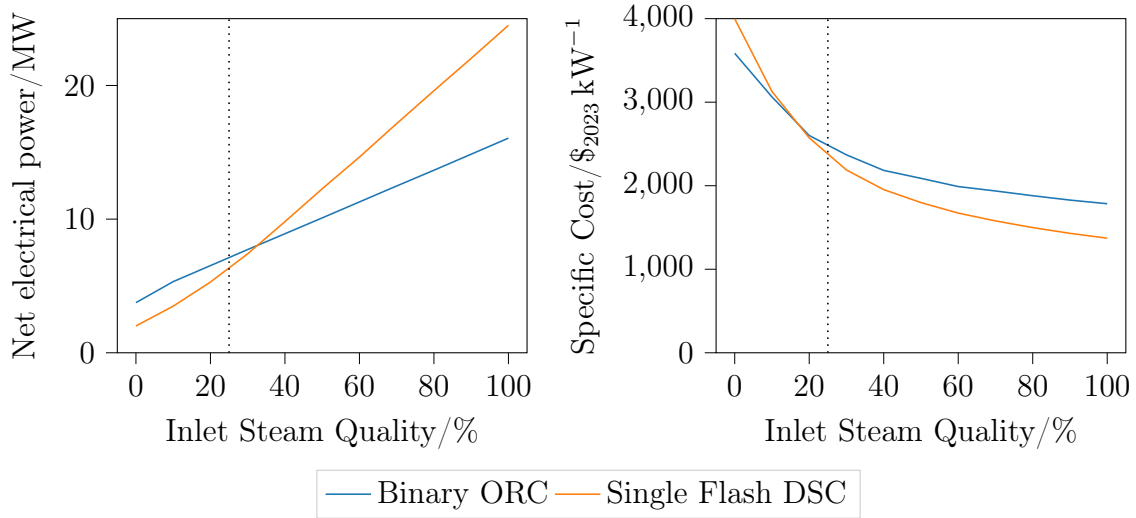


Figure 5.71: The net electrical power (left) and specific plant cost (right) of a thermodynamically optimised binary ORC using n-Butane as the working fluid and a thermodynamically optimised single flash DSC geothermal power plant, Section 5.2.

The geofluid mass flow rate is scaled to ensure a constant heat flow rate into the power plant (equal to that of pure water at the aforementioned conditions), Equation 5.9.

$$\dot{m}_{geo} = \dot{m}_{H_2O} * \frac{h_{H_2O}^{in} - h_{H_2O}^{ref}}{h_{geo}^{in} - h_{geo}^{ref}} \quad (5.9)$$

With this in mind, to minimise the scaling of the geofluid mass rate and to ensure that the geofluid compositions remain *similar*, for this study, the vapour quality of the geofluid is defined solely based on the fraction of the total amount of water that is in the vapour phase, Equation 5.10.

$$x_{geo} = \frac{\dot{n}_{H_2O}^{vap}}{\dot{n}_{H_2O}^{vap} + \dot{n}_{H_2O}^{liq}} \quad (5.10)$$

Table 5.8: The boundary conditions used for the single flash DSC and the binary ORC geothermal power plants.

Condition	Values
CO ₂ Content	$0 \text{ mol } \% \leq z_{NCG, in} \leq 15 \text{ mol } \%$
Inlet Temperature	473 K
Inlet Steam Quality	25 %
Inlet Pressure	calculated
NCG Outlet Pressure	1.1 bar
Brine/Condensate Outlet Pressure	$P_{brine/cond, out} = P_{brine/cond, in}$
Working Fluid	n-Butane

Optimisation Configuration

The two power plants are thermodynamically optimised (i.e. to maximise their net electrical power) using the same optimisation configuration as previously used in Section 5.2, see Table 5.9.

Table 5.9: The optimisation parameters used for the single flash DSC and the binary ORC geothermal power plants.

	Single Flash DSC	Binary ORC
Objective Function	$W_{net, elec}$	$W_{net, elec}$
Constraints	$\Delta T_{cond}^{min} \geq 5K$	$\Delta T_{cond}^{min} \geq 5K$ $\Delta T_{preh}^{min} \geq 5K$ $\Delta T_{evap}^{min} \geq 10K$ $\Delta T_{sh}^{min} \geq 10K$
Controls	$0.1 \text{ bar} \leq P_{cond} \leq 5.0 \text{ bar}$ $0.3 \leq \frac{P_{flash}}{P_{in}} \leq 1.0$	$303 \text{ K} \leq T_{cond} \leq 400 \text{ K}$ $0.2 \leq \frac{P_{evap}}{P_{crit}} \leq 0.8$ $3 \text{ K} \leq \Delta T_{sh} \leq 15 \text{ K}$

Results

The performance of the binary ORC is unaffected by the presence of NCG within the geofluid, Figure 5.72. This is a result of the heat flow being the same as in the pure water case, and with the pinch-point being located at the pre-heater inlet (on the working fluid side) the operating conditions of the ORC are unchanged. Moreover, as there are

no pressure losses in the PHE, the geofluid exits the PHE at a pressure equal to the inlet pressure, which is well above atmospheric pressure, Figure 5.73.

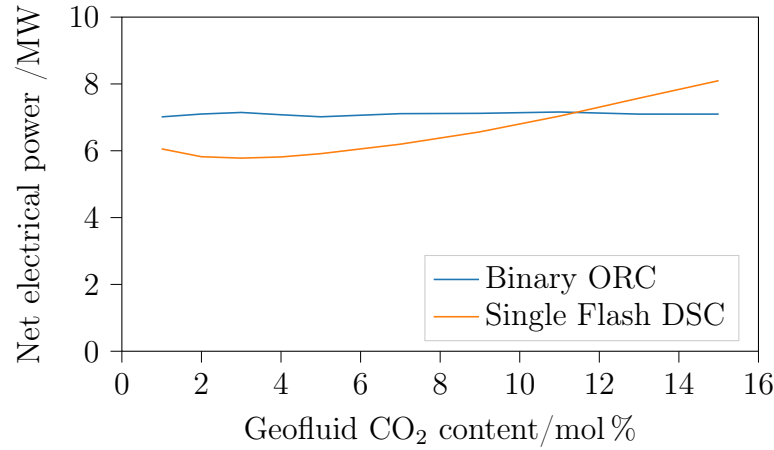


Figure 5.72: The net electrical power of thermodynamically optimised binary ORC (using n-Butane as the working fluid) and single flash DSC geothermal power plants with NCG venting to atmosphere.

On the other hand, the net electrical power of the single flash DSC initially decreases for geofluid CO₂ contents up to about 6%, but then exceeds the net power observed with pure water as the geofluid, Figure 5.72. The increase in net power can be attributed to the increase in geofluid inlet pressure, which allows for larger expansion ratios and higher turbine power, Figures 5.73 and 5.74. Although NCG handling power could be expected to increase inline with CO₂ content, reducing the degree of flashing, thus lowering the vapour mass rate, and raising the condensation pressure, thus lowering re-pressurisation power requirements, help to minimise this effect.

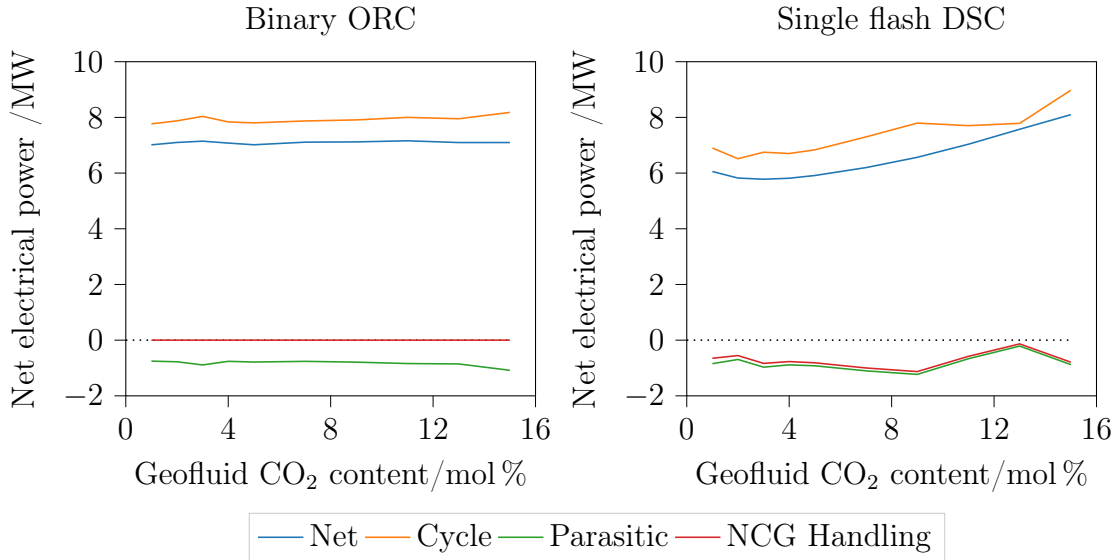


Figure 5.73: Breakdown of the net electrical power for thermodynamically optimised binary ORC (using n-Butane as the working fluid) (left) and single flash DSC (right) geothermal power plants with NCG venting to atmosphere.

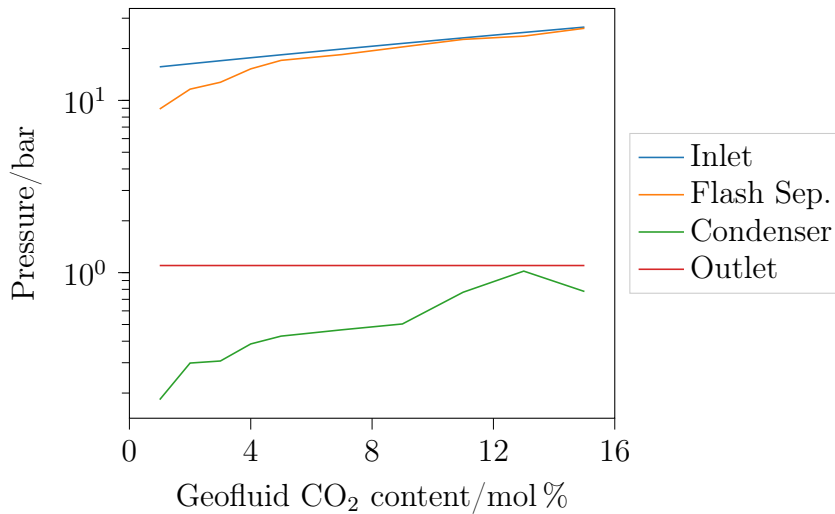


Figure 5.74: The pressures of the geofluid at different points in the power plant.

At higher geofluid CO₂ contents (above 9 %), the optimisation problem becomes degenerate as many combinations of process variables yield similar values for the objective function. For instance, increasing the degree of flashing and raising the condensation pressure has the same effect as reducing the degree of flashing and lowering the condensation pressure. While this does not significantly alter the maximum net electrical power found by the optimisation, it has a considerable impact on the cost of the power plant, Figure 5.75. This is because, in one case virtually no NCG re-pressurisation is required, while in the other it is required and represents a considerable cost item, Figure 5.76.

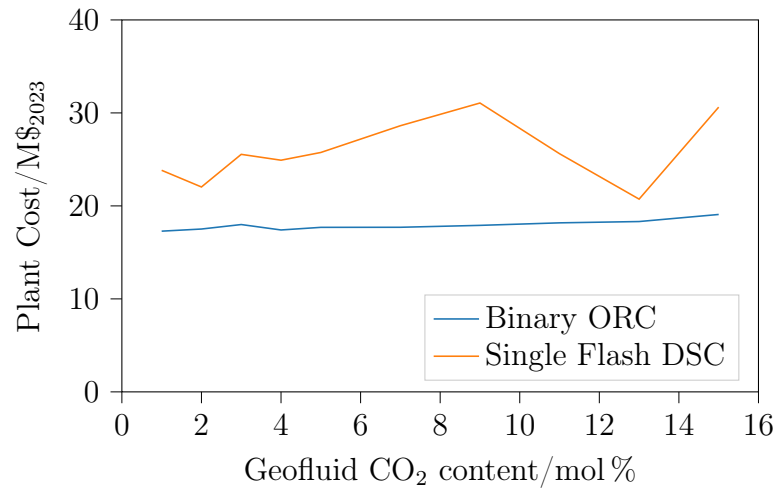


Figure 5.75: The total plant cost of thermodynamically optimised binary ORC (using n-Butane as the working fluid) and single flash DSC geothermal power plants with NCG venting to atmosphere.

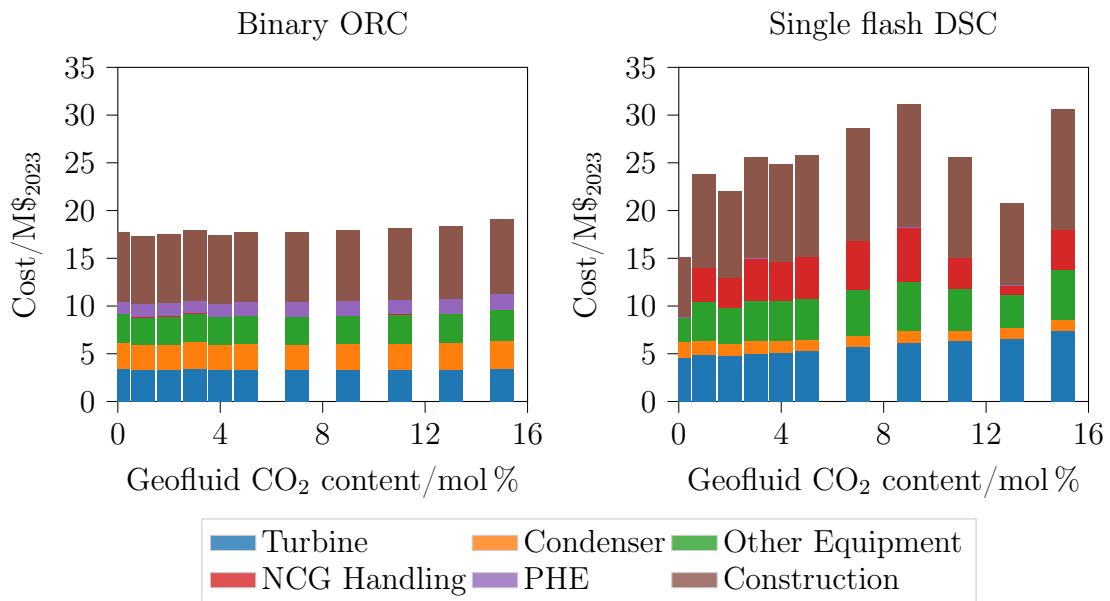


Figure 5.76: The cost breakdown of thermodynamically optimised binary ORC (using n-Butane as the working fluid) and single flash DSC geothermal power plants with NCG venting to atmosphere.

5.5.2. NCG Re-injection

In previous studies the geofluid was discharged at a pressure equal to the pressure at the power plant inlet, under the assumption that this would be sufficient to re-inject the geofluid into the reservoir. Even if higher pressures were required, as the geofluid was

assumed to be as pure water and in its liquid state at the outlet, the re-pressurisation to higher pressure would have been possible with only small reductions in net electrical power and small capital cost increases.

For geofluids comprised of water and NCG, the existence of an NCG-rich vapour phase is all but guaranteed, which poses a significant challenge for re-injection. Due to the low density of NCG, the pressures required for re-injection are about one to two orders of magnitude higher, and owing to the high compressibility of gases, the power required for compression is significant.

Note. Owing to the large differences in density between the liquid and vapour phases, injection of a two-phase fluid is likely to be technically challenging, if not impossible.

As the vapour has a lower density than the liquid, it has a natural tendency to rise in the wellbore (i.e. buoyancy). Hence, the liquid must exert a significant drag on the gas phase to prevent the vapour phase from moving upwards, towards the surface. This may be possible when the fluid is predominantly liquid (e.g. bubble flow) or predominantly vapour (i.e. mist flow), where the effect of buoyancy is reduced due to the significant drag between the bulk fluid and the bubbles/droplets.

For this reason, injection of single phase fluids is preferred. Where two-phase fluids are to be injected (e.g. brine and NCG), this can be achieved by means of a secondary tubing within the wellbore, with the one fluid flowing through the secondary tubing, and the other in the annular space between the primary and secondary tubing.

Note. The injection of liquids containing dissolved gases (e.g. brine containing dissolved NCG) is also not without risks. For instance, loss in wellhead pressure or increase in fluid temperature (i.e. during shut-in conditions), may result in previously dissolved gases coming out of solution. The presence of gas as well as its upward movement due to buoyancy, lightens the fluid in the wellbore resulting in a reducing in pressure all along the wellbore, causing more gas to come out of solution.

This run cascading effect could simply result in the accumulation of gas near the wellhead (if in shut-in conditions) or in the worst-case lead to a blow-out event.

Injection Pressure and Depth of Injection

To determine the maximum depth of injection, given the wellhead conditions of the geothermal brine and the NCG (i.e. temperature and pressure) it is useful to consider the

static pressure profiles within the wellbore.

The static pressure of the geothermal brine at a depth z can be estimated using Equation 5.11, assuming that the brine is pure water and in-compressible. Where, ρ_{brine} is the density of the brine, taken to be 1000 kg m^{-3} (i.e. independent of temperature and pressure), g the acceleration due to gravity and z the True Vertical Depth (TVD) along the wellbore.

$$P_{brine}^{static}(z) = \rho_{brine} \cdot g \cdot z \quad (5.11)$$

For the NCG, the static pressure was determined by assuming negligible heat transfer between the NCG, the brine and the surrounding formation along the wellbore, i.e. constant enthalpy. The enthalpy of the NCG at the wellhead is defined by the wellhead temperature and pressure. The static pressure along the wellbore is then determined by discretising the wellbore into N nodes and iteratively solving Equations 5.12 and 5.13. Here, P_i and P_{i+1} are the static pressure at node i and $i + 1$ respectively, g is the acceleration due to gravity, Δz is the difference in vertical depth between nodes $i + 1$ and i , and ρ_{av} is the average density between nodes i and $i + 1$. The inlet enthalpy and density are calculated using *CoolProp* treating the NCG as pure CO_2 .

$$P_{i+1} = P_i + \rho_{av} \cdot g \cdot \Delta z \quad (5.12)$$

$$\rho_{av} = \frac{\rho(h, P_i) + \rho(h, P_{i+1})}{2} \quad (5.13)$$

The depth at which the pressure of the brine and the pressure of the NCG are equal, is the maximum depth of injection. In reality, frictional losses, as well as heat transfer effects between the surrounding rock, the geothermal brine and the NCG result in injection at shallower depths.

The static pressure profiles for brine and NCG along a wellbore were calculated for a range of NCG injection pressures, Figure 5.77, assuming the brine to be pure water, a brine injection temperature and pressure (at the wellhead) of 298 K and 1 bar respectively, the NCG is pure CO_2 , and a NCG injection temperature (at the wellhead) of 298 K.

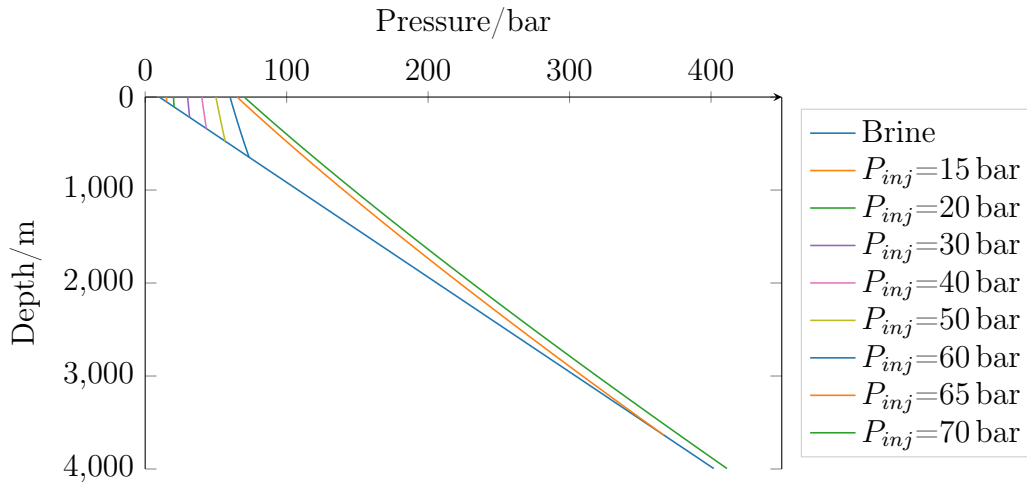


Figure 5.77: The static pressure with depth of NCG for a range of injection wellhead pressures.

From these static pressure profiles, Figure 5.77, the depth of injection can be seen to be a few hundreds of meters for NCG injection pressures up to 60 bar, which is insufficient for geothermal reservoirs. Injection depths of a few thousands of meters can be achieved with injection pressures in excess of 65 bar, which can be attributed to the CO_2 being a liquid at the wellhead. Liquefaction is possible in this case, as the NCG injection temperature at the wellhead (298 K) is below the critical temperature of CO_2 (304.12 K) and the injection pressure (65 bar) is above the saturation pressure of CO_2 (64.12 bar at 298 K).

Note.

For low NCG content geofluids, it can be thermodynamically possible to fully dissolve the NCG in the geofluids at these shallow depths of injection, allowing for the NCG to be carried to the reservoir. However, it is also important to consider the rate of mass transfer, as the dissolution must take place before the NCG can form large enough bubbles for buoyancy effects to manifest, which could lead to well unloading and a potentially catastrophic blow-out event.

To prevent this, large mass transfer coefficients and mass transfer area are required.

Besides the injection pressure, the depth of injection also depends on the temperature of the NCG at the wellhead, as this affects the density in the wellbore, Figure 5.78. For injection temperatures below 313 K, NCG can be injected to depths of 4000 m with injection pressures below 100 bar. For injection temperatures below 303 K similar depths can be obtained with just 80 bar of pressure at the wellhead.

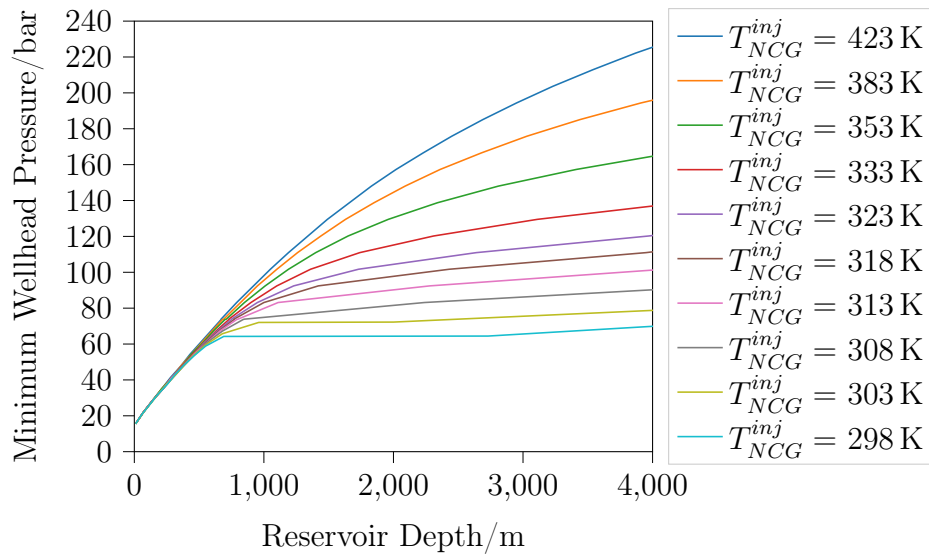


Figure 5.78: The minimum NCG injection pressure required to inject at a given depth for different NCG injection temperatures. The brine injection pressure is assumed to be 15.5 bar corresponding to the saturation pressure of pure water at 473 K.

Boundary Conditions

The boundary conditions used for this study resemble those used in the previous study, the only difference being the geofluid outlet pressure, which is assumed to be 75 bar for all outlet geofluid streams (i.e. brine, condensate and NCG).

Table 5.10: The boundary conditions used for the single flash DSC and the binary ORC geothermal power plants.

Condition	Values
CO ₂ Content	0 mol % $\leq z_{NCG, in} \leq$ 15 mol %
Inlet Temperature	473 K
Inlet Steam Quality	25 %
Inlet Pressure	calculated
Brine/Condensate/NCG Outlet Pressure	75 bar
NCG Liquefaction Temperature	300 K
Working Fluid	n-Butane

Plant Configurations

The power plants are extended with NCG handling facilities: the vapour and liquid streams are separated and then separately pressurised to the target outlet pressure of

75 bar, Figure 5.79. The brine and condensate streams (DSC only) are pressurised with pumps, and the NCG stream is pressurised to its saturation pressure at 298 K, around 64.1 bar, before liquefied and then pressurised to the target pressure.

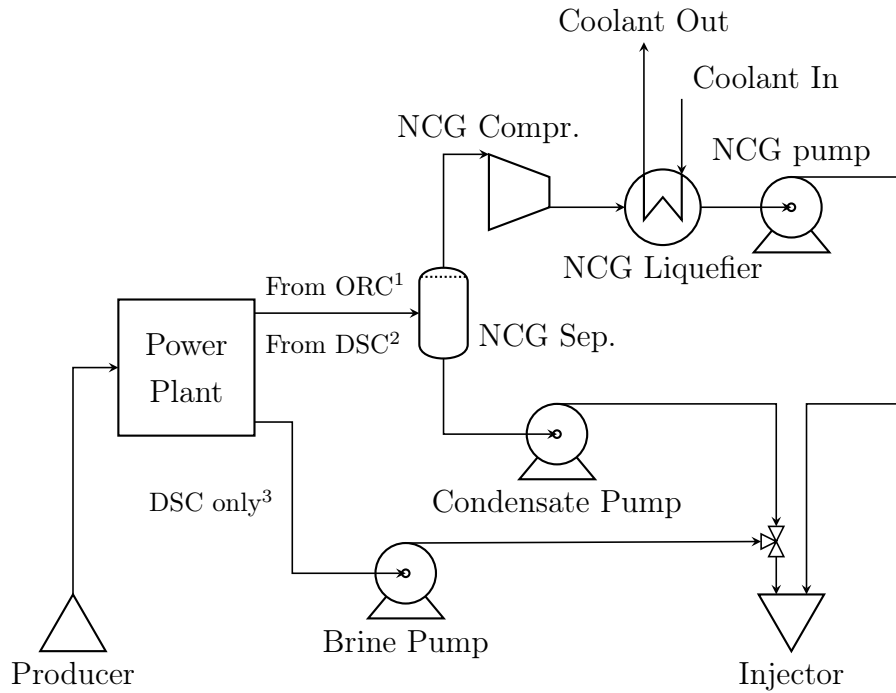


Figure 5.79: Binary ORC or single flash DSC geothermal power plants with NCG reinjection into the reservoir. ¹Geofluid from PHE. ²Condensate and NCG from Condenser. ³Brine from flash separator.

Optimisation Configuration

The power plants were optimised for the net electrical power based on the optimisation configuration used in the previous study, Section 5.5.1.

Results

Re-pressurisation of NCG for re-injection into the reservoir, significantly reduces the net electrical power of the DSC plant, with it just about breaking even at a geofluid CO₂ content of 15 % (i.e. a 100 % reduction compared to the pure water case), Figure 5.80. The net electrical power of the ORC, decreases by about 20 % over the full range of CO₂ contents studied. In both cases, the reduction can be seen to be driven entirely by the power requirements of the NCG re-pressurisation, Figure 5.81

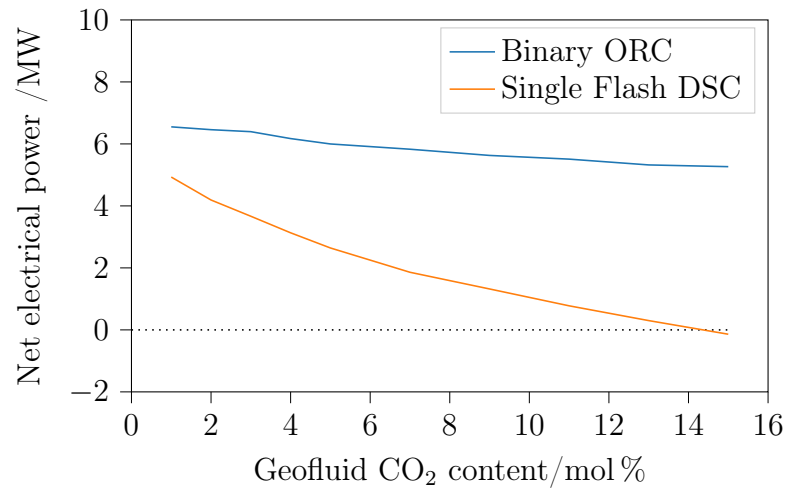


Figure 5.80: The net electrical power of thermodynamically optimised binary ORC (using n-Butane as the working fluid) and single flash DSC geothermal power plants with NCG re-pressurisation to 75 bar for re-injection into the reservoir.

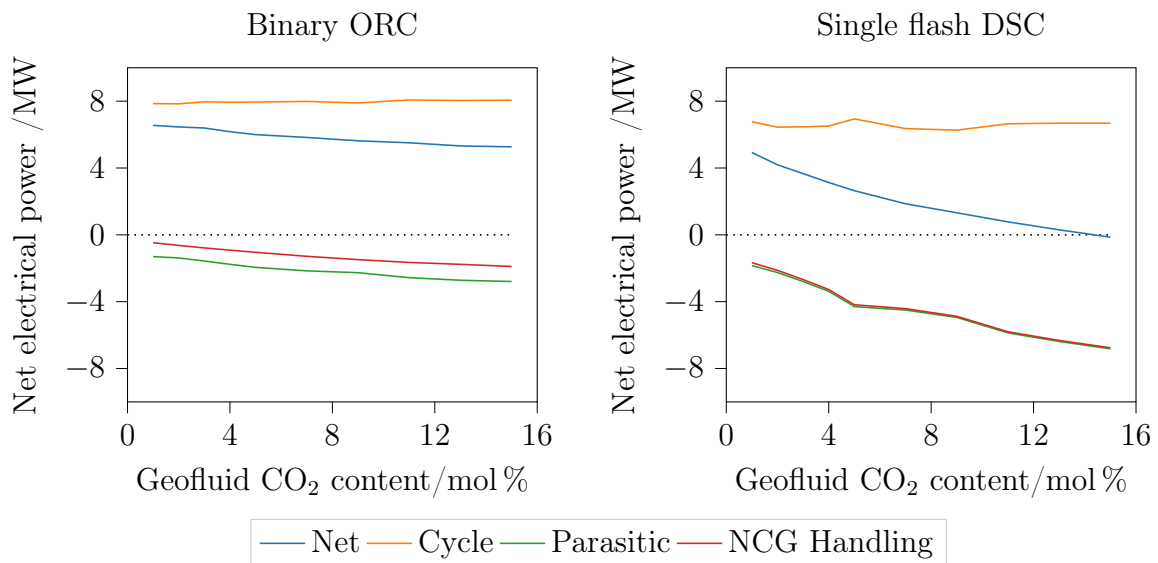


Figure 5.81: Breakdown of the net electrical power for thermodynamically optimised binary ORC (using n-Butane as the working fluid) (left) and single flash DSC (right) geothermal power plants with NCG re-pressurisation to 75 bar for re-injection into the reservoir.

However, unlike in the venting case, where the cycle (or turbine power) could be seen to marginally increase with geofluid CO_2 content for the single flash DSC, the cycle power is not strongly affected by geofluid CO_2 content. Given the re-pressurisation power is on a comparable magnitude to the turbine power, it is favourable to raise the condensation pressure to reduce the required compression ratio and hence power requirement,

Figure 5.82.

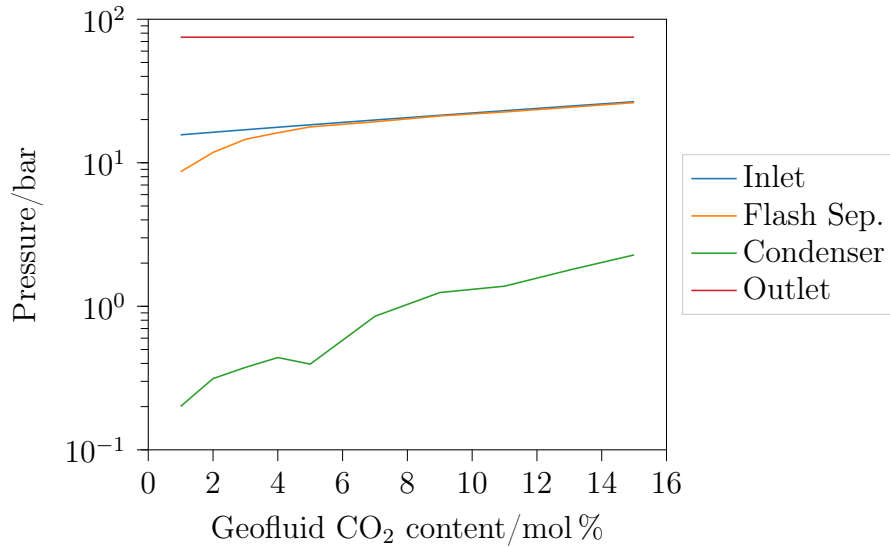


Figure 5.82: The pressures of the geofluid at different points in the single flash geothermal power plant.

The cost of the binary ORC roughly doubles compared to the pure water, while the single flash DSC increases by a factor of 2.6, Figure 5.83. Compared to the venting case, where NCG handling already presented a significant cost item for the DSC, the NCG handling is now the primary cost item for both the binary ORC and the DSC plant, Figure 5.84.

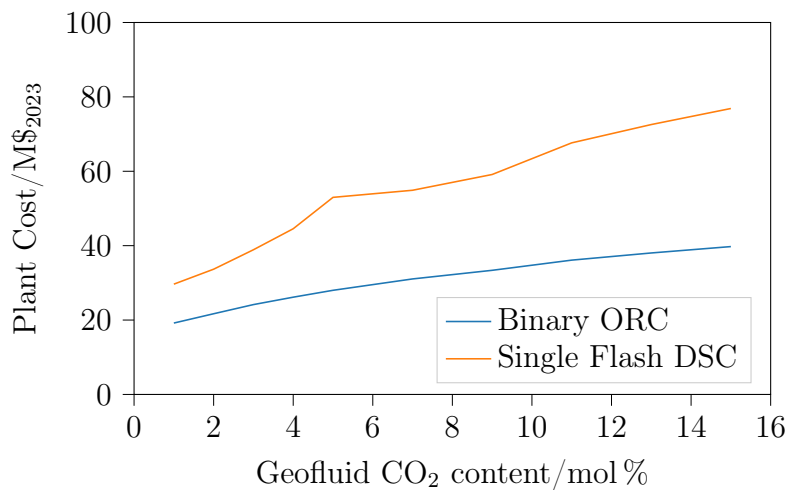


Figure 5.83: The total plant cost of thermodynamically optimised binary ORC (using n-Butane as the working fluid) and single flash DSC geothermal power plants with NCG re-pressurisation to 75 bar for re-injection into the reservoir.

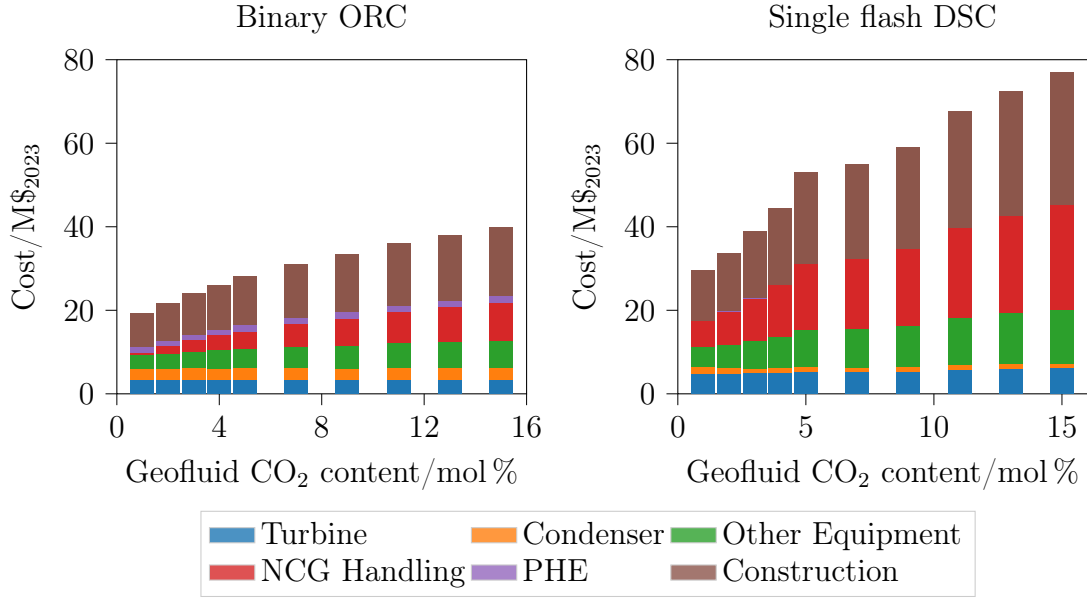


Figure 5.84: The cost breakdown of thermodynamically optimised binary ORC (using n-Butane as the working fluid) and single flash DSC geothermal power plants with NCG re-pressurisation to 75 bar for re-injection into the reservoir.

5.5.3. Re-injection with partial dissolution

To reduce the power requirements of pressurising the NCG to the re-injection pressure of 75 bar, it may be possible to re-dissolve some NCG in the brine. This could reduce the re-pressurisation power requirements by reducing the mass rate of NCG requiring further pressurisation to the target pressure.

Plant Configurations

The plant configuration shown for the previous study, Section 5.5.2, were adapted to include an absorption unit to redissolve the NCG in the brine.

The streams exiting the power plant, split into their constituent phases, which are then re-pressurised to a common absorption pressure P_{absorb} and then fed to an absorption column. The absorption column is modelled using a Mixer and a Separator element, to combine and equilibrate the streams and to then separate them into a vapour and liquid stream.

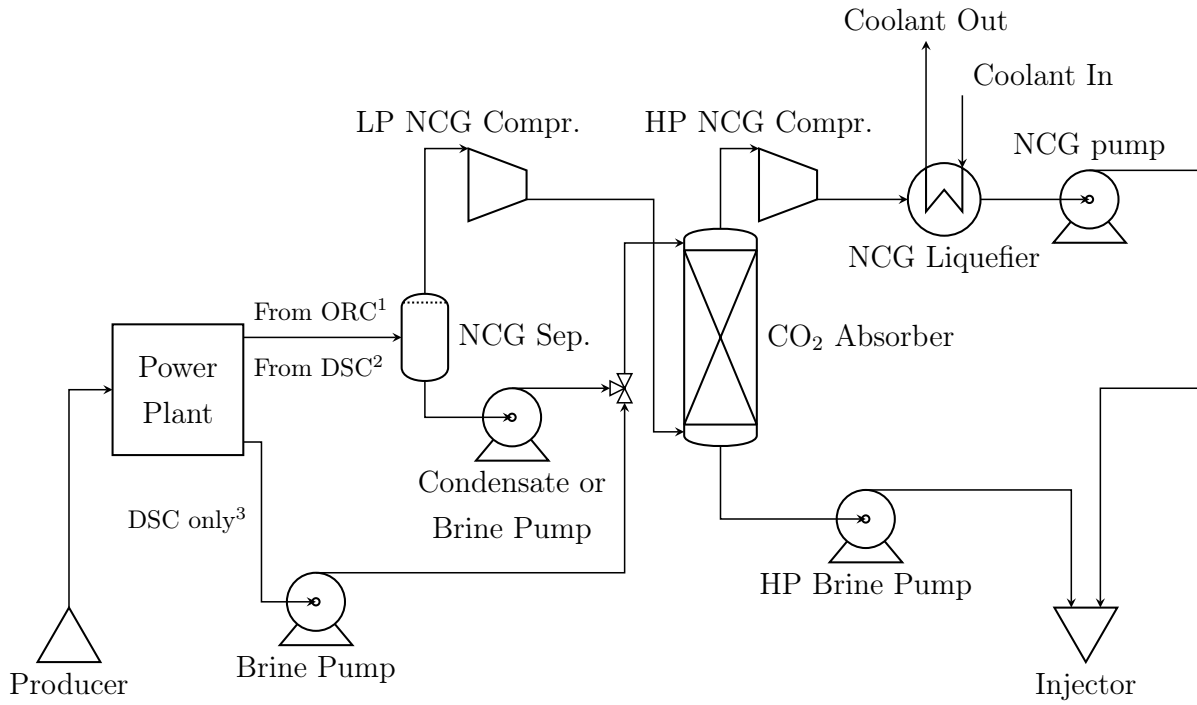


Figure 5.85: Binary ORC or single flash DSC geothermal power plants with partial dissolution of NCG subsequent re-injection into the reservoir. ¹Geofluid from PHE. ²Condensate and NCG from Condenser. ³Brine from flash separator.

Boundary Conditions

The same boundary conditions as in the previous study are used, see Section 5.5.2.

Optimisation Configuration

The binary ORC and single flash DSC power plants were thermodynamically optimised using the same optimisation configuration as used for previous studies, but with an additional optimisation variable, the absorption pressure P_{absorb} , which is allowed to range between the power plant outlet pressure and saturation pressure of NCG, Table 5.11.

Table 5.11: The optimisation parameters used for the single flash DSC and the binary ORC geothermal power plants.

	Single Flash DSC	Binary ORC
Objective Function	$W_{net, elec}$	$W_{net, elec}$
Constraints	$\Delta T_{cond}^{min} \geq 5K$	$\Delta T_{cond}^{min} \geq 5K$ $\Delta T_{preh}^{min} \geq 5K$ $\Delta T_{evap}^{min} \geq 10K$ $\Delta T_{sh}^{min} \geq 10K$
Controls	$0 \leq \frac{P_{absorb} - P_{geo}^{out}}{P_{sat} - P_{geo}^{out}} \leq 1$ $0.1 \text{ bar} \leq P_{cond} \leq 5.0 \text{ bar}$ $0.3 \leq \frac{P_{flash}}{P_{in}} \leq 1.0$	$0 \leq \frac{P_{absorb} - P_{geo}^{out}}{P_{sat} - P_{geo}^{out}} \leq 1$ $303 \text{ K} \leq T_{cond} \leq 400 \text{ K}$ $0.2 \leq \frac{P_{evap}}{P_{crit}} \leq 0.8$ $3 \text{ K} \leq \Delta T_{sh} \leq 15 \text{ K}$

Results

Partial dissolution can reduce the power requirements of NCG re-pressurisation in single flash DSC power plants for geofluid CO₂ contents of up to 8 mol %, beyond which an increase in pressurisation power compared to the direct pressurisation case, Figure 5.86.

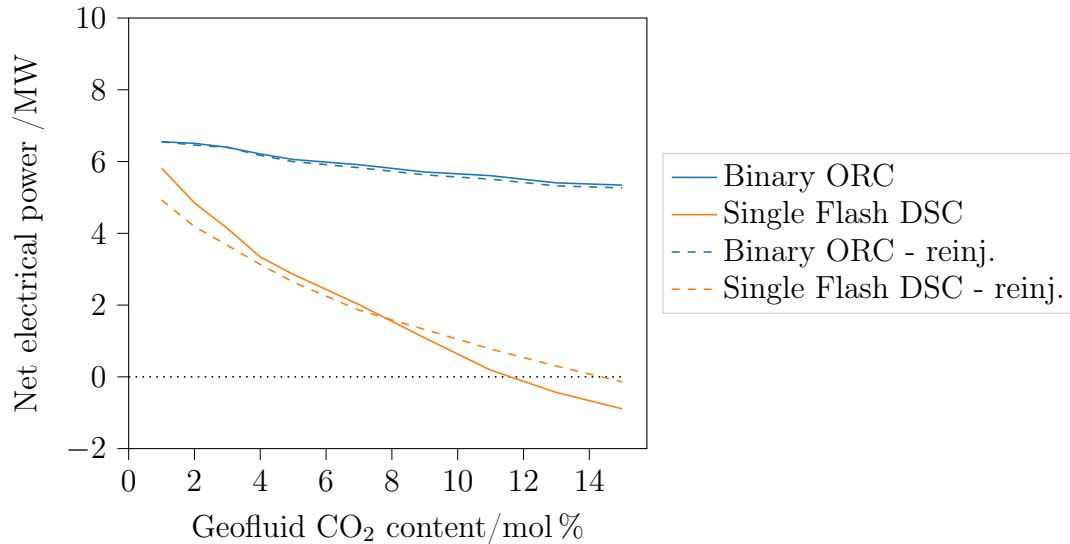


Figure 5.86: The net electrical power of thermodynamically optimised binary ORC (using n-Butane as the working fluid) and single flash DSC geothermal power plants with partial NCG re-dissolution and re-pressurisation to 75 bar for re-injection into the reservoir.

Partial dissolution is only effective at reducing the pressurisation power where 1) a sig-

nificant portion of the NCG stream can be absorbed by the brine and 2) the compression ratio for the secondary compression (i.e. from the absorption pressure P_{absorb} to the saturation pressure P_{sat} is large. This is illustrated in Equation 5.14, which can be derived assuming that the pressurisation power is approximately proportional to the product of the mass flow rate and the logarithm of the compression ratio.

$$\dot{W}_{compr}^{tot} \propto \dot{m}_{NCG} * \log \frac{P_{out}}{P_{in}} - \dot{m}_{absorbed} * \log \frac{P_{out}}{P_{absorb}} \quad (5.14)$$

However, in reality the fraction of the total NCG mass flow rate that can be dissolved in the geothermal brine diminishes as the geofluid CO_2 content increases. This is because the brine can only accommodate a few mol % of CO_2 , Figure 5.87, which represents a fraction of the total NCG contained within the geofluid. For example, at a temperature of 375 K and a pressure of around 30 bar the brine is saturated at just 0.5 mol % of CO_2 . For a geofluid CO_2 content of 1 mol % this represents a NCG mass rate reduction of 50 %, however this reduces to a reduction of just 3.3 % for geofluid CO_2 contents of 15 mol %. To achieve higher CO_2 concentrations in the brine, higher pressures are required, however this reduces the compression ratio of the secondary pressurisation and hence the overall reduction in pressurisation power.

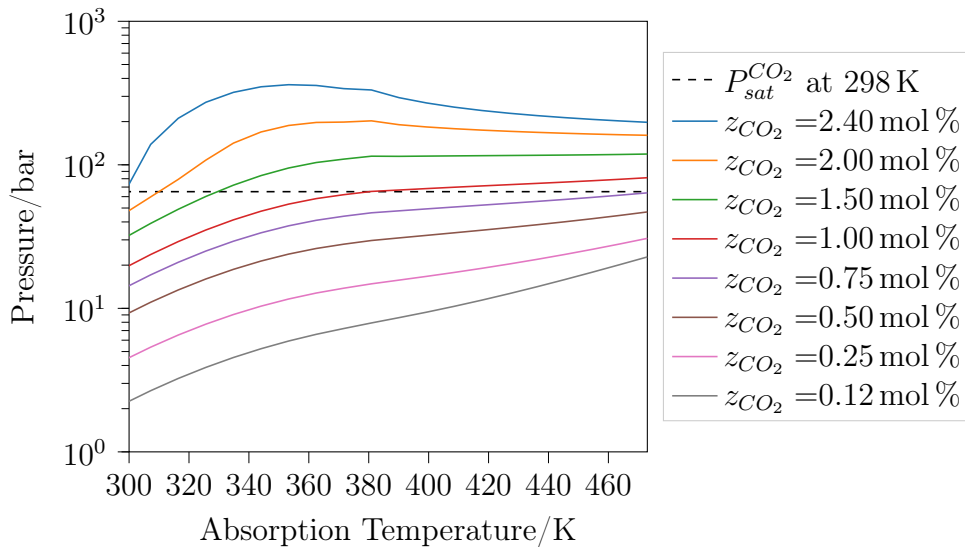


Figure 5.87: The bubble point pressure for different water-carbon dioxide mixtures as a function of temperature.

Another factor to consider is that, the average temperature of the NCG is higher in this process, due to its exposure to the hot brine in the absorption unit. In turn, this results in higher power consumption in the compressor, undoing any savings from reducing the

NCG mass rate. This is particularly evident at higher geofluid CO_2 contents, where the savings from partial dissolution are insignificant.

As for the binary ORC, partial dissolution somewhat reduces the pressurisation power requirement, however, as the overall compression ratio is smaller than for the DSC, the potential gains from partial dissolution are small.

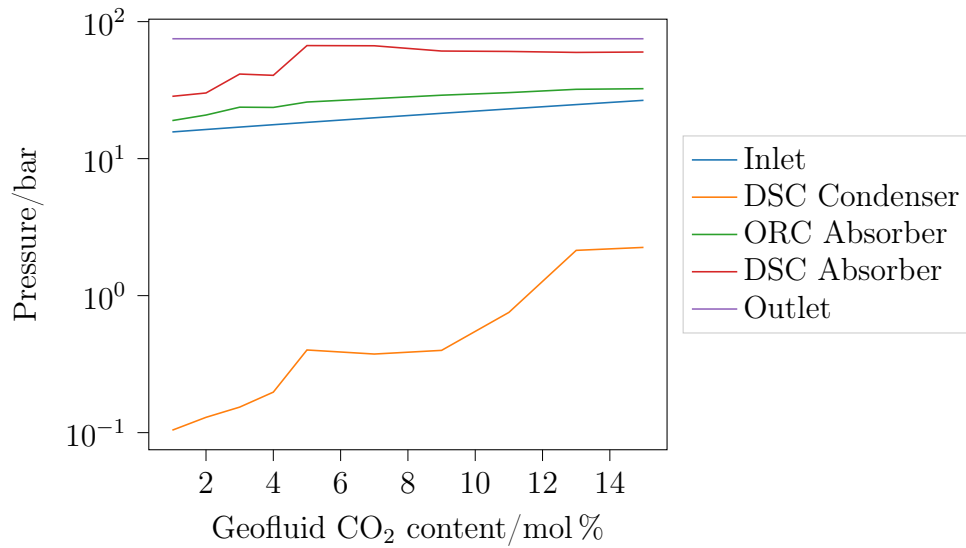


Figure 5.88: The pressures of the geofluid at different points in the power plant.

5.5.4. Conclusion

Single flash DSC geothermal power plants are particularly vulnerable to the presence of NCG because power is directly generated from the geofluid. On the other hand, binary ORC geothermal power plants are virtually unaffected by the presence of NCG in the geofluid.

With regards to NCG disposal, venting NCG to atmosphere is by far the least energy intensive option. While binary ORC do not require an re-pressurisation to vent NCG to the atmosphere, in single flash DSC power plants the re-pressurisation power requirements can be mitigated by raising the condensation pressure, however a net plant power reduced for NCG contents less than 7 mol %

NCG disposal by re-injection into the geothermal reservoir requires wellhead pressures in excess of 60 bar depending on the injection temperature and whether the NCG can be liquefied. For single flash DSCs, the re-pressurisation power requirements are significant, and increase with NCG content, ultimately resulting in zero net plant power for NCG contents higher than 14 mol %. Binary ORC plants are not as strongly affected due to the

smaller pressure differential across the power plant.

Partial dissolution of NCG, akin to the CarbFix process, could help reduce the repressurisation power requirements in single flash DSC geothermal power plants for geofluid NCG contents less than about 8 mol%. For binary ORC plants no significant power savings can be realised.

6 | Conclusions and future developments

This chapter aims to provide a summary of the main conclusions of this work. The main achievements are the development of *GeoProp* and *PowerCycle*. *GeoProp* can be used to compute the thermophysical properties and phase behaviour of geothermal geofluids. *PowerCycle* can be used to simulate different configurations and types of geothermal power plants for a variety of heat sources and both ideal and real geofluids.

6.1. Overall Motivation

Two-phase geothermal heat sources are traditionally exploited using DSC power plants. However, due to the higher temperatures and/or geological setting of these two-phase heat sources, co-production of NCG is more prevalent. The need for treatment and/or repressurisation prior to disposal is not only an operational challenge but also raises the cost of the power plant. By virtue of their closed-loop nature, binary ORC geothermal power plants could be better suited to handle and dispose NCG. Thus the overall objective of this work was to establish the thermodynamic and techno-economic application envelope of binary ORC power plants for two-phase sources, as well as the effect of impurities, such NCG, have on power production and plant operation.

6.2. Thermophysical Property Modelling

The simulation of geothermal power systems requires reliable and robust models for predicting the thermophysical properties and phase behaviour of the geofluid. Given the site-specificity of the composition of geothermal fluids, such models must be capable of capturing a broad range of compositions, temperatures and pressures to be holistically applicable.

A review of the literature identified three approaches for modelling geofluids: EOS that

provide high-fidelity predictions of thermophysical properties and phase behaviour of pure fluids and mixtures, but require extensive data for calibration; Chemically active systems, which allow virtually any arbitrary geofluid composition to be modelled, but require extensive input data for the underlying models; and empirical models that are computationally inexpensive but are restricted to specific applications, e.g. phase behaviour.

Recognising the synergies between the approaches presented above, *GeoProp* was developed, which couples existing partitioning and property models, extending their individual capabilities. The approach presented, allows the thermophysical properties and phase behaviour of geothermal brines for a wide range of temperatures, pressures and compositions to be calculated, which are required for the accurate simulation, and the proper design and evaluation, of direct steam cycle or binary cycle geothermal power plants. *GeoProp* is available on GitHub (<https://github.com/EASYGO-ITN/GeoProp>) under an Apache License 2.0 license.

6.3. Power Plant Modelling

Commercial softwares, such as *Aspen Plus v11*, provide a convenient basis for simulating simple geothermal power plants. Nevertheless, capturing non-standard physics, such as wet expansion effects in turbines, or complex fluids, such as geothermal brines, requires bespoke solutions.

PowerCycle was specifically developed with the challenges of geothermal power plant simulations in mind. The fluid properties module currently enables the use of both *CoolProp* and *GeoProp*, as well as the means for generating look-up tables, but is arbitrarily extendable. Component models for turbines, pumps/compressors/fans, heat exchangers, separators, joints/mixers, etc. are included, each calculating the component thermodynamic performance, exergy loss and cost. The geothermal power plant can then be calculated by means of a script, specifying the order in which the component are calculated. A number of power plant models for various DSC and binary ORC geothermal power plant configurations were formulated as part of this work. Although *PowerCycle* was created with geothermal power applications in mind, as the fluid properties and base component modules can be extended arbitrarily, in principles it could also be used in non-geothermal applications. *PowerCycle* is entirely written in Python and the codebase will be made available on GitHub under an open-source license.

6.4. Power Plant Simulations

The thermodynamic and techno-economic performance of single flash DSC and binary ORC geothermal power plants was investigated for both ideal (pure water) and real (water and carbon dioxide mixtures) two-phase geofluids using both commercial and bespoke modelling tools, i.e. *Aspen Plus v11* and *PowerCycle* respectively. The conclusions from the different studies are summarised below.

6.4.1. Commercial Software

The first comparative study of binary ORC and single flash DSC geothermal power plants was conducted using *Aspen Plus v11*, with each plant optimised to deliver the maximum specific net power. With increasing geofluid inlet temperature, the binary ORC was found to deliver comparable specific net power at increasingly higher geofluid inlet vapour qualities. At the lower temperatures, the single DSC outperforms the binary ORC across the full range of geofluid vapour qualities, which can be attributed to the critical temperatures of the selected working fluids being poorly aligned with the heat source.

The effect of impurities such as salinity and NCG on the performance was also investigated. The performance of both binary ORC and single flash DSC was found to be only weakly dependent on the salinity, as the presence of salts does not alter the heat flow to the power plant. On the other hand, the presence of NCG has a significant effect on the single flash DSC, while the binary ORC is virtually unaffected.

Several issues were encountered (i.e. crashes, difficulties in debugging, scenario initialisation, etc.) as part of the modelling, as well as doubts in the reliability accuracy of the underlying property model for water-carbon dioxide mixtures, ultimately led to the development of a bespoke alternative, *PowerCycle*.

6.4.2. Thermodynamic Optimisation

Optimising for the thermodynamic performance (i.e. maximum net electrical power), the performance of binary ORC and single flash DSC was investigated for a geofluid comprised of pure water and inlet temperatures of 423 K to 548 K and vapour qualities of 0 % to 100 % and a geofluid mass rate of 50 kg s^{-1} .

The net electrical power for both binary ORC and single flash DSC was found to increase with both geofluid inlet temperature and vapour quality. For the single flash DSC, the optimum condensation pressure was found to be independent of geofluid inlet condition,

but the optimum degree of flashing was found to increase with increasing geofluid inlet temperature and decreasing geofluid vapour quality, a result of the curvature of the quality lines in the pressure-enthalpy domain.

For the binary ORC, at low geofluid inlet temperatures and vapour quality the net electrical power is limited by temperature approach of the working fluid and geofluid in the PHE performance. However, as the location of pinch-point shifts towards the cold-side inlet of the heat exchanger with increasing geofluid inlet temperature and vapour quality, the net electrical power is only limited by the heat flow entering the power plant. While lighter working fluids (e.g. n-Butane) dominate at pinch-point constraint geofluid inlet conditions, the more complex working fluids (e.g. Cyclopentane) achieve the highest net electrical power. Super-heating is only used with the lighter working fluids to increase the cycle temperature, but the net power is not strongly dependent on the degree of super-heating. There is a significant spread in specific cost of the power plant as well as the cost contributions of the power plant equipment between light and heavy working fluids considered, which is almost solely attributed to size and cost of the turbine. Moreover, the heaviest working fluids (e.g. n-Heptane) require ORCs with sub-atmospheric condensation pressures, which can lead to operational issues due to air ingress into the system.

In line with results generated using *Aspen Plus*, it can be seen that binary ORCs can compete with single flash DSCs. When the focus is on net electrical power, binary ORCs can compete up to geofluid inlet vapour qualities of around 70 % (depending on the inlet temperature), although at a higher specific cost. Similarly, when the focus is on specific cost of the power plant, binary ORCs can achieve lower specific costs (and more net electrical power) for geofluid inlet vapour qualities around 10 % to 20 % across the range of temperatures investigated.

6.4.3. Techno-economic optimisation

Optimising for the techno-economic performance (i.e. minimum specific cost of the power plant), the performance of binary ORC and single flash DSC was investigated for a geofluid comprised of pure water and inlet temperatures of 423 K to 548 K and vapour qualities of 0 % to 100 % and a geofluid mass rate of 50 kg s^{-1} .

For the single flash DSC, specific cost reductions of about 6 % to 10 %, at the expense of around 10 % to 20 % of net electrical power were observed. The cost reductions are almost entirely a result of a reduction in condenser size, by raising the minimum approach temperature difference and condensation temperature.

For the binary ORC, larger cost reductions of about 20 % to 30 % were observed, at the expense of up to 65 % of net electrical power. For all fluids the condenser costs are reduced by raising the minimum approach temperature difference and condensation temperature, for the heavier working fluids simultaneously reducing the number of turbine stages from a maximum of 5 to a minimum of 1. Nevertheless, n-Butane achieves the lowest specific net electrical power across a broad range of geofluid inlet conditions.

From a specific cost perspective, techno-economically optimised binary ORCs can compete with single flash DSCs for geofluid inlet vapour qualities as high as 80 %, but produce significantly less power. Here, the envelope for competitive specific power and net electrical reduces from a geofluid inlet vapour quality of 20 % at a geofluid inlet temperature of 423 K to 0 % at 548 K.

When drilling costs are considered as part of the optimisation, the techno-economic and thermodynamic optimisations tend converge where drilling and plant costs are of comparable magnitude.

6.4.4. Impact and handling of NCG

The impact of the presence of NCG in geofluid on the performance of single flash DSC and binary ORC geothermal power plants was investigated for a series of NCG disposal scenarios and NCG contents.

Single flash DSC geothermal power plants are particularly vulnerable to the presence of NCG because power is directly generated from the geofluid. As such, the power generation and subsequent NCG handling process are closely coupled. For instance, the power required to re-pressurise is directly dependent on the geofluid condensation pressure (i.e. turbine discharge pressure), which drives the overall power generated in the power plant. On the other hand, binary ORC geothermal power plants are virtually unaffected by the presence of NCG in the geofluid.

As can be expected, venting NCG to atmosphere is by far the least energy intensive option. In fact, due to minimal pressure losses in the PHE, binary ORC geothermal power plants would not require any additional re-pressurisation power to vent the NCG to atmosphere. For single flash DSC a reduction in net plant power is observed for NCG content less than 7 mol %, however at higher NCG contents, with the assumptions considered in this work, the increase in geofluid inlet pressure leads to an increase in net plant power. This is in part facilitated by raising the condensation pressure thus reducing the need for subsequent NCG re-pressurisation.

NCG disposal by re-injection into the geothermal reservoir requires wellhead pressures in excess of 60 bar depending on the injection temperature and whether the NCG can be liquefied. For single flash DSCs, the re-pressurisation power requirements are significant, and increase with NCG content, ultimately resulting in zero net plant power for NCG contents higher than 14 mol %. Again, binary ORC plants are not as strongly affected because the pressure differential across the power plant is smaller, meaning that lower compression ratios are required to re-inject the NCG. Partial dissolution of NCG, akin to the *CarbFix* process, could help reduce the re-pressurisation power requirements in single flash DSC geothermal power plants for geofluid NCG contents less than about 8 mol %. For binary ORC plants no significant power savings can be realised.

Depending on the NCG composition, different handling and disposal approaches can be used. Given the power requirements of re-pressurisation, harmful components, such as H_2S , are best stripped from the NCG stream, for example using the *AMIS* process. The preferred method of CO_2 disposal is primarily a function of whether geothermal plant changes the overall emissions of the region (i.e. natural emissions and emissions from the power plant), relative to natural emissions prior to geothermal operations. Venting is a suitable option where there is no net increase in the overall emissions of CO_2 in the region. Where geothermal operations increase the overall emissions of CO_2 in the region, re-injection can be used to reduce the carbon footprint of the geothermal plant. For sufficiently high carbon prices, re-injection of CO_2 could be an additional income stream for the geothermal power plant, although this was not considered in this study.

The preferred method of CO_2 disposal is primarily a function of whether geothermal plant changes the overall emissions of the region (i.e. natural emissions and emissions from the power plant), relative to natural emissions prior to geothermal operations. Venting is a suitable option where there is no net increase in the overall emissions of CO_2 in the region. Where geothermal operations increase the overall emissions of CO_2 in the region, re-injection can be used to reduce the carbon footprint of the geothermal plant. For sufficiently high carbon prices, re-injection of CO_2 could be an additional income stream for the geothermal power plant, although this was not considered in this study.

6.5. Future Work

The component models in *PowerCycle* make a number of simplifying assumptions that could be constrained in future studies. For instance, for ORC turbines the isentropic efficiency is currently assumed to be constant for all working fluids and expansion conditions. This could be improved by also considering the effects of the volume ratio across

the turbine and the specific rotational speed of the turbine. Similarly for steam turbines, the effect of wetness on the isentropic turbine efficiency is currently captured using the empirical Baumann rule, which was originally developed for pure water, but in this context is also being used for mixtures of water and NCG. Perhaps more detailed turbine performance calculations could aid in the development of an analogous empirical model for such working fluid mixtures. Finally, the ORC evaporator unit was assumed to be capable of handling the simultaneous condensation of steam on the hot-side and evaporation on the cold side. Whether this can be realised using conventional heat exchanger designs (e.g. kettle reboiler or condensers) or, requires specialised heat exchanger designs, requires more detailed design calculations accounting for the heat transfer coefficients and two-phase behaviour of the fluids.

With respect to the handling of the NCG, the calculation of the required wellhead pressure for re-injecting NCG into the reservoir is also based on many simplifying assumptions (i.e. static pressures and no heat transfer). To provide more reliable estimates, as well as to explore alternative re-injection strategies (e.g. mixing in the wellbore at depth) requires more detailed wellbore simulations, including frictional pressure losses; heat transfer between surrounding formation, the brine and the NCG; mass transfer resistances (to capture the dissolution of NCG in the brine); distribution of phases within the wellbore; and flow instability detection. Particularly, simulations of "worst case scenarios", such as infinite mass transfer resistances may aid establish whether simultaneous injection of water and NCG is possible.

Given the particular focus on NCG, the work underpinning *GeoProp*, could be expanded to provide a tighter coupling between the empirical SP2009 partitioning model and the pure component HEOS models for H₂O and **CO₂** (**CO₂**!). Moreover to capture a wider range of NCG compositions, as opposed to just CO₂, further work could focus on expanding the SP2009 model to include other constituents such as H₂S or CH₄.

Bibliography

- [1] Électricité de strasbourg s.a. URL <https://groupe.es.fr/>.
- [2] Enbw. URL <https://www.enbw.com/>.
- [3] Orkuveita húsavík. URL <https://www.oh.is/is/fyrirtaekid/sagan>.
- [4] Utah forge. URL <https://utahforge.com/>.
- [5] I. M. Abdulagatov, L. A. Akhmedova-Azizova, R. M. Aliev, and G. B. Badavov. Measurements of the density, speed of sound, viscosity and derived thermodynamic properties of geothermal fluids from south russia geothermal field. part ii. *Applied Geochemistry*, 69:28–41, 6 2016. ISSN 08832927. doi: 10.1016/j.apgeochem.2016.04.003. URL <https://linkinghub.elsevier.com/retrieve/pii/S0883292716300567>.
- [6] B. Adams, J. Ogland-Hand, J. Bielicki, P. Schädle, and M. Saar. Estimating the geothermal electricity generation potential of sedimentary basins using gengeo (the generalizable geothermal techno-economic simulator). *pre-print*, 01 2021. doi: 10.26434/chemrxiv.13514440.
- [7] Airgas. Safety data sheets. URL <https://www.airgas.com/sds-search>.
- [8] M. Astolfi. An innovative approach for the techno-economic optimization of organic rankine cycles. 2014. URL <https://hdl.handle.net/10589/89363>.
- [9] M. Astolfi, R. Bini, E. Macchi, M. Paci, C. Pietra, N. Rossi, and A. Tizzanini. Testing of a new supercritical orc technology for efficient power generation from geothermal low temperature resources. In *ASME ORC 2013 Conference Proceedings*, 2013.
- [10] M. Astolfi, M. C. Romano, P. Bombarda, and E. Macchi. Binary orc (organic rankine cycles) power plants for the exploitation of medium–low temperature geothermal sources – part a: Thermodynamic optimization. *Energy*, 66:423–434, 3 2014. ISSN 03605442. doi: 10.1016/j.energy.2013.11.056.

- [11] M. Astolfi, M. C. Romano, P. Bombarda, and E. Macchi. Binary orc (organic rankine cycles) power plants for the exploitation of medium–low temperature geothermal sources – part b: Techno-economic optimization. *Energy*, 66:435–446, 3 2014. ISSN 03605442. doi: 10.1016/j.energy.2013.11.057.
- [12] L. Azzini, M. Pini, and P. Colonna. Semi-analytical model for the prediction of the wilson point for homogeneously condensing steam flows. *International Journal of Heat and Fluid Flow*, 70:1–14, 4 2018. ISSN 0142727X. doi: 10.1016/j.ijheatfluidflow.2018.01.004.
- [13] A. Baba and D. Chandrasekharam. Geothermal resources for sustainable development: A case study. *International Journal of Energy Research*, 46:20501–20518, 11 2022. ISSN 0363-907X. doi: 10.1002/er.7778.
- [14] A. F. Babatunde and O. O. Sunday. A review of working fluids for organic rankine cycle (orc) applications. *IOP Conference Series: Materials Science and Engineering*, 413:012019, 9 2018. ISSN 1757-899X. doi: 10.1088/1757-899X/413/1/012019.
- [15] A. Baldacci, M. Mannari, and F. Sansone. Greening of geothermal power: An innovative technology for abatement of hydrogen sulphide and mercury emission. 2005.
- [16] K. Baumann. Some recent developments in large steam turbine practice. *Journal of the Institution of Electrical Engineers*, 59:565–623, 6 1921. ISSN 2054-0612. doi: 10.1049/jiee-1.1921.0040.
- [17] K. Beckers, M. Ross, and J. Pezzino. Geophires-x, 2023. URL <https://github.com/NREL/GEOPHIRES-X>.
- [18] K. F. Beckers and K. McCabe. Geophires v2.0: updated geothermal techno-economic simulation tool. *Geothermal Energy*, 7:5, 12 2019. ISSN 2195-9706. doi: 10.1186/s40517-019-0119-6.
- [19] K. F. Beckers, N. Rangel-Jurado, H. Chandrasekar, A. J. Hawkins, P. M. Fulton, and J. W. Tester. Techno-economic performance of closed-loop geothermal systems for heat production and electricity generation. *Geothermics*, 100:102318, 3 2022. ISSN 03756505. doi: 10.1016/j.geothermics.2021.102318.
- [20] I. H. Bell, J. Wronski, S. Quoilin, and V. Lemort. Pure and pseudo-pure fluid thermophysical property evaluation and the open-source thermophysical property library coolprop. *Industrial & Engineering Chemistry Research*, 53:2498–2508,

2014. doi: 10.1021/ie4033999. URL <http://pubs.acs.org/doi/abs/10.1021/ie4033999><http://www.coolprop.org/>.
- [21] J. Blank and K. Deb. pymoo: Multi-objective optimization in python. *IEEE Access*, 8:89497–89509, 2020.
- [22] C. Bliem and G. Mines. Supersaturated turbine expansions for binary geothermal power plants. pages 105–109, 1992. URL <https://digital.library.unt.edu/ark:/67531/metadc874745/>.
- [23] M. P. Boyce. *Gas Turbine Engineering Handbook*. Elsevier, 2012. ISBN 9780123838421. doi: 10.1016/C2009-0-64242-2.
- [24] T. Buchanan, W. Posten, and S. Berryman. Repowering steamboat 2 and 3 plants with new axial flow turbines. 2010.
- [25] CarbFix. Carbfix. URL <https://www.carbfix.com/>.
- [26] W. Collins, R. Orbach, M. Bailey, S. Biraud, I. Coddington, D. DiCarlo, J. Peischl, A. Radhakrishnan, and D. Schimel. Monitoring methane emissions from oil and gas operations. *Opt. Express*, 30:24326–24351, 7 2022. doi: 10.1364/OE.464421. URL <https://opg.optica.org/oe/abstract.cfm?URI=oe-30-14-24326>.
- [27] P. Colonna, T. V. D. Stelt, and A. Guardone. Fluidprop (version 3.1): A program for the estimation of thermophysical properties of fluids., 2019.
- [28] N. Deichmann and D. Giardini. Earthquakes induced by the stimulation of an enhanced geothermal system below basel (switzerland). *Seismological Research Letters*, 80:784–798, 9 2009. ISSN 0895-0695. doi: 10.1785/gssrl.80.5.784.
- [29] E. Dick. *Fundamentals of Turbomachines*, volume 109. Springer Netherlands, 2015. ISBN 978-94-017-9626-2. doi: 10.1007/978-94-017-9627-9.
- [30] R. DiPippo. *Geothermal Power Plants*. Butterworth-Heinemann, 4th edition, 2016. ISBN 9780081008799. doi: 10.1016/C2014-0-02885-7.
- [31] Z. Duan and R. Sun. An improved model calculating co2 solubility in pure water and aqueous nacl solutions from 273 to 533 k and from 0 to 2000 bar. *Chemical Geology*, 193:257–271, 2 2003. ISSN 00092541. doi: 10.1016/S0009-2541(02)00263-2.
- [32] N. H. Duc, F. Chauvy, and J.-M. Herri. Co2 capture by hydrate crystallization – a potential solution for gas emission of steelmaking industry. *Energy Conversion and Management*, 48:1313–1322, 4 2007. ISSN 01968904. doi: 10.1016/j.enconman.2006.09.024.

- [33] Exergy. Exergy. URL <https://www.exergy-orc.com/>.
- [34] L. Galieti, P. Colonna, C. de Servi, B. P., P. Silva, and D. Alfani. On air-cooled condensers for orc systems operating with zeotropic mixtures. In *7th International Seminar on ORC power systems*, 2023.
- [35] G. J. Gernert. *A New Helmholtz Energy Model for Humid Gases and CCS Mixtures*. PhD thesis, Ruhr-Universität Bochum, 2013.
- [36] I. Gunnarsson, E. S. Aradottir, E. H. Oelkers, D. E. Clark, M. D. Arnarson, B. Sigfusson, S. O. Snæbjörnsdóttir, J. M. Matter, M. Stute, B. M. Júlíusson, and S. R. Gíslason. The rapid and cost-effective capture and subsurface mineral storage of carbon and sulfur at the carbfix2 site. *International Journal of Greenhouse Gas Control*, 79:117–126, 12 2018. ISSN 17505836. doi: 10.1016/j.ijggc.2018.08.014.
- [37] H. Gupta and S. Roy. *BASIC CONCEPTS*, pages 15–30. Elsevier, 2007. doi: 10.1016/B978-044452875-9/50002-2.
- [38] G. Gyarmathy. *Grundlagen einer theorie der nassdampfturbine*. PhD thesis, ETH Zurich, 1962.
- [39] E. P. Gyftopoulos and G. P. Beretta. *Thermodynamics: Foundations and Applications*. Dover Publications, 2005. ISBN 9780486439327.
- [40] A. H. C. H. *Geothermal energy : its past, present and future contributions to the energy needs of man*. E. & F.N. Spon, 1978. ISBN 978-04-7026-337-2.
- [41] A. R. Hagedorn and K. E. Brown. Experimental study of pressure gradients occurring during continuous two-phase flow in small-diameter vertical conduits. *Journal of Petroleum Technology*, 17:475–484, 4 1965. ISSN 0149-2136. doi: 10.2118/940-PA.
- [42] H. C. Helgeson, D. H. Kirkham, and G. C. Flowers. Theoretical prediction of the thermodynamic behavior of aqueous electrolytes by high pressures and temperatures; iv, calculation of activity coefficients, osmotic coefficients, and apparent molal and standard and relative partial molal properties to 600 degrees c and 5kb. *American Journal of Science*, 281:1249–1516, 12 1981. ISSN 0002-9599. doi: 10.2475/ajs.281.10.1249.
- [43] T. Hung, S. Wang, C. Kuo, B. Pei, and K. Tsai. A study of organic working fluids on system efficiency of an orc using low-grade energy sources. *Energy*, 35:1403–1411, 3 2010. ISSN 03605442. doi: 10.1016/j.energy.2009.11.025.

- [44] IAPWS. Main iapws thermodynamic property formulations, 2018. URL <http://www.iapws.org/newform.html>.
- [45] IEA. World energy outlook 2023, 2023. URL <https://www.iea.org/reports/world-energy-outlook-2023>.
- [46] F. P. Incropera, D. P. Dewitt, T. L. Bergman, and A. S. Lavine. *Fundamentals of heat and mass transfer / Frank P. Incropera ... [et al.]*. Wiley, 6. ed edition, 2007. ISBN 978-04-7145-728-2.
- [47] J. W. Johnson, E. H. Oelkers, and H. C. Helgeson. Supcrt92: A software package for calculating the standard molal thermodynamic properties of minerals, gases, aqueous species, and reactions from 1 to 5000 bar and 0 to 1000°C. *Computers & Geosciences*, 18:899–947, 8 1992. ISSN 00983004. doi: 10.1016/0098-3004(92)90029-Q.
- [48] A. Kottsova and M. Brehme. Database on hydrogeochemical properties of geothermal reservoirs in the Netherlands, Oct. 2022. URL <https://doi.org/10.5281/zenodo.7256942>.
- [49] P. Kruger, C. Otte, and A. Society. *Geothermal Energy: Resources, Production, Stimulation*. Stanford University Press, 1973. ISBN 9780804708227.
- [50] S. Kyas, D. Volpatto, M. O. Saar, and A. M. M. Leal. Accelerated reactive transport simulations in heterogeneous porous media using reaktoro and fire-drake. *Computational Geosciences*, 26:295–327, 4 2022. ISSN 1420-0597. doi: 10.1007/s10596-021-10126-2.
- [51] A. Leal. Reaktoro: An open-source unified framework for modeling chemically reactive systems., 2015. URL <https://reaktoro.org>.
- [52] A. Leal, S. Kyas, D. Kulik, and M. Saar. Accelerating reactive transport modeling: On-demand machine learning algorithm for chemical equilibrium calculations. *Transport in Porous Media*, 133:161–204, 2020. doi: <http://dx.doi.org/0.1007/s11242-020-01412-1>.
- [53] A. M. M. Leal, D. A. Kulik, W. R. Smith, and M. O. Saar. An overview of computational methods for chemical equilibrium and kinetic calculations for geochemical and reactive transport modeling. *Pure and Applied Chemistry*, 89: 597–643, 5 2017. ISSN 1365-3075. doi: 10.1515/pac-2016-1107. URL <https://www.degruyter.com/document/doi/10.1515/pac-2016-1107/html>.
- [54] E. W. Lemmon and R. T. Jacobsen. A generalized model for the thermodynamic

- properties of mixtures. *International Journal of Thermophysics*, 20:825–835, 1999. ISSN 0195928X. doi: 10.1023/A:1022627001338.
- [55] E. W. Lemmon and R. Span. Short fundamental equations of state for 20 industrial fluids. *Journal of Chemical & Engineering Data*, 51:785–850, 5 2006. ISSN 0021-9568. doi: 10.1021/je050186n.
- [56] E. W. Lemmon and R. Tillner-Roth. A helmholtz energy equation of state for calculating the thermodynamic properties of fluid mixtures. *Fluid Phase Equilibria*, 165:1–21, 11 1999. ISSN 03783812. doi: 10.1016/S0378-3812(99)00262-9.
- [57] E. W. Lemmon, I. H. Bell, M. L. Huber, and M. O. McLinden. Nist standard reference database 23: Reference fluid thermodynamic and transport properties-refprop, version 10.0, national institute of standards and technology, 2018. URL <https://www.nist.gov/srd/refprop>.
- [58] V. Leontidis, P. H. Niknam, I. Durgut, L. Talluri, G. Manfrida, D. Fiaschi, S. Akin, and M. Gainville. Modelling reinjection of two-phase non-condensable gases and water in geothermal wells. *Applied Thermal Engineering*, 223:120018, 3 2023. ISSN 13594311. doi: 10.1016/j.applthermaleng.2023.120018.
- [59] M. LLC. Historical eur usd exchange rate, 2024. URL <https://www.macrotrends.net/2548/euro-dollar-exchange-rate-historical-chart>.
- [60] H. P. Loh, J. Lyons, and C. W. White. Process equipment cost estimation, final report, 1 2002.
- [61] W. Luo, A. Kottsova, P. Vardon, A. Dieudonné, and M. Brehme. Mechanisms causing injectivity decline and enhancement in geothermal projects. *Renewable and Sustainable Energy Reviews*, 185:113623, 10 2023. ISSN 13640321. doi: 10.1016/j.rser.2023.113623.
- [62] A. E. Malek, B. M. Adams, E. Rossi, H. O. Schiegg, and M. O. Saar. Techno-economic analysis of advanced geothermal systems (ags). *Renewable Energy*, 186: 927–943, 3 2022. ISSN 09601481. doi: 10.1016/j.renene.2022.01.012.
- [63] A. Manzella, R. Bonciani, A. Allansdottir, S. Botteghi, A. Donato, S. Giamberini, A. Lenzi, M. Paci, A. Pellizzone, and D. Scrocca. Environmental and social aspects of geothermal energy in italy. *Geothermics*, 72:232–248, 3 2018. ISSN 03756505. doi: 10.1016/j.geothermics.2017.11.015.
- [64] J. E. McDONALD. *Homogeneous Nucleation of Vapor Condensation I. Thermody-*

- namic Aspects*, pages 225–237. Elsevier, 1974. doi: 10.1016/B978-0-12-038361-0.50016-8.
- [65] T. Merbecks, A. M. M. Leal, P. Bombarda, P. Silva, D. Alfani, and M. O. Saar. Geoprop: A thermophysical property modelling framework for single and two-phase geothermal geofluids. *Geothermics*, 2024. doi: <https://doi.org/10.1016/j.geothermics.2024.103146>.
- [66] F. J. Millero, R. Feistel, D. G. Wright, and T. J. McDougall. The composition of standard seawater and the definition of the reference-composition salinity scale. *Deep Sea Research Part I: Oceanographic Research Papers*, 55:50–72, 1 2008. ISSN 09670637. doi: 10.1016/j.dsr.2007.10.001.
- [67] G. Mines. Operation of mammoth pacific’s mp1-100 turbine with metastable, super-saturated expansions. Idaho National Engineering and Environmental Laboratory, 1997. URL <https://digital.library.unt.edu/ark:/67531/metadc670586/>.
- [68] G. Mines. Getem user manual, 2016. URL https://workingincaes.inl.gov/SiteAssets/CAESFiles/FORGE/inl_ext-16-38751GETEMUserManualFinal.pdf.
- [69] G. D. Miron, D. Kulik, A. Leal, and S. Dmytrieva. Thermofun: C++/python code to fetch standard thermodynamic data from thermohub database. European Association of Geochemistry, 2021. doi: 10.7185/gold2021.4489. URL <https://thermohub.org/thermofun/thermofun/>.
- [70] P. Morgan. *HEAT FLOW IN THE EARTH* *Heat flow in the earth*, pages 634–646. Springer US, Boston, MA, 1990. ISBN 978-0-387-30752-7. doi: 10.1007/0-387-30752-4_79. URL https://doi.org/10.1007/0-387-30752-4_79.
- [71] D. Mottaghy, R. Schellschmidt, Y. Popov, C. Clauser, I. Kukkonen, G. Nover, S. Milanovsky, and R. Romushkevich. New heat flow data from the immediate vicinity of the kola super-deep borehole: Vertical variation in heat flow confirmed and attributed to advection. *Tectonophysics*, 401:119–142, 5 2005. ISSN 00401951. doi: 10.1016/j.tecto.2005.03.005.
- [72] U. B. of Labour Statistics. Producer price index, 2024. URL <https://www.bls.gov/data/tools.htm>.
- [73] Ormat. Ormat. URL <https://www.ormat.com/>.
- [74] A. Peneloux, W. Abdoul, and E. Rauzy. Excess functions and equations of state. *Fluid Phase Equilibria*, 47:115–132, 8 1989. ISSN 03783812. doi: 10.1016/0378-3812(89)80172-4.

- [75] D. Peng and D. B. Robinson. A new two-constant equation of state. *Industrial & Engineering Chemistry Fundamentals*, 15:59–64, 2 1976. ISSN 0196-4313. doi: 10.1021/i160057a011.
- [76] M. Peters, K. Timmerhaus, and R. West. *Heat-Transfer Equipment - Design and Costs. Plant Design and Economics for Chemical Engineers*. McGrawHill, 5 edition, 2003.
- [77] K. S. Pitzer and G. Mayorga. Thermodynamics of electrolytes. ii. activity and osmotic coefficients for strong electrolytes with one or both ions univalent. *The Journal of Physical Chemistry*, 77:2300–2308, 9 1973. ISSN 0022-3654. doi: 10.1021/j100638a009. URL <https://doi.org/10.1021/j100638a009>. doi: 10.1021/j100638a009.
- [78] E. Preisegger, F. Flohr, G. Krakat, A. Glück, and D. Hunold. *D4 Properties of Industrial Heat Transfer Media*, pages 419–512. Springer Berlin Heidelberg, 2010. doi: 10.1007/978-3-540-77877-6_20.
- [79] R. Project. Fluid atlas. URL <https://www.reflect-h2020.eu/efa/>.
- [80] J. Pátek and J. Klomfar. A computationally effective formulation of the thermodynamic properties of libr-h2o solutions from 273 to 500k over full composition range. *International Journal of Refrigeration*, 29:566–578, 6 2006. ISSN 01407007. doi: 10.1016/j.ijrefrig.2005.10.007.
- [81] P. R., E. Robinson, and M. Smith. Method of extracting heat from dry geothermal reservoirs., 1974.
- [82] O. Redlich and J. N. S. Kwong. On the thermodynamics of solutions. v. an equation of state. fugacities of gaseous solutions. *Chemical Reviews*, 44:233–244, 2 1949. ISSN 0009-2665. doi: 10.1021/cr60137a013.
- [83] A. Rohatgi. Webplotdigitizer, 2024. URL <https://automeris.io/WebPlotDigitizer.html>.
- [84] M. I. Ross and K. Beckers. Geophires-x: An object-oriented update to geophires 2.0. pages 2145–2156. Geothermal Rising, 2023.
- [85] O. Secretariat. *Handbook for the Montreal Protocol on Substances that Deplete the Ozone Layer*. United Nations Environment Programme, 14 edition, 2020. ISBN 978-9966-076-79-3.

- [86] S. Senoo and A. White. *Analysis and design of wet-steam stages*, pages 165–218. Elsevier, 2017. doi: 10.1016/B978-0-08-100314-5.00009-9.
- [87] J. Setschenow. Über die konstitution der salzlösungen auf grund ihres verhaltens zu kohlendensäure. *Zeitschrift für Physikalische Chemie*, 4U:117–125, 7 1889. ISSN 2196-7156. doi: 10.1515/zpch-1889-0409.
- [88] U. Setzmann and W. Wagner. A new equation of state and tables of thermodynamic properties for methane covering the range from the melting line to 625 k at pressures up to 100 mpa. *Journal of Physical and Chemical Reference Data*, 20:1061–1155, 11 1991. ISSN 0047-2689. doi: 10.1063/1.555898.
- [89] M. H. Sharqawy, J. H. Lienhard, and S. M. Zubair. Thermophysical properties of seawater: a review of existing correlations and data. *Desalination and Water Treatment*, 16:354–380, 4 2010. ISSN 1944-3994. doi: 10.5004/dwt.2010.1079.
- [90] B. Sigfusson, M. D. Arnarson, S. O. Snaebjörnsdottir, M. R. Karlsdottir, E. S. Aradottir, and I. Gunnarsson. Reducing emissions of carbon dioxide and hydrogen sulphide at hellisheidi power plant in 2014-2017 and the role of carbfix in achieving the 2040 iceland climate goals. *Energy Procedia*, 146:135–145, 7 2018. ISSN 18766102. doi: 10.1016/j.egypro.2018.07.018.
- [91] R. Smith. *Chemical process design and integration*. J. Wiley, 2005. ISBN 978-04-7148-681-7.
- [92] G. Soave. Equilibrium constants from a modified redlich-kwong equation of state. *Chemical Engineering Science*, 27:1197–1203, 6 1972. ISSN 00092509. doi: 10.1016/0009-2509(72)80096-4.
- [93] T. S.p.A. Turboden. URL <https://www.turboden.com/>.
- [94] R. Span and W. Wagner. A new equation of state for carbon dioxide covering the fluid region from the triple-point temperature to 1100 k at pressures up to 800 mpa. *Journal of Physical and Chemical Reference Data*, 25:1509–1596, 11 1996. ISSN 0047-2689. doi: 10.1063/1.555991.
- [95] R. Span, E. W. Lemmon, R. T. Jacobsen, W. Wagner, and A. Yokozeki. A reference equation of state for the thermodynamic properties of nitrogen for temperatures from 63.151 to 1000 k and pressures to 2200 mpa. *Journal of Physical and Chemical Reference Data*, 29:1361–1433, 11 2000. ISSN 0047-2689. doi: 10.1063/1.1349047.
- [96] N. Spycher and K. Pruess. A phase-partitioning model for co₂-brine mixtures at elevated temperatures and pressures: Application to co₂-enhanced geother-

- mal systems. *Transport in Porous Media*, 82:173–196, 11 2009. doi: 10.1007/s11242-009-9425-y.
- [97] N. Spycher, K. Pruess, and J. Ennis-King. Co₂-h₂O mixtures in the geological sequestration of CO₂. i. assessment and calculation of mutual solubilities from 12 to 100°C and up to 600 bar. *Geochimica et Cosmochimica Acta*, 67:3015–3031, 8 2003. ISSN 00167037. doi: 10.1016/S0016-7037(03)00273-4.
- [98] TEMA. *Standards of the Tubular Exchanger Manufacturers Association*. TEMA, 10 edition, 2019.
- [99] TEMA. Tema, 2024. URL <https://tema.org/>.
- [100] Thermoflow. Thermoflex v31, 2021.
- [101] G. Topcu, G. A. Koç, A. Baba, and M. M. Demir. The injection of CO₂ to hypersaline geothermal brine: A case study for Tuzla region. *Geothermics*, 80:86–91, 7 2019. ISSN 03756505. doi: 10.1016/j.geothermics.2019.02.011.
- [102] G. Towler and R. Sinnott. *Chemical engineering design : principles, practice and economics of plant and process design / Gavin Towler, Ray Sinnott*. Butterworth-Heinemann, Oxford, 2. ed edition, 2013. ISBN 978-00-8096-659-5.
- [103] R. Turton. *Analysis, synthesis, and design of chemical processes / Richard Turton ... [et al.]*. Prentice Hall, 2012. ISBN 978-01-329-4029-0.
- [104] J. D. van der Waals. *Over de Continuïteit van den Gas-en Vloeistooftoestand*. PhD thesis, University of Leiden, 1873.
- [105] W. Wagner and A. Pruss. The IAPWS formulation 1995 for the thermodynamic properties of ordinary water substance for general and scientific use. *Journal of Physical and Chemical Reference Data*, 31:387–535, 6 2002. ISSN 0047-2689. doi: 10.1063/1.1461829.
- [106] W. Wagner, J. R. Cooper, A. Dittmann, J. Kijima, H.-J. Kretzschmar, A. Kruse, R. Maresch, K. Oguchi, H. Sato, I. Stöcker, O. Sifner, Y. Takaishi, I. Tanishita, J. Trubenbach, and T. Willkommen. The IAPWS industrial formulation 1997 for the thermodynamic properties of water and steam. *Journal of Engineering for Gas Turbines and Power*, 122:150–184, 1 2000. ISSN 0742-4795. doi: 10.1115/1.483186.
- [107] S. D. Walsh, N. Garapati, A. M. Leal, and M. O. Saar. Calculating thermophysical fluid properties during geothermal energy production with NIST and REFPROP.

- Geothermics*, 70:146–154, 11 2017. ISSN 03756505. doi: 10.1016/j.geothermics.2017.06.008.
- [108] K. Zimmer, Y. Zhang, P. Lu, Y. Chen, G. Zhang, M. Dalkilic, and C. Zhu. Supcrtbl: A revised and extended thermodynamic dataset and software package of supcrt92. *Computers & Geosciences*, 90:97–111, 5 2016. ISSN 00983004. doi: 10.1016/j.cageo.2016.02.013.
- [109] H. Ármannsson. Co2 emission from geothermal plants. 2003.
- [110] Åke Melinder. *Properties of Secondary Working Fluids (Secondary Refrigerants or Coolants, Heat Transfer Fluids) for Indirect Systems*. International Institute of Refrigeration, 2 edition, 2010. ISBN 9782913149830.

Nomenclature

Acronyms

Acronym	Description
BIC	Binary Interaction Coefficients (BIC)
CFC	chlorofluorocarbon (CFC)
DSC	Direct Steam Cycle (DSC)
EGS	Enhanced Geothermal System (EGS)
ESP	Electrical Submersible Pump (ESP)
GA	Genetic Algorithm (GA)
GWP	Global Warming Potential (GWP)
HCFC	hydrochlorofluorocarbon (HCFC)
HEOS	Helmholtz free energy EOS (HEOS)
HFC	hydrofluorocarbon (HFC)
IRR	internal rate of return (IRR)
LCOE	levelised cost of electricity (LCOE)
LSP	Line Shaft Pump (LSP)
NCG	Non-condensable gases (NCG)
NETL	National Energy Technology Laboratory (NETL)
NPV	net present value (NPV)
ODP	Ozone Depletion Potential (ODP)
ORC	Organic Rankine Cycle (ORC)
PPI	Producer Price Index (PPI)
PR	Reng-Robinson (PR)
RK	Redlich-Kwong (RK)
SRK	Soave-Redlich-Kwong (SRK)
SP2009	Spycher Pruess 2009 (SP2009)

Acronym	Description
SW	Span-Wagner (SW)
TEMA	Tubular Exchangers Manufacturers Association (TEMA)
TVD	True Vertical Depth (TVD)
VDW	van der Waals (VDW)
VLE	Vapour-Liquid Equilibrium (VLE)
WHP	Wellhead Pressure (WHP)
WP	Wagner-Pruß (WP)
Z	Compressibility Factor (Z)

Greek symbols

Variable	Description	SI unit
α	SRK and PR EOS attractive term coefficient	—
α	Molar Helmholtz energy	J mol^{-1}
α^0	Molar Helmholtz energy of ideal gas	J mol^{-1}
α^r	Residual molar Helmholtz energy	J mol^{-1}
α	Baumann Coefficient	-
δ	Reduced density	—
$\Delta \dot{E}_{loss}$	Exergy destruction rate	W
ΔH_{fg}	Latent Heat	J kg^{-1}
ΔT	Temperature difference	K
ΔT_{cond}^{min}	Minimum approach temperature difference in the condenser	K
ΔT_{evap}^{min}	Minimum approach temperature difference in the evaporator	K
ΔT_i^{min}	Minimum approach temperature difference in equipment i	K
ΔT_{lm}	Log-mean temperature difference	K
ΔT_{preh}^{min}	Minimum approach temperature difference in the pre-heater	K
ΔT_{sc}	Degree of super-cooling	K

Variable	Description	SI unit
ΔT_{sh}	Degree of super-heating	K
ΔT_{sh}^{min}	Minimum approach temperature difference in the super-heater	K
Δz	Difference in depth	m
η_{bf}^{II}	Second law brute-force efficiency	%
η_{cycle}	Cycle efficiency	%
η_{cycle}^{carnot}	Carnot cycle efficiency	%
η_{cycle}^{miced}	Mixed cycle efficiency	%
η_{cycle}^{tri}	Triangular cycle efficiency	%
$\eta_{dry,turb}$	Dry isentropic turbine efficiency	%
η_{func}^{II}	Second law functional efficiency	%
η_{gen}	Generator efficiency	%
η_{isen}	Isentropic efficiency	%
$\eta_{isen,comp}$	Isentropic compressor efficiency	%
$\eta_{isen,pump}$	Isentropic pump efficiency	%
$\eta_{isen,turb}$	Isentropic turbine efficiency	%
η_{motor}	Motor efficiency	%
η_{plant}	Plant efficiency	%
η_{recov}	Thermal recovery efficiency	%
η_{turb}^{wet}	Wet turbine efficiency	%
μ_i	Chemical potential of species i	J mol ⁻¹
Ψ_i	Placeholder for h_i , s_i , or v_i	
Ψ_i^{aq}	Placeholder for h_i , s_i , or v_i in the aqueous phase	
Ψ_i^s	Placeholder for h_i , s_i , or v_i in the solid phase	
Ψ_i^t	Placeholder for h_i , s_i , or v_i in the total phase	
ρ	Density	kg m ⁻³ or mol m ⁻³
ρ_c	Critical density	kg m ⁻³ or mol m ⁻³
ρ_i	Partial molar density	mol m ⁻³
τ	Reduced temperature	K

Latin symbols

Variable	Description	SI unit
a	VDW EOS attractive term constant	$\text{bar mol}^2\text{m}^{-6}$
a_i, a_j	a of species i and j respectively	-
a	Activity	-
a_i	a of species i	-
A	Area	m^2
A	Molar Helmholtz energy of mixture	J mol^{-1}
$A^{id\ mix}$	Molar Helmholtz energy of ideal mixture	J mol^{-1}
A^{excess}	Excess molar Helmholtz energy of mixture	J mol^{-1}
b	VDW EOS repulsive term constant	$\text{m}^3\text{mol}^{-1}$
b_i	b of species i	$\text{m}^3\text{mol}^{-1}$
e	Specific exergy	J kg^{-1}
\dot{E}	Exergy flow rate	W
\dot{E}_W	Work exergy flow rate	W
C	Cost	\$ or €
C_{comp}	Cost of compressor	\$ or €
C_{cond}	Cost of evaporator	\$ or €
C_{constr}	Cost of construction	\$
C_{evap}	Cost of evaporator	\$ or €
C_{fan}	Cost of fan	\$ or €
C_i	Cost of equipment i	\$ or €
C_{gen}	Cost of generator	\$ or €
C_{opi}	Operating cost in year i	\$
C_{op0}	Operating cost in year zero	\$
C_p	Specific heat capacity	$\text{J kg}^{-1}\text{K}^{-1}$
C_{preh}	Cost of pre-heater	\$ or €
$C_{primary}$	Cost of primary equipment	\$
C_{pump}	Cost of pump	\$ or €
C_{rec}	Cost of recuperator	\$ or €
C_{rev_i}	Revenue in year i	\$
$C_{secondary}$	Cost of secondary equipment	\$

Variable	Description	SI unit
C_{sh}	Cost of super-heater	\$ or €
C_{total}	Cost of power plant	\$
C_{turb}	Cost of turbine	\$ or €
$C_{turb,gen}$	Cost of turbine and generator	\$ or €
$f_{currency}$	Currency correction factor	-
$f_{disc\ rate}$	Discount rate	%
f_{inf}	Rate of inflation	%
f_{PPI}	PPI correction factor	-
f_{price}	Electricity price	\$ kWh ⁻¹
f_{tax}	Tax rate	%
g	Acceleration due to gravity	m s ⁻²
G	Gibbs free energy	J
h	Depth	m
h	Heat transfer coefficient	J s ⁻¹ m ⁻²
h_i	Partial molar enthalpy	J mol ⁻¹
h_{in}	Inlet specific enthalpy	J kg ⁻¹
$h_{out, isen}$	Outlet specific enthalpy from isentropic process	J kg ⁻¹
H	Enthalpy	J
i	Index	-
k_{ij}	BIC for species i and j	-
M_r	Molar mass	kg mol ⁻¹
M_{r_i}	Molar mass of species i	kg mol ⁻¹
m	Mass	kg
m_r	Mass of species i	kg
\dot{m}	Mass flow rate	kg s ⁻¹
\dot{m}_{max}	Mass flow rate of H ₂ O	kg s ⁻¹
\dot{m}_{geo}	Geofluid mass flow rate	kg s ⁻¹
\dot{m}_{max}	Maximum mass flow rate	kg s ⁻¹
n	Molar amount	mol
\mathbf{n}	Vector of molar amounts	mol
n_i	Molar amount of species i	mol
n_{stages}	Number of stages	-

Variable	Description	SI unit
N	Number of species	-
NPV	Net present value	\$
P	Pressure	bar, Pa
P_{absorb}	Absorption pressure	bar
P_{cond}	Condensation pressure	bar
P_{crit}	Critical pressure	bar
P_{evap}	Evaporation pressure	bar
P_{flash}	Flash pressure	bar
P_{geo}^{in}	Geofluid inlet pressure	bar
P_r	Reduced pressure	-
P_{sat}	Saturation pressure	bar
$P_{shut-in}$	Shut-in pressure of wellbore	bar, Pa
P^o	Reference pressure	Pa
\dot{Q}	Heat flow rate	W
\dot{Q}_i	Inter-stage cooling of stage i	W
\dot{Q}_{in}	Inlet heat flow rate	W
\dot{Q}_{max}	Maximum heat flow power	W
R	Universal gas constant	bar m ³ mol ⁻¹ K ⁻¹
R_f	Fouling resistance	m ² K J ⁻¹
R_m	Material resistance	m ² K J ⁻¹
s_i	Partial molar entropy	J mol ⁻¹ K ⁻¹
s_{NaCl}	Salinity	kg kg ⁻¹
s_{NCG}	NCG content	kg kg ⁻¹
s_{NaCl}^{eff}	Effective salinity	kg kg ⁻¹
s_{NCG}^{eff}	Effective NCG content	kg kg ⁻¹
S	Entropy	J K ⁻¹
SP	Size parameter	m ^{1.5} kg ^{0.25} s ^{-0.5} J ^{-0.25}
T	Temperature	K
T_c	Critical temperature	K
T_{cond}	Condensation temperature	K
T_{cycle}^{max}	Maximum cycle temperature	K
T_C	Temperature of surroundings	K

Variable	Description	SI unit
T_{geo}^{in}	Geofluid inlet temperature	K
T_{min}	Minimum cycle temperature	K
T_o	Reference temperature	K
T_H	Temperature of heat source	K
u	Tangential velocity	m s^{-1}
U	Internal energy	J
U	Overall heat transfer coefficient	$\text{J m}^{-2} \text{K}^{-1}$
v	Fluid velocity	m s^{-1}
v_i	Partial molar volume	$\text{m}^3 \text{mol}^{-1}$
V	Volume	m^3
V_m	Molar volume	$\text{m}^3 \text{mol}^{-1}$
\dot{V}	Volumetric flow rate	$\text{m}^3 \text{s}^{-1}$
w	Relative velocity	m s^{-1}
\dot{W}_i	Compression power of stage i	W
\dot{W}_{net}	Net power	W
\dot{w}_{net}	Specific net power	W kg^{-1}
x	Mole fraction	mol %
x	Steam quality	kg kg^{-1} or mass %
x	Vapour quality	mol mol^{-1} or mol %
x_{geo}^{in}	Geofluid inlet vapour quality	mol %
x_i, x_j	x of species i and j respectively	-
X_{constr}	Construction cost coefficient	-
X_{sec}	Secondary equipment cost coefficient	-
\mathbf{y}	Vector of mole fractions	-
y_m	Average wetness	%
\mathbf{y}^o	Reference vector of mole fractions	-
z	TVD	m
Z	Compressibility factor	-

List of Figures

1.1	The sub-surface temperature for different geothermal gradients	3
1.2	Schematic of a hydrothermal system	5
1.3	Schematic of a dry steam geothermal power plant.	8
1.4	Schematic of a direct steam cycle with flash geothermal power plant. . . .	9
1.5	Schematic of a direct steam cycle with double flash geothermal power plant.	10
1.6	Schematic of a binary ORC geothermal power plant.	11
2.1	Saturation curves of water and carbon dioxide	17
2.2	Convergence maps of the water-carbon dioxide binary HEOS mixture im- plemented in <i>CoolProp</i> for a range of compositions.	18
2.3	Schematic of a possible chemical reactive system describing a geofluid . . .	20
2.4	The specific volume of water as calculated with <i>Reaktoro</i>	24
2.5	The deviation of saturation temperature from the WP EOS	25
2.6	Flow diagram of GeoProp for partitioning geofluids and calculating their thermophysical properties	28
2.7	The density of various brines as a function of temperature at 1 bar pressure. Solid circles represent “measured” data and lines represent property models	31
2.8	The specific enthalpy of various brines as a function of temperature at 1 bar pressure.	31
2.9	The specific entropy of various brines as a function of temperature at 1 bar pressure.	32
2.10	Flow diagram of GeoProp v2 for partitioning geofluids and calculating their thermophysical properties	33
2.11	The temperature and heat released by different geofluids as well as the corresponding vapour quality.	36
2.12	Comparison of the equilibrium mole fractions of water in a carbon dioxide- rich phase	37
2.13	Comparison of the equilibrium mole fractions of carbon dioxide in a water- rich phase. Part 1.	38

2.14 Comparison of the equilibrium mole fractions of carbon dioxide in a water-rich phase. Part 2.	38
3.1 Schematic of a dry steam geothermal power plant. Adapted from [30] . . .	40
3.2 T-S diagram of a typical dry steam geothermal power plant.	40
3.3 Schematic of a flash steam geothermal power plant. Adapted from [30] . .	41
3.4 T-S diagram of a typical flash steam geothermal power plant.	41
3.5 Schematic of a dual flash steam geothermal power plant. Adapted from [30]	42
3.6 T-S diagram of a typical dual flash steam geothermal power plant.	42
3.7 Optimisation of the WHP to maximise the turbine power.	44
3.8 Optimisation of the flash temperature to maximise the turbine power. . . .	45
3.9 Maximisation of the turbine power by considering the inter-relation of the well performance curve and the enthalpy change across the turbine.	46
3.10 The optimum turbine power as a function of the number of flash stages. . .	47
3.11 Schematic of a binary geothermal power plant.	47
3.12 TS and TQ diagrams of a saturated Rankine cycle.	48
3.13 TS and TQ diagrams of a super-heated Rankine cycle.	49
3.14 Schematic of a binary ORC geothermal power plant. Adapted from [30] . .	49
3.15 TS and TQ diagrams of a binary ORC geothermal power plant using n-Butane as the working fluid.	50
3.16 Temperature-Entropy phase envelopes of dry, wet, isentropic fluids. [14] . .	51
3.17 Critical temperatures and pressures of various ORC working fluids, [10, 20]	52
3.18 Schematic of a binary ORC geothermal power plant with recuperation. . .	53
3.19 TS and TQ diagrams of a recuperative binary ORC using n-Butane as the working fluid.	54
3.20 Schematic of a double pressure binary ORC geothermal power plant. . . .	55
3.21 TS and TQ diagram of a double pressure binary ORC geothermal plant using n-Butane as the working fluid.	55
3.22 Schematic of a dual fluid binary ORC geothermal power plant.	56
3.23 TS and TQ diagrams of a dual fluid binary ORC geothermal power plant using n-Butane and n-Pentane as the working fluids.	57
3.24 Schematic of an interlocking dual fluid binary ORC geothermal power plant.	58
3.25 TS and TQ diagrams of a super-critical binary ORC geothermal power plant using n-Butane as the working fluid.	59
3.26 TS and TQ diagrams of a binary ORC geothermal power plant using a 50:50 mixture of n-Butane and n-Pentane as the working fluid.	60

3.27	Optimisation of the maximum cycle temperature for saturated binary ORC geothermal power plant.	61
3.28	TS and TQ diagrams of a saturated binary ORC with the maximum cycle temperature optimised for maximum net power.	62
3.29	Optimisation of the geofluid working fluid mass rate ratio for a liquid dominated heat source.	63
3.30	Optimisation of the geofluid working fluid mass rate ratio for a two-phase heat source.	64
3.31	TS and TQ diagrams of a binary ORC geothermal power plant with optimised geofluid working fluid mass rate ratio	65
3.32	Temperature-Entropy diagram of the Rectangular cycle, left, and the Triangular cycle, right	66
3.33	Temperature-Duty diagram of the geofluid and the rectangular cycle.	67
3.34	The overall plant efficiency for different latent heats as a function of maximum cycle temperature.	70
3.35	Temperature-Duty diagram of the geofluid and the triangular cycle.	71
3.36	The overall plant efficiency for different latent heats as a function of cycle temperature for a Rectangular and Triangular cycle.	74
3.37	Fluid, blade and relative velocity vectors at the inlet and outlet of the blade.	80
3.38	Velocity Triangles.	80
3.39	Configuration of an impulse turbine stage and the corresponding fluid pressure and velocity profiles.	81
3.40	Configuration of a reaction turbine stage and the corresponding fluid pressure and velocity profiles.	82
3.41	Inlet and outlet streams of an axial turbine.	82
3.42	Inlet and outlet streams of a radial inflow turbine.	83
3.43	Inlet and outlet streams of a radial-outflow turbine.	83
3.44	Mechanism for liquid formation in a steam turbine.	85
3.45	Shell & Tube heat exchanger.	91
3.46	Steam turbine specific cost correlations.	93
3.47	ORC turbine specific cost correlations.	94
3.48	Shell and tube specific cost correlations.	95
3.49	Condenser specific cost correlations.	96
3.50	Pump specific cost correlations.	97
3.51	Compressor specific cost correlations.	98

3.52	Fan specific cost correlations. Citations in order of appearance [103], [91]. ^a Assuming a pressure drop of 120 Pa, an fan efficiency of 60 %, resulting in a air enthalpy of 0.16 kJ kg^{-1} and a density of 1.18 kg m^{-3}	99
3.53	Plant cost correlations of a sub-critical binary ORC and a single flash DSC.	100
3.54	Specific cost cost correlations of a sub-critical binary ORC and a single flash DSC.	100
4.1	Component diagram of PowerCycle	101
4.2	Architecture of the fluid properties module	103
4.3	The calculation regions when using GeoProp. The <i>Trivial</i> region covers the temperature and pressure conditions for which the SP2009 is used, but because the natural state of water is gaseous, the fluid as a whole is considered gaseous.	104
4.4	The process streams entering and exiting a turbine	106
4.5	Comparing the Baumann-corrected isentropic turbine efficiency as calcu- lated from mole- or mass-based vapour quality for geofluids of different CO ₂ content.	107
4.6	The process streams entering and exiting a heat exchanger	109
4.7	The process streams entering and exiting a pump and compressor	113
4.8	The process streams entering and exiting a stage of a multi-stage compressor	114
4.9	The process streams entering and exiting a mixer	116
4.10	The process streams entering and exiting a separator	117
4.11	USD-EUR exchanger rate between 2002 and 2023 [59]	119
4.12	PPI for turbines (WPU1197), heat exchangers (WPU1075) and pumps/- compressors (PCU33391-33391) between 2002 and 2023 [72]	119
4.13	Process diagram of the <i>Aspen Plus v11</i> simulation used to calculate the enthalpy, entropy and density of different fluids	121
4.14	Comparison of the thermophysical properties of water calculated by <i>Aspen Plus</i> and <i>PowerCycle</i>	122
4.15	Process diagram of the <i>Aspen Plus v11</i> simulation used to calculate the performance of a turbine, assuming dry expansion	123
4.16	Process diagram of the <i>Aspen Plus</i> simulation used to calculate the perfor- mance of a heat exchanger.	124
4.17	Comparison of the temperature duty profiles calculated in <i>Aspen Plus</i> and <i>PowerCycle</i> for scenario 1.	126
4.18	The saturation temperature of n-butane at 32 bar in <i>Aspen Plus</i> using a Heater element	127

4.19	Process flow diagram of the <i>Aspen Plus v11</i> simulation used to calculate the performance of a heat exchanger	128
4.20	Comparing the heat exchanger performance calculations between Power-Cycle and Aspen Plus v11	130
4.21	Process diagram of the <i>Aspen Plus</i> simulation used to calculate the performance of a direct steam cycle	131
4.22	Process diagram of the <i>Aspen Plus</i> simulation used to calculate the performance of a binary ORC	134
5.1	DSC geothermal power plant.	138
5.2	Binary ORC geothermal power plant.	139
5.3	Temperature Heat Transferred diagram for the Binary ORC geothermal power plant shown in Figure 5.3. For an inlet temperature of 165 °C and a vapour quality of 25 %.	139
5.4	Maximum specific net power from a geofluid of pure water.	142
5.5	Specific net power from a geofluid of pure water by working fluid as a function of temperature.	142
5.6	Specific net power from a geofluid of pure water by working fluid as a function of steam quality.	143
5.7	Geofluid saturation pressure as a function of temperature for a range of effective salinity and NCG content.	144
5.8	Deviation of liquid and vapour heat flow from pure water/steam for a range of effective salinity and NCG content.	144
5.9	Process flow diagram of the <i>Aspen Plus v11</i> simulation used to calculate the mutual solubilities of water and carbon dioxide	145
5.10	Comparison of the equilibrium mole fraction of water in a carbon dioxide-rich phase predictions.	146
5.11	Comparison of the equilibrium mole fraction of carbon dioxide in a water-rich phase predictions. Part 1.	147
5.12	Comparison of the equilibrium mole fraction of carbon dioxide in a water-rich phase predictions. Part 2.	147
5.13	Reported stream composition with the ELECNRTL model in <i>Aspen Plus v11</i> for supercritical conditions	148
5.14	Maximum specific net power from a DSC or a binary ORC as a function of salinity and NCG content.	149
5.15	Specific net power as a function of NCG content.	149
5.16	Single flash DSC geothermal power plant.	151

5.17	Binary ORC geothermal power plant.	152
5.18	The critical temperature and pressure of the ORC working fluids considered.	153
5.19	The phase envelopes in the temperature-entropy domain of the ORC working fluids considered.	154
5.20	The net electrical power of the single flash DSC geothermal power plant as a function of inlet steam quality at different inlet temperatures.	155
5.21	The geofluid inlet pressure and optimised flash and condensation pressures for the single flash DSC geothermal power plant.	156
5.22	The degree of flashing X_{flash} for a single flash DSC geothermal power plant as a function of geofluid inlet temperature and vapour quality.	157
5.23	The inlet geofluid vapour quality and the resultant vapour quality following a 50 % flash.	158
5.24	The absolute cost (left) and relative cost (right) of plant components of a single flash DSC geothermal power plant.	159
5.25	The specific plant cost (left) and the LCOE (right) of the single flash DSC geothermal power plant.	159
5.26	The net electrical power for a binary ORC using IsoPentane as the working fluid.	160
5.27	TQ diagrams for a binary ORC using Isopentane as the working fluid by steam quality.	161
5.28	TQ diagrams for a binary ORC using Isopentane as the working fluid by inlet temperature.	162
5.29	The optimised reduced pressure P_r for a binary ORC using Isopentane as the working fluid.	163
5.30	The minimum cycle temperature T_{min} and the maximum cycle temperatures T_{max} for a binary ORC using Isopentane as the working fluid.	163
5.31	The degrees of super-heating ΔT_{sh} for a binary ORC using Isopentane.	164
5.32	The normalised objective function space for a binary ORC using IsoPentane as the working fluid.	165
5.33	The normalised objective function convergence for a binary ORC using IsoPentane as the working fluid.	165
5.34	The net electrical power by working fluid.	166
5.35	The 1 st law cycle, thermal recovery and plant efficiency of the binary ORC plant.	167
5.36	The net electrical power and the corresponding specific plant cost for the best performing working fluid.	168

5.37	The specific plant cost as a function of inlet steam quality at different inlet temperatures for a range of working fluids.	169
5.38	The specific plant cost (left) and the corresponding net power (right) for the best performing working fluid.	170
5.39	The absolute cost and relative cost of plant components of a binary ORC geothermal power plant by working fluids.	171
5.40	The turbine cost fluid normalised by the plant power by working for a geofluid inlet temperature of 548 K as a function of inlet vapour quality. . .	172
5.41	The turbine stages and size parameter SP by working fluid for a geofluid inlet temperature of 548 K as a function of inlet vapour quality.	172
5.42	The condenser cost fluid normalised by the plant power by working for a geofluid inlet temperature of 548 K as a function of inlet vapour quality. . .	173
5.43	The net electrical power and the corresponding specific cost of the single flash DSC and the binary ORC geothermal power plants.	174
5.44	The brute-force and functional second law efficiency of the single flash DSC and the binary ORC geothermal power plants.	175
5.45	The geofluid inlet conditions for which the binary ORC and single flash DSC geothermal power plants deliver equal net electrical power and have equal specific plant cost.	176
5.46	The geofluid inlet conditions for which the binary ORC and single flash DSC geothermal power plants deliver equal net electrical power by working fluid.	176
5.47	The specific plant cost and the corresponding net electrical power of the single flash DSC and the binary ORC.	177
5.48	The geofluid inlet conditions for which binary ORC and single flash DSC geothermal power plants deliver equal net electrical power and have equal specific plant costs.	177
5.49	The specific plant cost of the techno-economically optimised single flash DSC.	180
5.50	The net electrical power of the techno-economically optimised single flash DSC.	180
5.51	The absolute cost of plant components for a techno-economically optimised and thermodynamically optimised single flash DSC geothermal power plant. .	181
5.52	The minimum approach temperature in the condenser and condensation pressure for a techno-economically and a thermodynamically optimised single flash DSC geothermal power plant.	182

5.53	The degree of flashing X_{flash} a techno-economically (left) and a thermodynamically (right) optimised single flash DSC geothermal power plant. . . .	182
5.54	The minimum specific cost of the techno-economically optimised binary ORC.	183
5.55	The maximum net electrical power of the techno-economically optimised binary ORC.	183
5.56	The absolute cost of plant components for techno-economically optimised and thermodynamically optimised binary ORC geothermal power plants by working fluid.	184
5.57	The number of turbine stages of the techno-economically optimised binary ORC geothermal power plant.	185
5.58	The turbine size parameter of the techno-economically optimised binary ORC.	185
5.59	The techno-economically and thermodynamically optimised reduced pressure for some working fluids.	186
5.60	The techno-economically and thermodynamically optimised minimum cycle temperature for some working fluids.	187
5.61	The techno-economically and thermodynamically optimised condenser minimum approach temperature difference for some working fluids.	188
5.62	The techno-economically and thermodynamically optimised pre-heater minimum approach temperature difference for some working fluids.	189
5.63	The specific plant cost and the corresponding net electrical power of the single flash DSC and the binary ORC.	190
5.64	The geofluid inlet conditions for which the binary ORC and single flash DSC geothermal power plants deliver equal net electrical power and have equal specific plant costs.	191
5.65	The net electrical plant power and the corresponding specific plant cost of the single flash DSC and the binary ORC.	191
5.66	The geofluid inlet conditions for which the binary ORC and single flash DSC geothermal power plants deliver equal net electrical power and have equal specific plant costs.	192
5.67	The specific plant cost (excl. drilling costs) and net electrical power (right) obtained from thermodynamic and techno-economic optimisations using n-Butane as the working fluid.	196
5.68	The specific plant cost (excl. drilling costs) and net electrical power (right) obtained from thermodynamic and techno-economic optimisations using CycloPentane as the working fluid.	196

5.69	Single flash DSC geothermal power plant with NCG re-pressurisation to atmospheric pressure to allow venting.	198
5.70	Binary ORC geothermal power plant with NCG venting to atmosphere. . .	198
5.71	The net electrical power and specific plant cost of a thermodynamically optimised binary ORC using n-Butane as the working fluid and a single flash DSC geothermal power plant.	199
5.72	The net electrical power of a thermodynamically optimised binary ORC and single flash DSC geothermal power plants venting NCG to atmosphere.	201
5.73	Breakdown of the net electrical power for thermodynamically optimised binary ORC (using n-Butane as the working fluid) (left) and single flash DSC (right) geothermal power plants with NCG venting to atmosphere. . .	202
5.74	The pressures of the geofluid at different points in the power plant. . . .	202
5.75	The total plant cost of thermodynamically optimised binary ORC (using n-Butane as the working fluid) and single flash DSC geothermal power plants with NCG venting to atmosphere.	203
5.76	The cost breakdown of thermodynamically optimised binary ORC (using n-Butane as the working fluid) and single flash DSC geothermal power plants with NCG venting to atmosphere.	203
5.77	The static pressure with depth of NCG for a range of injection wellhead pressures.	206
5.78	The minimum NCG injection pressure required to inject at a given depth for different NCG injection temperatures.	207
5.79	Binary ORC or single flash DSC geothermal power plants with NCG reinjection into the reservoir.	208
5.80	The net electrical power of thermodynamically optimised binary ORC and single flash DSC geothermal power plants re-injecting NCG into the reservoir.	209
5.81	Breakdown of the net electrical power for thermodynamically optimised binary ORC and single flash DSC geothermal power plants re-injecting NCG into the reservoir.	209
5.82	The pressures of the geofluid at different points in the single flash geothermal power plant.	210
5.83	The total plant cost of thermodynamically optimised binary ORC and single flash DSC geothermal power plants re-injecting NCG into the reservoir.	210
5.84	The cost breakdown of thermodynamically optimised binary ORC and single flash DSC geothermal power plants re-injecting NCG into the reservoir.	211
5.85	Binary ORC or single flash DSC geothermal power plants with partial dissolution of NCG subsequent re-injection into the reservoir.	212

5.86	The net electrical power of thermodynamically optimised binary ORC and single flash DSC geothermal power plants partially dissolving and re-injecting NCG into the reservoir.	213
5.87	The bubble point pressure for different water-carbon dioxide mixtures as a function of temperature.	214
5.88	The pressures of the geofluid at different points in the power plant.	215
B.1	Comparison of the equilibrium mole fraction of water in a carbon dioxide-rich phase as calculated by Spycher et al. and Spycher and Pruess against our implementation of their model	272
B.2	Comparison of the equilibrium mole fraction of carbon dioxide in a water-rich phase as calculated by Spycher et al. and Spycher and Pruess against our implementation of their model	273
E.1	Comparing properties of n-Butane as calculated by Aspen Plus v11 and PowerCycle (using CoolProp)	281
E.2	Comparing properties of n-Pentane as calculated by Aspen Plus v11 and PowerCycle (using CoolProp)	282
E.3	Process flow diagram of the <i>Aspen Plus v11</i> simulation used to calculate the performance of a turbine for a wet expansion	283
E.4	Process flow diagram of the <i>Aspen Plus v11</i> simulation used to calculate the performance of a pump	284
E.5	Process flow diagram of the <i>Aspen Plus v11</i> simulation used to calculate the performance of a pump	286
E.6	Process diagram of the <i>Aspen Plus</i> simulation used to calculate the performance of a multi-stage compressor	288

List of Tables

1.1	Half-life and heat production by radioactive isotope [37].	2
2.1	The applicability range of various incompressible fluid EOS.	19
2.2	The definition of the auxiliary variable and function by partial molar property.	22
2.3	The composition of the geothermal fluid samples near Makhachkala [5] in mg L ⁻¹ . Species exclusively below the detection threshold of 0.1 mg L ⁻¹ have been omitted.	30
2.4	<i>Model</i> capabilities.	33
2.5	Used compositions and models of the considered geofluids.	34
2.6	Used compositions and models of the considered geofluids.	35
3.1	Environmental and Health properties of candidate working fluids [30] . . .	52
3.2	Film heat transfer coefficients for different fluids [8].	90
3.3	Fouling resistances for different fluids.	91
3.4	Steam turbine cost correlations.	92
3.5	ORC turbine cost correlations.	94
3.6	Cost correlations for shell and tube heat exchangers.	95
3.7	Cost correlations for condensers.	96
3.8	Cost correlations for pumps.	97
3.9	Cost correlations for compressors.	97
3.10	Cost correlations for fans. \dot{V} is the volumetric flow rate in m ³ s ⁻¹ and \dot{W} is the fan power in kW.	98
4.1	State variable pairs.	105
4.2	Estimated overall heat transfer coefficients in the PHE and recuperator for different fluid combinations.	112
4.3	Estimated overall heat transfer coefficients in air-cooled condensers for dif- ferent fluid combinations.	112
4.4	The boundary conditions for the turbine performance validation calcula- tions for a dry expansion	123

4.5	The turbine performance calculation results for Aspen Plus v11 and PowerCycle for a dry expansion process	124
4.6	The boundary conditions for the heat exchanger performance calculation validation for scenario 1	125
4.7	The heat exchanger performance calculation results for <i>Aspen Plus v11</i> and <i>PowerCycle</i> for scenario 1	127
4.8	The boundary conditions for the heat exchanger performance calculation validation for scenario 2	128
4.9	The heat exchanger performance calculation results for <i>Aspen Plus v11</i> and <i>PowerCycle</i> for scenario 2	129
4.10	The boundary conditions for the direct steam cycle performance calculation validation	131
4.11	The single flash DSC performance calculation results for <i>Aspen Plus v11</i> and <i>PowerCycle</i>	133
4.12	The boundary conditions for the direct steam cycle performance calculation validation	133
4.13	The binary ORC performance calculation results for <i>Aspen Plus v11</i> and <i>PowerCycle</i>	134
5.1	The model parameters used for the single flash DSC component models. . .	152
5.2	The model parameters used for the binary ORC component models. . . .	153
5.3	The boundary conditions used for the single flash DSC and the binary ORC geothermal power plants.	154
5.4	The optimisation parameters used for the single flash DSC and the binary ORC geothermal power plants.	155
5.5	The optimisation parameters used for the single flash DSC and the binary ORC geothermal power plants.	179
5.6	The boundary conditions used for the single flash DSC and the binary ORC geothermal power plants.	194
5.7	The optimisation parameters used for the single flash DSC and the binary ORC geothermal power plants.	195
5.8	The boundary conditions used for the single flash DSC and the binary ORC geothermal power plants.	200
5.9	The optimisation parameters used for the single flash DSC and the binary ORC geothermal power plants.	200
5.10	The boundary conditions used for the single flash DSC and the binary ORC geothermal power plants.	207

5.11	The optimisation parameters used for the single flash DSC and the binary ORC geothermal power plants.	213
B.1	Low temperature parameters: 285.15 K to 382.15 K , 1 bar to 600 bar [97].	268
B.2	High temperature parameters: 372.15 K to 573.15 K, 1 bar to 600 bar [96].	268
B.3	Low temperature parameters: 285.15 K to 382.15 K , 1 bar to 600 bar [97].	269
B.4	High temperature parameters: 372.15 K to 573.15 K, 1 bar to 600 bar [96].	269
B.5	High temperature parameters: 372.15 K to 573.15 K, 1 bar to 600 bar [96].	271
E.1	The turbine performance calculation results for Aspen Plus v11 and PowerCycle for a wet expansion process	283
E.2	Comparing the pump performance calculations between PowerCycle and Aspen Plus v11	284
E.3	The pump performance calculation results for <i>Aspen Plus v11</i> and <i>PowerCycle</i>	285
E.4	Comparison of the compressor performance calculations between <i>PowerCycle</i> and <i>Aspen Plus</i>	285
E.5	The compressor performance calculation results for <i>Aspen Plus</i> and <i>PowerCycle</i>	286
E.6	Comparison of the multi-stage compressor performance calculations between <i>PowerCycle</i> and <i>Aspen Plus</i>	287
E.7	The multi-stage compressor performance calculation results for <i>Aspen Plus v11</i> and <i>PowerCycle</i>	289

List of Listings

4.1	Configuration of a fluid properties calculation in <i>PowerCycle</i> for water at a given temperature T and pressure P	121
4.2	Configuration of a turbine performance calculation in <i>PowerCycle</i> for saturated steam at temperature T assuming dry expansion	123
4.3	Configuration of a heat exchanger performance calculation in <i>PowerCycle</i> for a fixed mass rate ratio, and hot inlet, cold inlet and cold outlet stream conditions	125
4.4	Configuration of a heat exchanger performance calculation in <i>PowerCycle</i> for a fixed mass rate ratio, and hot inlet, cold inlet and cold outlet stream conditions	129
4.5	Configuration of a direct steam cycle performance calculation in <i>PowerCycle</i>	132
4.6	Configuration of a binary ORC performance calculation in <i>PowerCycle</i> . .	135
D.1	Example for using GeoProp to equilibrate a fluid comprised of water, carbon dioxide and sodium chloride	279
E.1	Configuration of a turbine performance calculation in <i>PowerCycle</i> for saturated steam at temperature T assuming wet expansion	283
E.2	Configuration of a pump performance calculation in <i>PowerCycle</i>	285
E.3	Configuration of a compressor performance calculation in <i>PowerCycle</i> . . .	286
E.4	Configuration of a multi-stage compressor performance calculation in <i>PowerCycle</i>	288

List of Publications

International journals

Published

- Merbecks T., Leal A.M.M, Bombarda P., Silva P., Alfani D., Saar M. O. "Geo-Prop: A thermophysical property modelling framework for single and two-phase geothermal geofluids". *Geothermics*

International conference proceedings

- Merbecks T., Bombarda P., Saar M. O., Silva P., Alfani D. "Investigating the design of ORC heat introduction for single- and two-phase geofluid brines with and without non-condensable gases". *Proceedings of the European Geothermal Congress 2022*
- Merbecks T., Pietra C., Bombarda P., Saar M. O., Silva P., Alfani D. "Investigating the application range of ORC power plants for the exploitation of two-phase geothermal resources". *Proceedings of the ORC 2023* doi: 10.12795/9788447227457_104
- Merbecks T., Bombarda P., Silva P., Alfani D. "On the thermodynamic and economic performance of binary power plant configurations for the exploitation of two-phase geothermal resources". *Proceedings of the Stanford Geothermal Workshop 2024*

Conference presentations & posters

- Merbecks T., Bombarda P., Saar M. O., Silva P., Alfani D. "Design and Operation of a Binary ORC Plant for the Exploitation of Different Geothermal Sources, Including Two-Phase Sources". *EGPD 2022* - Poster
- Merbecks T., Bombarda P., Saar M. O., Silva P., Alfani D. "A novel thermophysical

property model for single and two-phase geothermal brines and non-condensable gas". *EGPD 2023* - Poster & Presentation

- Merbecks T., Pietra C., Bombarda P., Saar M. O., Silva P., Alfani D. "Investigating the thermodynamic application envelope of different geothermal power plant technologies and configurations". *EGPD 2023* - Poster
- Merbecks T., Galieti L., Bombarda P., Saar M. O., Silva P., Alfani D. de Servi C., Colonna P. "On novel binary power plant configurations for the exploitation of two-phase geothermal resources". *EGW 2023* - Poster & Presentation

Easygo Workshops

- 1st Training Week. Delft, Netherlands. 2021
- 2nd Training Week. Aachen, Germany. 2022
- 3rd Training Week. Volterra, Italy. 2023
- Final Training Week. Zurich, Switzerland. 2024

Easygo deliverables

- Merbecks T., Bombarda P., Saar M. O., Silva P., Alfani D. "D1.7: Thermodynamic model of fluid mixtures including CO₂".
- EASYGO-ITN, Kottsova, A., Luo, W., Naranjo, D., Eltayieb, M., Galieti, L. Söding, H., Rangel Jurado, N., Türkdoğan, S., Ouf, J., Santoso, R., Balza Morales, A.E., Gómez Diaz, E., Merbecks, T. "D4.2: Geothermal energy - an introduction to the topic and key issues". https://easygo-itn.github.io/Deliverable_4_2/
- Merbecks T., Bombarda P., Saar M. O., Silva P., Alfani D. "D1.14: Report on optimised operating conditions and maintenance strategy for geothermal plants operating with two-phase fluids at real scale".

A | Chemical Equilibrium

For a closed system at constant temperature and pressure, equilibrium is established when the Gibbs free energy reaches a global minimum [39]. The Gibbs free energy, G , is defined in Equation (A.1), where H is the enthalpy, S , is the entropy and T is the absolute temperature.

$$G = H - TS \quad (\text{A.1})$$

Equation (A.2) gives the differential form of Equation (A.1), where U is the internal energy, P is the absolute pressure and V is the volume. At constant temperature and pressure Equation (A.2) reduces to Equation (A.3).

$$dG = dU + PdV + VdP - TdS - SdT \quad (\text{A.2})$$

$$dG|_{P,T} = dU + PdV - TdS \quad (\text{A.3})$$

The change in internal energy can be attributed to either a heat or work interaction, see Equation (A.4), where δQ is heat added to the system and δW is the work done on the system. The work done captures both mechanical (i.e. pressure-volume) and non-mechanical (i.e. electromagnetic) work, see Equation (A.5), where δW_x is the non-mechanical work.

$$dU = \delta Q + \delta W \quad (\text{A.4})$$

$$\delta W = -PdV + \delta W_x \quad (\text{A.5})$$

Substituting Equations (A.4) and (A.5) into (A.3), reduces the differential form of the Gibbs free energy, yielding Equation (A.6).

$$dG|_{P,T} = \delta Q + \delta W_x - TdS \quad (\text{A.6})$$

Since $Q \leq TdS$, from the second law of thermodynamics; it follows that $Q - TdS \leq 0$, yielding Equation (A.7), meaning that in the absence of non-mechanical work (i.e. $\delta W_x = 0$) the change in Gibbs free energy is strictly negative, see Equation (A.8). Hence, as the system approaches equilibrium, the Gibbs free energy tends towards a global minimum.

$$dG|_{P,T} \leq \delta W_x \quad (\text{A.7})$$

$$dG|_{P,T} \leq 0 \quad (\text{A.8})$$

From the second law of thermodynamics, equilibrium is established when the entropy of the system no longer changes (i.e. $dS = 0$). The Gibbs free energy also provides a derived equilibrium condition, whereby equilibrium (at constant temperature and pressure for closed systems) is established when the Gibbs Energy no longer changes (i.e. $dG = 0$).

B | Spycher-Pruess Partition Model

In their 2009 paper, Spycher and Pruess [96] provide a model for computing the mutual solubilities of water and carbon dioxide. This model is based on a simplified chemically active system approach, where two reversible reactions are taking place, water migrating to the carbon dioxide-rich phase, and carbon dioxide migrating to the water-rich phase. Salts may be present but are considered nonreactive and are thus confined to the water-rich phase.



For each reaction an equilibrium constant is defined based on the species activity in the aqueous (water-rich phase) and the fugacity in the gaseous (carbon dioxide-rich phase), see Equations (B.3) and (B.4).

$$K_{H_2O} = f_{H_2O} / a_{H_2O} \quad (B.3)$$

$$K_{CO_2} = f_{CO_2} / a_{CO_2} \quad (B.4)$$

Where f_i is taken to be the ratio of the component fugacity and the reference fugacity - $f_i = f_i(P, T, y) / f_i^o$ - and the reference fugacity, f_i^o , is defined to be 1 bar. In turn, f_i can be calculated from the component's fugacity coefficient and mole fraction in the carbon dioxide-rich phase as well as the total pressure, see Equation (B.5). Similarly, the component's activity is calculated from its activity coefficient and water rich phase mole fraction, see Equations (B.6) and (B.7).

$$f_i = \Phi_i * y_i * P_{tot} \quad (B.5)$$

$$a_{H_2O} = \gamma_{H_2O} * x_{H_2O} \quad (B.6)$$

$$a_{CO_2} = \gamma'_{CO_2} * \gamma_{CO_2} * x_{CO_2} \quad (B.7)$$

Substituting Equations (B.5), (B.6) and (B.7) into the respective expression for the equilibrium constant (i.e. Equations (B.3) and (B.4)) and using the fact that that mole fractions ought to sum to one, expressions for the mole fraction of water in the carbon dioxide rich phase and the mole fraction of carbon dioxide in the water rich phase can be obtained, see Equations (B.8) and (B.9).

$$y_{H_2O} = A * (1 - x_{CO_2} - x_{salt}) \quad (B.8)$$

$$x_{CO_2} = B' * (1 - y_{H_2O}) \quad (B.9)$$

$$A = \frac{K_{H_2O} * \gamma_{H_2O}}{\Phi_{H_2O} * P_{tot}} \quad (B.10)$$

$$B' = \frac{\Phi_{CO_2} * P_{tot}}{55.508 * \gamma'_{CO_2} * \gamma_{CO_2} * K_{CO_2}} \quad (B.11)$$

Parameters x_{salt} and m_{CO_2} can be calculated from (B.12) and (B.13) respectively.

$$x_{salt} = \frac{v * m_{salt}}{55.508 + v * m_{salt} + m_{CO_2}} \quad (B.12)$$

$$m_{CO_2} = \frac{55.508 * x_{CO_2}}{x_{H_2O}} \quad (B.13)$$

Equations (B.8) and (B.9) can either be solved by iteration or by substitution using Equation (B.14) below, followed by substituting the result into Equation (B.9) to obtain x_{CO_2} .

$$y_{H_2O} = \frac{55.508 * (1 - B')}{\left(\frac{1}{A} - B'\right)(v * m_{salt} + 55.508) + v * m_{salt} B'} \quad (B.14)$$

Thus, to calculate the mutual solubilities, a total of six parameters, three for water and three for carbon dioxide must be calculated:

- The equilibrium constant
- The fugacity coefficient

- The activity coefficient

Subsequently, a mole balance can be used to estimate vapour fraction, α , see Equation (B.15). Note, z_{H_2O} is the mole fraction across all phases.

$$\alpha = \frac{z_{H_2O} - x_{H_2O}}{y_{H_2O} - x_{H_2O}} \quad (\text{B.15})$$

If $\alpha \leq 0$, the geofluid is entirely liquid, i.e. all carbon dioxide is contained within the water-rich phase, whereas if $\alpha \geq 1$, the geofluid is entirely vapour, i.e. all water is contained within the carbon dioxide rich phase. Only when $0 < \alpha < 1$ can the water and carbon dioxide rich phases coexist.

Note. If the pressure is below the saturation pressure of pure water then the geofluid is also assumed to be fully vapour.

A Python implementation of this model is available from the following Github repository: <https://github.com/EASYGO-ITN/GeoProp>.

B.1. The Equilibrium Constant

The equilibrium constant is calculated as per Equation (B.16). K_i^o and P_i^{ref} are calculated from polynomials of the form of (B.17), while \bar{V}_i is calculated using (B.18). The coefficients can be found in Tables B.1 and B.2.

$$K_i(T, P) = K_i^o(T) * \exp \frac{(P - P_i^{ref})\bar{V}_i}{RT} \quad (\text{B.16})$$

$$F(T) = a + b(T - 273.15) + c(T - 273.15)^2 + d(T - 273.15)^3 + e(T - 273.15)^4 \quad (\text{B.17})$$

$$\bar{V}_i = a + b(T - 373.15) \quad (\text{B.18})$$

Table B.1: Low temperature parameters: 285.15 K to 382.15 K , 1 bar to 600 bar [97].

Parameter	Units	a	b	c	d	e
$\log_{10} K_{H_2O}^o$	bar	-2.21	3.097E-02	-1.098E-04	2.048E-07	0.000E+00
$\log_{10} K_{CO_2}^o(L)$	bar mol ⁻¹	1.169	1.368E-02	-5.380E-05	-	-
$\log_{10} K_{CO_2}^o$	bar mol ⁻¹	1.189	1.304E-02	-5.446E-05	-	-
\bar{V}_{CO_2}	cm ³ mol ⁻¹	32.6	-	-	-	-
\bar{V}_{H_2O}	cm ³ mol ⁻¹	18.1	-	-	-	-
P_{ref}	bar	1	-	-	-	-

Table B.2: High temperature parameters: 372.15 K to 573.15 K, 1 bar to 600 bar [96].

Parameter	Units	a	b	c	d	e
$\log_{10} K_{H_2O}^o$	bar	-2.11	2.813E-02	-8.430E-05	1.497E-07	-1.1812E-10
$\log_{10} K_{CO_2}^o$	bar mol ⁻¹	1.668	3.992E-03	-1.156E-05	1.593E-09	0.000E+00
\bar{V}_{CO_2}	cm ³ mol ⁻¹	32.6	3.413E-02	-	-	-
\bar{V}_{H_2O}	cm ³ mol ⁻¹	18.1	3.137E-02	-	-	-
$P_{ref}, T \leq 373.15K$	bar	1	-	-	-	-
$P_{ref}, T > 373.15K$	bar	0.19906	2.0471E-03	1.0152E-04	-1.4234E-06	1.4168E-08

B.2. The Fugacity Coefficient

A Soave-Redlich-Kwong stlye cubic equation of state with asymmetric binary interaction coefficients is used to calculate the fugacity of water and carbon dioxide in the carbon dioxide-rich phase, see Equation (B.19)

$$P = \frac{RT}{V - b_{mix}} - \frac{a_{mix}}{\sqrt{T} * V(V - b_{mix})} \quad (B.19)$$

a_{mix} and b_{mix} are calculate using the following mixing rules:

$$b_{mix} = \sum_{i=1}^N y_i * b_i \quad (B.20)$$

$$a_{mix} = \sum_{i=1}^N \sum_{j=1}^N y_i y_j * a_{ij} \quad (B.21)$$

$$a_{ij} = \sqrt{a_i a_j} (1 - k_{ij}) \quad (\text{B.22})$$

$$k_{ij} = K_{ij} y_i + K_{ji} y_j \quad (\text{B.23})$$

Parameters a_i , b_i and K_{ij} are calculated from polynomials of the form of Equation (B.24). The coefficients can be found in Tables B.3 and B.4

$$F(T) = a + bT \quad (\text{B.24})$$

Table B.3: Low temperature parameters: 285.15 K to 382.15 K , 1 bar to 600 bar [97].

Parameter	Units	a	b
a_{CO_2}	bar cm ⁶ K ^{0.5} mol ⁻²	7.54E+07	-4.13E+04
a_{H_2O}	bar cm ⁶ K ^{0.5} mol ⁻²	0	-
$a_{CO_2-H_2O}$	bar cm ⁶ K ^{0.5} mol ⁻²	7.89E+07	-
b_{CO_2}	cm ³ mol ⁻¹	27.8	-
a_{H_2O}	cm ³ mol ⁻¹	18.18	-

Table B.4: High temperature parameters: 372.15 K to 573.15 K, 1 bar to 600 bar [96].

Parameter	Units	a	b
a_{CO_2}	bar cm ⁶ K ^{0.5} mol ⁻²	8.008E+07	-4.984E+07
a_{H_2O}	bar cm ⁶ K ^{0.5} mol ⁻²	1.337E+08	-1.400E+04
$K_{H_2O-CO_2}$	-	1.427E-02	-4.037E-04
$K_{CO_2-H_2O}$	-	4.228E-01	-7.422E-04
b_{CO_2}	cm ³ mol ⁻¹	28.25	-
b_{H_2O}	cm ³ mol ⁻¹	15.70	-

Determining the fugacity coefficient requires the volume to be determined, which can be achieved by recasting Equation (B.19) into its cubic form, (B.25), and then applying the Cadorna method (or similar) to obtain the roots.

$$V^3 + a_1 V^2 + a_2 V + a_3 = 0 \quad (\text{B.25})$$

$$a_1 = -\frac{RT}{P} \quad (\text{B.26})$$

$$a_2 = - \left(\frac{RTb_{mix}}{P} - \frac{a_{mix}}{P\sqrt{T}} + b_{mix}^2 \right) \quad (\text{B.27})$$

$$a_3 = - \frac{a_{mix}b_{mix}}{P\sqrt{T}} \quad (\text{B.28})$$

If a single real root is found then this corresponds to the stable phase, however if three or more roots are found, the smallest root corresponds to the liquid phase and the largest root to the vapour phase. To determine, which is stable the following auxiliary parameters need to be calculated, Equation (B.31) and (B.32). If $w_2 - w_1 \geq 0$, then largest root is accepted (i.e. stable vapour), otherwise the smallest root is taken (i.e. stable liquid).

$$V_{liq} = \min V_1, V_2, V_3 \quad (\text{B.29})$$

$$V_{vap} = \max V_1, V_2, V_3 \quad (\text{B.30})$$

$$w_1 = P(V_{gas} - V_{liq}) \quad (\text{B.31})$$

$$w_2 = RT * \ln \frac{V_{gas} - b_{mix}}{V_{liq} - b_{mix}} + \frac{a_{mix}}{b_{mix}\sqrt{T}} \ln \frac{(V_{gas} + b_{mix}) * V_{liq}}{(V_{liq} + b_{mix}) * V_{gas}} \quad (\text{B.32})$$

With this in place the fugacity coefficient can be calculated using Equation (B.33).

$$\ln \Phi_i = \frac{b_k}{b_{mix}} \left(\frac{PV}{RT} - 1 \right) - \ln \frac{P(V - b_{mix})}{RT} + \frac{a_{mix}}{b_{mix}RT^{1.5}} \ln \frac{V}{V + b_{mix}} \left(\begin{aligned} & \frac{1}{a_{mix}} \sum_{i=1}^N y_i (a_{ik} - a_{ki}) \\ & - \frac{1}{a_{mix}} \sum_{i=1}^N \sum_{j=1}^N y_i^2 y_j (\mathbf{K}_{ij} - \mathbf{K}_{ji}) \sqrt{a_i a_j} \\ & + \frac{1}{a_{mix}} y_k \sum_{i=1}^N y_i (\mathbf{K}_{ki} - \mathbf{K}_{ik}) \sqrt{a_i a_k} \\ & - \frac{b_k}{b_{mix}} \end{aligned} \right) \quad (\text{B.33})$$

Note. There appears to be a misprint in the original paper by Spycher and Pruess, whereby the K_{ij} highlighted above are instead written as k_{ij} . This has the effect that since $k_{ij} = k_{ji}$ by definition, most terms cancel out.

B.3. The Activity Coefficient

The activity coefficients for water and carbon dioxide in the water-rich phase are defined as per Equations (B.34) and (B.35)

$$\ln \gamma_{H_2O} = (A_M - 2A_M * x_{H_2O}) * x_{CO_2}^2 \quad (B.34)$$

$$\ln \gamma_{CO_2} = 2A_M * x_{CO_2} * x_{H_2O}^2 \quad (B.35)$$

$$A_M = \begin{cases} 0, & T \leq 373.15K \\ a * (T - 373.15) + b * (T - 373.15)^2, & T > 373.15K \end{cases} \quad (B.36)$$

To account for salinity effects, a correction term for the activity of carbon dioxide in the water-rich phase is provided, see Equation (B.37), where parameters λ and ξ are calculated using Equation (B.38).

$$\gamma_{CO_2}' = \left(1 + \frac{\sum m_{i \neq CO_2}}{55.508}\right) \exp \left(\begin{aligned} &2\gamma(m_{Na^+} + m_{K^+} + 2m_{Ca^{+2}} + 2m_{Mg^{+2}}) \\ &+ \xi m_{Cl^-}(m_{Na^+} + m_{K^+} + m_{Ca^{+2}} + m_{Mg^{+2}}) \\ &- 0.07m_{SO_4^{2-}} \end{aligned} \right) \quad (B.37)$$

$$F(T) = aT + \frac{b}{T} + \frac{c}{T^2} \quad (B.38)$$

The coefficients for Equations (B.36) and (B.38) can be found in Table B.5

Table B.5: High temperature parameters: 372.15 K to 573.15 K, 1 bar to 600 bar [96].

Parameter	Units	a	b	c
A_M	-	-3.084E-02	1.927E-05	-
λ	-	2.217E-04	1.074	2648
ξ	-	1.300E-05	-20.12	5259

B.4. Validation

The above equations were implemented in Python and then validated by digitalising the plots of the equilibrium mole fraction of water/carbon dioxide for different temperatures as calculated by Spycher and Pruess. The plots were digitalised using WebPlotDigitizer [83]. From Figures B.1 and B.2 it can be seen that our implementation of the model presented by Spycher and Pruess matches their calculations for a wide range of temperatures and pressures

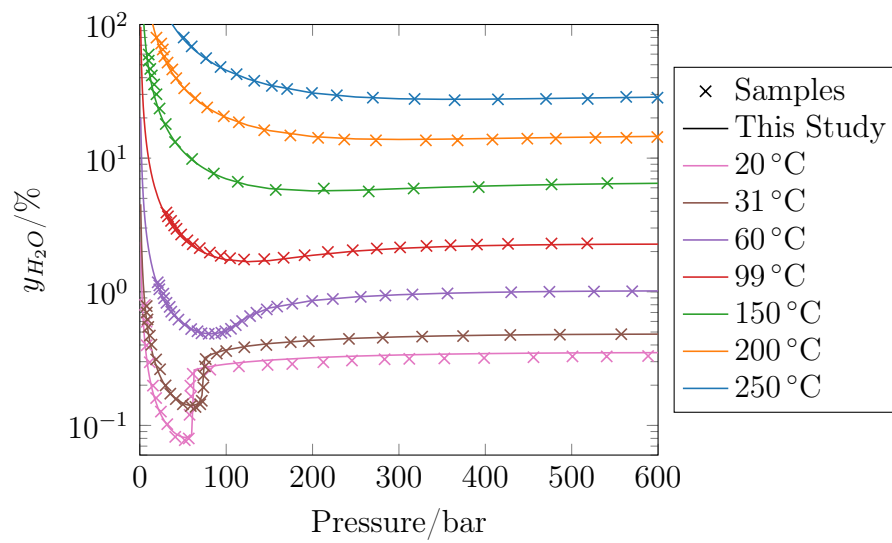


Figure B.1: Comparison of the equilibrium mole fraction of water in a carbon dioxide-rich phase as calculated by Spycher et al. and Spycher and Pruess against our implementation of their model

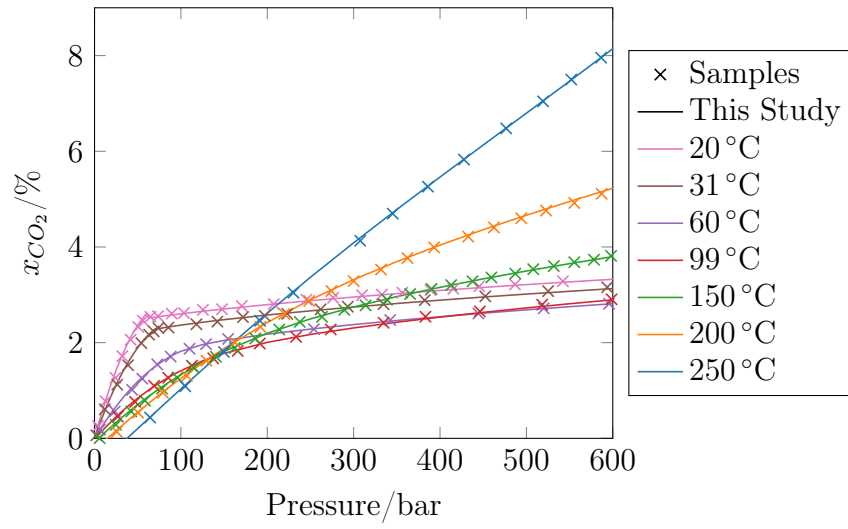


Figure B.2: Comparison of the equilibrium mole fraction of carbon dioxide in a water-rich phase as calculated by Spycher et al. and Spycher and Pruess against our implementation of their model

C | Exergy Analysis

C.1. Exergy Analysis

Exergy is a measurement of the maximum work that can be extracted from a substance relative to its surroundings. This makes it a useful metric for bench-marking the performance of different power plant configurations.

C.1.1. Exergy

For an open system at steady state (i.e. the system boundaries permit mass and energy transfer and the systems thermodynamic properties do not change with time), the exergy can be calculated by considering the First and Second Law of Thermodynamics. The general forms are given by Equations (C.1) and (C.2) respectively, where

\dot{Q} = is the rate of heat transfer into the system

\dot{W} = is the rate of work done by the system

i = is the index of a system inlet/outlet

N = is the total number of inlets and outlets to the system

\dot{m} = is the mass rate through inlet/outlet i into the system

h_i = is the specific enthalpy of the fluid at inlet/outlet i

v_i = is the fluid velocity at inlet/outlet i

z_i = is the relative elevation of inlet/outlet i

g = is the gravitational acceleration

$\dot{\theta}$ = is the rate of production of entropy within the system

τ = is time

s_i = is the specific entropy of the fluid at inlet/outlet i

$T =$ is the absolute temperature

$$\dot{Q} - \dot{W} = - \sum_{i=1}^N \dot{m}_i * (h_i + \frac{1}{2}v_i^2 + gz_i) \quad (C.1)$$

$$\dot{\theta} = - \sum_{i=1}^N \dot{m}_i s_i - \int_{\tau_1}^{\tau_2} \frac{1}{T} \frac{dQ}{d\tau} \quad (C.2)$$

For such a system the maximum work can be extracted if the following conditions are met:

1. All processes within the system are reversible
2. Streams leaving the system are in thermodynamic equilibrium with the surroundings

With the above in mind, consider a simplified open system at steady state with one inlet and one outlet. As the system is at steady state, by mass balance the inlet and outlet mass rates must balance ($\dot{m}_1 = \dot{m}_2 \equiv \dot{m}$). By condition 2, the outlet stream is in thermodynamic equilibrium with the surroundings, thus no more work can be extracted and it can be considered in its *dead state*, denoted by a 0 subscript. Similarly, as heat is only transferred between the system and the surroundings $\int_{\tau_1}^{\tau_2} \frac{1}{T} \frac{dQ}{d\tau} = \frac{Q_0}{T_0}$. By condition 1 all processes are fully reversible and so $\dot{\theta} = 0$. For simplicity, the kinetic and potential energy are ignored.

$$\dot{Q}_0 - \dot{W} = \dot{m} * (h_0 - h_1) \quad (C.3)$$

$$0 = \dot{m} * (s_0 - s_1) - \frac{Q_0}{T_0} \quad (C.4)$$

Combining Equations (C.3) and (C.4), we obtain Equation (C.5).

$$\dot{W} = \dot{m} * [(h_1 - h_0) - T_0 * (s_1 - s_0)] \quad (C.5)$$

As the outlet stream is in its *dead state*, Equation (C.5) represents the maximum work that can be extracted from the inlet stream - i.e. the Exergy, E . The specific exergy of a stream can thus be calculated from Equation (C.6)

$$e = (h - h_0) - T_0 * (s - s_0) \quad (C.6)$$

For completeness, the exergy associated with a heat transfer Q at a temperature T , can be calculated assuming a reversible Carnot cycle operating between a reservoir of temperature T and the *dead state* at temperature T_0 , see Equation (C.7).

$$E_Q = \left(1 - \frac{T_0}{T}\right) * Q \quad (\text{C.7})$$

And somewhat trivially the exergy associated with a work interaction, is the work done itself, see Equation (C.8).

$$E_W = W \quad (\text{C.8})$$

C.1.2. Open System Analysis

Considering an open system with multiple inlet and outlet streams at steady state, accounting for the exergy entering and leaving the system it is possible to asses how closely to thermodynamic ideality the system is operating.

Equations (C.9) and (C.10) can be used to determine the total exergy entering, \dot{E}_{in} , and leaving, \dot{E}_{out} , the system. $\Delta\dot{E}_{loss}$, the difference between the two terms, see Equation (C.11), is the exergy *destroyed* within the system - its value is strictly positive.

$$\dot{E}_{in} = \dot{E}_Q + \sum_{i=1}^N \dot{m}_i * e_i \quad (\text{C.9})$$

$$\dot{E}_{out} = \dot{E}_W + \sum_{j=1}^M \dot{m}_j * e_j \quad (\text{C.10})$$

$$\Delta\dot{E}_{loss} = \dot{E}_{in} - \dot{E}_{out} \quad (\text{C.11})$$

Equation (C.11) allows the destruction of exergetic potential in various plant components to be quantified and can help to identify optimisation opportunities.

It is also useful to define efficiencies to asses the conservation of exergy within a system. Although there are no standardised definitions, two distinct approaches are generally taken.

The *brute-force* approach compares the total outlet exergy to the total inlet exergy, see Equation (C.12).

$$\eta_{bf}^{II} = \frac{\dot{E}_{out}}{\dot{E}_{in}} \quad (\text{C.12})$$

The *functional* approach compares the exergy of the desired output to the exergy destroyed in the process. However as the definition of *desired* varies across application it is not possible to define a general formula.

D | GeoProp Code Examples

The following chapter aims to provide some code examples for using the various software tools created.

D.1. GeoProp

D.1.1. Getting Started

Listing D.1: Example for using GeoProp to equilibrate a fluid comprised of water, carbon dioxide and sodium chloride

Input:

```

1  from GeoProp.Model.Fluid import Fluid
2  from GeoProp.Model.Databases import Comp
3  from GeoProp.Model.PartitionModel import Partition
4  from GeoProp.Model.PropertyModel import PropertyModel
5
6  components = [Comp.WATER, Comp.NaCl_aq, Comp.CARBONDIOXIDE]
7  composition = [1, 0.1, 0.02]
8
9  brine = Fluid(components=components, composition=composition)
10
11  P = 101325  # in Pa
12  T = 350    # in K
13
14  brine = Partition().calc(brine, P, T)
15  brine = PropertyModel().calc(brine, P, T)
16
17  print(brine)

```

Output:

Phase: TOTAL

Components:

METHANE, CO_g, CARBONDIOXIDE, Ethylene_g, HYDROGEN, STEAM, OXYGEN, Phenol_g, m-Cresol_g, o-Cresol_g, p-Cresol_g, CO_aq, CO2_aq, CO3_minus2, Cl_minus, ClO_minus, ClO2_minus, ClO3_minus, ClO4_minus,

H_plus, H2_aq, WATER, H2O2_aq, HCO3_minus, HCl_aq, HClO_aq, HClO2_aq, H2O_minus, Na_plus, NaCl_aq, NaOH_aq, O2_aq, OH_minus, Diamond, Graphite, Halite

Composition:

Component	Mass, kg	MassFrac, -	Moles, mol	MoleFrac, -	In Phase	
CARBONDIOXIDE	1.963e-02	1.753e-02	4.461e-01	7.567e-03	GASEOUS	
STEAM	4.880e-03	4.357e-03	2.709e-01	4.595e-03	GASEOUS	
CO2_aq	3.656e-04	3.264e-04	8.307e-03	1.409e-04	AQUEOUS	
Cl_minus	4.532e-02	4.047e-02	1.278e+00	2.169e-02	AQUEOUS	
H_plus	5.760e-08	5.143e-08	5.714e-05	9.693e-07	AQUEOUS	
WATER	9.951e-01	8.885e-01	5.524e+01	9.370e-01	AQUEOUS	
HCO3_minus	4.205e-06	3.755e-06	6.892e-05	1.169e-06	AQUEOUS	
HCl_aq	4.283e-07	3.824e-07	1.175e-05	1.993e-07	AQUEOUS	
Na_plus	2.939e-02	2.624e-02	1.278e+00	2.168e-02	AQUEOUS	
NaCl_aq	2.529e-02	2.258e-02	4.327e-01	7.340e-03	AQUEOUS	
NaOH_aq	1.258e-10	1.124e-10	3.146e-09	5.337e-11	AQUEOUS	
OH_minus	6.015e-11	5.371e-11	3.537e-09	6.000e-11	AQUEOUS	

Properties:

Pressure: 101325.0 Pa

Temperature: 350.0 K

Phase	Enthalpy, kJ/kg	Entropy, kJ/kg/K	Rho, kg/m3	Volume, m3/kg	Mass, kg	
AQUEOUS	1.948e+02	6.024e-01	1.038e+03	9.636e-04	1.095e+00	
GASEOUS	5.135e+02	1.548e+00	1.204e+00	8.303e-01	2.451e-02	
MINERAL	0.000e+00	0.000e+00	0.000e+00	0.000e+00	8.246e-18	
TOTAL	2.018e+02	6.231e-01	5.232e+01	1.911e-02	1.120e+00	

The following had to be excluded: Diamond, Graphite, Halite

This corresponds to a mass of 8.2464e-18 kg or 7.3629e-16 % of the total

E | Power Cycle Validation

E.1. Fluid Properties

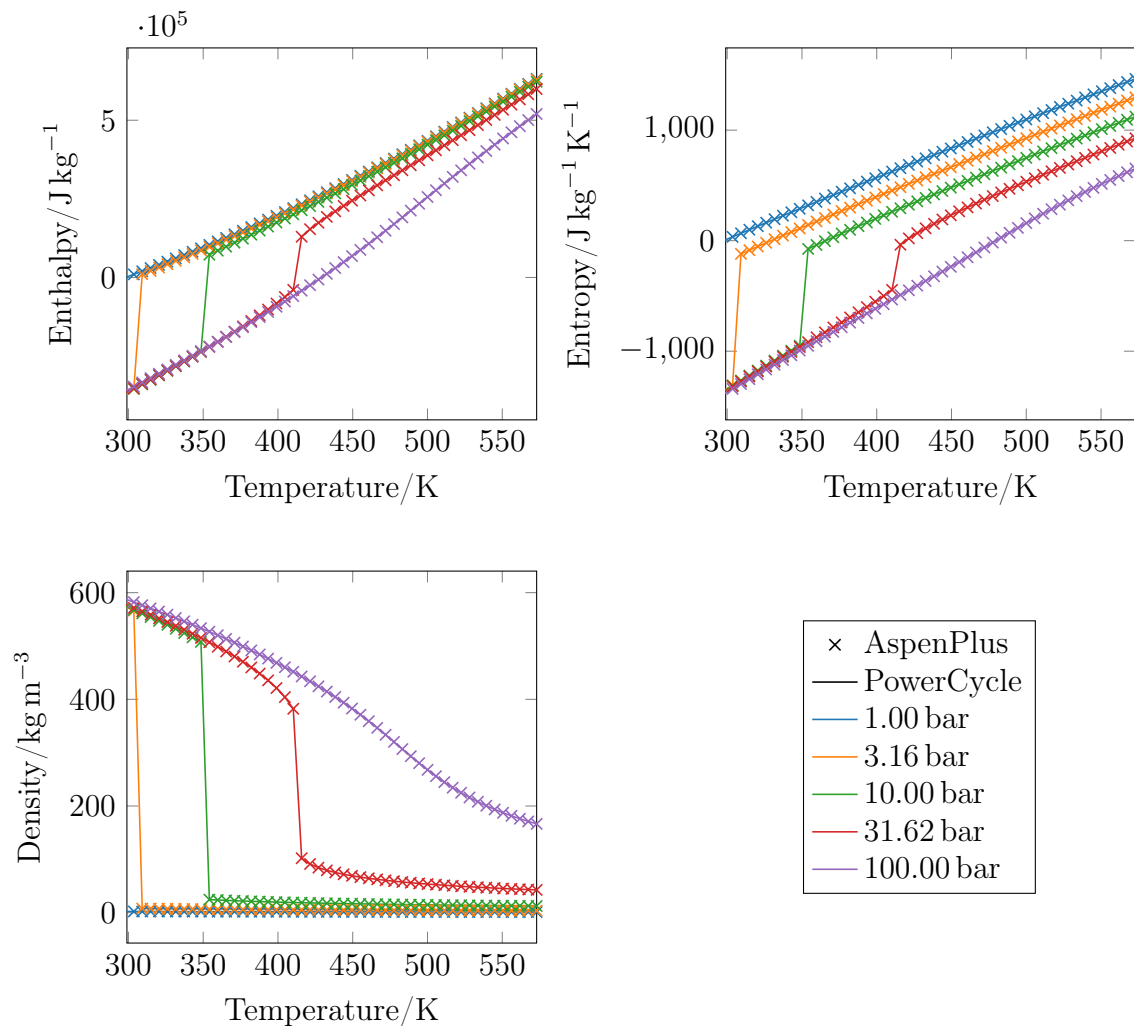


Figure E.1: Comparing properties of n-Butane as calculated by Aspen Plus v11 and PowerCycle (using CoolProp)

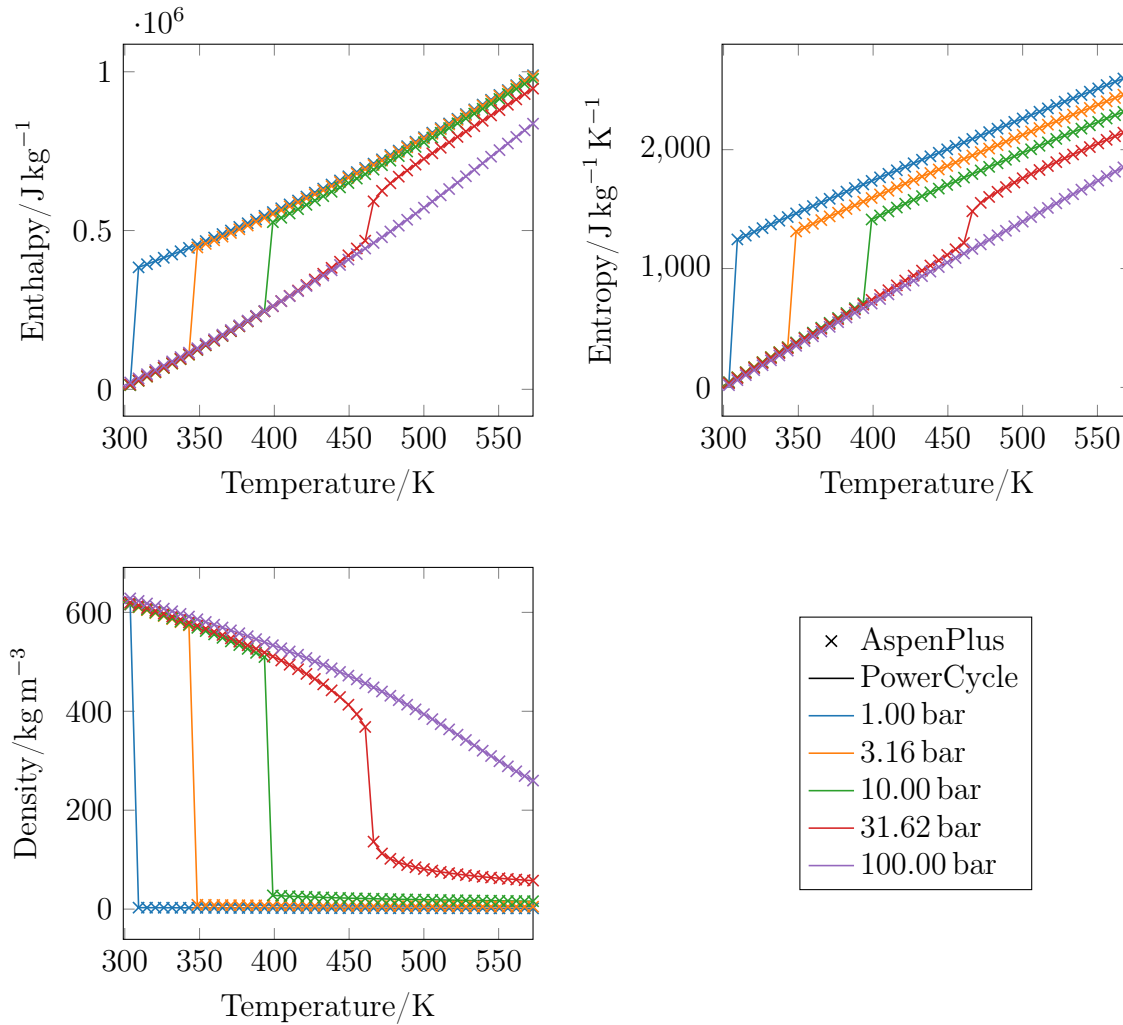


Figure E.2: Comparing properties of n-Pentane as calculated by Aspen Plus v11 and PowerCycle (using CoolProp)

E.2. Turbine - Wet expansion

Unlike *PowerCycle*, *Aspen Plus v11* does not provide native methodologies for handling wet fluid expansion across turbines, such as the Baumann Rule. Nevertheless, the Baumann Rule, or similar, can be implemented through the use of a *Design Spec*, see Figure E.3, by, in the case of the Baumann Rule, iterating on the isentropic efficiency until the value agrees with the prediction from the Baumann Rule. The implementation of a wet expansion turbine in *PowerCycle* is shown in Listing E.1.

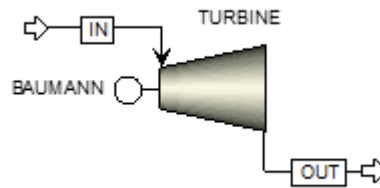


Figure E.3: Process flow diagram of the *Aspen Plus v11* simulation used to calculate the performance of a turbine for a wet expansion

Listing E.1 Configuration of a turbine performance calculation in *PowerCycle* for saturated steam at temperature T assuming wet expansion

```

1  import Simulator
2  from Simulator.streams import MaterialStream
3  from FluidProperties.fluid import Fluid
4
5  inlet = Fluid(["water", 1])
6  inlet = MaterialStream(inlet, m=1)
7  inlet.update("TQ", Tin, Qin)
8
9  pump = Simulator.turbine(0.85, mech_eff=0.95, BaumannCorrection=True)
10 pump.set_inputs(inlet, Pout)
11 outlet = pump.calc()

```

Assuming the same boundary conditions as the dry expansion case, Section 4.6.2, the calculation results for a wet expansion using *PowerCycle* and *Aspen Plus* can be seen to be in close agreement, with negligible differences, see Table E.1.

Table E.1: The turbine performance calculation results for Aspen Plus v11 and Power-Cycle for a wet expansion process

Parameter	Units	Aspen Plus v11	Power Cycle	Difference/%
T_{out}	K	318.96	318.96	0.00
Q_{out}	kg kg^{-1}	0.8398	0.8398	0.00
\dot{W}	kW	-591.38	-591.40	-0.00
\dot{W}_{elec}	kW	-561.81	-561.83	-0.00

E.3. Pump

The inlet stream was initialised to a temperature of 298 K (25 °C) and a pressure of 1 bar. The pump isentropic and motor efficiencies were assumed to be 85 % and 95 % respectively. The outlet pressure was set to 10 bar. For a summary of the inlet conditions, see Table E.2.

Table E.2: Comparing the pump performance calculations between PowerCycle and Aspen Plus v11

Parameter	Units	Value
Fluid	-	Water
\dot{m}	kg s^{-1}	1
P_{in}	bar	1
T_{in}	K	298
P_{out}	bar	10

A standalone pump was modelled in *Aspen Plus*, see Figure E.4, and *PowerCycle*, see Listing E.2. The performance calculation results were found to be in good agreement, Table E.3.

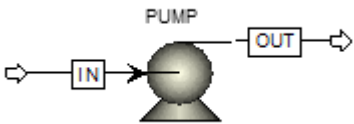


Figure E.4: Process flow diagram of the *Aspen Plus v11* simulation used to calculate the performance of a pump

Listing E.2 Configuration of a pump performance calculation in *PowerCycle*

```

1 import Simulator
2 from Simulator.streams import MaterialStream
3 from FluidProperties.fluid import Fluid
4
5 inlet = Fluid(["water", 1])
6 inlet = MaterialStream(inlet, m=1)
7 inlet.update("PT", Pin, Tin)
8
9 pump = Simulator.pump(0.85, mech_eff=0.95)
10 pump.set_inputs(inlet, Pout)
11 outlet = pump.calc()

```

Table E.3: The pump performance calculation results for *Aspen Plus v11* and *PowerCycle*

Parameter	Units	Aspen Plus v11	Power Cycle	Difference/%
T_{out}	K	298.05	298.05	0.00
\dot{W}	kW	1.06	1.06	0.02
\dot{W}_{elec}	kW	1.12	1.12	0.02

E.4. Compressor

The inlet stream was initialised to a temperature of 298 K (25 °C) and a pressure of 1 bar. The compressor isentropic and mechanical efficiencies were assumed to be 85 % and 95 % respectively. The outlet pressure was set to 10 bar. For a summary of the inlet conditions, see Table E.4.

Table E.4: Comparison of the compressor performance calculations between *PowerCycle* and *Aspen Plus*

Parameter	Units	Aspen Plus v11	Power Cycle	Difference/%
Fluid	-	Carbon Dioxide		
\dot{m}	kg s ⁻¹	1		
P_{in}	bar	0.1		
T_{in}	K	298		
P_{out}	bar	10		

A standalone compressor was modelled in *Aspen Plus v11* and *PowerCycle*, see Figure E.5, and Listing E.3. The performance calculation results were found to be in good agreement, Table E.5.

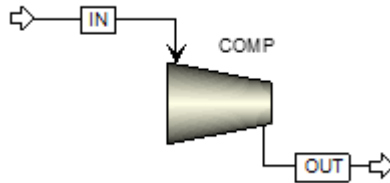


Figure E.5: Process flow diagram of the *Aspen Plus v11* simulation used to calculate the performance of a pump

Listing E.3 Configuration of a compressor performance calculation in *PowerCycle*

```

1  import Simulator
2  from Simulator.streams import MaterialStream
3  from FluidProperties.fluid import Fluid
4
5  inlet = Fluid(["carbondioxide", 1])
6  inlet = MaterialStream(inlet, m=1)
7  inlet.update("PT", Pin, Tin)
8
9  compressor = Simulator.pump(0.85, mech_eff=0.95)
10 compressor.set_inputs(inlet, Pout)
11 outlet = compressor.calc()
  
```

Table E.5: The compressor performance calculation results for *Aspen Plus* and *PowerCycle*

Parameter	Units	Aspen Plus v11	Power Cycle	Difference/%
T_{out}	K	784.65	784.65	0.00
\dot{W}	kW	499.53	499.53	0.00
\dot{W}_{elec}	kW	525.82	525.82	0.00

E.5. Multi-Stage Compressor

The inlet stream was initialised to a temperature of 298 K (25 °C) and a pressure of 1 bar. The compressor isentropic and mechanical efficiencies were assumed to be 85 % and 95 %

respectively. The outlet pressure was set to 10 bar. For a summary of the inlet conditions, see Table E.6.

Table E.6: Comparison of the multi-stage compressor performance calculations between *PowerCycle* and *Aspen Plus*

Parameter	Units	Value
Fluid	-	Carbon Dioxide
\dot{m}	kg s^{-1}	1
P_{in}	bar	0.1
T_{in}	K	298
P_{out}	bar	10
n_{stages}	-	3

The multi-stage compressor performance calculations in *Aspen Plus* and *PowerCycle* were compared using corresponding standalone multi-stage compressor models, see Figure E.6, and Listing E.4. The performance calculation results were found to be in good agreement, Table E.7.

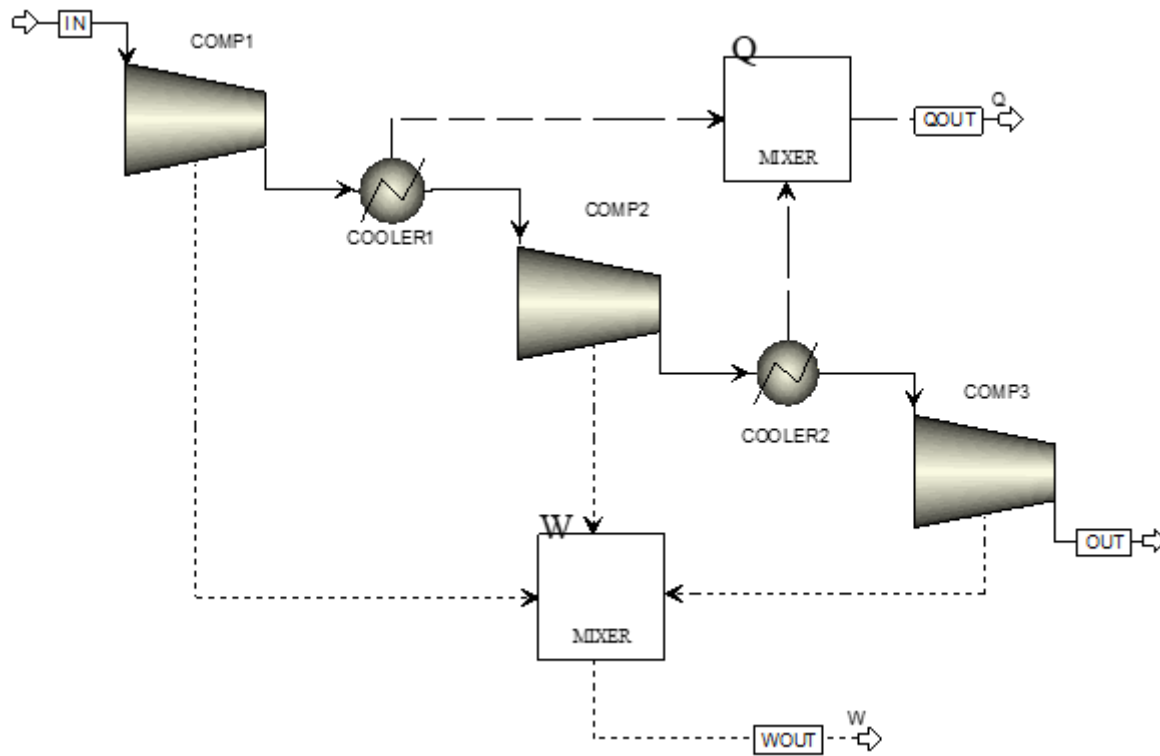


Figure E.6: Process diagram of the *Aspen Plus* simulation used to calculate the performance of a multi-stage compressor

Listing E.4 Configuration of a multi-stage compressor performance calculation in *PowerCycle*

```

1  import Simulator
2  from Simulator.streams import MaterialStream
3  from FluidProperties.fluid import Fluid
4
5  inlet = Fluid(["carbondioxide", 1])
6  inlet = MaterialStream(inlet, m=1)
7  inlet.update("PT", Pin, Tin)
8
9  compressor = Simulator.multistage_compression(0.85, 1, mech_eff=0.95)
10 compressor.set_inputs(inlet, Pout, findN=True)
11 outlet = compressor.calc()

```

Table E.7: The multi-stage compressor performance calculation results for *Aspen Plus v11* and *PowerCycle*

Parameter	Units	Aspen Plus v11	Power Cycle	Difference/%
T_{out}	K	431.75	431.94	-0.04
\dot{W}	kW	359.56	359.67	-0.03
\dot{W}_{elec}	kW	378.48	378.60	-0.03
$\dot{Q}_{cooling}$	kW	242.43	242.36	0.03

